



Norbert Zehentner, Dipl.-Ing., Bakk.techn.

# **Kinematic orbit positioning applying the raw observation approach to observe time variable gravity**

## **Doctoral Thesis**

to achieve the University degree of

Doktor der technischen Wissenschaften

submitted to

**Graz University of Technology**

Supervisor

Univ.-Prof. Dr.-Ing. Torsten Mayer-Gürr

Institute of Geodesy

Working group Theoretical Geodesy and Satellite Geodesy

---

Graz, November 2016

## AFFIDAVIT

I declare that I have authored this thesis independently, that I have not used other than the declared sources/resources, and that I have explicitly indicated all material which has been quoted either literally or by content from the sources used. The text document uploaded to TUGRAZonline is identical to the present doctoral thesis.

---

Date

---

Signature

## Acknowledgment

A lot of people contributed to the successful creation of this thesis in some way. This is the place to express my sincere thanks to all of them. I would not have finished this work without their advice, guidance, and support.

First of all I want to thank my supervisor Torsten Mayer-Gürr for giving me the possibility to work on this interesting topic. During the past years his door, as well as his mind, was always open for fruitful discussions. He guided me through the whole process and gave advice and helpful hints whenever a problem arose.

I also thank Adrian Jäggi, not only for acting as external reviewer and second referee, but also for many interesting discussions during the past years and his willingness to share his experience.

I want to also thank my colleagues at the Institute of Geodesy for their help and for the numerous joyful moments playing table soccer, which were a welcome distraction during all times. Special thanks go to Christian Pock, for being a great office mate and for the numerous talks on more or less scientific topics.

I am grateful to my mother and my father for their support in every chapter of my life. They gave me the confidence to follow my dreams.

Finally, my sincere thanks go to Claudia, for her patience, her loyalty, her faith in me, and her love.

To all of you, including those I did not mention explicitly, I say:

Thank you

## Abstract

Observing temporal changes of gravity has become a vital source of information about changes in the system Earth. Currently these variations are observed by the satellite mission Gravity Recovery and Climate Experiment (GRACE). Besides this mission no other technique is capable of providing the same resolution, both in space and time. Although a follow-on mission is under preparation, it is likely that the highly valuable observational record might be interrupted. Hence, there is a great interest in developing an additional opportunity to observe variations in the Earth's gravity field.

One possible method to observe the gravity field is based on precise positions of low Earth orbiting satellites. The position of the satellite can be observed by an on-board Global Navigation Satellite System (GNSS) receiver. It provides measurements which can be used to compute a kinematic orbit without introducing a priori information. Subsequently the positions can be used to estimate the Earth's gravity field. The approach, denoted as Satellite-to-Satellite Tracking in high-low mode (SST-hl), is well known and widely used. However, the accuracy of the derived gravity field solutions depends on the quality of the introduced orbit positions. Current state-of-the-art orbits are only capable of resolving the largest gravity variations. Available orbit estimates are degraded by systematic effects or the measurement noise exceeds the amplitude of the sought for signals.

The goal of this work was to develop a new method for kinematic orbit determination based on raw GNSS measurements. The essence of the proposed raw observation approach is to leave the GNSS measurements unchanged and process all observables jointly in an iterative least-squares adjustment. Systematic effects are either corrected or set up as additional parameters. The combination of different observation types necessitates a realistic weighting scheme in combination with a flexible outlier detection. The validation of computed kinematic orbits revealed that the raw observation approach is capable of producing orbit positions with the same or better accuracy than existing methods.

Estimated satellite positions were then used to generate monthly gravity field solutions. Investigations based on a 13 year time series, including data from 15 satellites, showed that it is possible to observe gravity changes. An analysis of major river basins revealed that mass variations can be detected for areas larger than 500 000 km<sup>2</sup>, if the amplitude of the signal is sufficiently large. In view of the continuously increasing number of satellites equipped with GNSS receivers and the ongoing evolution of GNSS in general, the results obtained in this work suggest that SST-hl could be a true alternative or at least a supplement to other technologies.

## Kurzfassung

Die Beobachtung zeitlicher Veränderungen im Erdschwerefeld stellt eine wichtige Informationsquelle bei der Erforschung des Systems Erde dar. Derzeit wird dies nur durch die Satellitenmission Gravity Recovery and Climate Experiment (GRACE) ermöglicht. Abgesehen davon gibt es keine Technologie, welche in der Lage ist die gleiche zeitliche und räumliche Auflösung zu liefern. Trotz geplanter Nachfolgemission ist es wahrscheinlich, dass die Messzeitreihe unterbrochen wird. Daher besteht ein reges Interesse an einer zusätzlichen Methode zur Beobachtung von Veränderungen im Erdschwerefeld.

Eine Möglichkeit zur Bestimmung des Erdschwerefeldes basiert auf präzisen Orbitpositionen von niedrig fliegenden Satelliten. Die Berechnung der Satellitenposition erfolgt dabei mittels Global Navigation Satellite System (GNSS) Empfängern. Deren Messungen werden verwendet um ohne Einführung von Vorinformationen einen kinematischen Orbit zu berechnen. In weiterer Folge wird aus den Positionen das Schwerefeld abgeleitet. Diese Methode wird auch als Satellite-to-Satellite Tracking in high-low mode (SST-hl) bezeichnet und wurde bereits vielfach angewendet. Die Genauigkeit der Schwerefeldbestimmung ist jedoch abhängig von der Qualität der verwendeten Positionen. Mit derzeit verfügbaren Orbits sind nur die größten Veränderungen messbar, da das Signal durch systematische Effekte oder das Messrauschen überlagert wird.

Ziel dieser Arbeit war es eine Methode zur kinematischen Orbitbestimmung, basierend auf rohen GNSS Beobachtungen, zu entwickeln. Der Kern des verwendeten Raw Observation Approach ist es die Messungen unverändert zu lassen und die verfügbaren Beobachtungen in einem iterativen Kleinste-Quadrate Ausgleich zu verarbeiten. Systematische Effekte werden dabei entweder korrigiert oder als Parameter mitgeschätzt. Die Kombination von verschiedenen Beobachtungsarten erfordert eine realistische Gewichtung sowie eine flexible Ausreißerdetektion. Vergleiche haben gezeigt, dass der Raw Observation Approach gleiche oder bessere Resultate liefert als aktuelle Methoden.

Um eine 13 Jahre lange Zeitreihe von monatlichen Schwerefeldern zu erzeugen, wurden die Daten von insgesamt 15 Satelliten verwendet. Diese Messreihe ermöglicht nun die Beobachtung von zeitlichen Variationen. Eine Analyse der weltweit größten Flussbecken hat gezeigt, dass eine Detektion von Veränderungen möglich ist für Gebiete  $>500\,000\text{ km}^2$ , sofern das Signal eine ausreichende Amplitude aufweist. Im Lichte der immer größeren Anzahl an Satelliten mit GNSS Empfängern und der grundsätzlichen Weiterentwicklung von GNSS, zeigen die Resultate dieser Arbeit, dass SST-hl eine Alternative oder eine wertvolle Ergänzung zu anderen Technologien darstellt.

# Contents

<b>Abstract</b>	<b>ii</b>
<b>Kurzfassung</b>	<b>iii</b>
<b>1 Introduction</b>	<b>1</b>
<b>2 Basic concepts</b>	<b>3</b>
2.1 Satellite Orbits . . . . .	3
2.2 Coordinate systems . . . . .	4
2.2.1 Celestial Reference System . . . . .	4
2.2.2 Earth Fixed Reference System . . . . .	5
2.2.3 Local orbit reference frame . . . . .	5
2.2.4 Satellite Body Frame . . . . .	6
2.2.5 Antenna Frame . . . . .	6
2.3 The Earth's gravity field . . . . .	7
2.4 Gravity field estimation . . . . .	9
2.5 Least squares adjustment . . . . .	11
2.6 Variance Component Estimation . . . . .	12
<b>3 Satellite missions</b>	<b>13</b>
3.1 CHAMP . . . . .	13
3.1.1 Instruments . . . . .	13
3.1.2 GPS receiver . . . . .	15
3.2 GRACE . . . . .	16
3.2.1 Microwave ranging system . . . . .	17
3.2.2 GPS receiver . . . . .	18
3.3 GOCE . . . . .	18
3.3.1 Electrostatic Gravity Gradiometer . . . . .	19
3.3.2 GPS receiver . . . . .	19
3.4 Non-dedicated gravity field satellites . . . . .	21
3.4.1 Swarm . . . . .	21
3.4.2 TerraSAR-X . . . . .	22
3.4.3 TanDEM-X . . . . .	23
3.4.4 MetOp A and B . . . . .	24
3.4.5 SAC-C . . . . .	26
3.4.6 Jason 1 and 2 . . . . .	27

## Contents

3.4.7	C/NOFS . . . . .	28
3.4.8	FORMOSAT-3/COSMIC . . . . .	29
3.5	Comparison of satellite characteristics . . . . .	30
<b>4</b>	<b>Orbit determination</b> . . . . .	<b>32</b>
4.1	Global Navigation Satellite Systems . . . . .	32
4.1.1	History . . . . .	32
4.1.2	Principles of GNSS . . . . .	32
4.1.3	Observation types . . . . .	33
4.1.4	Derived observation types . . . . .	35
4.1.5	Systematic effects and noise . . . . .	37
4.1.5.1	Transmitter effects . . . . .	37
4.1.5.2	Propagation effects . . . . .	41
4.1.5.3	Receiver effects and measurement noise . . . . .	45
4.2	Positioning methods . . . . .	50
4.2.1	Single point positioning . . . . .	50
4.2.2	Precise point positioning . . . . .	50
4.3	Precise orbit determination . . . . .	52
4.3.1	Raw observation approach . . . . .	53
4.3.1.1	Antenna center variations . . . . .	55
4.3.1.2	Ionospheric influence . . . . .	58
4.3.1.3	Observation weighting . . . . .	62
4.3.1.4	Outlier detection . . . . .	63
4.3.1.5	Cycle slip detection . . . . .	64
4.3.1.6	Receiver code bias . . . . .	65
<b>5</b>	<b>Orbit processing</b> . . . . .	<b>67</b>
5.1	General software description . . . . .	67
5.1.1	Basic functionality and data structure . . . . .	67
5.1.2	GnssNetwork . . . . .	69
5.2	Kinematic orbit determination . . . . .	71
<b>6</b>	<b>Kinematic POD for different missions</b> . . . . .	<b>74</b>
6.1	Satellite data and orbits . . . . .	74
6.1.1	Mission data description . . . . .	74
6.1.2	Resulting orbit products . . . . .	77
6.2	Specific aspects of real data processing . . . . .	80
6.2.1	Estimation of receiver antenna center variations . . . . .	80
6.2.2	Estimation of transmitter antenna center variations . . . . .	83
6.2.3	Receiver bias estimation . . . . .	89
6.2.4	Generation of observation weight mask . . . . .	90
6.2.5	Observation weight scaling . . . . .	94
6.2.6	2-antenna issue with FORMOSAT-3/COSMIC data . . . . .	97

## Contents

<b>7 Orbit and gravity field validation</b>	<b>99</b>
7.1 Orbit comparisons . . . . .	99
7.2 GRACE K-band validation . . . . .	118
7.3 SLR validation . . . . .	119
7.4 Gravity field . . . . .	126
7.4.1 Monthly gravity field solutions . . . . .	127
7.4.1.1 Single mission solutions . . . . .	128
7.4.1.2 Combined solutions . . . . .	131
7.4.2 Mass variations . . . . .	134
<b>8 Conclusions</b>	<b>140</b>
<b>Bibliography</b>	<b>143</b>
<b>Acronyms</b>	<b>160</b>
<b>List of figures</b>	<b>166</b>
<b>List of tables</b>	<b>167</b>

# 1 Introduction

Lithosphere, hydrosphere, atmosphere, biosphere and anthroposphere are the main constituents of a complex system named Earth — our home. All parts are highly complex and strongly interact with each other. In times of increasing changes in this system, reliable information about the different constituents is of crucial importance. To increase knowledge about the processes in, on and above the Earth's surface is not only of scientific interest. In fact, information about changes in the environment has become more and more important for society and especially for politics. Global climate change is one of the most important and most challenging topics in the 21st century (IPCC, 2014). Irrespective of the question whether the currently ongoing changes are triggered by human mankind or not, the changes will affect life on Earth.

To improve the knowledge about the environment and to understand different aspects and their interactions, scientists of different fields are observing, measuring and investigating the Earth and its surrounding. There are numerous methods to assess all kinds of physical processes of the environment. One of these methods is to observe the Earth's gravity field. In the context of global climate change it is of special interest to investigate time variations of the gravity field. In the last two decades specially designed satellite missions provided a major step forward in the field of gravity research. The main goal of these missions was to provide accurate information about the static gravity field of the Earth. The second goal, which has become even more important, is to provide information about changes in the gravity field.

An important and successful gravity mission is the Gravity Recovery and Climate Experiment (GRACE) (Tapley et al., 2004). This mission is capable of providing gravity field information with high spatial and temporal resolution. The results obtained by this mission are a valuable source of information for a wide range of scientific fields. Observations of gravity variations are used to study hydrological processes, ocean circulation, ice mass variations, geologic changes, global sea level rise and many more (Cazenave and J. Chen, 2010). As the value of any observations dealing with time variable signals is strongly depending on the length of the measured time series, it is of high importance to prolong the existing record. The very successful GRACE mission was launched in 2002 and is now in operation for more than 14 years. Although there is a follow on mission under preparation (Flechtner et al., 2014), it is important to develop alternative methods to observe changes in the Earth's gravity field. This is not only necessary to fill possible gaps in the time series. It is equally important to provide

## 1 Introduction

an independent measurement technique, to facilitate a combination and benefit of the advantages of different methods. In addition, it is also important to validate findings based on existing measurements.

A potential method is Satellite-to-Satellite Tracking in high-low mode (SST-hl). This technique is based on the observation of Low Earth Orbit (LEO) satellite positions. For most LEO satellites an on-board Global Navigation Satellite System (GNSS) receiver is used to provide accurate information about the satellite orbit. The observations of the GNSS receiver are used to measure the positions of the satellite, with accuracies in the range of a few centimeters (Švehla and Rothacher, 2005). The main aspect of the SST-hl approach is to compute the satellite positions without introducing information other than the geometric GNSS observations. As a result of this restriction, the generated orbit is purely kinematic. The precise positions may then be used as pseudo-observations to estimate the Earth's gravity field.

The primary goal of this thesis was to implement a method to exploit raw GNSS measurements for precise orbit determination. In a second step the computed positions were used to generate a time series of global gravity field estimates. Based on this time series the possibility to derive mass variations was investigated. The thesis describes all necessary basics for GNSS based orbit determination as well as gravity field determination using orbit positions. The method was applied to Global Positioning System (GPS) observations from dedicated gravity field satellites as well as non-dedicated LEO satellites.

After this introduction, basic concepts of satellite geodesy are introduced in chapter 2. In chapter 3 the used satellite missions and their scientific instruments are briefly described. Chapter 4 focuses on the methods applied for precise orbit determination. In particular this chapter describes the newly developed method for orbit determination based on raw GNSS measurements. Chapter 5 introduces the developed software and outlines the principle processing chain to achieve highly accurate kinematic orbits. Chapter 6 describes in detail the used real data sets from different satellite missions, the resulting orbit products, and addresses specific aspects of kinematic orbit determination, which all have an influence on the achievable accuracy.

Chapter 7 describes the validation of the generated orbits. This is done by comparing to independent orbit solutions and Satellite Laser Ranging (SLR) observations. Finally gravity field solutions derived from kinematic orbit positions are presented. The results are validated against gravity field products from different processing centers. The final part of this chapter deals with the derivation of time variable signals on the basis of the produced gravity field time series. This part will answer the question to what extent it is possible to derive mass variations solely from SST-hl observations. It will quantify to what extent an assessment of such signals is possible, in terms of spatial resolution.

The final chapter 8 summarizes the achieved results and gives a brief outlook into further possible research in the context of Precise Orbit Determination (POD), gravity field estimation and the derivation of time variable signals.

## 2 Basic concepts

### 2.1 Satellite Orbits

In the context of this thesis the term satellite always denotes artificial satellites in an orbit around the Earth. In contrast to natural satellites, like the moon, these satellites were placed intentionally in a selected orbit. According to Kepler's laws the orbit of a satellite around a massive central body is a conic section. When it comes to satellites orbiting the Earth a simple and descriptive way to describe the orbit is to use the Keplerian elements.

- Semi-major axis  $a$
- Eccentricity  $e$
- Inclination  $i$
- Right ascension of the ascending node  $\Omega$
- Argument of perigee  $\omega$
- True anomaly  $\nu$  at time  $t_0$

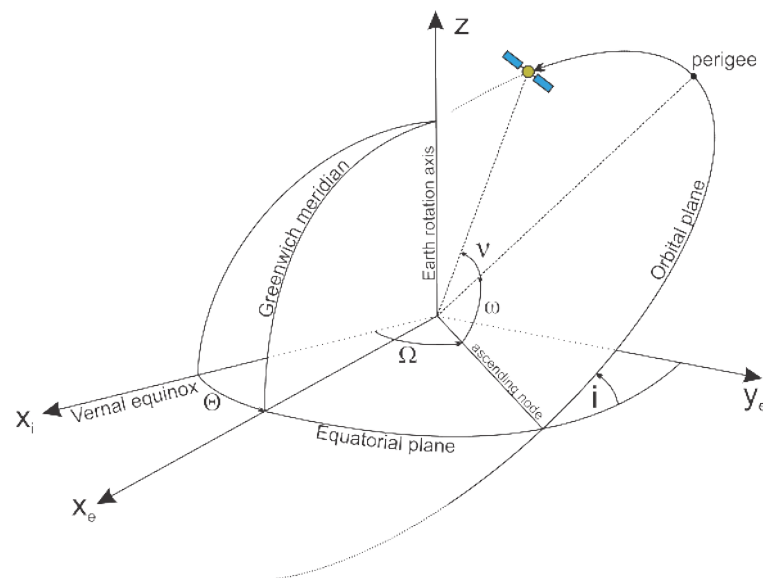


Figure 2.1: Illustration of Keplerian elements describing a satellite orbit in the inertial frame.

Figure 2.1 illustrates the definition of the Keplerian elements in the inertial frame and the approximate relation to the Earth fixed reference frame via the sidereal time  $\Theta$ .  $a$  and  $e$  determine the shape of the ellipse,  $i$  and  $\Omega$  the orientation of the orbital plane,  $\omega$  the orientation of the ellipse in the orbital plane and  $\nu$  the actual position of the satellite at a specific time  $t_0$ .

## 2 Basic concepts

In principle satellites can be placed in any kind of orbit. However, there are a few categories of satellite orbits which are most often used. According to some orbit characteristics satellites are associated to one of the groups listed in table 2.1 (Montenbruck and Gill, 2000).

Name	Property
Low Earth Orbit (LEO)	orbiting altitudes from 200 to 2000 km
Medium Earth Orbit (MEO)	orbiting altitudes from 2000 to 35 786 km
Geostationary Earth Orbit (GEO)	orbit altitude of 35 786 km with $0^\circ$ inclination
Geosynchronous Orbit (GSO)	orbit altitude of 35 786 km, inclination $\neq 0^\circ$
Highly Elliptical Orbit (HEO)	orbit with large eccentricity (low perigee, high apogee)

Table 2.1: Orbit categories and their characteristics.

## 2.2 Coordinate systems

Applications in any geoscientific field involve coordinates in different ways. Either as the position of a single observation point somewhere on the Earth's surface or as pixel coordinates in a satellite image. For a proper handling of different coordinates the underlying coordinate systems are described. In the context of satellite observations there are several coordinate systems used.

### 2.2.1 Celestial Reference System

The celestial reference system is a three dimensional right-handed Cartesian coordinate system. It is often denoted as quasi-inertial reference system, as no real inertial system can be realized due to the movement of the whole solar system and the presence of large masses. A quasi standard is the definition of systems provided by the International Astronomical Union (IAU) (IAU, 2000). The definition includes a Geocentric Celestial Reference System (GCRS) as well as a Barycentric Celestial Reference System (BCRS). For applications on or near the Earth, it is advisable to make use of the GCRS as its origin is located in the Earth's center of mass. The xy-plane is defined as the equatorial plane for the epoch J2000.0. The positive z-axis points towards the North Pole and corresponds to the rotation axis of the Earth. The positive x-axis points towards the vernal equinox for the epoch J2000.0. The system is completed by the y-axis that is perpendicular to the xz-plane. This definition is also adopted by the International Earth Rotation Service (IERS) conventions 2010 (Petit and Luzum, 2010).

### 2.2.2 Earth Fixed Reference System

An Earth fixed reference system, or also Terrestrial Reference System (TRS), is a three dimensional Cartesian coordinate system connected to the Earth's crust and therefore co-rotating with it. Point coordinates on the Earth's surface expressed in a TRS are constant and undergo only small changes due to geophysical processes like tectonic plate movement. A TRS is the definition of a reference system. More important for practical applications is the Terrestrial Reference Frame (TRF), which is the actual realization of the system definition. The most important realization of a TRS is the International Terrestrial Reference Frame (ITRF). It is defined and maintained by the IERS and adopted as standard global TRF in the IERS conventions 2010 (Petit and Luzum, 2010). The currently used realization of the ITRF is the ITRF2008 (Altamimi et al., 2011). It is represented by 934 observation stations at 580 sites. The ITRF2008 solution is based on four measurement techniques, Very Long Baseline Interferometry (VLBI), SLR, GNSS and Doppler Orbitography and Radiopositioning Integrated by Satellite (DORIS). The IERS provides transformation parameters to convert between the ITRF2008 and previous realizations (Petit and Luzum, 2010). There are four different ways to access the ITRF2008:

- Use coordinates of an ITRF station
- Use International GNSS Service (IGS) products (e.g. GPS orbits and clocks) for a GNSS analysis
- Use ITRF stations as reference station in GNSS analysis
- Use transformation parameters from a TRF to the ITRF

### 2.2.3 Local orbit reference frame

The Local Orbit Reference Frame (LORF) is defined as a three dimensional Cartesian coordinate system with its origin in the satellite's Center of Mass (CoM). The orientation is given by the inertial velocity of the CoM and the instantaneous orbital plane in the following way:

$$\begin{aligned} \mathbf{x}_{lorf} &= \frac{\mathbf{v}_i}{|\mathbf{v}_i|} \\ \mathbf{y}_{lorf} &= \frac{\mathbf{r}_i \times \mathbf{v}_i}{|\mathbf{r}_i \times \mathbf{v}_i|} \\ \mathbf{z}_{lorf} &= \mathbf{x}_{lorf} \times \mathbf{y}_{lorf} \end{aligned} \quad (2.1)$$

$x$ ,  $y$  and  $z$  are the coordinate axes of the LORF expressed in the inertial frame.  $v_i$  denotes the satellite velocity in inertial frame and  $r_i$  the corresponding position. More descriptive names often used for the three axes are along-track, cross-track and radial component, although following this definition the radial component is not exactly radial. The definition could be also strictly aligned with the radial component. In this case the  $x$ -axis and the velocity direction would deviate from each other. Sometimes the cross-track component is also denoted as out-of-plane, which more precisely describes the definition of the axis as being perpendicular to the instantaneous orbital plane.

### 2.2.4 Satellite Body Frame

To define the whole structure of the satellite during the design and implementation of the space craft a body fixed coordinate system is necessary. The definition is somehow arbitrary. The origin is sometimes located near the center of mass or at a distinct point of the main satellite bus, like for example a corner or the center of the mounting ring. The axes are commonly aligned with the edges of the main satellite bus. Figure 2.2 shows the relation between LORF, body frame and antenna frame, described in the next section. The relation between satellite body frame and inertial reference frame is denoted as the satellite attitude. For precise observations of the satellite attitude star cameras are used. Some satellites also make use of Sun or Earth sensors in combination with a magnetometer. Knowledge about the satellite attitude is needed to relate all kinds of observations to the inertial reference frame.

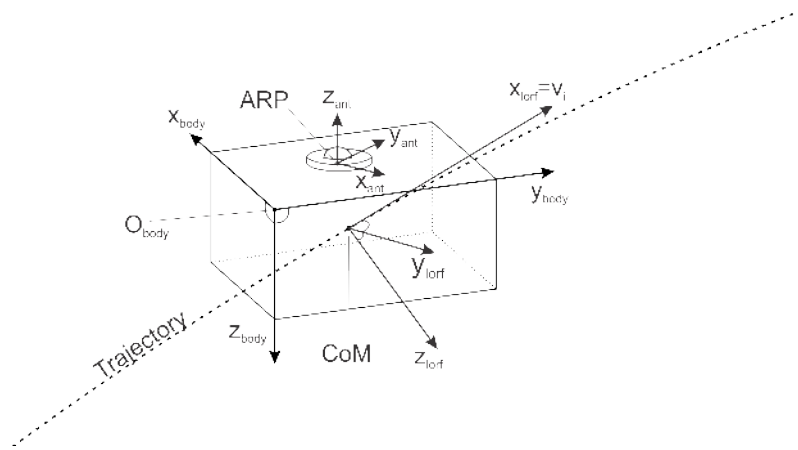


Figure 2.2: Illustration of the three coordinate systems related to the orbit, the satellite and the antenna.

### 2.2.5 Antenna Frame

The antenna frame has its origin in the Antenna Reference Point (ARP), defined by the antenna manufacturer. In practice this is mostly the center of the mounting. The antenna frame is a right handed Cartesian coordinate system. The definition follows those for ground based antennas which represent a local North-East-Up system. As all procedures dealing with GNSS antennas, for example calibration methods, were based on this definition it was also used for satellite applications. To explore antenna properties, observations or residuals are transformed into the antenna frame and then examined with respect to systematic errors or special aspects. In most cases polar coordinates are used in the antenna frame, rather than Cartesian. The angles are denoted as azimuth and elevation. The azimuth is defined as the angle between the y-axis and the projected vector in the x-y plane and the elevation is the angle above the x-y plane. For ground based observations elevation corresponds to the angle above the local horizon and the azimuth counts clockwise from the north direction towards the east direction. On most satellites

the antenna is mounted in a way that the bore sight vector points towards the zenith and the y-axis of the antenna frame is parallel to the nominal along-track direction.

## 2.3 The Earth's gravity field

The Earth's gravity field is determined by the distribution of masses inside the whole system Earth. According to Newton's law of gravitation, two bodies with non-zero masses attract each other with a certain force, depending on the distance between the two objects. The force is described by

$$F = G \frac{m_1 m_2}{l^2} \quad (2.2)$$

with  $G$  being Newton's gravitational constant,  $m_1$  and  $m_2$  are the masses of the two considered bodies, and  $l$  the distance between the objects. The gravitational constant  $G$  is a physical constant determined as (Mohr et al., 2008)

$$G = 6.67428 \cdot 10^{-11} \pm 6.7 \cdot 10^{-15} m^3 kg^{-1} s^{-2}. \quad (2.3)$$

If one of the masses is considered to be far bigger than the second, which is the case for relations like for example the Earth with respect to the sun or for artificial satellites in relation to the Earth, the smaller mass can be set to unity. Then equation 2.2 simplifies to

$$F = G \frac{M}{l^2}, \quad (2.4)$$

where  $M$  is the mass of the larger body.  $F$  now describes the force exerted on an object with unity mass by the central body with mass  $M$ . After introducing a rectangular coordinate system and the scalar function

$$V = G \frac{m}{l} \quad (2.5)$$

the force  $F$  may be represented as a vector  $\mathbf{F}$ , which is obtained by differentiating the scalar function by all three components. This is also seen as  $\mathbf{F}$  being the gradient of the scalar function  $V$ . Due to the fact that the Earth has a specific extend and in addition a non-uniform distribution of masses inside the body, the gravity field of the Earth is the sum of forces caused by all mass particles contained in the Earth's body. If spherical coordinates are used, this leads to the description of the gravitational potential as a series of spherical harmonics (Heiskanen and Moritz, 1967)

$$V(\lambda, \theta, r) = \frac{GM}{R} \sum_{n=0}^{\infty} \sum_{m=0}^n \left(\frac{R}{r}\right)^{n+1} (c_{nm} C_{nm}(\lambda, \theta) + s_{nm} S_{nm}(\lambda, \theta)). \quad (2.6)$$

$\lambda$ ,  $\theta$ , and  $r$  are spherical coordinates in the Earth fixed reference frame.  $M$  is the Earth's mass,  $R$  the Earth's reference radius,  $c_{nm}$  and  $s_{nm}$  are coefficients describing the mass distribution, and  $C_{nm}$  and  $S_{nm}$  are the base functions defined as

$$C_{nm}(\lambda, \theta) = \cos(m\lambda) \bar{P}_{nm}(\cos \theta), \quad (2.7)$$

## 2 Basic concepts

$$S_{nm}(\lambda, \theta) = \sin(m\lambda) \bar{P}_{nm}(\cos \theta). \quad (2.8)$$

$\bar{P}_{nm}$  are the associated Legendre functions, and  $C_{nm}$  and  $S_{nm}$  are called spherical harmonics. This formulation as a series of spherical harmonics is the standard way of describing the Earth's gravity field by providing numerical values for the coefficients  $c_{nm}$  and  $s_{nm}$ . These coefficients can be determined from various types of measurements by applying the principle of least squares adjustment, described in section 2.5.

In order to compare different models of the Earth's gravity field an often used measure are the so called degree variances or amplitudes (van Gelderen and Koop, 1997). They are computed for each degree of the model separately using the following formulation for variances

$$\sigma^2 = \sum_{m=0}^n (c_{nm}^2 + s_{nm}^2). \quad (2.9)$$

Taking the square root of  $\sigma^2$  would lead to degree amplitudes.

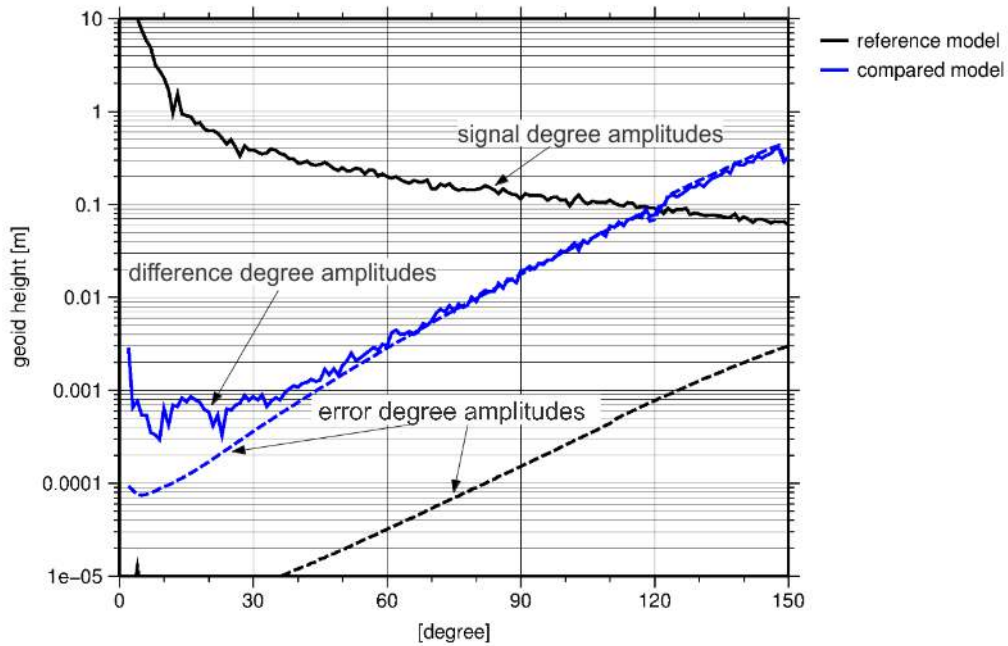


Figure 2.3: Three different variations of degree amplitudes.

If coefficients are used directly one gets the total signal content for each degree, denoted as signal degree variances or amplitudes, depending on whether the squared  $\sigma$  is used or the square root of it. The coefficients can be replaced by their formal errors to compute the error degree variances. To compare two data sets, usually the coefficients are replaced by coefficient differences, which then lead to the difference degree variances. If one of the two solutions is much more accurate than the second, error degree variances and difference degree variances should show the same behavior. Figure 2.3 shows a degree amplitude plot to illustrate the three different versions of degree amplitudes.

## 2.4 Gravity field estimation

There are numerous methods and concepts to estimate the Earth's gravity field (Johannessen et al., 2003). In this work the focus lies on the concept of SST-hl (Johannessen et al., 2003). A satellite at a low altitude is tracking signals emitted by high altitude satellites. The signals are used to measure ranges or range rates. As the inhomogeneous gravity field of the Earth is the main contributor to variations of the satellite orbit, these observations can be related to the gravity field. In the frame of this thesis data from satellites realizing the approach by using an on board GNSS receiver, tracking the signals of high GNSS satellites. Other forces acting on the satellite must be taken into account, either by measurements or models.

There are two different ways to exploit the observations of a space borne GNSS receiver. Either by directly linking the observations to the gravity field parameters in one common estimation process (Reigber et al., 2003) or by following a two-step approach (Gerlach et al., 2003). The latter is commonly used in the scientific community. The following explanations will concentrate on the two-step approach, as it is also the method used within this work.

The first step is to use the GNSS observations to derive a kinematic orbit of the LEO satellite. In a second step the estimated orbit positions are introduced as pseudo-observations for the gravity field determination. This approach has several advantages. First of all, the computational complexity is split into two separate parts, which makes it easier to exchange things in one or the other component. Secondly, for processing the GNSS measurements, already existing technologies, developed for ground based applications, might be used and tailored for this specific application. The situation is similar for the second component. There are several methods available to estimate gravity field parameters from derived orbit positions. Furthermore, it is possible to interchange intermediate results, the orbit positions, between different scientific institutions and use them for an inter-comparison or a combination of different approaches. Last but not least, the generated orbit products might be also used for any other application.

An important aspect for the orbit estimation is the fact that the computed positions shall be purely based on geometric observations. This type of orbit solution is denoted as kinematic orbit (Švehla and Rothacher, 2003) and does not rely on a priori force models for the LEO satellite. Positions are estimated for each measurement epoch, as long as enough observations are available. In contrast to this, reduced-dynamic or dynamic orbits rely on force models for the orbit integration (S. C. Wu et al., 1991; Švehla and Rothacher, 2003; Jäggi, 2007). This would mean that a gravity field model derived from such an orbit product could be biased towards these models as shown by Gerlach et al. (2003).

As already mentioned, there are several methods available to derive gravity fields from kinematic orbit positions. Widely used are the celestial mechanics approach (Beutler

## 2 Basic concepts

et al., 2010), the acceleration approach (Reubelt et al., 2003), the energy balance approach (Han, 2002), or the short arc integral approach (Mayer-Gürr, 2006). In this work the method of choice was the short arc integral approach. Recent investigations have shown that all methods, except the energy balance approach, feature equal results (Baur et al., 2014).

**Short arc integral approach** The short arc integral approach is described in detail by Mayer-Gürr (2006). It has been used to generate several global gravity field models based on Challenging Minisatellite Payload (CHAMP) and GRACE data, namely the ITG-GRACE (Mayer-Gürr, 2007; Mayer-Gürr et al., 2010) and ITG-CHAMP (Ilk et al., 2005) models, as well as the recently released ITSG-Grace2014 (Mayer-Gürr et al., 2014).

The basic relation between the orbit and the accelerations acting on the satellite is realized by Newton's law of motion

$$\ddot{\mathbf{r}}(t) = \mathbf{f}(t, \mathbf{r}, \dot{\mathbf{r}}) \quad (2.10)$$

where  $\mathbf{r}$ ,  $\dot{\mathbf{r}}$ , and  $\ddot{\mathbf{r}}$  are position, velocity, and acceleration vectors of the satellite, given in the inertial frame. The solution can be formulated as boundary value problem (Schneider, 1968) in the form

$$\mathbf{r}(\tau) = (1 - \tau)\mathbf{r}_A + \tau\mathbf{r}_B - T^2 \int_0^1 K(\tau, \tau') \mathbf{f}(\tau') d\tau' \quad (2.11)$$

with the integral kernel defined as

$$K(\tau, \tau') = \begin{cases} \tau'(1 - \tau) & \text{for } \tau' \leq \tau \\ \tau(1 - \tau') & \text{for } \tau' > \tau \end{cases} \quad (2.12)$$

and the normalized time variable

$$\tau = \frac{t - t_A}{T} \quad \text{with } T = t_B - t_A \quad (2.13)$$

and the unknown boundary positions  $\mathbf{r}_A$  and  $\mathbf{r}_B$  at times  $t_A$  and  $t_B$ . If equation 2.11 is evaluated at every epoch of a continuous satellite arc, this yields a system of equations.

$$\mathbf{l} = \mathbf{B}\mathbf{b} + \mathbf{h} \quad (2.14)$$

$\mathbf{l}$  is a vector containing the observations (satellite positions),  $\mathbf{b}$  are the boundary values,  $\mathbf{B}$  are the corresponding times, and  $\mathbf{h}$  contains the integral evaluated for the observation times, which is a functional of the gravitational potential, eq. 2.6. After eliminating the boundary values by means of parameter elimination (Meissl, 1982), the system of equations is solved by applying the method of least squares adjustment (see sect. 2.5). For a detailed description of the short arc integral approach and aspects of real data application the reader is referred to Mayer-Gürr (2006).

## 2.5 Least squares adjustment

The principle of least squares adjustment (see for example Meissl (1982) or Koch (2004)) to get the best linear unbiased estimate of parameters in an overdetermined system of equations is widely used in the field of geodesy. Within this work least squares adjustment is used to estimate satellite orbits from GNSS observations as well as to derive the gravity field coefficients from kinematic orbit positions. The basic assumption is that there exists a mathematical relation between the observations and the sought for parameters in the form

$$\mathbf{l} = \mathbf{A}\mathbf{x} + \mathbf{e}, \quad (2.15)$$

where  $\mathbf{l}$  are the observations,  $\mathbf{e}$  are observation residuals,  $\mathbf{A}$  is the design matrix containing the functional model  $f$ , and  $\mathbf{x}$  are the parameters to be determined. If the mathematical relation between observations and parameters is not linear, the functional model  $f$  is expanded in a Taylor series and truncated after the linear term. The linearized form of the functional model can be written as

$$\mathbf{l} - f(\mathbf{x}_0) = \left. \frac{\partial f(\mathbf{x}_0)}{\partial \mathbf{x}} \right|_0 \mathbf{x} + \mathbf{e}, \quad (2.16)$$

where  $\mathbf{x}_0$  are a priori estimates for the parameters and  $\mathbf{x}$  then represents a supplement to the a priori values. The term  $\mathbf{l} - f(\mathbf{x}_0)$  is often referred to as '*observed minus computed*' or the reduced observations and  $\left. \frac{\partial f(\mathbf{x}_0)}{\partial \mathbf{x}} \right|_0$  are the elements of the design matrix  $\mathbf{A}$ . For sake of simplicity further discussions always assume either a linear or linearized system of normal equations, where  $\mathbf{l}$  stands for observations or reduced observations. The same holds for the design matrix  $\mathbf{A}$ , containing either the linear or the linearized function  $f$ , relating observations and parameters. Similar for  $\mathbf{x}$ , which is then representing either the parameters themselves or the supplement to the initial values.

In general this formulation is denoted as a linearized Gauss-Markov model. Solving the system of equations in a least squares sense leads to

$$\hat{\mathbf{x}} = (\mathbf{A}^T \mathbf{A})^{-1} \mathbf{A}^T \mathbf{l}. \quad (2.17)$$

$\hat{\mathbf{x}}$  are the adjusted parameters or the improvements to the initial values. If variable accuracies of observations shall be taken into account a weight matrix  $\mathbf{P}$ , dependent on the known accuracies of the measurements, is introduced,

$$\Sigma(\mathbf{l}) = \sigma^2 \mathbf{P}^{-1}. \quad (2.18)$$

This leads to a slightly modified formulation of equation 2.17

$$\hat{\mathbf{x}} = (\mathbf{A}^T \mathbf{P} \mathbf{A})^{-1} \mathbf{A}^T \mathbf{P} \mathbf{l} \quad (2.19)$$

and after some modifications this can be written as

$$\mathbf{N} \hat{\mathbf{x}} = \mathbf{n} \text{ with } \mathbf{N} = \mathbf{A}^T \mathbf{P} \mathbf{A} \text{ and } \mathbf{n} = \mathbf{A}^T \mathbf{P} \mathbf{l}. \quad (2.20)$$

This is referred to as the system of normal equations.

## 2.6 Variance Component Estimation

For different applications, it is often necessary to combine observations of different nature and thus differing accuracies. To not only rely on the a priori assumed measurement accuracies it would be beneficial to estimate the relative weighting of several observation groups from the measurements themselves. Therefore the method of variance component estimation has been established. The following formulation is based on the approach described by Koch and Kusche (2002). It starts from equation 2.20 and assumes that

$$\mathbf{N}\hat{\mathbf{x}} = \mathbf{n} \text{ with } \mathbf{N} = \sum_k \frac{1}{\hat{\sigma}_k^2} \mathbf{N}_k \text{ and } \mathbf{n} = \sum_k \frac{1}{\hat{\sigma}_k^2} \mathbf{n}_k, \quad (2.21)$$

where the index  $k$  denotes a group of observations. The variance for each group  $\hat{\sigma}_k^2$  is defined as

$$\hat{\sigma}_k^2 = \frac{\Omega_k}{r_k} \text{ with } \Omega_k = \hat{\mathbf{e}}_k^T \hat{\mathbf{e}}_k \text{ and } r_k = m_k - \frac{1}{\sigma_k^2} \text{trace}(\mathbf{N}_k \mathbf{N}^{-1}). \quad (2.22)$$

$m_k$  is the number of observations in the group and  $r_k$  is the corresponding redundancy. The computation of residuals  $\hat{\mathbf{e}}$ , defined as  $\hat{\mathbf{e}} = \mathbf{1} - \mathbf{A}\hat{\mathbf{x}}$ , requires a solution for  $\hat{\mathbf{x}}$ . Thus the whole process of solving the system of normal equations is carried out iteratively. This repeated computation is continued until a predefined convergence criterion is met. It might be defined as a threshold in the changes of the parameters from the previous to the current iteration or as a threshold for the relative change in the estimated variances. In this work variance component estimation is used for several aspects. In the kinematic orbit processing software it is used to estimate a posteriori variances for different observation types to find bad measurements and to reduce their weight in the least squares adjustment. For gravity field processing variance component estimation is essential to find proper weights for individual arcs as well as for different monthly solutions in a combined estimation.

## 3 Satellite missions

The subsequent chapter briefly introduces the satellite missions used in the frame of this thesis. This includes dedicated gravity field missions as well as several non-dedicated missions.

### 3.1 CHAMP

The first dedicated gravity field mission Challenging Minisatellite Payload (CHAMP) (Reigber et al., 2002) was proposed, built and operated by the German Research Center for Geosciences (GFZ) in close cooperation with the German Aerospace Center (DLR) and the European aerospace industry. Preparations for the mission started in 1997. The satellite was finally launched on July 15, 2000 from the Russian Cosmodrome Plesetsk on a Russian Kosmos-3M launcher. The mission was dedicated to the study of Earth's magnetic field, Earth's gravity field, and atmospheric research by means of radio occultation (Reigber et al., 1999). In the context of magnetic field research CHAMP was the successor to the very successful mission Oersted (Thomsen and Hansen, 1999) and should provide new insights into the temporal behavior of the magnetic field. For gravity field determination and investigations of the atmosphere the satellite carried a high quality GPS receiver (Kuang et al., 2001). CHAMP was injected into a near polar orbit (87° inclination) with a mean altitude of 460 km (Reigber et al., 2002). Over its lifetime of 10 years, the satellite slowly decayed until it finally burned in the atmosphere on September 19, 2010. CHAMP data has been used by different institutions to compute gravity field models, for example AIUB-CHAMP03S (Prange, 2010), EIGEN-CHAMP05S (Flechtner et al., 2010), ITG-CHAMP01 (Ilk et al., 2005).

#### 3.1.1 Instruments

CHAMP carried several instruments to map the Earth's magnetic field. The two main components were a vector magnetometer and an absolute magnetometer (Reigber et al., 2002). The two instruments were placed on a 4 m boom which was deployed after launching the satellite into space. The separation of the magnetometers and the main satellite body was crucial to minimize the influence of the satellite's own magnetic signature on the measurements. Figure 3.1 shows an artist's impression of the satellite in orbit.

### 3 Satellite missions

In addition the satellite carried several instruments for different applications. One of them was the BlackJack GPS receiver developed and built at Jet Propulsion Laboratory (JPL) (Kuang et al., 2001). This receiver was designed to fulfill four different tasks within the CHAMP mission. The first task was to provide highly accurate satellite positioning to geolocate the measurements of all on-board instruments. The second application was to use the positions of the satellite to estimate the Earth's gravity field by applying the principle of SST-hl. For those two tasks the receiver used a zenith looking choke ring antenna. The third task was to observe signals of rising or setting GPS satellites to facilitate occultation measurements, which are used to study the Earth's atmosphere (Mannucci et al., 2008). These observations were carried out with an aft looking antenna mounted at the back of the satellite. The fourth task was to observe GPS signals with a nadir looking antenna. The technique is denoted as GPS reflectometry (Martin-Neira, 1993). The principle is to track GPS signals which were reflected by the Earth's surface. In combination with the precisely known satellite position, these observations can be used to determine the height of the reflecting surface. The method is pretty similar to Radio Detection and Ranging (radar) or Light Amplification by Stimulated Emission of Radiation (Laser) altimetry, except the fact that the signal transmitter is located on a different satellite, in this case on the GPS satellite.

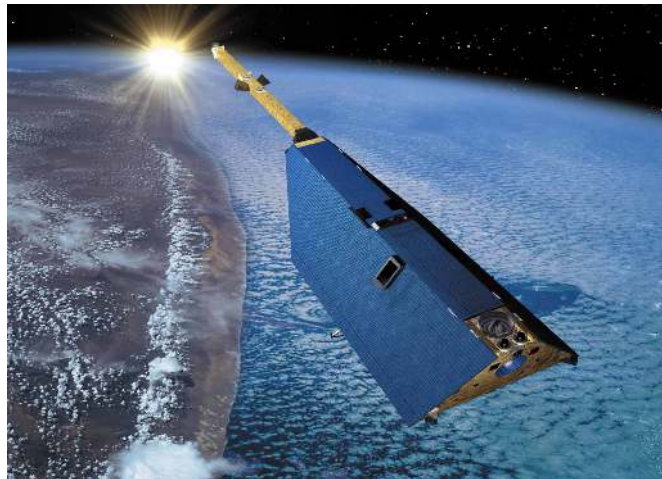


Figure 3.1: Artist's impression of the CHAMP satellite. ©EADS Astrium

As a second measurement technique to determine the satellite orbit, a Laser retro reflector was mounted at the bottom of the satellite. A retro reflector is a passive instrument which reflects Laser pulses emitted by ground stations. By means of run time measurement the distance to the satellite is determined. Depending on the ground station, the sampling rate is in the range of some Hz up to kHz. Due to the fact that the global network of SLR stations is sparse and the observations are limited by local weather conditions, the technique is in most cases used as backup or validation tool. The retro reflector used for CHAMP was developed and built at German Research Center for Geosciences (GFZ) (Reigber et al., 2002).

To fully exploit the highly accurate satellite positions for the purpose of gravity field estimation, it is important to take non-gravitational accelerations acting on the satellite

### 3 Satellite missions

body into account. To measure the effect of air drag, solar radiation, Earth albedo, thruster firings and other non-conservative forces the CHAMP satellite carried an accelerometer on-board. The instrument was placed in the center of mass of the satellite. The accelerometer used for CHAMP was provided by Centre National d'Études Spatiales (CNES) and manufactured by Office National d'Études et de Recherches Aérospatiales (ONERA) (Touboul et al., 1998; Touboul et al., 1999). A freely floating proof mass inside the accelerometer is used to measure linear and angular accelerations. Electrodes on each side of the proof mass are used for capacitive positioning and for force generation to keep the mass stable (Touboul et al., 1999).

To determine the orientation of the satellite in space, CHAMP made use of a star camera assembly developed at the Technical University of Denmark. The star imager design consisted of four camera head units and a central data processing unit. Two cameras were placed on the magnetometer boom to provide accurate orientation for the magnetic instruments. The other two camera heads were placed on the main satellite body to provide its orientation. The specified accuracy for attitude determination was approximately 5 arcseconds (Jørgensen, 1999). The measurements of the star camera assembly were also used as input for the attitude control system to maintain the nominal satellite attitude. The scientific payload was complemented by a nadir looking S-Band antenna for data transmission and communication with ground control stations.

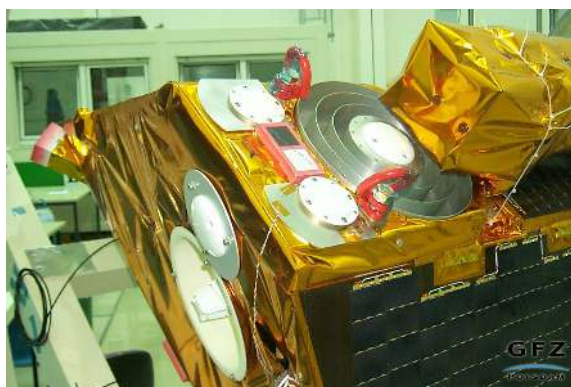


Figure 3.2: Rear section of the CHAMP satellite with three different GPS antennas. ©GFZ

#### 3.1.2 GPS receiver

The Turbo Rogue Space Receiver (TRSR), also known as BlackJack receiver, used on CHAMP was developed and built by National Aeronautics and Space Administration (NASA)'s Jet Propulsion Laboratory (JPL) (NASA, 2001). The receiver used four different antennas for various scientific tasks, a zenith looking patch antenna with choke rings for POD, a backup POD antenna on the aft panel, a high-gain helix antenna on the aft panel for occultation measurements, and a similar nadir-looking helix antenna for GPS altimetry experiments. To carry out different tasks simultaneously, the receiver featured 16 tracking channels. Initially 12 channels were intended to be used for tracking signals with the main POD antenna. The actual number changed due to receiver firmware

### 3 Satellite missions

changes (Grunwaldt and Meehan, 2003). A summary of all changes can be found in Prange (2010). The remaining 4 channels were used to conduct different experiments with the occultation or altimeter antennas. During most of the satellite's lifetime these channels were used to generate occultation measurements on an operational basis. The specified measurement accuracy was  $< 0.2$  cm and  $< 30$  cm for ionosphere-free phase and code observations respectively. Observations for spacecraft positioning were collected with a sampling frequency of 0.1 Hz. Figure 3.2 shows a picture of the rear section of the satellite containing the main POD antenna, as well as the occultation and the backup POD antennas.

The most important properties of the GPS receiver assembly used for CHAMP and GRACE are:

- GPS tracking only
- dual frequency receiver
- up to 12 satellites tracked simultaneously
- codeless tracking of P-code
- three code observations (C/A-Code, P1 and P2)
- three carrier measurements (L1C, L1P and L2P)
- patch antenna with choke rings

## 3.2 GRACE

The Gravity Recovery and Climate Experiment (GRACE) mission is a joint project of NASA and DLR. The mission proposed by Center for Space Research (CSR) at the University of Texas at Austin, GFZ and JPL in 1996, is the second mission in NASA's Earth System Science Pathfinder program (Tapley et al., 2004). The main objective of the mission is to provide measurements of the Earth's gravity field and in this context especially variations in time are of high interest. The mission consists of two identical satellites following each other on the same orbit separated by approximately 200 km in along-track direction. The two satellites carry several scientific instruments as there are star cameras for attitude determination, an accelerometer to measure non-conservative forces, a geodetic GPS receiver for positioning and radio occultation measurements, and a SLR retro reflector for orbit validation (Tapley et al., 2004). However, the main instrument is a K-band ranging system, which measures ranges and range rates between the two spacecraft (Tapley et al., 2004). Observed changes of the distance between the two satellites can be used to measure the inhomogeneities of the Earth's gravity field. Figure 3.3 shows the two spacecraft following each other on their orbit around the Earth.

Based on the satellite bus developed for the CHAMP mission Astrium GmbH and Space Systems/Loral built main parts of the satellites. The satellites are almost identical, except for some differences in the S-band radio communication equipment. After instrument

### 3 Satellite missions

integration and intensive pre-flight testing the satellites were finally launched on March 17, 2002 with a Rockot launch vehicle from the Russian Cosmodrome Plesetsk. GRACE was placed in a nearly circular ( $e < 0.005$ ) and almost polar orbit ( $i = 89.0^\circ$ ) with an initial orbital altitude of approximately 500 km (Tapley et al., 2004). During mission lifetime the altitude is slowly decreasing due to atmospheric drag. To maintain the altitude, the attitude and the alignment of the satellites they are equipped with an attitude and orbit control system. An ensemble of sensors and actuators maintains spacecraft attitude and provides orbital control to fulfill the mission requirements. The system relies on cold gas propulsion, magnetic torque rods, star sensors, the BlackJack GPS receiver, an Earth and Sun sensor, a three-axis inertial reference unit, and a three-axis magnetometer to control the satellite state.

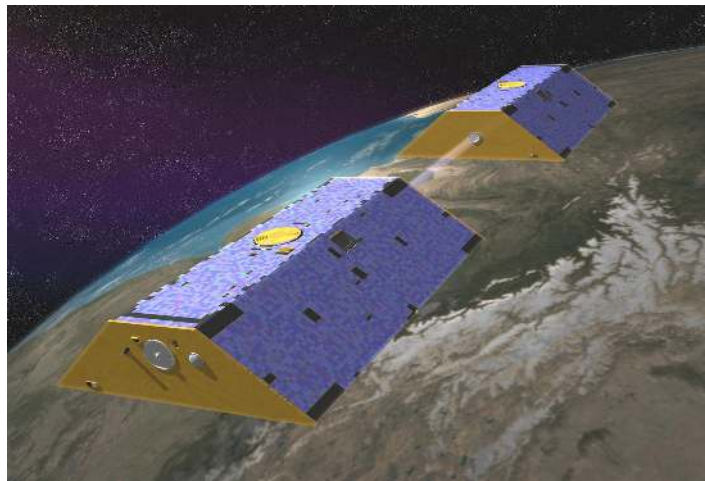


Figure 3.3: Artist's impression of the GRACE satellites in orbit. ©NASA

As already mentioned the scientific payload consists of several instruments. The microwave ranging system and the GPS receiver are described in the following two sections. The Laser retro reflector developed at GFZ is mounted at the bottom of the satellites and used for orbit validation. Attitude determination is performed with two star cameras, which are directly connected to the accelerometer. A SuperSTAR accelerometer, built by ONERA, is placed in the center of gravity of each satellite to observe non-conservative forces (Touboul et al., 1999). All in all, the two satellites benefited from a strong heritage of the developments made for the CHAMP mission.

#### 3.2.1 Microwave ranging system

The main scientific payload is the microwave ranging instrument (C. Dunn et al., 2003; Tapley et al., 2004). Developed at JPL, the instrument includes an ultra-stable oscillator, the microwave assembly, the horn, and the instrument processing unit. The oscillator provides the basic signal which is used to generate the two microwave signals with frequencies of 24 and 32 GHz. The horn is used for signal transmission and reception and the instrument processing unit is responsible for analog digital conversion and signal processing. The observed change in the phase gives a highly accurate measurement of the

### 3 Satellite missions

range. By combining the two different frequencies the ionospheric influence is eliminated. Due to the nature of phase measurements the measured range is not absolute but biased by an unknown number of wavelengths. The measurement accuracy is  $< 10 \mu\text{m}$  and  $< 0.2 \mu\text{m s}^{-1}$  for ranges and range rates, respectively.

#### 3.2.2 GPS receiver

GPS observations are carried out by a BlackJack GPS receiver in conjunction with three different antennas (C. Dunn et al., 2003). The receiver is in principle the same as it has been used for the CHAMP mission. One antenna is mounted on top of the satellite to collect signals for precise orbit determination. The second antenna is located at the aft looking panel to collect radio occultation measurements to setting or rising satellites and the third antenna is a backup antenna for POD and also placed on the aft panel. The receiver is capable of tracking up to 24 dual frequency signals, which enables simultaneous acquisition of POD and occultation measurements. The main characteristics of the BlackJack receiver are listed in section 3.1.2. In the course of GRACE level 1B data generation GPS observations undergo a pre-processing step. It includes code smoothing with phase observations, approximate correction of the receiver clock error, and phase ranges are corrected by initial ambiguity estimates (S.-c. Wu et al., 2006). In addition the originally 1 Hz sampled phase observations are resampled to 0.1 Hz by polynomial interpolation (S.-c. Wu et al., 2006).

### 3.3 GOCE

The Gravity Field and Steady-State Ocean Circulation Explorer (GOCE) satellite was the first of European Space Agency (ESA)'s Earth Explorer missions (Drinkwater et al., 2007). First investigations for this mission started in the early 90s of the past century. After final decision on GOCE being the first Earth explorer core mission within ESA's Living Planet program a consortium of 45 European companies developed the satellite under an ESA contract. The challenging mission objectives triggered the development of new and unique technologies. After a few delays the satellite was finally launched on March 17, 2009 from the Russian Cosmodrome Plesetsk on a Rockot launch vehicle (Floberghagen et al., 2011). Figure 3.4 shows the satellite and gives an impression of the aerodynamic spacecraft design.

The satellite was placed in a sun-synchronous orbit at a very low altitude of approximately 255 km. At such a low altitude satellites suffer from a significant amount of air drag and thus would immediately start to decay. To counter act the air drag, GOCE was equipped with electric ion thrusters. These thrusters were designed to operate continuously and compensate acting forces in real-time. This flight mode is denoted as drag-free mode. Accelerometers inside the satellite accurately measure the sum of disturbing forces such

### 3 Satellite missions

as for example air drag or solar radiation pressure. Based on these observations the necessary forces are determined and the thrusters are steered to compensate these effects. In addition the satellite featured an aerodynamic design to further reduce the influence of the atmosphere. The two main scientific instruments, a GPS receiver and the Electrostatic Gravity Gradiometer (EGG), are described in the following two sections.



Figure 3.4: Artist's impression of the GOCE satellite in orbit around the Earth. ©ESA

#### 3.3.1 Electrostatic Gravity Gradiometer

The EGG is the main scientific instrument on board the GOCE satellite (Floberghagen et al., 2011). The satellite was designed in a way, that there is no distinct division between satellite bus and science instrumentation. In fact, the whole satellite acts as measurement device. The EGG consists of three pairs of 3-axis accelerometers mounted in a diamond configuration on an ultra-stable structure. Each accelerometer pair represents one gradiometer axis mounted orthogonally in along-track, cross-track and radial direction. The two accelerometers are separated by 50 cm. Due to the slightly different positions of each accelerometer the gravitational pull acting on them is slightly different for each measurement unit. This enables to directly measure the gravity gradient in all three directions (Rummel et al., 2011). The instrument was placed in the center of mass of the satellite to minimize the influence of rotations. The six accelerometers used for the gradiometer were based on the same measurement principle as already described in section 3.1.1 developed and manufactured by ONERA.

#### 3.3.2 GPS receiver

Due to limitations concerning the high accuracy measurement bandwidth of the gradiometer it was necessary to supplement the gradiometer observations with additional information (Floberghagen et al., 2011), especially to recover the long wavelengths of the Earth's gravity field. Therefore, the satellite was equipped with a geodetic GPS receiver (Intelisano et al., 2008). In case of GOCE it was denoted as Satellite-to-Satellite Tracking

### 3 Satellite missions

Instrument (SSTI). The instrument used for GOCE consisted of a dual-frequency GPS receiver and two L-band helix antennas. The receiver was capable of tracking 12 satellites simultaneously with a sampling rate of 1 Hz (Thales Alenia Space, 2012; Zin et al., 2006). It delivered code and phase observations on both GPS frequencies and a real-time navigation solution. The two antennas, one main and one backup, were mounted on top of the satellite to ensure a maximum of visible GPS satellites to be tracked. The SSTI is based on the LABEN GNSS Receiver for Advanced Navigation, Geodesy and Experiments (LAGRANGE) receiver architecture (Thales Alenia Space, 2012) and uses ESA developed Advanced GPS/GLONASS ASIC (AGGA)-2 chips (Sinander and Silvestrin, 2000) for code and carrier tracking. Nevertheless, the SSTI was configured for GPS-only tracking. The instrument was developed and built by ThalesAlenia Space (Thales Alenia Space, 2012). Figure 3.5 shows the receiver housing and the used helix antenna.

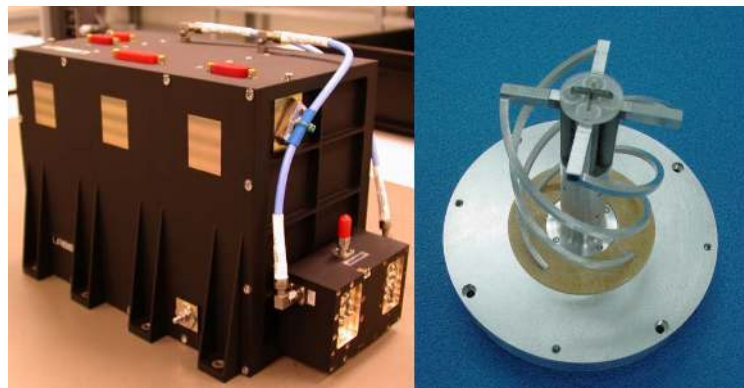


Figure 3.5: LAGRANGE receiver (left) and helix antenna (right) used for the GOCE mission.

Most important receiver specifications are:

- GPS tracking only
- dual frequency receiver
- 12 dual-frequency channels
- semi-codeless tracking
- three code observations (C/A-Code, P1 and P2)
- two carrier measurements (L1C and L2P)
- L1/L2 quadrifilar helix antenna

### 3.4 Non-dedicated gravity field satellites

The only instrument that is absolutely necessary to apply the method of SST-hl is a high quality GNSS receiver. Hence, the approach can be transferred to any satellite equipped with a geodetic grade GNSS receiver. Precise knowledge of the satellite orbit is of crucial importance for the success of a satellite mission in various applications. In the past decade GNSS has become the most widely used method for precise orbit determination, with accuracy requirements in the range of one meter down to a few centimeters (e.g. Schutz et al. (1994), Kuang et al. (2001), and Yoon et al. (2009)). Some of the advantages are high sampling rate, high accuracy, robustness and all at a relatively low price. The list of satellites using GNSS steadily increases and includes for example altimetry, Earth observation, radar, or radio occultation satellites. The following sections provide a short description of the used satellites and their characteristics. A summary of the most important orbital characteristics and satellite properties is given in section 3.5.

#### 3.4.1 Swarm

The European satellite mission Swarm, built and operated by ESA, was developed to study the Earth's magnetic field. The mission consists of three identical satellites, with one in a higher and two in a lower orbit. Equipped with instruments to measure the strength and the direction of the magnetic field, the observations made by the three satellites will provide new insights in the Earth's magnetic field. The chosen constellation of various altitudes enables to observe variations and structures in the magnetic field, with unprecedented accuracy and resolution (Haagmans et al., 2013).



Figure 3.6: Illustration of the three Swarm satellites. ©ESA

The main payload, consisting of: vector field magnetometer, absolute scalar magnetometer and an electric field instrument, is supplemented by the secondary payload: GPS receiver, accelerometer, a laser retro reflector and a star tracker assembly. The originally foreseen task of the GPS receiver is to provide accurate positioning information to geolocate the

### 3 Satellite missions

magnetic field measurements. In addition, the instrument can be used to infer information about the Earth's gravity field by applying the approach of SST-hl (see section 2.4). Basically, the three Swarm satellites all carry the same instrumentation as the first gravity field mission CHAMP. A GPS receiver for orbit determination, a star tracker assembly to accurately observe the orientation of the satellite and an accelerometer to observe non-conservative forces, like air drag and solar radiation pressure (Haagmans et al., 2013). The GPS receiver used for the Swarm satellites is denoted as GPS/GNSS Receiver (GPSR). It is based on the ESA developed AGGA chip (Sinander and Silvestrin, 2000). The Swarm satellites have two zenith mounted GPS antennas for POD, shown in figure 3.7. The key properties of the GPS receiver assembly are:

- GPS tracking only
- dual frequency receiver
- up to 8 satellites tracked simultaneously
- semi-codeless tracking
- three code observations (C/A-Code, P1 and P2)
- two carrier measurements (L1C and L2P)
- patch excited cup antenna



Figure 3.7: Patch excited cup antenna used on all Swarm satellites. ©RUAG Space AB

#### 3.4.2 TerraSAR-X

The TerraSAR-X satellite mission is a German Synthetic Aperture radar (SAR) mission launched in 2007. It was realized through a cooperation of public institutions and private companies. Main contributors are DLR and the ASTRIUM GmbH. The satellite orbits around the Earth at an altitude of approximately 515 km with an inclination of 98° (Rothacher et al., 2007). The orbit is sun-synchronous, nearly circular and has a repeat cycle of 11 days. For its main mission objective the satellite carries an X-Band radar instrument operating at 9.65 GHz (Buckreuss et al., 2003). The instrument is capable of operating in different modes, featuring varying ground resolutions and coverages. In order to fully exploit the high measurement accuracy of the radar instrument a precise orbit determination is of high importance. Therefore, the satellite is equipped with the Tracking, Occultation and Ranging (TOR) instrument package (Rothacher et al., 2007),

which consists of a dual-frequency GPS receiver and laser retro-reflector array. With these two components orbit position estimation at the centimeter level is possible (Wermuth et al., 2009).



Figure 3.8: Artist's view of the two satellites TerraSAR-X and TanDEM-X in close formation above the Earth's surface. ©Airbus Defence & Space

The used GPS receiver is based on the BlackJack architecture developed at JPL and already used for previous missions, e.g. CHAMP and GRACE (Rothacher et al., 2007). The version flown on TerraSAR-X is denoted as Integrated GPS and Occultation Receiver (IGOR) and provided by CSR at the University of Texas. It is not only used for precise orbit determination, but also to make occultation observations used in atmospheric research and numerical weather modeling. Figure 3.9 shows the IGOR receiver and the POD antennas used for TerraSAR-X and TanDEM-X. Key properties of the receiver are:

- GPS tracking only
- dual frequency receiver
- up to 12 satellites for POD and 2 for occultation tracked simultaneously
- semi-codeless tracking
- three code observations (C/A-Code, P1 and P2)
- three carrier measurements (L1C, L1P and L2P)
- L1/L2 patch antennas with choke rings

#### 3.4.3 TanDEM-X

TanDEM-X is a German SAR satellite mission launched in 2010 and designed as supplement to TerraSAR-X. The satellite itself is pretty similar to TerraSAR-X, based on the same bus and comprising the same instrumentation. TanDEM-X was placed in almost the same orbit as TerraSAR-X with a mean altitude of 515 km and an inclination of  $98^\circ$  (Bartusch et al., 2009). The usual separation between the two satellites is in the range of a few hundreds of meters up to a few kilometers. This close formation gives the possibility of new measurement modes. In contrast to classical SAR observations the combination of

### 3 Satellite missions

two satellites enables SAR-interferometry. Depending on the separation, across-track or along-track SAR-interferometry can be applied. This new observation method opens a bunch of new applications as for example in geology, hydrology, land use and vegetation, navigation and others (Bartusch et al., 2009).

In terms of GNSS instrumentation the TanDEM-X satellite is equipped with the same IGOR receiver as the TerraSAR-X satellite. Figure 3.9 shows an image of the GPS receiver and the antenna assembly used for the TerraSAR-X and TanDEM-X missions. Due to the close formation of TerraSAR-X and TanDEM-X it is possible to apply GNSS methods for base line determination (Jäggi et al., 2012).

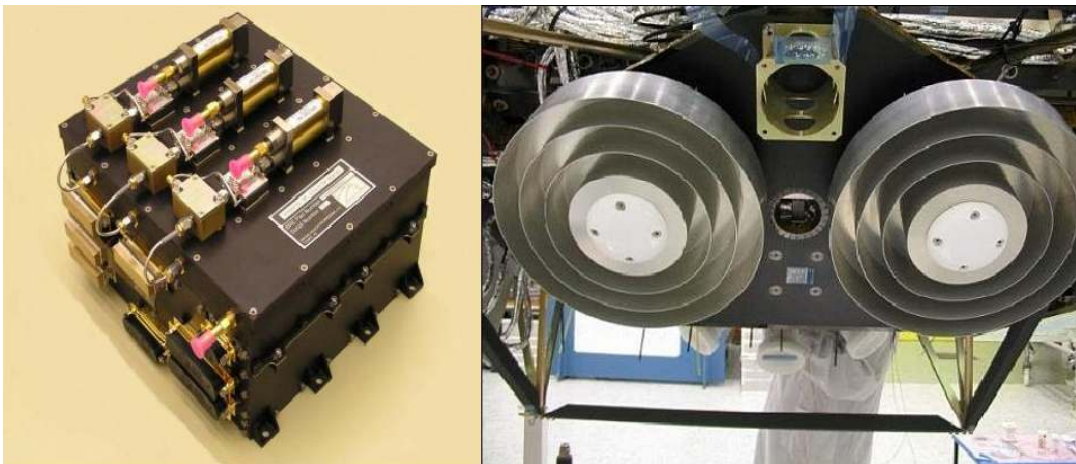


Figure 3.9: IGOR receiver used on TerraSAR-X and TanDEM-X for POD and radio occultation (left) ©Broad Reach Engineering. Main and redundant GPS antennas with choke rings used for POD (right) ©EADS Astrium.

#### 3.4.4 MetOp A and B

The Meteorological Operational Satellite (MetOp) satellites are a series of European weather satellites orbiting in a near polar LEO orbit. Up to now, the satellites A and B were launched in 2006 and 2012, respectively. The next satellite C is scheduled for launch in 2018. The MetOp program is jointly implemented and operated by the European Organisation for the Exploitation of Meteorological Satellites (EUMETSAT) and ESA, with contributions from Astrium, CNES and National Oceanic and Atmospheric Administration (NOAA). The satellites are used for operational weather monitoring and climate modeling (Edwards et al., 2006).

Both satellites were launched into a near polar orbit with an inclination of  $98^\circ$  and a mean altitude of 820 km (Edwards et al., 2006). The satellites carry a wide range of instruments for weather monitoring as for example an infrared atmospheric sounding interferometer, a microwave humidity sounder, a high resolution infrared radiation sounder, an advanced very high resolution radiometer, just to name a few (Edwards et al., 2006). In total, MetOp A features 13 different instruments. Among those is a GPS receiver used for POD and radio occultation. The GNSS Receiver for Atmospheric Sounding (GRAS) instrument

### 3 Satellite missions

uses the same signal processing chips (AGGA-2 (Sinander and Silvestrin, 2000)) as the SSTI aboard of GOCE. In contrast to the GOCE SSTI, the GRAS receiver is optimized for



Figure 3.10: The MetOp A satellite in its orbit above the Earth. ©ESA

radio occultation and thus includes two occultation antennas in anti-velocity and velocity direction (Loiselet et al., 2000). The reception of GPS signal via the main POD antenna, which is zenith mounted and consists of two separated annular patch elements for L1 and L2, is limited to a maximum of eight tracked satellites (Montenbruck et al., 2008). This is due to the limited number of channels and the need to reserve some of them for the occultation antennas. The same combination of receiver and antenna is used for MetOp B. Figure 3.11 shows the GRAS instrument and the POD antenna. Several institutions have already used MetOp A data successfully to compute reduced-dynamic and kinematic orbits (Montenbruck et al., 2008).

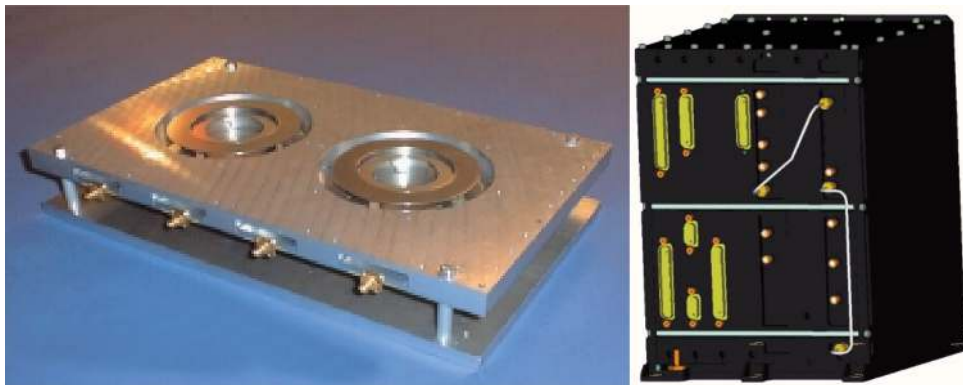


Figure 3.11: The POD antenna (left) and the GRAS electronics unit (right) used for both MetOp missions. ©ESA (Loiselet et al., 2000)

Key features of the GRAS receiver are:

- GPS tracking only
- dual frequency receiver
- up to 8 satellites for POD and 2 on each occultation antenna
- codeless tracking
- three code observations (C/A-Code, P1 and P2)
- three carrier measurements (L1C, L1P and L2P)
- two annular patch elements (L1 and L2)

#### 3.4.5 SAC-C

The satellite mission Satélite de Aplicaciones Científicas-C (SAC-C) was built in co-operation by NASA and the Comisión Nacional de Actividades Espaciales (CONAE), with contributions from CNES, the Brazilian Space Agency, the Danish Space Research Institute, and the Italian Space Agency (Colomb et al., 2004). The satellite was launched in 2000 and remained active until 2013. SAC-C was launched into a sun-synchronous orbit with an average altitude of 705 km and an inclination of 98°. The mission had four main science objectives: provide multispectral images of the Earth; GPS radio occultation; magnetic field measurements; and observe high-energy radiation, trapped particle intensities and the energy distribution. In accordance with the science goals, the instrumentation consisted of a multispectral medium resolution scanner, a high resolution camera, a high sensitivity camera, star trackers, a whale tracker experiment, the influence of space radiation on advanced components experiment, a scalar helium magnetometer, a compact spherical coil vector magnetometer, and GPS Occultation and Passive reflection Experiment (GOLPE) (Alonso and Hofmann, 2002).

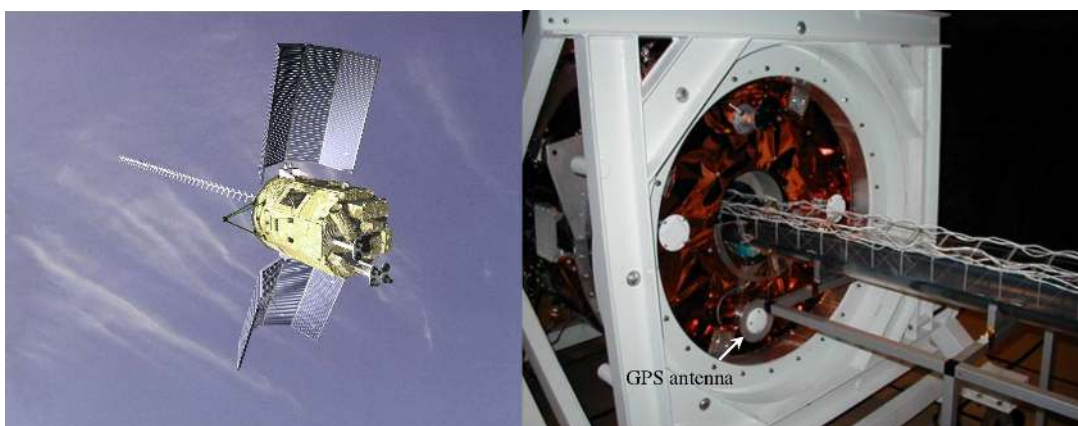


Figure 3.12: The Argentinian satellite SAC-C in orbit around the Earth. (left) ©CONAE Location of the POD antenna on the spacecraft. (right) ©JPL

GOLPE was provided by JPL and consisted of a BlackJack receiver in combination with four high gain antennas, facing up, down, fore and aft directions. The right panel of figure 3.12 shows the location of the POD antenna on the satellite body. As it can be

### 3 Satellite missions

seen the deployable boom carrying the magnetometer instruments is situated next to the GPS antenna and represents a disturbance in the sky view. Although the satellite was operating until mid-2013, the GOLPE payload experienced failures in mid-2011 and the maximum number of tracked satellites was reduced to seven. Major characteristics of the receiver on board of SAC-C are:

- GPS tracking only
- dual frequency receiver
- maximum 8 tracked satellites for POD
- semi-codeless tracking
- three code observations (C/A-Code, P1 and P2)
- two carrier measurements (L1C and L2P)
- L1/L2 patch antenna

#### 3.4.6 Jason 1 and 2

Jason 1 and 2 are radar altimeter satellites continuing the observation record of the TOPEX/Poseidon mission (Zieger et al., 1991). Main objective of these missions was and still is to observe the ocean surface topography. Jason 1 was launched in 2001 and was active until 2013. Its successor Jason 2, also denoted as Ocean Surface Topography Mission (OSTM), was launched in 2008 and is still operational. Both satellites were launched into the same orbit with an altitude of approximately 1330 km and an inclination of  $66^\circ$  (Neeck and Vaze, 2008). In 2009, Jason 1 was moved to the opposite side of the Earth with regard to Jason 2. This enables a higher spatial and temporal resolution of the ocean topography observations.



Figure 3.13: Illustration of the Jason 2/OSTM satellite in orbit (left) and GPS antennas with choke rings for POD (right). ©NASA

The primary instrument on both satellites is the Poseidon radar altimeter. However, for ocean surface mapping highly accurate knowledge of the satellite orbit - mainly the radial component - is of crucial importance. To enable high accuracy positioning, the satellites carry a DORIS receiver, a Laser retro-reflector, and a GPS receiver. The used GPS receiver is a BlackJack receiver built by Spectrum Astro Inc. It features 16 dual frequency channels

and is connected to a patch antenna with choke rings (Haines et al., 2011), shown in figure 3.13.

Starting in 2006, the two GPS receivers of Jason 1 — main and redundant unit — have experienced critical failures (G. M. Shirtliffe, 2007). The redundant receiver was completely lost, whereas the main unit was working until 2009, but with reduced accuracy and reduced amount of data collected (G. M. Shirtliffe, 2007). In case of Jason 2 the main GPS unit suffered from a critical failure in August 2014. After this incident the redundant unit was switched on. Main characteristics of the GPS payload are listed below:

- GPS tracking only
- dual frequency receiver
- 16 channels (configured to a maximum number of 12)
- semi-codeless tracking
- three code observations (C/A-Code, P1 and P2)
- three carrier measurements (L1C, L1P and L2P)
- L1/L2 patch antenna with choke rings

#### 3.4.7 C/NOFS

The Communications/Navigation Outage Forecasting System (C/NOFS) mission was planned and operated by the Air Force Research Laboratory (de La Beaujardière, 2004), a scientific organization maintained by the United States Air Force. The satellite was launched on April 16, 2008 into an elliptical inclined LEO orbit. The orbit has an inclination of  $13^\circ$  and an eccentricity of 0.032. This leads to a perigee of 405 km and an apogee of 853 km. Main purpose of the satellite is to investigate ionospheric scintillations. A secondary mission goal is to provide observations for a real time forecasting system of ionospheric irregularities. The system will be used to forecast possible navigation or communication outages for United States military forces (de La Beaujardière, 2004). Figure 3.14 shows an artist's impression of the satellite.

To accomplish the scientific objectives the satellite is equipped with six different sensors to study the Earth's ionosphere. A planar Langmuir probe is used to monitor plasma densities by observing electron densities and temperatures. The ion velocity meter provides measurements of the local ion drift vector. A neutral wind meter observes the neutral wind speed and vector. The vector electric field instrument measures the direct current electric fields, causing plasma drifts, which make the ionosphere unstable. The coherent electromagnetic radio tomography instrument uses three different frequencies and ground receivers to study plasma densities between the satellite and the ground station. It can be also used to observe electron density profiles. The C/NOFS Occultation Receiver for Ionospheric Sensing and Specification (CORISS) is a dual frequency GPS receiver used to measure the Total Electron Content (TEC) between the receiver and GPS satellites as well as performing radio occultation observations to derive vertical electron

### 3 Satellite missions

density profiles (de La Beaujardière, 2004). The CORISS receiver can be also used to compute accurate kinematic orbits for the C/NOFS satellite and thus the satellite can be used for the purpose of gravity field estimation. Main characteristics of the CORISS payload are listed below:

- GPS tracking only
- dual frequency receiver
- semi-codeless tracking
- three code observations (C/A-Code, P1 and P2)
- three carrier measurements (L1C, L1P and L2P)
- L1/L2 patch antenna



Figure 3.14: Illustration of the C/NOFS satellite in orbit. ©NASA

#### 3.4.8 FORMOSAT-3/COSMIC

The satellite mission Constellation Observing System for Meteorology, Ionosphere, and Climate (FORMOSAT-3/COSMIC) is a bilateral cooperation between Taiwan and the United States (B.-H. Wu et al., 2005a). It is the third mission in a series of Earth observation missions designed and operated by the National Space Program Office of Taiwan. University Corporation for Atmospheric Research (UCAR) is the main contributor from the United States. In April 2006, a Minotaur-1 launcher brought the six identical satellites into an initial orbit with an altitude of approximately 500 km. After a first calibration and validation phase, five of six spacecraft were raised to an altitude of 800 km. The main scientific goal of the FORMOSAT-3/COSMIC mission is to provide a large number of radio-occultation observations. These measurements are used for atmosphere profiling, which can be incorporated into weather models, climate models, or help to understand different processes in the Earth's atmosphere. Figure 3.15 shows an illustration of the satellites in orbit and all six satellites stacked on the launcher interface. Further information can be found in B.-H. Wu et al. (2005a) or Rocken et al. (2000).

### 3 Satellite missions

The main scientific payload is the GPS Occultation Experiment (GOX) or also referred to as IGOR. The employed GPS receiver is based on the BlackJack design, developed at JPL and built by Broad Reach Engineering (B.-H. Wu et al., 2005a). It is capable of operating fully autonomous and will track all satellites in view, including two or more occulting satellites. This high tracking capacity is enabled by the capability to use all four available GPS antennas at the same time. One fore and one aft locking antenna, tilted by  $15^\circ$  towards the zenith, are used for POD, while two additional high gain antennas in fore and aft direction are used to track satellites near the limb. Main characteristics of the GOX payload are listed below:

- GPS tracking only
- dual frequency receiver
- 16 channels
- semi-codeless tracking
- three code observations (C/A-Code, P1 and P2)
- three carrier measurements (L1C, L1P and L2P)
- two simultaneously operated L1/L2 patch antennas



Figure 3.15: Illustration of the FORMOSAT-3/COSMIC satellites in orbit (left) and a picture of all six satellites stacked and prepared for launcher integration (right). ©UCAR

The spacecraft also carries a Tiny Ionosphere Photometer and a Coherent Electromagnetic Radio Tomography/Triband Beacon Transmitter. Both instruments are also used to measure parameters of the Earth's atmosphere. The attitude of the satellites is determined by using Sun and Earth sensors in combination with a magnetometer (Tseng et al., 2012).

### 3.5 Comparison of satellite characteristics

The performance of a satellite in terms of gravity field estimation depends on several properties related to the satellite and its instrumentation or the orbital characteristics. The most important aspects for all used satellites are summarized in table 3.1.

Satellite name	Time frame	Altitude [km]	Inclination [°]	Receiver	Observation sampling [s]	attitude
CHAMP	2000-2010	450 (300 EoL)	87.3	BlackJack	10	star camera <sup>1</sup>
GRACE A & B	2002-	485 (300 EoL)	89.0	BlackJack	10	star camera <sup>1</sup>
GOCE	2009-2013	255 (120 EoL)	96.7	Lagrange	1	star camera
Swarm 1, 2, & 3	2013-	450/530	87.0	GPSR	1 (10 until July 2014)	star camera
TerraSAR-X	2007-	515	97.4	IGOR	10	star camera
TanDEM-X	2010-	515	97.4	IGOR	10	star camera
MetOp A	2006-	820	98.7	GRAS	1	computed
MetOp B	2012-	820	98.7	GRAS	1	computed
SAC-C	2000-2013	700	98.2	BlackJack	10	computed
Jason 1	2001-2013	1330	66.0	BlackJack	10	star camera
Jason 2	2008-	1330	66.0	BlackJack	10	star camera
C/N/OFS	2010-2011	400-850	13.0	BlackJack	10	computed
FORMOSAT-3/COSMIC FM 1-6	2006-	500/800	73.0	BlackJack	1	Sun sensor, Earth sensor and magnetometer <sup>2</sup>

<sup>1</sup>  $1\sigma < 5''$  (Jørgensen, 1999)

<sup>2</sup>  $1\sigma < 5^\circ$  (Tseng et al., 2012)

Table 3.1: Most important properties of all used satellites. (EoL: end of life)

## 4 Orbit determination

The present chapter describes the method used for POD in this work. Starting with the very basics of GNSS continued by a special discussion on different observation types and processing methods. The core of this chapter introduces the raw observation approach and related processing aspects developed in the frame of this thesis.

### 4.1 Global Navigation Satellite Systems

#### 4.1.1 History

The development and implementation of Global Navigation Satellite Systems (GNSS) already started in the 1950s. The first operational navigation system was called Transit, developed and operated by the US Navy. The system was based on the principle of the Doppler shift and used signal frequencies of 150 and 400 MHz. The system consisted of up to six polar orbiting satellites and was operational until 1996. A rather similar system based on Doppler shift observations was also developed in the Soviet Union denoted as KOSMOS or Parus/Zikada. Based on experiences made with Transit or KOSMOS, the United States and also the Soviet Union started the development of a more sophisticated system in the late 1970s. These efforts lead to the parallel implementation of Global Positioning System (GPS) and the Globalnaja nawigazionnaja sputnikowaja sistema (GLONASS), which is the Russian name for Global Navigation Satellite System. Although the two systems were developed in parallel, under cold war conditions, they are based on the same principles, which will be shortly described in the subsequent section. Apart from GPS and GLONASS, which are currently fully operational, new systems are being installed by Europe, China, India and Japan. Further information on the history and current developments concerning GNSS, from basic introductory to scientific literature, can be found in a wide range of books ,e.g. by Hofmann-Wellenhof et al. (2008) or Misra and Enge (2006) or on the internet (e.g. <http://mgex.igs.org>).

#### 4.1.2 Principles of GNSS

The basic principle of position determination with GNSS is range intersection in space. The signals emitted by the GNSS satellites are used to measure distances between a transmitter and a receiver. Under the assumption that the position of the transmitter

is known, three observed distances to different satellites are sufficient to compute the position of the receiver at a distinct measurement epoch. In general this configuration has two possible solutions, however one might be discarded by using a plausibility test. The distance is calculated by measuring the travel time of the signal from the transmitter to the receiver. Due to the fact that the receiver clock is not synchronized with the system time, all range observations are biased by a receiver clock error. This receiver clock error is common to all observations and can be estimated. This leads to the situation that at least four observations are necessary at each epoch to estimate three coordinates and the clock error. Due to the clock bias the observed ranges are often denoted as pseudo ranges. Figure 4.1 illustrates the principle of pseudo range positioning in 2-dimensional space. For this case three biased observations are needed to correctly determine the position of the receiver and the receiver clock error  $\Delta t_r$ , with respect to the known positions of the satellites. High quality GNSS receivers feature not only one pseudo range measurement per satellite. In fact, there are several different observation types available, which will be described in subsection 4.1.3.

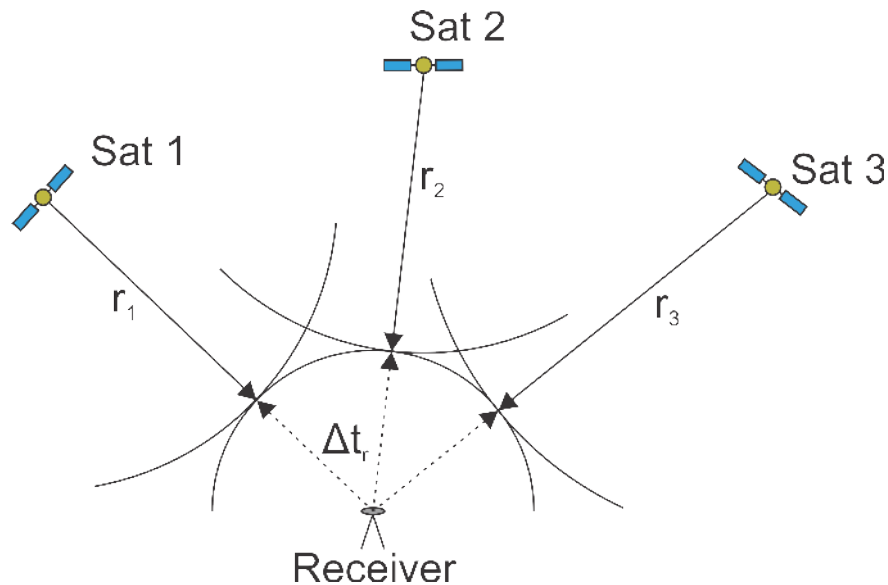


Figure 4.1: Principle of pseudo range positioning in 2D space.

### 4.1.3 Observation types

The signal emitted by GNSS satellites is in principle composed of three different components, the basic carrier frequency, the ranging code and the navigation message. The carrier frequency is an electromagnetic wave in the microwave spectrum with a pre-defined wavelength. Current GNSS constellations make use of two different carrier frequencies, denoted as L1 and L2. The used frequencies are 1575.42 and 1227.60 MHz, which correspond to wavelengths of 19 cm and 24 cm respectively. GPS uses exactly those two frequencies, whereas GLONASS uses slightly varying frequencies for the different satellites centered around the main frequency. In the course of the ongoing modernization

## 4 Orbit determination

of GPS a third frequency (L5) is available at 1176.45 MHz, already emitted by satellites of the last generation.

The second part of the signal, the ranging code, is modulated onto the carrier frequency. The used codes are pseudo random noise codes with a chip length of several hundred meters. In case of GPS the chip length is approximately 300 m for the freely accessible code. Apart from the open access ranging code, also an encrypted ranging code only usable by authorized users is modulated onto the signal.

The third part, the navigation message, is also added to the signal by modulation. It contains information about the emitting satellite, its orbit and in addition also coarse orbit information about all other satellites active in the system. The satellite specific part is denoted as broadcast ephemeris and used to calculate the satellite position. The coarse information about all other active satellites is named Almanac. The information contained in the Almanac is used by the receiver to check for possibly visible satellites and hence improve the signal acquisition and tracking of additional satellites.

In principle the signal is composed of these three different parts. However, each system has its own exact definition of the signal components (M. J. Dunn, 2013), which are also different for the used carrier frequencies. For example, the signal emitted on GPS L1 consists of an open access ranging code, the Coarse Acquisition Code (C/A-Code), the encrypted P-code, and the broadcast navigation message. In the course of an ongoing modernization of GPS, also the signal components are changed. For example, new satellites are transmitting an open access ranging code on L2 and a new military ranging code on both frequencies. In addition, all new satellites are transmitting on an additional carrier called L5, with a frequency of 1.1 GHz. In case of GLONASS, a modernization is also currently under preparation. It involves new civil signals and the change from Frequency Division Multiple Access (FDMA) to Code Division Multiple Access (CDMA), which is used by GPS and will be used by Galileo.

Apart from pseudo range measurements obtained from the modulated ranging code, it is also possible to use the basic carrier to facilitate pseudo range measurements. This type of observation is based on the principle of measuring the phase of the carrier signal. The signal tracking algorithm starts at an arbitrary value and keeps track of the changes. In contrast to the code measurements the phase observations are additionally biased by an unknown number of full carrier wavelengths, called ambiguity. Due to this fact, it is not possible to use phase observations for position estimation of a single epoch. The main advantage of phase observations is the higher accuracy, in the range of millimeters, in contrast to some decimeters in case of code observations. The achievable positioning accuracy is influenced by several error source, discussed in section 4.1.5.

#### 4.1.4 Derived observation types

GNSS receivers are capable of providing different observation types and make use of different carrier frequencies. This facilitates the generation of derived observations on the basis of the original measurements. The main advantage of using derived observations is the fact that some systematic errors are eliminated or at least greatly reduced. This enables a position estimation with higher accuracy. Thus, on the one hand it is possible to eliminate systematic effects, on the other hand the combination increases the stochastic noise. In general, it is always a question of available hardware and application which determines the appropriate method in combination with the best suitable observation type.

**Ionosphere-free linear combination** As the name already suggests, this kind of linear combination eliminates the influence of the ionosphere. This is achieved by combining observations from two different carrier frequencies.

$$L_3 = \frac{1}{f_1^2 - f_2^2} (f_1^2 L_1 - f_2^2 L_2) \quad (4.1)$$

The combination is sometimes denoted as  $L_3$  to show the heritage from the  $L_1$  and  $L_2$  phase observations and demonstrate that this observation is also some type of phase observation. The ionosphere-free linear combination has an approximate wavelength of 11 cm and is also denoted as Narrow-Lane combination. The same combination can be formed with code observations.

$$P_3 = \frac{1}{f_1^2 - f_2^2} (f_1^2 P_1 - f_2^2 P_2) \quad (4.2)$$

In both cases the influence of the ionosphere is greatly reduced but not completely eliminated. The combination only removes the ionospheric influence of first order. Higher order errors are still present in the ionosphere-free combination. However, it is still acceptable to call this combination ionosphere-free as the first order error accounts for more than 99% (M. M. Hoque and Jakowski, 2012) of the total ionospheric influence.

**Geometry-free combination** The geometry-free combination is characterized by the following relationship

$$L_4 = L_1 - L_2. \quad (4.3)$$

The combination is often named  $L_4$ . It eliminates the influence of receiver position, receiver clock, satellite clocks and satellite position. The remaining parts are the ionospheric influence and the ambiguities. The geometry-free combination represents all influences and errors which are frequency dependent. The same combination can be formed using code observations.

**Melbourne-Wübbena linear combination** The Melbourne-Wübbena linear combination mixes two phase and two code observations to get rid of most of the errors contained in the original observations. It is formed by

$$L_6 = \frac{1}{f_1 - f_2}(f_1 L_1 - f_2 L_2) - \frac{1}{f_1 + f_2}(f_1 P_1 + f_2 P_2). \quad (4.4)$$

The combination removes the influence of the ionosphere, the troposphere, the geometry, and the clock errors. The resulting observation only contains a combined ambiguity of L1 and L2. The noise of the Melbourne-Wübbena combination is mainly determined by the quality of the involved code observations. Typically the standard deviation is in the range of a few decimeters. Due to the fact that the ambiguity is constant over a continuous satellite arc, the Melbourne-Wübbena combination should also stay constant. If jumps occur in the Melbourne-Wübbena combination, this shows errors in the observations, mainly cycle slips occurring on one of the phase observations. This makes the Melbourne-Wübbena combination well suited to search for cycle slips or any other discontinuities in the observations.

**Observation differences** Apart from above mentioned combinations, differences between observations are a useful tool to minimize systematic errors in order to facilitate the position estimation of a receiver. There are several possibilities to form differences. In principle, differences are formed between two observations of the same type but from different receivers, transmitters or epochs. In addition, it is also possible to form differences of differences. They are denoted as single, double or triple differences, indicating how often an observation has been combined (Hofmann-Wellenhof et al., 2008).

The first possibility is to form a single difference. This can be done by subtracting two observations of the same type, recorded by the same receiver at the same epoch but from two individual GPS satellites. Another possibility would be to use observations from the same transmitter but two different receivers.

The second possibility is to form the difference between two single differences, called double difference. How the difference can be formed depends on the type of single difference formed previously.

The third option is to form the difference between two double differences, which is then called triple difference. This combination in total contains eight original observations and thus the noise of the derived observation is much higher than for the basic observations. Therefore, triple differences are not very well suited to get good position estimations. However, they can be used for data screening or an initial position computation to serve as a starting point for further iterations incorporating other observation types.

Double differences are very often used in relative positioning applications, as for example in terrestrial static GPS surveys. This method is well-known and was the first technology used to reach positioning accuracies in the range of centimeters or millimeters. The

applied methods have been further developed since the first GPS campaigns in the 1980s. In principle also modern technologies, as for example network Real Time Kinematic (RTK) rely on the same basic principles. In case of LEO orbit processing observation differences are used to observe the base line between two satellites with high accuracy, for example the German SAR missions TanDEM-X and TerraSAR-X (Jäggi et al., 2012). These two satellites are flying in very close formation with separations around 200 m and the baseline between them is determined with millimeter precision by relative GPS.

### 4.1.5 Systematic effects and noise

GNSS measurements are influenced by a wide range of systematic effects. All of these effects determine the achievable positioning accuracy and contribute to the error budget. Depending on the used observation types, the positioning method and the environmental conditions, different levels of accuracy can be reached. In general, the different errors can be divided into three main groups. In chronological order these are transmitter, propagation, and receiver errors.

#### 4.1.5.1 Transmitter effects

Transmitter errors are all influences attributed to the transmitting satellite. These errors are not the same for each satellite in a GNSS constellation. They depend on the model series of the transmitter, the used on-board clock, and the signal type. Due to continuously ongoing developments, not only on the receiver side, but also concerning the transmitters, the induced errors are different for each satellite. The following explanations should give a brief overview of the effects and give an indication on the expected size of the error.

**Transmitter orbit** The knowledge of the transmitter position is a prerequisite to solve for the receiver position in applications like Single Point Positioning (SPP) or Precise Point Positioning (PPP). In principle these methods are based on the assumption that the transmitter position is known and distance measurements relative to them can be used to determine the position of the receiver. Hence, the accuracy of the transmitter position directly affects the achievable accuracy of the receiver position.

There are different ways to get information about the GNSS satellite orbits. The easiest and most convenient way is to use the orbit information contained in the navigation message broadcast by the transmitter itself. This information is computed by the system operator and typically features an accuracy of a few meters. The limited accuracy is on the one hand due to the fact that these orbits are only updated every few hours and are predictions. On the other hand, the limited accuracy is also intended to prevent users from achieving high positioning accuracies. These orbits, denoted as broadcast ephemeris, have been worsened intentionally until May 2000 by the operator of GPS. This measure,

known as selective availability, was used to generate a strategic advantage for certain users, i.e. the US military forces. An alternative way is to use orbit products provided by an institution independent from the system operators. The most prominent example is the International GNSS Service (IGS) (Dow et al., 2009). An international cooperation of research facilities, with the goal to provide highly accurate GNSS products, based on a worldwide network of continuously operating GNSS stations. Currently the IGS and its individual Analysis Centers (ACs) provide a wide range of products. From highly accurate post-processed to less accurate near-real time or predicted products, the IGS provides the basis for a huge number of scientific applications. The product accuracies are in the range of a few centimeters (Griffiths, 2013). In general it can be said, the higher the latency of the product the higher the accuracy. Finally, the last and most complex method is to compute the transmitter orbits on your own. This can be achieved in the same way as the other two products are generated. Observations from a worldwide network of GNSS stations can be used to compute GNSS orbits. However, this method is not advisable for a standard GNSS user, as it requires a high level of knowledge about GNSS processing and generally huge processing capacities. In this case the accuracy depends on the users experience, the used software and the used observation data. In the context of LEO orbit processing it may be beneficial to process the transmitter orbits and the LEO orbit with the same software, as it improves the consistency within the processing chain and thus might improve the overall positioning quality.

**Transmitter clock** The basic observation types in GNSS are one way range or range rate measurements, which is in principle an observation of the signal travel time. Hence, it is equally important to know the transmitter clock behavior, as to know the transmitter position. The signal emitted by a GNSS satellite depends on the on-board clock, realized by an Ultra Stable Oscillator (USO). Depending on the block-type, different oscillators have been used. Today most active GNSS satellites rely on rubidium frequency standards. Although these atomic clocks feature a high frequency stability, they are subject to drifts and short term instabilities which must be taken into account to achieve high positioning accuracies. The broadcast ephemeris provided by the system operator also include a rough correction for the transmitter clock. This information provides approximately the same accuracy as the orbit solution contained in the broadcast message, in the range of a few meters. To achieve better positioning results, the clock error must be known with higher accuracy. Similar to the orbit products, the IGS also provides clock products, with different latencies and different sampling rates. For the most demanding applications the IGS provides clock information with a sampling interval of just 30 s, for each transmitter in the GPS constellation. The Center for Orbit Determination in Europe (CODE), one of the IGS ACs, even provides corrections every 5 s (Bock et al., 2009a). Figure 4.2 shows transmitter clock corrections for some GPS satellites for the time span of one day. This comparison of GNSS transmitter clock errors makes it clear that for a high positioning accuracy highly accurate clock information is of crucial importance.

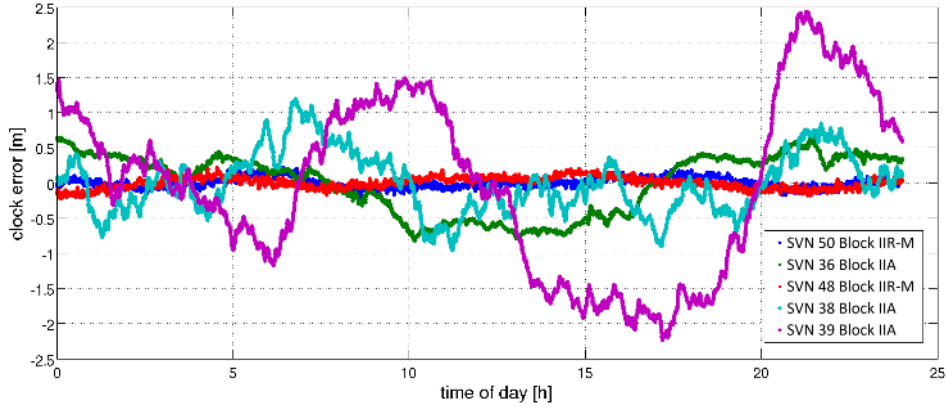


Figure 4.2: Example of CODE 5s GPS clock corrections for 5 different satellites for January 1<sup>st</sup>, 2014. The values are multiplied by the speed of light and a linear trend is reduced.

**Transmitter antenna center** GPS range measurements represent the distance between the two involved antennas. On the one end it is the transmitting antenna and on the other end the receiver antenna, to which the observations are related. More precisely the electronic center of the antennas is the point of interest.

In case of the transmitter antenna, there are two different deviations to be considered. First of all, the offset to the center of mass of the satellite must be taken into account and on the other hand there are deviations depending on the signal direction, also denoted as Antenna Center Variations (ACVs). The offset between a mean antenna center and the satellites center of mass is in principle a fixed value, which could be measured on ground before launch. In case of GPS, this information is not publicly available. However, there are ways to estimate these offsets and the IGS provides center of mass offsets for the whole satellite constellation, currently active satellites as well as already decommissioned spacecraft (Schmid et al., 2007; Schmid et al., 2016).

**Transmitter signal biases** In addition to the antenna offsets and variations, there is another error induced by the transmitting satellite itself. These errors, called signal biases, are frequency and observation type dependent. The sources for these errors are small manufacturing irregularities. For example, slight differences in the process of signal generation for L1 and L2 frequency cause systematic deviations between the two frequencies. The same holds for the different code generators. The frequency dependent component is often referred to as the inter-frequency bias (Holaschutz et al., 2008).

The most prominent and currently the only biases available and used routinely for example by the IGS, are the Differential Code Biases (DCBs). Defined as the difference between two code biases, e.g.  $B_{P1} - B_{P2} = B_{P1P2}$  or similar for C/A-Code observations  $B_{P1} - B_{CA} = B_{P1CA}$ . The bias, also named group delay bias  $T_{GD}$ , is addressed in the interface specification document (M. J. Dunn, 2013) or by Wilson et al. (1999). From equation 4.5 it can be seen that the difference between the bias  $B_{p1p2}$  and the  $T_{GD}$  is just

a factor and a constant offset.

$$T_{GD} = -1.55 \cdot B_{P1P2} + B_0 \quad (4.5)$$

The absolute value of the code biases is not accessible, neither for transmitters nor for receivers, due to the fact that such a constant shift is not separable from the transmitter and the receiver clock error. The definition is thus based on the difference between  $P1$  and  $P2$  bias. The estimation of transmitter specific DCBs is some sort of by-product of the TEC map production, see for example in Schaer (1999).

By definition all IGS products, GPS broadcast ephemerides as well as clocks, refer to the ionosphere-free linear combination. Hence, all other observables must be corrected for the DCBs to be consistent with the used orbit and clock products. The correct application for different observation types can be found in Dach et al. (2015).

Apart from DCBs, there are the so-called phase delays. These are errors due to different internal hardware delays for the different satellites. Different methods to estimate these biases, as well as a variety of names have been proposed within the last decade.

Shi (2012) nicely reviews the different methods for phase bias handling. He divides the methods into two major groups. On the one hand there are methods which he calls ambiguity correction methods, on the other hand there is a category of approaches dealing with integer clocks. In principle all these methods aim at the same goal: fixing ambiguities to integer values within a PPP solution. The difficulty is more or less to calculate the satellite specific phase biases and their application to real-time or post-processed PPP computations.

The first category of approaches using ambiguity corrections to achieve integer fixed values was also named PPP-RTK by Wübbena et al. (2005), who also proposed their own method for integer ambiguity resolution in a network of permanent stations. Other methods have been presented by Ge et al. (2008), Wang and Gao (2006), Geng et al. (2009), Mervart et al. (2008), and W. Bertiger et al. (2010). The methods differ slightly from each other and the names used for the bias term are manifold. Wang and Gao (2006) call it fractional bias, pretty similar to fractional cycle bias chosen by Geng et al. (2009). Ge et al. (2008) call it Uncalibrated Phase Delay (UPD), whereas Mervart et al. (2008) use the term Modified Satellite Clock Correction (MSCC) and finally W. Bertiger et al. (2010) utilize the expression ambiguity correction.

The methods of the second category mentioned by Shi (2012) treat the phase biases as some sort of additional clock error and estimate a modified clock correction for code and phase observations separately which can be disseminated and applied by a user to account for the apparent biases and utilize the resolution of integer ambiguities in a PPP solution. Methods were for example proposed by Collins et al. (2008) or Laurichesse et al. (2010). They have called their approaches decoupled clock model or integer phase clock model, respectively.

However, all above mentioned methods address the same issue: separation of integer phase ambiguities from non-integer biases. There are biases present in phase observations at transmitter, as well as at receiver side, which make the original ambiguity, contained in the observation, non-integer. Collins et al. (2008) showed that in principle there are biases for each frequency and each observation type. Their approach requires in total eight decoupled clocks, if dual frequency code and phase observations are used.

### 4.1.5.2 Propagation effects

GPS satellites are flying at an approximate altitude of 20 200 km above the Earth's surface. Depending on the constellation, the signal travels between 20 000 and 26 000 km from the transmitter to the receiver. Taking into account the speed of light, this gives an average travel time of 0.08 s. Due to the Earth's atmosphere, the electromagnetic signal is subject to some distortions. Under vacuum conditions, the speed of light is constant. This is not the case for GNSS signals travelling through the Earth's atmosphere. The effect of the atmosphere on electromagnetic waves can be divided into two main parts, according to the composition of certain atmospheric regions. The first part is the ionospheric influence and the second effect is caused by the troposphere. Both influences are described in the following sections.

**Ionosphere** The ionosphere is part of the Earth's atmosphere and ranges from altitudes of approximately 100 to 1000 km. It is characterized by a high concentration of ions and free electrons. The composition of the ionosphere heavily depends on the illumination by the sun. The ionosphere can be divided into several layers denoted as D-, E-, and F-layer (Budden, 1985). A schematic overview of the different layers and their extent in altitude is shown in figure 4.3. The definition of the layers is according to their characteristic ion and electron composition. The F-region is the most important layer as it features the highest electron concentration. It is also the only layer still present during the night. The ionosphere is of practical importance, especially for radio transmission in the high frequency domain, because it reflects signals with frequencies between 3 and 30 MHz (Budden, 1985). This special aspect facilitates intercontinental radio communication. On other signal bands the ionosphere has a less positive effect as it refracts, dampens or even absorbs certain frequencies.

The formation of the ionosphere is caused by the interaction of the ultraviolet radiation of the sun with the molecules in the higher atmosphere. During the day, radiation coming from the sun, mainly ultraviolet and X-ray radiation, forces atoms to release electrons, which generates free electrons and positively charged ions. In higher regions the radiation is strong but the concentration of gas molecules is lower. On the way towards the Earth, the radiation is more and more absorbed, but the concentration of molecules is increasing. Additionally, in the lower parts of the ionosphere, D- and E-layer, where the atom concentration is higher, the recombination rate of free electrons and

## 4 Orbit determination

ions is high. The balance between ionization and recombination determines the electron density at a certain height. This principle was described by Chapman (1931), who also defined functions to describe the electron density depending on the height. This type of function is today known as Chapman layer and widely used to model the ionosphere.

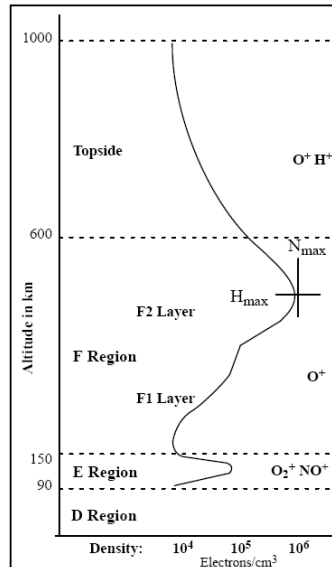


Figure 4.3: Schematic view of the ionospheric structure. ©NOAA

Due to the higher recombination rate in lower regions (D- and E-layer), those two layers vanish within the first hour after sunset. The situation is different for the F-layer. Due to the low concentration of elements in the upper part of the atmosphere, the probability of an interaction between ions and electrons is highly reduced. The rate of recombination is small, thus the F-layer persists throughout the whole night. Nevertheless, the electron concentration as well as the height of the layer decrease during the night. Although the gas concentration in the F-layer is lower, it is the layer with the highest density of free electrons within the ionosphere, as shown in figure 4.3. Due to the absence of solar radiation in general the conditions within the ionosphere are calmest during the night, especially shortly before sunrise. Whereas during daytime the ionosphere is subject to severe changes and disturbances. Highest electron densities in the ionosphere are observed around 1 o'clock pm. local time, whereas the fastest changes and strongest irregularities occur at the transition between day and night.

In addition to the time dependence, the ionosphere is also influenced by the Earth's magnetic field. This generates some special features within the ionosphere. The most important effect is called the fountain effect. It forms two bands of higher ionization north and south of the Earth's magnetic equator. Free electrons are raised to higher altitudes by an interaction between magnetic and electric fields. Once raised, the electrons travel along the geomagnetic field lines north- or southwards producing the two regions of higher electron concentration, located 10° north and south of the geomagnetic equator (Anderson, 1973).

A further effect of the magnetic field is concentrated around the magnetic poles. Particles

#### 4 Orbit determination

of the solar wind are directed towards the magnetic poles along the magnetic field lines and penetrate the Earth's atmosphere to very low altitudes. These high energetic particles contribute considerably to the ionization. The different ionospheric layers are not separable and strong variations in the particle flux coming from the sun, cause heavy unpredictable turbulence in the ionosphere. A well-known effect of these disturbances is the Aurora Borealis.

Due to the interaction of the ionosphere with the Earth's magnetic field and its influence on GNSS observations, the ionosphere is often divided into three different regions according to their importance for GNSS users. They are: 1) the auroral and polar caps, 2) the mid-latitudes, and 3) the equatorial "anomaly" region. The largest region is the equatorial region spanning latitudes of 20° north and south of the magnetic equator. The smallest regions in terms of area are the polar caps reaching down to latitudes of approximately 75° north and south, respectively. The remaining area is considered as the mid-latitudes, which is in terms of ionospheric activity the calmest region.

With respect to GNSS measurements, with frequencies in the microwave spectrum, the ionosphere is a dispersive medium. This means that the influence on the signal propagation depends on the used frequency. It must be distinguished between two major effects on electromagnetic waves. On the one hand the traveling speed of the wave is changed, on the other hand the signal is bended.

In general the influence of a medium on a signal is characterized by the refractive index. It can be written as

$$n = \frac{c}{v} \quad (4.6)$$

where  $c$  is the speed of light in vacuum and  $v$  the speed of the wave in the medium. In case of ionospheric refraction the index is described by the Appleton-Hartree equation, see for example in Budden (1985). Above frequencies of 100 MHz the ionospheric refraction can be expressed as series expansion in dependency of the signal frequency. According to Brunner and Gu (1991) it can be written as

$$n_{ion} = 1 - \frac{C_x}{2f^2} N_e \pm \frac{C_x C_y}{2f^3} N_e (H_0 \cos \theta) - \frac{C_x^2}{8f^4} N_e^2 \quad (4.7)$$

where  $C_x$  and  $C_y$  are defined as

$$C_x = \frac{e^2}{4\pi^2 \epsilon_0 m} \quad (4.8)$$

$$C_y = \frac{\mu_0 e}{2\pi m}. \quad (4.9)$$

$N_e$  is the electron density,  $m$  is the mass of an electron,  $e$  is the electron charge,  $\epsilon_0$  is the permittivity in vacuum,  $\mu_0$  is the permeability in vacuum,  $H_0$  is the amplitude of the geomagnetic field,  $\theta$  is the angle between the geomagnetic field vector and the signal direction, and  $f$  is the used signal frequency. The different signs for the third term are to take the polarization of the wave into account. The second term is by far bigger than all following terms together, which are therefore often neglected. If numerical values

#### 4 Orbit determination

are substituted for electron charge and mass, as well as the permittivity in vacuum the equation simplifies to

$$n_{ion} = 1 - \frac{40.3}{f^2} N_e. \quad (4.10)$$

From equations 4.7 and 4.10 it can be seen that the refractive index  $n$  for signals in the ionosphere is smaller than 1. Thus, according to equation 4.6 the phase velocity is higher than the speed of light in vacuum.

Considering a signal modulated on the carrier signal, like the GNSS navigation code, the relation is reversed and the group refractive index is given by

$$n_{Gion} = 1 + \frac{40.3}{f^2} N_e. \quad (4.11)$$

This means that the group refractive index is always greater than 1 and opposed to the effect on the carrier wave.

Speaking in terms of observables the above outlined relation indicates that code observations are delayed whereas phase observations are advanced by the ionosphere. This gives the opportunity to eliminate the ionospheric effect by combining different observations in a certain way. These derived observation types (e.g. the ionosphere-free combination of code or phase observations) are described in section 4.1.4.

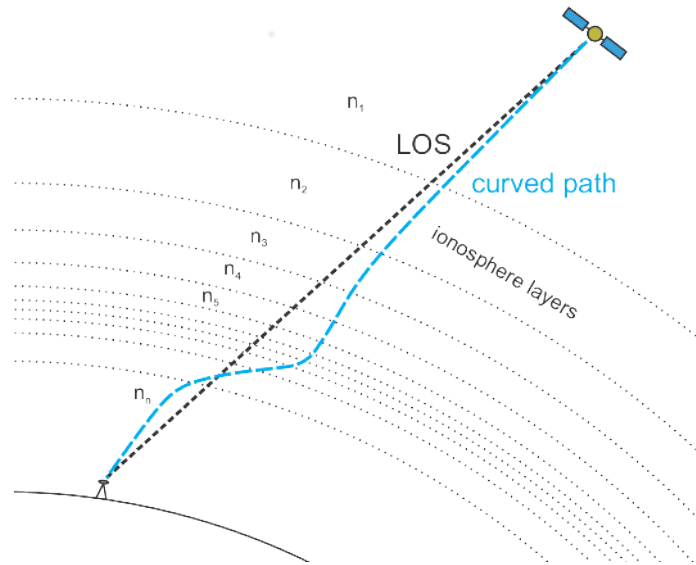


Figure 4.4: Illustration of the ionospheric bending effect on GNSS signals.

The second effect, the bending of the signal, is caused by the changing refractive index along the signal path. According to the law of signal propagation an electromagnetic wave changes the travelling direction if it propagates from one medium to another with slightly different refractive indices. In total, these small changes cause the signal to deviate from the straight Euclidean distance between two points. Under heavy ionospheric conditions the deviation in lateral direction can range up to several hundreds of meters (Brunner and Gu, 1991). Due to this lateral deviation from the line-of-sight, the signal path is longer than the Euclidean distance. This difference is in the range of a few millimeters up to

several centimeters under severe ionospheric conditions (Petrie et al., 2010; Brunner and Gu, 1991). Figure 4.4 illustrates the effect of signal bending in the ionosphere. Layers with different refractive indices ( $n_1, \dots, n_n$ ) indicate the structure of the ionosphere responsible for the deviation of the signal from the straight line.

All descriptions so far are dealing with the physical fundamentals underlying the interaction between the ionosphere and an electromagnetic wave travelling in it. All considerations were made in the context of their effect on GNSS signals and observations in particular. The mathematical formulation to parametrize the ionospheric influence in a least squares adjustment or the formulas used for a priori correction of some effects are described in detail in section 4.3.1.2.

**Troposphere** The troposphere is part of the Earth's atmosphere and extends from ground to heights of approximately 10–15 km, depending on location and season. The troposphere is followed by the stratosphere which reaches up to 50 km. With respect to GNSS signal propagation the troposphere and the stratosphere are a non-dispersive medium. This means that the signal refraction is independent of the carrier frequency. Both layers together make up the neutral atmosphere and their effect on GNSS observations is commonly referred to as the tropospheric delay. Different approaches exist to deal with the tropospheric influence on GNSS measurements, which are for example described in Hofmann-Wellenhof et al. (2008). In case of space borne GNSS observables it is not necessary to take tropospheric influence into account as all satellites are flying at altitudes far beyond the troposphere. Even one of the lowest ever operated satellites, GOCE, stopped tracking GNSS signals at an altitude of 110 km shortly before it burned in the atmosphere. Hence, no further detailed discussion of this topic is required and the reader is referred to GNSS books like Hofmann-Wellenhof et al. (2008) or Misra and Enge (2006).

### 4.1.5.3 Receiver effects and measurement noise

The quality of the employed receiver highly influences the accuracy of GNSS measurements. There are several aspects which affect the observational quality in either a positive or negative manner. Due to this fact and due to the wide range of possible applications for a GNSS receiver, there is a huge variety of different receivers available from different manufacturers. The spectrum of GNSS receivers ranges from cheap and small chips used in cellular phones to high-end geodetic receivers build for special applications, like for example satellite missions. According to the different fields of applications also the costs range from a few dollars up to half a million dollars. As this thesis deals with GNSS based satellite orbit determination, high-end receivers for scientific applications are considered in the following sections.

**Receiver clock** One of the main error sources connected to the used receiver is the clock error. GNSS observations, no matter if code or phase measurements are considered, are in principle run time observations. The problem is that the time measurement involves two different clocks, on the one hand the highly stable transmitter clocks, on the other hand a less stable receiver clock. The ideal case would be that the two clocks are synchronized and represent the same time frame. However, it is not possible to continuously synchronize the receiver clock to the system time with sufficient accuracy. Therefore, all measurements are biased by an offset of the receiver clock from the GNSS system time. This error is common to all observations of one epoch. This enables the estimation of the clock error along with the position parameters. Due to this clock bias, it is necessary to observe at least four satellites at each epoch to solve for the additional clock parameter.

**Receiver antenna center** Reception of electromagnetic signals always involves a dedicated antenna connected to the receiver. As already mentioned for transmitters, the actual point where the measurements rely to is the electronic center of the antenna. The electronic center of an antenna is not a physically defined point inside the antenna. Manufacturers are taking measures to keep the difference between the electric center of the antenna and a defined point as small as possible. But small differences in the range of several millimeters up to centimeters remain (Jäggi et al., 2009b; Schmid et al., 2007).

These differences are often divided into two parts. The first part is due to the fact that in most cases the same antenna is used to receive signals with different frequencies. This difference between frequencies is denoted as Phase Center Offset (PCO) (Montenbruck et al., 2009). It defines a frequency dependent offset from an average antenna center. In addition to this frequency dependent part, the electric center also depends on the incoming direction of the signal. In general, GNSS antennas are directed towards the zenith as this is the direction from which the signals can be expected. Therefore, the antennas are designed to just acquire signals from the upward looking hemisphere. The direction of the signal is usually described by azimuth and elevation with respect to the local horizon. The different incoming directions cause additional small deviations of the electric center from the frequency dependent antenna center, which are commonly denoted as Phase Center Variations (PCVs). Within this work the term Antenna Center Variations (ACVs) is used, due to the fact that variations are taken into account for phase and code observables. Current standard procedures only consider variations for phase measurements.

Both effects, PCO as well as ACVs, do influence position estimates. As the effect on the range measurements is in the range of a few millimeters up to some centimeters, ACVs shall be considered in case of high accuracy applications. For example, surveying or scientific applications with accuracy requirements in the range of millimeters or centimeters. In case of LEO orbit determination it has been shown that PCO and PCVs contribute considerably to the achievable accuracy (Jäggi et al., 2009b; Jäggi et al., 2011a).

The question is how to calibrate the used antennas. Different methods have been developed and applied. For geodetic antennas used in surveying applications, there are two common ways for antenna calibration. One method is the so-called chamber calibration (Görres et al., 2006). The antenna is mounted inside an isolated chamber and artificial GNSS signals are sent into the chamber and received by the antenna. Due to the precisely known geometry of the calibration set up, the difference between observation and "true" value can be calculated and used to generate a map of corrections characteristic for the tested antenna. The second method uses real GNSS signals and a precisely known reference point in combination with a robot arm. The robot arm rotates the antenna around all three axes to cover the whole hemisphere and to cancel out influences caused by the environment (Wübbena et al., 2000). These two methods are used to generate antenna specific calibrations. For a certain antenna type several individual calibrations are averaged and provided to the user. For example the IGS provides antenna calibrations for most geodetic GNSS antennas (IGS Antenna Working Group, 2012).

In case of space borne receivers the situation is slightly different. Although it is also possible to use the aforementioned methods to calibrate antennas used for satellite missions, it has been shown that the different environment in orbit affects the antenna (Montenbruck et al., 2009). Ground based calibrations then do not match the actual errors induced by the differing signal directions. To overcome this limitation, methods for in orbit calibration of the antenna have been developed. One method is based on reduced-dynamic or kinematic observation residuals which are averaged over a long time span (Jäggi et al., 2009b). The antenna hemisphere is divided into a regular grid and the residuals are assigned to one grid cell according to their azimuth and elevation. By averaging over time, a map of ACVs is generated. This map is then used for example in a kinematic orbit determination to correct the observations. Another possibility is to estimate ACVs directly in the orbit determination process (Jäggi et al., 2009b). Parameters representing the ACVs are added to the least squares adjustment. Possible parametrizations are for example piecewise linear functions, spherical harmonics, radial basis functions or any other functions defined on a sphere. The latter approach is adopted in this thesis and is described in detail in section 4.3.1.1.

**Receiver signal biases** The third major group of receiver induced errors are so-called receiver biases. It can be distinguished between frequency or observation type dependent errors. These biases arise from inconsistencies in the observation processing within the receiver. They may be caused by slight manufacturing differences in the receiver electronics, by the slightly different behavior of the involved correlators or by small variations in the oscillator (Banville et al., 2008). In most cases, when using single or double differences, these errors are in fact eliminated. However, in case of PPP these errors do not cancel. Taking into account the achievable accuracy in the range of centimeters those biases come into play. The question is how to determine these biases. As already mentioned, for transmitters, these errors are not directly estimable. In most cases they

are not separable from other parameters, such as the ambiguities or the clock error. The different methods developed in recent years have been already mentioned in section 4.1.5.1.

The only corrections considered in most positioning methods are DCBs. They are provided for GPS satellites and ground stations by CODE (Dach et al., 2009) as part of their daily TEC maps or as monthly mean values. If transmitter specific DCBs are applied in a PPP solution, the position estimation is consistent with the IGS orbit and clock products. Moreover, there is a bias which is related to the employed receiver hardware. For the IGS stations used in the CODE processing, DCBs are also provided in the mentioned products. But as soon as data from a different receiver shall be used the question of how to estimate the specific receiver DCBs arises. A method for receiver code bias estimation, developed in the frame of this work, is introduced in section 4.3.1.6.

**Measurement noise** The effect ultimately limiting the achievable accuracy of any measurement set up is the observational noise if all other models are of sufficient quality. Langley (1997) defined noise as “any unwanted disturbances, superimposed on a signal, that tend to obscure a signal’s usefulness or information content.” This statement should be slightly modified to: Noise is the sum of any unwanted disturbances, superimposed on a signal, that tend to obscure a signal’s usefulness or information content. In case of GNSS observables, the noise is always the sum of several sources that contribute to the total noise level of a certain observation type. Although the different sources of noise can be distinguished and it is possible to investigate a single component, it is not possible to separate the different contributors on the observation level. Once the measurement set up is defined, which includes antenna, cables, receiver and surrounding, the basic contributors to the noise level are settled. Following the notation of Langley (1997), there are four main components that can be distinguished. The following discussion of noise types is based on the paper published by Langley (1997).

The first and most basic type is thermal noise. It is produced by the arbitrary movement of electrons in any conductor with a temperature above absolute zero ( $0^\circ\text{K}$ ). The available noise power is proportional to the temperature of the conductor. In general, the noise can be classified as white noise, meaning that the noise is present on a broad frequency spectrum, and the power in a certain band is independent of the chosen center frequency.

The second type of noise can be named as antenna noise. The GNSS antenna picks up naturally produced electromagnetic radiation, which is present in all frequencies. This radiation received by the antenna comes from the sky, the ground, the surrounding or any object in the vicinity of the antenna. The sky radiation originates from the Earth’s atmosphere, cosmic background radiation left from the big bang, the Sun, the Milky Way and other cosmic objects.

The third contributor is called antenna temperature. It is an antenna characteristic that depends on the antenna gain pattern. The noise actually received by an antenna coming from a certain source depends on the incoming direction of the signal. In case of sky radiation, it would be in principle the whole hemisphere, but others are more or less single sources. GNSS antennas are in principle omnidirectional with a loss of antenna gain towards lower elevation angles. It is not possible to totally avoid small side or back lobes, thus a zenith looking GNSS antenna also observes some radiation coming from the ground or from below the defined horizon. The antenna temperature is not a measure of the actual temperature of the antenna but a measure of the noise power produced by the antenna.

The fourth component is, similar to the antenna temperature, a measure for the noise power introduced by the receiver and therefore called receiver's equivalent noise temperature. It is a combination of cable loss and internally generated noise. Any signal transmitted via a cable is subject to attenuation and increased noise. The internally generated noise is that, of a noise source input to an ideal noiseless receiver that would produce the same output noise. A typical GNSS receiver comprises several components and all contribute to the total receiver temperature.

All these components add up and determine the total noise level of a specific measurement set up. Depending on the incoming direction and the observation type, the measurement noise is determined by this basic configuration. The dependency on the observation type comes from the different techniques used to generate code and phase observations. The first type is produced in the code-tracking loop, or Delay Lock Loop (DLL), where as the latter, is generated inside the carrier-tracking loop, or Phase Lock Loop (PLL). Performance of both tracking types depends on the used configuration. An important parameter in this context is the chosen noise bandwidth. A smaller bandwidth gives lower measurement noise, but the bandwidth must be wide enough to follow the receiver dynamics. So there is always some sort of trade-off between possible receiver dynamics and measurement accuracy. The limitation concerning the measurement bandwidth of DLL and PLL is of special interest for space borne receivers. First of all they exhibit large velocities which in relation to the transmitting satellites cause huge relative accelerations. Additionally, due to the high velocities they also exhibit rapid changes in ionospheric conditions which would never occur for a receiver on ground.

Depending on the chosen measurement set up, the noise level for code observations is in the range of some decimeters up to a few meters and for the phase observations somewhere around one millimeter or slightly higher. This is true for the original observation types as provided by the receiver. If derived observation types, described in section 4.1.4, are used the noise is somewhat increased depending on the combination used. In section 4.3.1.3 an approach to estimate the measurement noise for each observation type individually is presented. The application of the approach to real data and exemplary results for some satellite missions are shown in section 6.2.4.

In addition to the noise of a single observation, there is sometimes also a correlation between different observation types. This has for example been shown by Tiberius and Kenselaar (2000) for phase observations on GPS L1 and L2 as well as for the C/A and P1 code observations. Tiberius and Kenselaar (2000) also showed that the P1 and P2 code observations are in principle uncorrelated and that the correlation between code and phase observations is almost zero. However, the correlation between different observations always depends on the type of receiver and the correlators used to obtain code and phase observations. But it should be kept in mind that the assumption of uncorrelated observables made in most GNSS processing methods is not necessarily true.

## 4.2 Positioning methods

### 4.2.1 Single point positioning

The basic and most simple concept to obtain a position solution with GNSS observations is Single Point Positioning (SPP). This approach only relies on the signals received from the GNSS satellites, no additional information is needed to obtain a position solution. Nowadays, this method is widely used in everyday life, for example in cell phones, car navigation, or pedestrian navigation. The position computation is based on code observations in combination with the GNSS orbit information provided by the system operator. Apart from code observations, also phase or Doppler measurements can be used for SPP. The mathematical formulation for SPP with different observation types can be found in Hofmann-Wellenhof et al. (2008).

For SPP, four satellites or more have to be tracked at each epoch to provide a position estimate. The accuracy depends on the accuracy of the code observations as well as on the quality of the broadcast ephemeris of the transmitting satellites. In general, the accuracy is in the range of a few meters. In the context of space borne applications this method is used to generate the so-called on-board navigation solution in real time (Young, 2001). These on-board solutions are important for collision avoidance or to provide accurate timing information for other on-board sensors. For scientific applications, requiring highest positioning accuracies, SPP is not applicable due to its reduced quality.

### 4.2.2 Precise point positioning

The basic principle of Precise Point Positioning (PPP) is the same as for SPP. The only difference is that for PPP additional information is used to reduce the influence of several error sources on the position solution (Zumberge et al., 1997). Different methods developed for PPP try to take as many error sources as possible into account. To achieve highest accuracies by means of PPP the following supplementary materials are needed:

- Knowledge of transmitter errors
  - Precise GNSS orbits
  - Precise GNSS clock correction
  - Transmitter CoM offsets
  - Transmitter ACVs
  - Transmitter biases (e.g. DCB)
- Knowledge or mitigation of propagation errors
  - Estimation or elimination of the ionospheric influence
  - Estimation or elimination of the troposphere delay
- Knowledge of receiver errors
  - Antenna offset
  - Receiver ACVs
  - Receiver biases (e.g. code or phase biases)

If all these influences are considered, PPP positioning accuracy is in the range of a few centimeters. Currently most published methods for PPP rely on the ionosphere-free combination for code and phase observations to mitigate the ionospheric influence (Zumberge et al., 1997; Ge et al., 2008; Shi and Gao, 2014). An important aspect for real-time PPP is the convergence time of the solution. At the beginning of a PPP session it takes some time until the ambiguities are determined with sufficient accuracy. This also influences the position parameters and thus the highest accuracy is only achieved after some minutes of convergence time. There are numerous approaches to reduce the convergence time or to provide fixed ambiguities in short time. Witchayangkoon (2000) provides a basic description of all necessary steps for PPP.

In recent years, real time capability has become an important topic in the context of PPP. Several research institutions and companies provide experimental or operational services for real time PPP (X. Chen et al., 2011; Caissy et al., 2012; Laurichesse et al., 2009). These efforts are triggered by the big advantage of PPP compared to other methods like Differential GPS (DGPS) or relative positioning. In principle, PPP works globally and independent of a local reference station or a dense reference station network. If the needed precise information about satellite orbits and clocks is provided via a satellite link, the method is even independent of a network connection. Nevertheless, for the generation of the precise orbit and clock products a globally distributed network of permanent stations is needed, but the required station density is much lower than it is the case for conventional RTK networks.

For space borne applications, like in this thesis, real-time capabilities are not as important. LEO satellites are not able to continuously down link their measured data to a ground station. In general, observations of all on board sensors are cached and downloaded to a ground station once the satellite is in view of a down link station. Although most satellite operators have several ground stations available, down links are usually performed once per orbital revolution. Due to this fact real-time applications are difficult to realize, except if on board processing would be used (Montenbruck et al., 2013).

The most important advantage of PPP in post-processing is that all observations of a certain time frame are available and can be processed in one step. No sequential approach or Kalman filter approach to update the position estimate from epoch to epoch is needed. A least-squares adjustment can be set up for an arbitrary time frame and solved in one step. First of all this removes the problem of the convergence time, as observations of the whole time frame contribute to the estimation of all parameters. The second advantage is that also post-processed supplementary data can be used, like precise GNSS orbits and clocks.

### 4.3 Precise orbit determination

The term POD stands for all available methods for precise position determination of artificial satellites in an orbit around the Earth. There is no defined accuracy level to distinguish between POD and orbit determination in general. It is more or less a classification based on the methods applied. In most cases POD is performed in post-processing and aims at the highest possible accuracy by taking into account every known errors and influences on the measurements used.

In the context of POD it can be distinguished between three types of orbits.

- Dynamic orbit
- Reduced-dynamic orbit
- Kinematic orbit

In case of dynamic orbit determination the satellite's movement around the Earth is modeled by considering every known force acting on the satellite, see for example in (W. I. Bertiger et al., 1994; Schutz et al., 1994; Beutler, 2005). All forces, like the gravity field, tides or the solar radiation pressure, are taken into account by using state of the art models. The goal is to reproduce the real world, in terms of acting forces, as close as possible. The computation of the satellite position for a specific epoch is then achieved by integrating the force function over time.

A reduced-dynamic orbit is achieved by estimating empirical parameters in addition to the dynamic orbit parameters (Švehla and Rothacher, 2003; Swatschina, 2012; Jäggi, 2007). The empirical parameters are used to fit the dynamic orbit to observations in a least-squares sense. It is common practice to estimate empirical accelerations for the three different coordinate axes or instant velocity changes in a predefined interval as additional parameters. The type can be chosen arbitrarily, either as single value, polynomial, spline or any other function.

The third type, kinematic orbit determination, only uses geometric observations to estimate the satellite position (Švehla and Rothacher, 2003; Jäggi, 2007). No force function is used to propagate the satellite position from one epoch to the next. The drawback

of this method is that it relies on the availability of a huge amount of observations providing 3-dimensional information. Only if enough observations are available for one epoch the position is estimable. The application of this method is not restricted to GNSS. However, on-board GNSS is the only technology featuring a sufficiently high number of observations with a continuous sampling rate and global coverage. In addition to the good coverage and availability of the observations, the accuracy of GNSS pseudo range measurements is very high.

### 4.3.1 Raw observation approach

Since the first GPS receivers have been developed in the mid-1980s, a lot of approaches have been developed to make use of the different observations (Hofmann-Wellenhof et al., 2008). The same holds for the specific application of orbit determination by GNSS measurements (Bock, 2003; Švehla and Rothacher, 2003; Jäggi, 2007; Swatschina, 2012; van den IJssel et al., 2015). In general, they all rely on derived observations, described in section 4.1.4. Methods based on the ionosphere-free combination are most commonly used in scientific applications. In this work an approach based on raw undifferenced observations is used. The method was first presented by Zehentner and Mayer-Gürr (2012) and later published by Zehentner and Mayer-Gürr (2014) and Zehentner and Mayer-Gürr (2015). A similar approach, but applied to ground based observations, was used by Schönemann (2014).

The key concept of the approach can be formulated as follows:

**USE ALL AVAILABLE OBSERVATIONS, AS THEY ARE OBSERVED BY  
THE RECEIVER, IN A COMMON LEAST-SQUARES ADJUSTMENT.**

The statement can be divided into three parts, each of them containing a specific rule. The first part *'Use all available observations'* addresses the huge variety of available observation types. Currently, at least in space borne applications, the standard case is that the receiver provides phase and code observables on two frequencies. This means that four different measurements are provided. In case of code ranges there are already now three observables available (C/A-Code, P1, and P2). Some receivers even provide three phase measurements - two on L1 and one on L2. As far as these range measurements are independent of each other, which is not the case for observables based on the same carrier frequency (Tiberius and Kenselaar, 2000), all of them shall be incorporated into the position estimation.

The second part *'as they are observed by the receiver'* determines in which way the observations are used. Specifically, this means that no linear combinations or differences shall be used. In GNSS based orbit determination the most commonly applied methods are all based on the ionosphere-free combination to mitigate the influence of the ionosphere. Regardless, which type of combination is used, derived observation types always feature

## 4 Orbit determination

a higher noise level than original observations. However, if original measurements are used, additional parameters must be included for certain effects, e.g. the ionospheric influence.

The final part of the statement '*in a common least-squares adjustment*' expresses the requirement to process all observations together in a joint parameter estimation. The process shall not be divided into sub compartments, where one group of measurements is used to estimate parameters which are then kept fixed and the second group of observations is used to determine the remaining parameters.

After introducing the basic principles of the raw observation approach, let's take a look at the mathematical formulation. The basic observation equation for GNSS measurements, as stated in Hofmann-Wellenhof et al. (2008)

$$R = \rho + c\delta t \quad (4.12)$$

$$\Phi = \rho + \lambda n + c\delta t, \quad (4.13)$$

is used as a starting point.  $R$  and  $\Phi$  denote the code respectively the phase measurement,  $\rho$  is the distance between transmitter and receiver,  $\delta t$  is the combined clock error of receiver and transmitter with respect to the system time,  $n$  the unknown number of phase cycles between transmitter and receiver,  $\lambda$  the specific wavelength of the carrier frequency, and finally  $c$  is the speed of light. The range  $\rho$  contains the position of the transmitter, which must be known, and the receiver position, which is the primarily sought for parameter. From the previous discussion of error sources, section 4.1.5, it is known that there is a wide range of influences affecting GNSS observables. Since none of the errors are eliminated when using raw observations, all of them must be taken into account either by applying a known correction or by estimating it as a parameter in the least squares adjustment. Consequently the raw observation approach can be classified as a PPP method.

Influences that can be modeled with sufficient accuracy or are provided externally, will be a priori reduced from the observations. These are:

- Transmitter clock error
- Relativistic effects (Ashby, 2003)
- Space-time curvature (Ashby, 2003)
- Phase wind-up correction (J. T. Wu et al., 1992)
- Receiver and transmitter code biases

Others are added as additional parameters to the observation equation, as there are:

- Ionospheric delay/advance
- Tropospheric delay

The remaining influences, which are either added as parameters or if already determined introduced as a priori correction, are:

- Transmitter ACVs
- Receiver ACVs

All known corrections are now summed up and subtracted at the left hand side of equation. The right hand side of equations 4.12 and 4.13 are extended by all unknown influences. Once, additional indices are added to separate between transmitters ( $t$ ), receivers ( $r$ ), carrier frequencies ( $i$ ), and observation type ( $R$  or  $\Phi$ ), this finally leads to the following formulation of the observation equations:

$$R_{ri}^t - \Delta R_{ri}^t = \rho_r^t + c\delta t_r + \Delta I_{R_i} STEC + \Delta T + ACV_{ri}^R + ACV_i^{tR} \quad (4.14)$$

$$\Phi_{ri}^t - \Delta \Phi_{ri}^t = \rho_r^t + \lambda_i n_{ri}^t + c\delta t_r + \Delta I_{\Phi_i} STEC + \Delta T + ACV_{ri}^\Phi + ACV_i^{t\Phi}. \quad (4.15)$$

$\Delta R_{ri}^t$  and  $\Delta \Phi_{ri}^t$  represent the sum of all known corrections for code and phase observations.  $\Delta I_{g_i}$  and  $\Delta I_{\Phi_i}$  are the parameters for the ionospheric influence, described in detail in section 4.3.1.2.  $\Delta T$  is the tropospheric delay, which can be omitted in space borne applications, and the four  $ACV$  terms are the parameters for the ACVs described in the two subsequent sections. Based on this extended observation equations, the least squares adjustment for position estimation is set up and solved iteratively, applying the principles of variance component estimation to down weight outliers (see sec. 4.3.1.4). A detailed description of the implemented software and the applied processing scheme is given in chapter 5.

### 4.3.1.1 Antenna center variations

As already outlined in section 4.1.5.3 and 4.1.5.1 ACVs are a major contributor to the total error budget of a position solution. The problem however is that ACVs are only provided for the transmitting satellites and for major geodetic antennas used in classical surveying applications. As most LEO satellite manufacturers or operators do not provide this kind of information, it is necessary to implement a method to estimate receiver ACVs. The IGS provides corrections for the transmitting satellites, but only nadir angle dependent values. As the goal of the proposed approach is to take all possible systematic errors into account, a method to estimate transmitter ACVs is also included. The following two sections describe in detail how the estimation of ACVs is implemented and what parametrization is used.

**Receiver antenna center variations** Antenna calibration and in this context the derivation of correction maps is a highly relevant topic in terrestrial GNSS analysis (Schmid et al., 2016; Jean and Dach, 2015). Several methods have been developed (Wübbena et al., 1996; Schmid et al., 2007; Menge, 2003). There have been attempts to also apply these methods to space borne antennas. The calibrations were made on ground prior to the satellite launch. However, in-orbit validations have shown that the ground calibrations are not always applicable (Jäggi et al., 2009b; Montenbruck

et al., 2009). The results achieved by analyzing observation residuals showed differing systematics than ground calibrations, because near-field multipath and cross-talk from other system components is not covered by a ground calibration.

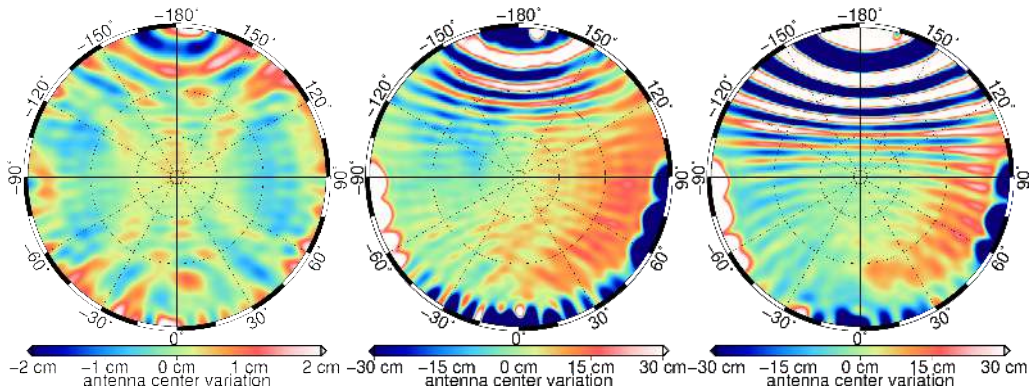


Figure 4.5: Estimated receiver ACVs for GRACE A, combined L1 and L2 correction (left), P1 (middle), and P2 (right).

In this work, receiver ACVs are added to the observation equations as additional parameters. These are then estimated by using a long time span of data (>1 month). All other parameters are eliminated from the system of normal equations to facilitate the combination of longer time spans, for example on the basis of daily or monthly normal equations. Once the ACVs are determined, they are introduced as known correction for subsequent computations. In most cases the antennas of LEO satellites are zenith looking and nothing narrows their view on the sky. Hence, the complete hemisphere is used to track visible satellites down to elevation angles of  $0^\circ$  or in some cases even below. Due to the complete coverage of one hemisphere, the parametrization of ACVs can make use of functions defined on a sphere. A well-known method to parametrize functions on a sphere is to use spherical harmonics. In general, the same formulation as for the gravity field modeling is used. Spherical coordinates are replaced by azimuth and elevation in the antenna reference frame. Thus the following formulation can be used:

$$ACV(\alpha, E) = \sum_{n=2}^N \sum_{m=0}^n (c_{nm} \cos(m\alpha) P_{nm}(\sin E) + s_{nm} \sin(m\alpha) P_{nm}(\sin E)) \quad (4.16)$$

where  $\alpha$  is the azimuth,  $E$  is the elevation,  $P_{nm}$  are the Legendre functions, and  $c_{nm}$  and  $s_{nm}$  are the coefficients of the harmonics expansion. There are two limitations that must be taken into account. First, degree 0 and 1 terms are not estimable. These harmonics correspond to a scale and a shift of the origin (Hofmann-Wellenhof and Moritz, 2006), which is not separable from the clock error and the receiver position. A second restriction must be made due to the missing observations on one hemisphere. Due to this fact the expansion is restricted to only include harmonics which are symmetric to the equator. Figure 4.5 shows estimated receiver ACVs for GRACE A, for phase as well as code observations.

**Transmitter antenna center variations** For transmitter antennas the situation is slightly different to the one for receivers. Due to the high altitude of all GNSS satellites

#### 4 Orbit determination

of approximately 20 000 km, the antenna view angle to cover the whole Earth is just  $14^\circ$ . In case of space borne receivers on LEO satellites, the angle might extend up to  $17^\circ$ , depending on the altitude of the LEO. This narrow field of view makes a parametrization by spherical harmonics impossible. Therefore, a more suitable type of parametrization should be used. One possible option is to use radial basis functions. They can be used to model a signal on the sphere in a small restricted area. A detailed discussion on radial basis functions is given by Eicker (2008).

For a parametrization with radial basis functions an important aspect is to find an appropriate distribution function. In principle, the considered area for transmitter ACVs can be seen as the 'polar region' of the antenna hemisphere. Thus, a simple regular grid based on azimuth and elevation would be very dense at the pole with increasing spacing towards higher nadir angles. The triangle vertex distribution, described by Kenner (1976) and Eicker (2008), is a point distribution which remains almost equidistant, even at the poles. Figure 4.6 shows an example triangle vertex distribution of radial basis functions for a polar cap of  $17^\circ$ . The triangle vertex concept is adopted in this work for distribution of the radial basis functions.

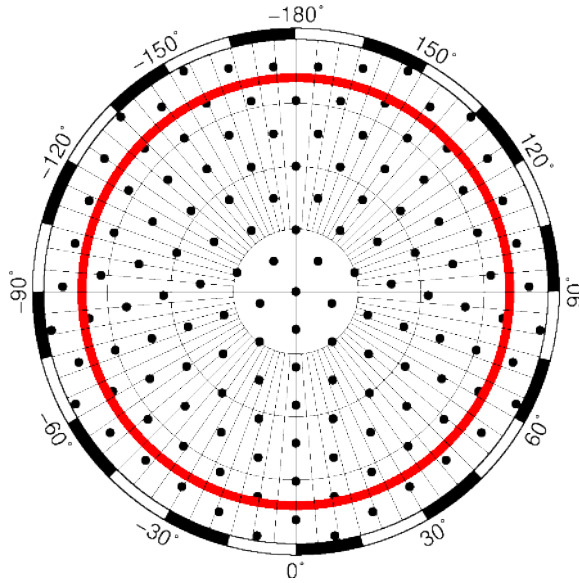


Figure 4.6: Triangle vertex distribution of level 20 (black dots) and border of  $17^\circ$  spherical cap (red). Separation of black circles  $5^\circ$ .

The parametrization of the ACVs can be written as

$$ACV(\alpha, E) = \sum_{i=1}^I a_i \Phi_i(\cos \psi) \quad (4.17)$$

where

$$\Phi_i(\cos \psi) = \sum_{n=2}^N \sqrt{2n+1} \cdot P_n(\cos \psi). \quad (4.18)$$

Again the ACVs are modeled in dependence of azimuth  $\alpha$  and elevation  $E$  (or nadir angle). More specifically, they depend on the spherical distance  $\psi$  between actual point and the location of the base function. The base functions  $\Phi_i$  are represented by sum of

Legendre polynomials  $P_n$  in combination with the specific coefficient  $a_i$ .  $i$ , the index of the base functions, runs from 1 up to the total number of considered base functions  $I$ . The summation in equation 4.18 only starts at degree 2, due to the same reason as for receiver ACVs. Degree 0 and 1 are not distinguishable from a scale or shift in the satellite position. Figure 4.7 shows some examples of estimated transmitter ACVs and the location of the base functions are indicated by the black dots.

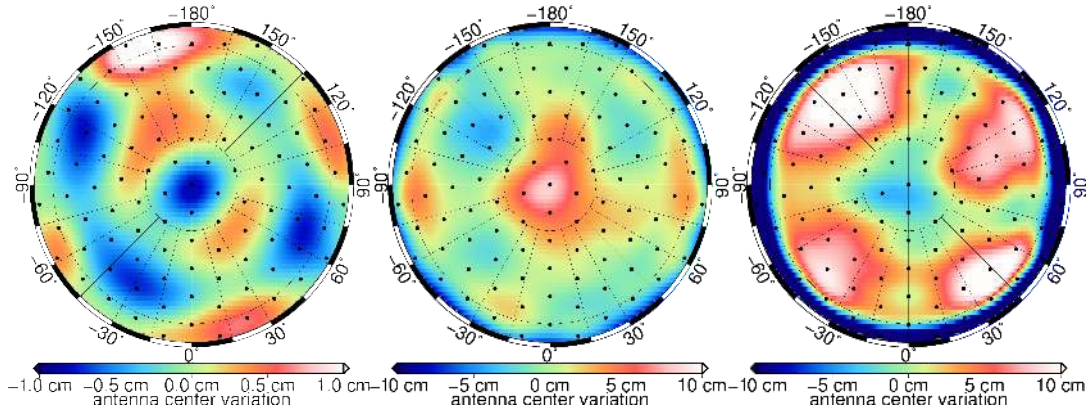


Figure 4.7: Estimated transmitter ACVs for SVN 44, combined L1 and L2 correction (left), P1 (middle), and P2 (right).

#### 4.3.1.2 Ionospheric influence

The basic principles of the ionosphere and its influence on GNSS observables have been already discussed in section 4.1.5.2. This paragraph deals with the mathematical implementation and available concepts for correcting the ionospheric influence.

**Slant TEC** Almost all modern techniques in dual frequency GNSS processing make use of the ionosphere-free combination or observation differences to get rid of the ionospheric influence on the measurements. In case of single frequency observations the ionosphere is approximated by TEC maps or an analytical model. Bock et al. (2009b) discuss different single-frequency methods in case of LEO orbit processing. For general information on different mitigation strategies refer to Hofmann-Wellenhof et al. (2008).

In case of the proposed method the ionospheric influence shall be estimated as Slant TEC (STEC) for each used transmitter in each epoch. This can be achieved by starting from equation 4.10. The STEC is defined as sum of electrons along the line of sight in an area of one square meter. According to equation 4.10 the relation for a simple phase measurement would be

$$\Phi_i = \rho + n_i \lambda_i - \frac{40.3}{f_i^2} \int N_e dL. \quad (4.19)$$

Where  $\Phi$  is the observation,  $\rho$  the Euclidean distance between transmitter and receiver,  $f$  the carrier frequency, and  $\int N_e dL$  the integral along the signal path of the electron concentration. This integral is equivalent to the sum of the electrons or in other words

#### 4 Orbit determination

the STEC. The same relation is valid for code observations, except for the reversed sign of the factor  $40.3/f^2$ .

The above used simple representation of the ionospheric influence on GNSS observations only covers the first order term, but already captures more than 99 % of the effect (M. M. Hoque and Jakowski, 2012). According to previous investigations by Brunner and Gu (1991), Bassiri and Hajj (1993), or Fritsche et al. (2005) it is necessary to include second and third order terms if highest accuracies shall be achieved. Second and third order terms are related to  $f^3$  and  $f^4$  and can have magnitudes of up to several centimeters under severe ionospheric conditions (Brunner and Gu, 1991). Bassiri and Hajj (1993) introduced the following notation:

$$R_i = \rho + \frac{q}{f_i^2} + \frac{s}{f_i^3} + \frac{r}{f_i^4} \quad (4.20)$$

$$\Phi_i = \rho + n_i \lambda_i - \frac{q}{f_i^2} - \frac{1}{2} \frac{s}{f_i^3} - \frac{1}{3} \frac{r}{f_i^4} \quad (4.21)$$

where

$$q = 40.3 \int N_e dL = 40.3 \text{ STEC} \quad (4.22)$$

$$s = \pm 7527 \cdot c \int N_e |\mathbf{B}_0| \cos \theta_B dL \quad (4.23)$$

$$r = 2437 \int N_e^2 dL + 4.74 \cdot 10^{22} \int N_e \mathbf{B}_0^2 (1 + \cos^2 \Theta_B) dL. \quad (4.24)$$

The subscript  $i$  indicates the used frequency,  $c$  is the speed of light,  $\mathbf{B}_0$  the magnetic field vector at the intersection of the signal path and the ionosphere layer, and  $\Theta_B$  the angle between the magnetic field vector and the signal direction. The (+) and (−) signs in equation 4.23 are to distinguish between extraordinary and ordinary waves respectively. As GNSS signals are in general right-hand circular polarized and the left-hand circular polarized component has less than 3% of the signal power, only the (+) sign is of relevance for GNSS applications (Bassiri and Hajj, 1993).

After some simplifications and replacing the integral  $\int N_e dL$  by the STEC the first, second and third order corrections can be written as:

$$\Delta I_{R_i}^{(1)} = -\Delta I_{\Phi_i}^{(2)} = \frac{40.3}{f_i^2} \cdot \text{STEC} \quad (4.25)$$

$$\Delta I_{R_i}^{(2)} = \frac{7527}{c^2} \lambda_i^3 (\mathbf{B}_0 \cdot \mathbf{k}) \cdot \text{STEC} \quad (4.26)$$

$$\Delta I_{\Phi_i}^{(2)} = -\frac{1}{2} \Delta I_{R_i}^{(2)} \quad (4.27)$$

$$\Delta I_{R_i}^{(3)} = \frac{2437}{c^4} \lambda_i^4 N_{max} \eta \cdot \text{STEC} \quad (4.28)$$

$$\Delta I_{\Phi_i}^{(3)} = -\frac{1}{3} \Delta I_{R_i}^{(3)}. \quad (4.29)$$

For the third order term (eq. 4.28) two additional values were introduced by Brunner and Gu (1991), a shape parameter  $\eta$ , a good approximation is 0.66 (Brunner and Gu, 1991),

#### 4 Orbit determination

and the peak electron density along the signal path  $N_{max}$ , which is approximated by a linear interpolation taking the actual TEC into account:

$$N_{max}[m^{-3}] = \frac{(20 - 6) \cdot 10^{12}}{(4.55 - 1.38) \cdot 10^{18}} \cdot STEC. \quad (4.30)$$

By using the above described parametrization the basic observation equations of code and phase observations are extended by the following term, already indicated in equations 4.14 and 4.15:

$$\Delta I_{R_i} STEC = \Delta I_{R_i}^{(1)} + \Delta I_{R_i}^{(2)} + \Delta I_{R_i}^{(3)} \quad (4.31)$$

$$\Delta I_{\Phi_i} STEC = \Delta I_{\Phi_i}^{(1)} + \Delta I_{\Phi_i}^{(2)} + \Delta I_{\Phi_i}^{(3)}. \quad (4.32)$$

On the right-hand side the estimated STEC parameter is contained in the three terms  $\Delta I^{(1)}$ ,  $\Delta I^{(2)}$ , and  $\Delta I^{(3)}$ , as it can be seen from equations 4.25-4.29.

**Ionospheric bending** Several studies have been conducted dealing with the bending term of the ionospheric range error. Hartmann and Leitinger (1984) have been the first to take ionospheric bending of signals into account. They provided the following correction formula

$$b \approx c^r \left( \frac{A_p^2}{f^4} \right) VTEC^2 \left( \frac{\eta}{VTEC/N_m F_2} - \frac{1}{h_s} \right) \text{ with } c^r = \frac{\tan^2 z'}{8 \cos z'}, \quad (4.33)$$

where  $b$  is the correction in  $m$ ,  $z'$  the zenith angle of the signal at mean ionospheric height,  $\eta$  is a shape factor,  $VTEC$  is the vertical TEC,  $N_m F_2$  is the peak electron density height,  $h_s$  the height of the transmitter and  $A_p$  is a physical constant with a value of  $80.6 \text{ m}^3 \text{ s}^{-2}$ .

The second study dedicated to ionospheric bending was published by Brunner and Gu (1991). They also derive an empirical formula to compute a correction for the signal bending effect.

$$b \approx 4.70 \cdot 10^5 \frac{A_p^2}{8f_1^4} N_m^2 \cos^2 \beta \cot \beta \quad (4.34)$$

where  $\beta$  is the elevation angle and  $N_m$  is the maximum electron density. In addition to this formula, valid only for the L1 frequency, they provide a small correction term to calculate the correction also for L2.

Furthermore, Jakowski et al. (1994) provide a correction for the bending effect. The work by M. Hoque and Jakowski (2008) is then based on the previous work and provides an updated version of the correction. They furthermore distinguish between the geometric bending and a range error due to TEC differences at two frequencies. The second term is also called dTEC bending error. For the geometric part of the bending effect they provide the equation

$$b \approx \frac{7.5 \cdot 10^{-5} \cdot STEC^2 \cdot \exp(-2.13\beta)}{f^4 HF_2 \cdot (h_m F_2)^{1/8}} \quad (4.35)$$

where  $HF_2$  is the  $F_2$  layer scale height and  $h_m F_2$  the  $F_2$  height of the peak electron density. Both values given in km, STEC in TEC units, frequency  $f$  in GHz and the elevation  $\beta$  in radians features the bending correction in millimeters.

#### 4 Orbit determination

The dTEC bending error can be explained by the fact that due to the bending effect, signals with different frequencies are refracted slightly different and hence travel along different paths. Due to this fact, both observations represent different STEC values. In the estimation process one common STEC shall be estimated and therefore a correction is necessary to take this small difference into account.

$$\Delta TEC = \frac{0.1108 \cdot STEC^2 \cdot \exp(-2.1844\beta)}{f^2 HF_2 \cdot (h_m F_2)^{0.3}} \quad (4.36)$$

where  $\beta$  is in radians, STEC is in electrons/ $m^2$ ,  $HF_2$  and  $h_m F_2$  are in km and  $f$  is in Hz. The resulting correction is given in electrons/ $m^2$  and can be converted to a range correction by applying the formula used for the first order ionospheric influence, given in equation 4.19.

Petrie et al. (2010) compared the different empirical formulas and showed that they produce similar corrections. None of the methods proved to be more accurate than another. Due to the fact that the correction proposed by M. Hoque and Jakowski (2008) also includes a correction for the TEC difference range error, this method is used in this work. The right choice for  $HF_2$  and  $h_m F_2$  is also discussed by Petrie et al. (2010).

There are several possible ways to come up with values for the F2 peak electron density height and the F2 layer scale height. A first approximation would be to use global mean values derived from model analysis or observations. M. Hoque and Jakowski (2008) suggested to use 350 km and 70 km respectively. However, the peak electron density can vary significantly, depending on solar activity, time of day and geographic location. Nevertheless, these values represent a good compromise. A more realistic approach is to derive  $h_m F_2$  from a model, like the International Reference Ionosphere (IRI) (Bilitza et al., 2011). In general, the IRI model gives a good approximation of the ionospheric conditions, but the model is based on monthly average values for different ionospheric components and thus does not represent the actual ionospheric conditions. One could also try to derive estimates for  $h_m F_2$  and  $HF_2$  from observed STEC values, as proposed by Fritsche et al. (2005).

In view of an average F2 layer height of 350–450 km and orbit altitudes of 250–1500 km a fixed height seems not appropriate for LEO satellites. Only a few satellites will be situated below the ionosphere layer. Others would be at the same height or even above the thin shell. Taking this fact into account leads to the conclusion that it is more important to situate the thin shell above the satellite as to find a realistic peak electron density height. Therefore,  $h_m F_2$  is set to satellite altitude plus 50 km in combination with  $HF_2$  set to a mean value of 60 km (Petrie et al., 2010). Investigations have shown that orbit results are almost insensitive to changes in the peak electron density height and the layer scale height.

### 4.3.1.3 Observation weighting

Observation weighting is an important aspect in any least-squares adjustment. It is even more important if different types of observations, with varying accuracies, are involved in the same estimation. This is the case for the applied method for POD as all observations are introduced in their original constitution. The two available observation classes are code on the one hand and phase measurements on the other hand. Generally code observations are considered to have a standard deviation of several decimeters. Phase measurements feature higher accuracy in the range of a few millimeters. For a general discussion of observation quality in GNSS the reader is referred to Hofmann-Wellenhof et al. (2008).

There are several possible ways to define the weight of GNSS observations in the context of a least-squares adjustment. The first one is to use predefined fixed values for each observation type. The values used could be some global assumption on the accuracy of space borne GNSS observations or they may be taken from the receiver specifications. The only effect of this weighting scheme is a relative weighting between various observation types.

A widely used scheme for observation weighting in GNSS is to apply an elevation dependent scaling of a priori values. This gives a more realistic representation of the actual observation quality. GNSS antennas feature the highest gain in zenith direction and the gain gradually reduces for lower elevation angles (Ingvarson et al., 2007). In addition to the antenna characteristics, signals received at lower elevation angles travel a longer way, especially the distance through the ionosphere is longer than for signals at high elevations. This leads to a stronger signal attenuation, more scattering of the signal, and thus to a lower Signal to Noise Ratio (SNR), which in turn means reduced observation quality. For elevation dependent weighting typically the term  $1 / \sin E$  is used in some way to scale the a priori standard deviation of observations.

In addition to code and phase observations, GNSS receivers also provide a measure of the signal quality. This is denoted as SNR and in most cases given in the Receiver Independent Exchange Format (RINEX) observation file (Gurtner and Estey, 2007). The RINEX format provides two different ways how the observation quality can be represented. The first option is to include the SNR as additional observation in the RINEX file. The second possibility is to map the actual SNR value to a standardized quality flag. This quality flag is limited to values from 0 to 9, with 9 being the best quality and 0 the worst. This value is given in the RINEX file directly after each observation. These two quality measures can be used to adjust the weight of each observation individually. The advantage of this method is the fact that the SNR value is a direct indicator of the current signal quality at the time of observation.

Similar to the inhomogeneous structure of ACVs, also the tracking quality strongly depends on the incoming direction of the signal. Hence, the most sophisticated method to

represent the observation quality is to apply an elevation and azimuth dependent function. This can be achieved by analyzing observation residuals of a longer time span. By taking into account the redundancy of each single observation, it is possible to estimate an accuracy map covering the whole hemisphere. Systematic effects, in particular the ACVs, must be considered, otherwise these errors would affect the estimated accuracies.

The antenna hemisphere is divided into regular grid cells with equidistant spacing in azimuth and elevation. All available observation residuals are then associated to a grid cell according to their elevation and azimuth. Afterwards, all residuals within one cell are used to compute an empirical standard deviation for this particular cell. This is done for each observation type individually. The produced map represents the empirical standard deviation of an observation type with azimuth and elevation dependency.

The computation of the standard deviation for each cell can be written as

$$\sigma^2(\alpha, E) = \frac{\sum e_i^2}{\sum r_i}. \quad (4.37)$$

where  $e_i$  are the residuals and  $r_i$  are the corresponding redundancies coming from the preceding position estimation (see sections 2.5 and 2.6). Figure 4.8 shows three examples of empirical accuracy maps, generated from observations residuals. It can be seen that in principle the structure is homogenous and pretty stable with a clear elevation dependency. But there are also some small deviations, for example in the pattern for P2 code observations, some small irregularities are visible. A detailed discussion of results for different satellites is given in section 6.2.4.

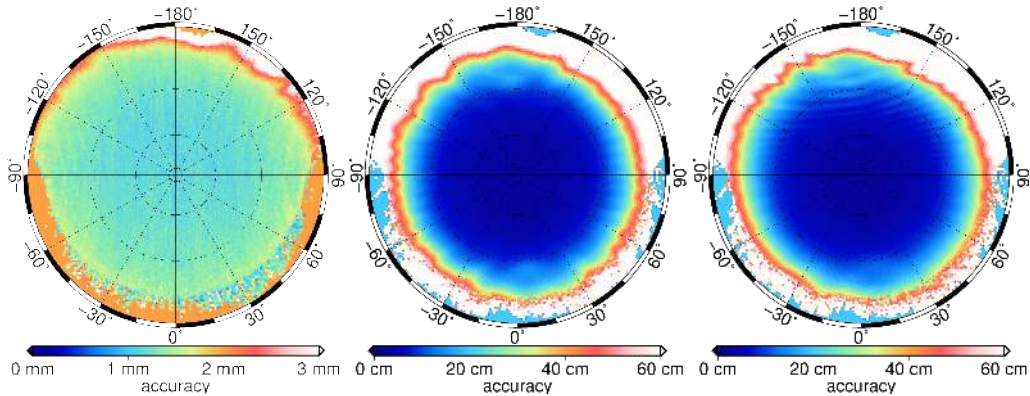


Figure 4.8: Estimated observation accuracies for GRACE A, L1 (left), P1 (middle), and P2 (right). Azimuth  $0^\circ$  corresponds to the flight direction.

#### 4.3.1.4 Outlier detection

Any kind of measurement record, be it analog or digital, contains outliers. If these observations are combined in a least-squares sense to quantify any physical process, outliers will significantly distort the results. Hence, it is important to identify errors in the observations and take appropriate action to avoid incorrect results. The azimuth and elevation dependent weighting scheme, introduced in the previous section, already

provides a realistic description of the stochastic properties of GNSS measurements. Nevertheless, random outliers are not considered within the a priori assumption of the observation accuracy.

A possible method to identify outliers in the course of an iterative least-squares adjustment is the method of variance component estimation (Koch, 2004). The basic principle is described in section 2.6. Based on the residuals and redundancies for a group of observations an empirical variance is computed. It is defined as

$$\hat{\sigma}_k^2 = \frac{\Omega_k}{r_k} \quad (4.38)$$

where  $\hat{\sigma}_k^2$  is the empirical variance,  $\Omega_k$  is the squared sum of residuals  $\Omega_k = \hat{\mathbf{e}}_k^T \hat{\mathbf{e}}_k$ , and  $r_k$  is the sum of observation redundancies. The residuals are given by

$$\hat{\mathbf{e}}_k = \mathbf{A}_k \hat{\mathbf{x}} - \mathbf{l}_k. \quad (4.39)$$

The redundancy  $r_k$  can be derived by

$$r_k = m_k - \frac{1}{\sigma_k^2} \text{trace}(\mathbf{N}_k \mathbf{N}^{-1}), \quad (4.40)$$

where  $\mathbf{N}_k$  is the normal equation of the considered group of observations,  $\mathbf{N}$  is the full normal equation, and  $m_k$  is the number of observations within the group. The subscript  $k$  in equations 4.38, 4.39, and 4.40 denotes the observation group.

This approach is used to estimate an empirical variance for each tracked satellite, in each epoch, separately for code and phase observations. Under current conditions (only GPS L1 and L2 frequencies used), this means that a common variance is estimated for two observations, either two code or two phase measurements. The empirical variance is then compared to the given a priori value. If these two values differ significantly from each other, a new weight, determined by the estimated variance, is assigned to the observations. This is only done if the empirical variance is significantly higher than the a priori variance. The decision on the significance of the difference is made by applying a modified Huber M-estimator (Koch, 2004).

This way the weight of outliers is continuously reduced, according to the size of the residuals but taking the available redundancy for these observations into account. The used approach features two advantages. Firstly, there is no need for an a priori outlier detection algorithm to remove bad observations. Secondly, epochs with a small number of observations are still solvable, which would not be the case if bad measurements were removed in advance. The only drawback is the fact that it is important to have enough observations available to guarantee a reliable detection of outliers.

#### 4.3.1.5 Cycle slip detection

For any GNSS position estimation including phase observations the definition of the ambiguity parameter is essential. In general, this parameter is constant for a continuous

track of one transmitting satellite. This means, as long as the receiver observes a specific transmitter without interruptions, the ambiguity remains constant. However, GNSS phase observations sometimes suffer from an effect called cycle slip. In this case the ambiguity changes instantaneously from one observation epoch to the next. The occurring change in the ambiguity is an arbitrary number of cycles. It might be only one cycle as well as several hundreds or thousands of cycles. The reasons for these instant jumps are manifold. Maybe it occurs due to a short loss of signal between two measurement epochs, due to strong disturbances of the signal, or it can be related to large accelerations of the receiver. In any case the ability of the receiver to correctly track the GNSS signal is somehow corrupted. Cycle slips might occur on different frequencies or for different transmitters being tracked at that time or just on one single frequency for one specific transmitter. In any case it is of crucial importance to detect these jumps and set up a new ambiguity parameter after the jump occurred.

In this work the cycle slip detection is based on the Melbourne-Wübbena combination (see sec. 4.1.4). As this particular combination removes all effects, except for the ambiguity, it should remain constant over a continuous track of one GNSS satellite. In case a cycle slip occurs on one of the two frequencies, the Melbourne-Wübbena combination also exhibits a change. This coherence is used to find epochs in which a cycle slip occurs.

All available observation tracks are checked separately. The used approach is based on a robust mean estimation by using the median. The median of all Melbourne-Wübbena values preceding a certain epoch, is compared to the median of all subsequent values. If the difference exceeds a predefined threshold it is assumed that a cycle slip occurred. To avoid false decisions the mean before and after the jump is re-estimated by a weighted least-squares adjustment including variance component estimation to detect outliers. The new mean values are again compared to each other. If the newly computed difference still exceeds the threshold the location of the possible cycle slip is confirmed. Otherwise the decision is revised and not considered as a cycle slip. After the process was carried out for all observations, the definition of the ambiguity parameters is found and kept fixed for all iterations of the least-squares adjustment.

### 4.3.1.6 Receiver code bias

In case of PPP on the basis of raw GNSS observations it is possible to estimate the characteristic receiver DCBs, described in section 4.1.5.3, from the estimated STEC. The receiver DCB is considered as one bias common to all code observations. It mainly affects the absolute value of the estimated STEC. Due to the fact that the STEC depends on the geometry, azimuth and elevation, but the DCB does not, it is possible to separate them. By converting the STEC into a Vertical TEC (VTEC) by application of a mapping function the DCB can be estimated. Similar approaches have been used for ground-based investigations by Lanyi and Roth (1988) or Themens et al. (2015).

#### 4 Orbit determination

The STEC can be converted into VTEC by a projection into the vertical direction with the help of a mapping function.

$$STEC = \frac{VTEC}{\cos z'} \quad \text{with} \quad \sin z' = \frac{R}{R+H} \sin(\alpha z) \quad (4.41)$$

where  $R$  is the mean radius of the Earth,  $H$  is the height of the ionospheric single layer above the Earth's surface,  $z'$  is the zenith angle at the ionospheric pierce point, and  $\alpha$  is a predefined constant (0.9782) (Schaer, 1999). In order to take the DCB into account equation 4.41 is extended to

$$STEC = \frac{VTEC}{\cos z'} + \frac{1.5457 c f_1^2}{40.3 \cdot 10^{16}} DCB \quad (4.42)$$

where  $c$  is the speed of light, 40.3 is a constant related to the electron mass, the electron charge and the permittivity of the free space, in units of  $\text{m}^3 \text{s}^{-2}$  (Petrie et al., 2010). The relation given in equation 4.42 is valid for GPS frequency L1 and the value 1.5457 is derived from the equation

$$\frac{f_2^2}{(f_1^2 - f_2^2)} = 1.5457. \quad (4.43)$$

If GPS frequency L2 would be used the value changes to 2.5457, which in turn multiplied by the speed of light and the squared frequency  $f_2$  results in the same constant value as denominator for the second term of equation 4.42. By applying this relationship to estimated STEC values of one or more epochs, it is possible to estimate the receiver specific DCB.

## 5 Orbit processing

The present chapter shortly introduces the developed software for POD and different tools developed for data handling and preparation. The second part of the chapter describes the adopted processing scheme, from the first ACV estimation to the final orbit computation.

### 5.1 General software description

The working group Theoretical Geodesy and Satellite Geodesy at the Institute of Geodesy (IfG) develops and maintains a software package, Gravity Recovery Object Oriented Programming System (GROOPS), dedicated to all kinds of tasks related to gravity field recovery. Initially the software was implemented by Prof. Dr.-Ing. Mayer-Gürr during his studies and employments at the University of Bonn, Germany. Since 2011 development and software maintenance is conducted at the IfG. The core functionality of GROOPS concentrates on gravity field determination from different satellite observations. Besides the main functionality, the software features a wide range of tools for data handling, conversion, and visualization. Currently the whole package comprises approximately 200 individual tools written in c++ programming language. In principle GROOPS is a command line tool controlled by configuration files in Extensible Markup Language (XML)-format. In order to facilitate easy handling and control of the software a Graphical User Interface (GUI) is available, which generates the XML file in the background. A screen shot of the user interface is shown in figure 5.1.

#### 5.1.1 Basic functionality and data structure

A wide range of different observations are involved in the process of gravity field estimation, regardless of the method used. Depending on the satellite mission, data is distributed in different formats. For example, orbit positions are either distributed in the sp3-format (Hilla, 2010), defined and proposed by the IGS, or in a simple American Standard Code for Information Interchange (ASCII) format or in a binary format, as for example GRACE orbit data. Due to the inhomogeneity of data formats, GROOPS internally uses its own formats for all data sets. In the frame of this work a variety of programs for data conversion have been developed to read the different observations of all satellite missions. Conversion routines have been implemented to import GPS

## 5 Orbit processing

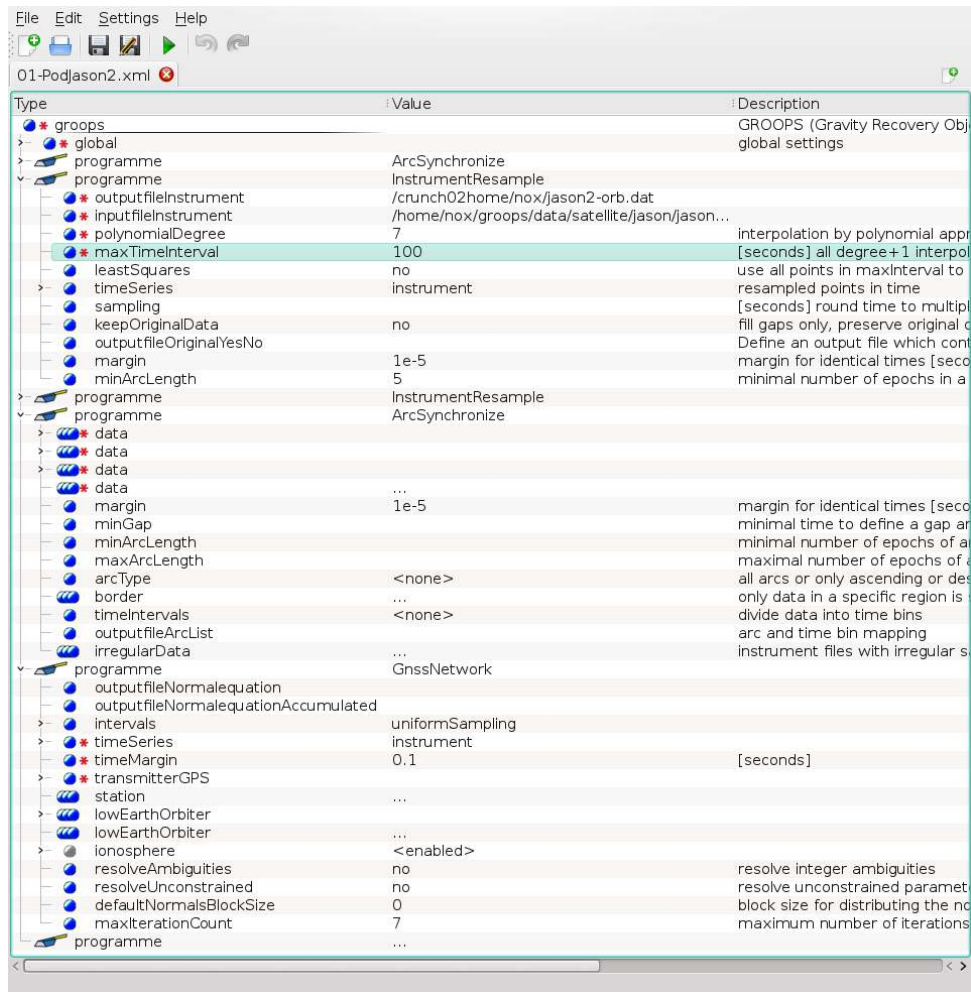


Figure 5.1: Screen shot of the GROOPS GUI showing an example configuration for POD.

observations, attitude data, accelerometer observations, and a priori or reference orbit solutions. It was necessary to write individual tools for almost every satellite mission and every observation type. Currently the following data types are defined within GROOPS

- Orbit positions
- Satellite attitude
- Accelerometer observations
- Gradiometer observations
- Satellite tracking observations
- Gravity measurements
- Position covariance information
- Altimeter observations
- GNSS observations
- Magnetometer observations
- Thruster events
- Satellite mass information
- Star camera covariance information

In principle, the definition of the internal formats is the same for all data types. Thus it is possible to use the same tools for different data types. Some of the most important tools used in this work are listed in table 5.1 along with a short explanation.

Name	Tasks
arcSynchronize	data organization, time synchronization of different data files
instrumentResample	interpolate data to predefined time stamps (orbit positions, accelerometer measurements, ...)
instrumentReduceSampling	thin out data
instrumentOutlierRemove	find and remove outliers

Table 5.1: Important data handling tools available in GROOPS.

Within the GUI it is possible to combine several tools, which are then executed sequentially. This offers countless possibilities to combine the available tools and to generate the desired outcome. For example, in figure 5.1 five programs are lined up. In addition, it can be seen that each of these tools needs to be configured by setting some parameters or input and output files. A description of all available programs and their possible settings would go far beyond this work and thus only the GNSS processing tool *GnssNetwork* is described in detail in the following subsection.

### 5.1.2 GnssNetwork

The most important tool developed and used in the frame of this work is *GnssNetwork*. It contains all necessary functionality to process GNSS observations of satellite missions and generate highly accurate kinematic orbit positions. Based on input data and settings, the program sets up observation equations, accumulates normal equations, and if desired solves for position parameters. Depending on the chosen settings orbit positions, the corresponding covariance information, observation residuals, or accumulated normal equations are saved. All input and output data uses the GROOPS internal format definitions. Thus, *GnssNetwork* is always preceded by a number of tools for data conversion and synchronization. Table 5.2 lists all settings available in *GnssNetwork*, followed by table 5.3 describing parameters of the items *transmitterGPS* and *lowEarthOrbiter*.

Caption	Description
outputfileNormalequation	Output file for complete normal equation
outputfileNormalequation-Accumulated	Output file for accumulated normal equation of static parameters (e.g. ACVs)
intervals	Processing interval to be used (usually days)
timeSeries	Time series of epochs for which a position shall be computed

Caption	Description
<code>timeMargin</code>	Defines a time margin around epochs defined in <code>timeSeries</code>
<code>transmitterGPS</code>	All settings related to the transmitting GPS satellites, see table 5.3
<code>station</code>	All settings related to a ground based receiver
<code>lowEarthOrbiter</code>	All settings related to a space borne receiver, see table 5.3
<code>ionosphere</code>	Possible input of a priori information about the ionospheric conditions (e.g. TEC maps)
<code>resolveUnconstrained</code>	Solve for static parameters (e.g. ACVs)
<code>defaultNormalsBlockSize</code>	Maximum size of normal equations, otherwise split into several files
<code>maxIterationCount</code>	Maximum number of iterations

Table 5.2: Basic settings available in the program *GnssNetwork*.

Caption	Description
<i>transmitterGPS</i>	
<code>inputfileGpsSatelliteInfo</code>	File containing satellite information (SVN, type, start and end date, ...)
<code>inputfileAntennaDefinition</code>	File containing information about antenna offsets and variations
<code>inputfileSignalBias</code>	File containing transmitter signal biases
<code>inputfileGpsOrbit</code>	File containing precise satellite orbits
<code>inputfileGpsClock</code>	File containing precise satellite clock information
<code>interpolationDegree</code>	Polynomial degree for position interpolation
<code>antennaCenterVariations</code>	Definition of ACVs to be estimated
<code>timeStartACV</code>	Start time of ACVs to be estimated
<code>timeEndACV</code>	End time of ACVs to be estimated
<i>lowEarthOrbiter</i>	
<code>outputfileOrbit</code>	Destination file for orbit results
<code>outputfileCovariancePod-Epoch</code>	Destination file for estimated covariance information (3x3 covariance matrix for each epoch)
<code>outputfileResiduals</code>	Destination file for observation residuals
<code>inputfileStationInfo</code>	Definition of station parameters (receiver name, offset to center of mass, antenna name, ...)
<code>inputfileAntennaDefinition</code>	Definition of antenna parameters (ACVs, PCOs, ...)
<code>inputfileAccuracyDefinition</code>	Definition of accuracy patterns
<code>inputfileSignalBias</code>	File containing signal biases for the receiver
<code>inputfileObservations</code>	File containing GNSS observations

Caption	Description
inputfileOrbit	File containing a priori satellite orbit
inputfileStarCamera	File containing attitude information
elevationCutOff	Definition of the applied elevation cut off angle
minimumTrackLength	Definition of minimum observation track length
snrWeightFunction	Definition of a SNR dependent observation weighting
weightFactorFunction	Definition of a scale function for the observation weight depending on the Rate of TEC Index (ROTI), TEC rate of change, or scintillation indices
mwFactor	Factor to define the threshold in the cycle slip detection algorithm
useType	Defines observation types to be used
ignoreType	Defines observation types to be ignored
antennaCenterVariations	Defines parametrization of ACVs to be estimated
timeStartACV	Start time of antenna definitions to be considered
timeEndACV	End time of antenna definitions to be considered

Table 5.3: Settings for *transmitterGPS* and *lowEarthOrbiter*.

Some of the above mentioned settings and input data sets are rather straight forward to choose, whereas others are more or less a matter of experience or trial and error. In fact, the processing scheme must be adapted to the specific properties of each satellite mission. For example, the minimum track length must be chosen according to the sampling of the available GPS observations and their quality. Similarly, scaling of a priori observation weights by SNR, ROTI or any other quantity is not beneficial for every mission. Or the parametrization of receiver ACVs must be adjusted to receiver and antenna properties. These three examples already illustrate the high complexity of finding optimal settings for each mission.

## 5.2 Kinematic orbit determination

Intensive testing and data investigations revealed an optimal processing scheme to achieve high accuracies in terms of the positioning error. In general, it is a four-stage process to finally produce accurate kinematic orbit positions. Figure 5.2 shows a flow chart which outlines the basic principles of the adopted processing scheme.

The first step is to estimate ACVs for the receiver. Therefore, an orbit computation is carried out in which receiver ACVs are set up as additional parameters in the observation equation, according to the description given in section 4.3.1.1. Transmitter ACVs are omitted in this first step. The orbit computation is iterated several times in order to down weight outliers as described in section 4.3.1.4. This iterative outlier detection is performed in every step. After the last iteration all parameters, except the ACVs, are

## 5 Orbit processing

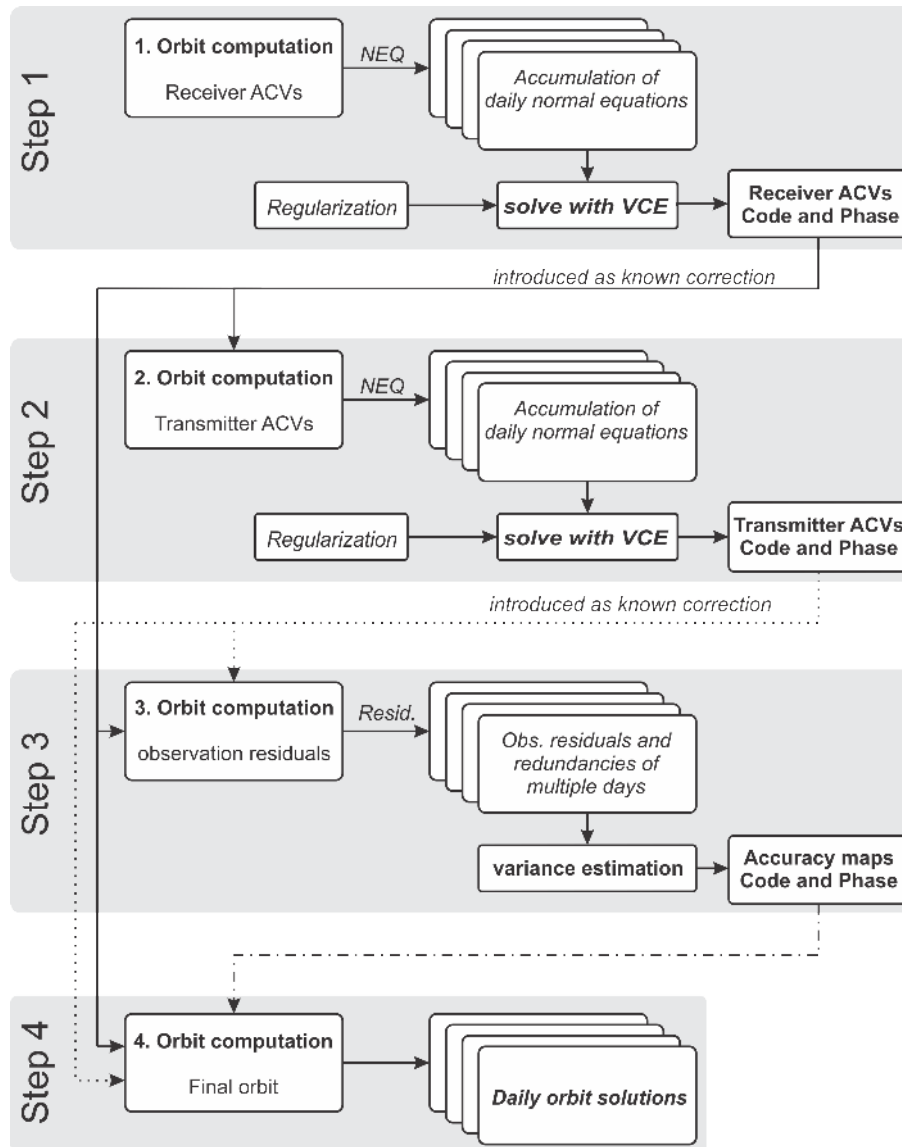


Figure 5.2: Flow chart of necessary steps for precise kinematic orbit determination.

eliminated by means of parameter elimination and the remaining normal equations are saved. Thus, kinematic orbit positions, receiver clock errors, and ionosphere parameters are implicitly contained in the system of normal equations. Afterwards, normal equations covering a long time span ( $> 1$  month) are combined and solved by applying the principles of variance component estimation. In some cases large observation errors or an inhomogeneous data distribution may distort the estimated parameters. Thus, the process may also include a Tikhonov regularization (Tikhonov, 1963) for the ACV parameters, to guarantee a stable and reliable estimate. From the estimated ACV parameters, i.e. the coefficients of a spherical harmonics expansion, correction maps are generated, which are subsequently introduced as known corrections to the observations.

The second step is to estimate the ACVs for the transmitting satellites. In principle, the approach is the same as for receiver ACVs. In this case the previously estimated receiver ACVs are already introduced as known corrections. The coefficients of the radial basis function representation are set up as additional parameters in the observation equations,

other parameters are eliminated, and the normal equations are saved. The applied parametrization is explained in section 4.3.1.1. Again variance component estimation is used to combine data from a long time span ( $> 1$  year) to solve for the parameters. Again including a Tikhonov regularization can be used to stabilize the estimated parameters. This approach also gives the possibility to combine normal equations from different satellite missions to further stabilize the solution. The radial basis function representation is then evaluated on a regular grid to produce correction maps for the transmitting satellites. In the next step these correction maps are again introduced as known corrections to the observations.

The third step is to generate accuracy maps for each receiver and observation type, according to the approach described in section 4.3.1.3. Therefore, the third orbit computation is carried out and in this case it is essential that a posteriori observation residuals and their corresponding redundancies are computed and saved. Residuals of a long time span ( $> 1$  week) are then used to generate accuracy maps for each individual observation type. These maps are then used to determine the a priori weight of each observation in the final orbit computation.

The fourth and final step is to introduce all estimated corrections and perform the final orbit computation. Receiver and transmitter ACVs are introduced as known corrections and are a priori subtracted from the observations. Accuracy maps are used to define the weight of each observation individually, depending on type and incoming direction. The following parameters are set up in the observation equation for each epoch: kinematic orbit position, receiver clock error and one STEC parameter for each tracked transmitter. As epoch independent parameters the phase ambiguities for each continuous track of a transmitter are set up. Finally the kinematic orbit, along with epoch-wise covariance information, is computed and saved.

## 6 Kinematic POD for different missions

This chapter addresses the application of the implemented raw observation approach to real observation data from several missions. The first part shortly lists the different data sets for the different satellite missions which were used for the orbit estimation, followed by a short description of the generated orbit products, which are then validated in chapter 7. The second part of this chapter addresses some specific aspects of real data processing encountered in the course of this work. It deals with mission specific effects as well as with processing details in general.

### 6.1 Satellite data and orbits

Several missions, described in chapter 3, were used in the frame of this thesis to estimate kinematic orbits and subsequently also gravity field solutions. To use the different satellites, observational data from the on-board GNSS receiver as well as auxiliary information is needed. The data sets were obtained from different data sources or different satellite operators. All of the used data is in general available free of charge. Some require a dedicated registration as data user whereas others are directly accessible, for example via anonymous ftp.

#### 6.1.1 Mission data description

**CHAMP** The data distribution to scientific users is managed by GFZ via an online portal, the Information System and Data Center (ISDC). Authorized users are granted access to scientific data of several satellite missions, one of them being CHAMP. For the purpose of kinematic orbit determination and subsequently gravity field processing the following data sets are necessary: raw GPS observables from the GNSS receiver, satellite attitude information derived from star camera observations, and accelerometer measurements to account for non-gravitational accelerations in the gravity field processing. Apart from these time dependent observations of different instruments, auxiliary information like the CoM offset for the GPS antenna as well as antenna characteristics like PCO values are needed. CHAMP observation data for the whole mission lifetime was retrieved from ISDC<sup>1</sup>.

---

<sup>1</sup><http://isdc.gfz-potsdam.de>

The observations of the BlackJack receiver are provided in RINEX format 2.10 (Gurtner, 2007). Due to the fact that this receiver provides two different types of L1 phase observations, some modifications were needed to take this into account (Köhler, 2001). Apart from the GPS observations, attitude and accelerometer data is provided together in a special format (Schwintzer et al., 2002) defined for the CHAMP mission. Auxiliary information about the satellite, such as CoM offset or coordinate system definitions are obtained from Lühr et al. (2002).

**GRACE** GRACE data is available free of charge from either ISDC or from Physical Oceanography Distributed Active Archive Center (PO.DAAC)<sup>1</sup>. All distributed data sets use a special binary format defined for the GRACE mission and described in Case et al. (2010). For both GRACE satellites raw GPS observations, attitude information coming from the star camera observations, and accelerometer measurements are available.

**GOCE** GOCE data is provided to registered users by ESA via the GOCE Virtual Archive. Apart from that, the IfG was part of the European GOCE Gravity Consortium (EGG-C) and thus had direct access to level 1 and level 2 data. For the distribution of the different data sets ESA used its earth explorer ground segment file format (Viau, 2003) with some modifications and additions for GOCE level 1 data (SERCO/DATAMAT Consortium, 2006). Except the raw GPS observations were provided in standard RINEX format 2.20 (Gurtner and Estey, 2002). Attitude information, derived from star tracker observations and non-gravitational accelerations measured with the six accelerometers of the gradiometer, combined to form the so-called common mode accelerations, were also used in the gravity field processing. In case of GOCE, additional information concerning the evolution of the satellite's CoM is necessary, because the satellite continuously used propellant and thus the CoM was changing over the whole lifetime. The total movement of the CoM during lifetime is in the range of 3 cm.

**Swarm** Data from the magnetic field mission Swarm is provided by ESA to registered users via an ftp server, using existing format definitions. For the raw GPS observables the new RINEX version 3.00 is used (Gurtner and Estey, 2007). For other data sets, like satellite attitude, the well-known Network Common Data Format (NetCDF) (Rew and Davis, 1990) was chosen. Although the Swarm satellites each carry an accelerometer, this information was not used in this thesis, as all three instruments suffer from problems like temperature dependency, sudden jumps, and drifts (Siemes et al., 2015).

**TerraSAR-X and TanDEM-X** Observation data for TerraSAR-X and TanDEM-X is provided by ISDC to registered users. The raw GPS data is stored in RINEX 2.10 format (Gurtner, 2007) with a similar extension as for CHAMP to include both phase

---

<sup>1</sup><ftp://podaac-ftp.jpl.nasa.gov>

observations on the L1 carrier frequency. For providing the orientation information a simple ASCII format, containing time and attitude quaternions, is used by ISDC.

**MetOp A and B** Observation data for both MetOp satellites is available from UCAR via FORMOSAT-3/COSMIC Data Analysis and Archive Center (CDAAC) for registered users. For raw GPS observations RINEX 2.20 format is used, with the same extension as used for CHAMP data. The provided attitude information also uses the same data format as it was used for the CHAMP mission (Schwintzer et al., 2002). However, the orientation of the MetOp satellites is not observed by star cameras, thus the information provided by UCAR is only of theoretical nature based on the satellite attitude law. This means that the attitude is calculated from the orbit and represents the nominal orientation of the satellite. Therefore, it does not contain any orbit maneuvers or attitude changes.

**SAC-C** Data for the SAC-C satellite is available from Crustal Dynamics Data Information System (CDDIS) operated by Goddard Space Flight Center (GSFC) via anonymous ftp access<sup>1</sup>. The only data provided on CDDIS are the raw GPS observations in RINEX 2.20 format. No attitude information for SAC-C is provided and thus was computed from an a priori orbit and the nominal attitude law to enable precise orbit and gravity field estimation.

**Jason 1 and 2** Jason 1 and 2 GPS observation data is available from the altimeter data center AVISO+<sup>2</sup> operated by CNES. For both satellites the measurement data is provided in the RINEX 2.20 format. The attitude information derived from on-board star cameras is provided by CDDIS<sup>3</sup>.

**C/NOFS** Raw GPS observation data for C/NOFS is available from CDAAC in RINEX 2.20 format. Apart from the GPS data no additional information is provided. Hence, the attitude information must be computed from an a priori orbit and a nominal attitude law.

**FORMOSAT-3/COSMIC** FORMOSAT-3/COSMIC data is available from CDAAC maintained by UCAR. The raw GPS observations are available for all six satellites in the RINEX 2.20 format. A special aspect of FORMOSAT-3/COSMIC is the fact that not only one GPS antenna is used for POD but two inclined antennas. These two antennas are operated simultaneously and thus two observation files are provided for each day. For attitude information, derived from a combination of magnetometer, Earth and Sun sensor data, UCAR uses the data format developed for CHAMP attitude data (Schwintzer

---

<sup>1</sup><ftp://cddis.gsfc.nasa.gov/pub/doris/ancillary/quaternions/>

<sup>2</sup><ftp://avisoftp.cnes.fr/AVISO/pub/doris/>

<sup>3</sup>See footnote 1

et al., 2002). Although this attitude information is derived from sensor observations, the accuracy is far less than for star camera observations.

**Auxiliary data** To enable kinematic orbit computations with highest accuracies additional data and information is necessary for each satellite mission. A major prerequisite are precise GPS satellite orbits and clock products. These products were obtained from CODE (Dach et al., 2009). In order to fully exploit the quality of the observation data final orbit and clock products were used. Due to varying availability of CODE data the considered time frame from 2002 until 2015 was divided into four parts. The first section covers the whole year 2002, for which CODE precise orbits and 30 s clock corrections were used. For the second time frame from 2003 until end of 2006 data from the CODE reprocessing campaign 2008 were used, featuring 5 s clock information. The third section started in January 2007 and lasted until May 2008. For this time frame no high rate clock corrections are available and hence the 30 s corrections were used. Starting with May 2008, CODE started to routinely process 5 s clock products. Until May 16, 2011 all used CODE products are given in the IGS05 reference frame and in the IGS08 frame thereafter.

Apart from precise GPS orbits and clocks additional information about the LEO satellites is needed. For example, information about the CoM offset for the POD antenna. For some satellites this information is contained in the RINEX header for others the values are provided by the satellite operator in dedicated documents. Used antenna offsets are summarized in table 6.1. In some cases the antenna offset to the CoM varies in time. Due to the fuel consumption of the satellite the location of the CoM changes. For some antennas also PCO values are available, these are summarized in table 6.2. The same information is needed for the GPS constellation. The IGS provides CoM offsets for the whole GPS constellation along with nadir angle dependent ACVs (only applies to phase observations). The information is available in the so-called antex file (Rothacher and Schmid, 2010). For precise orbit and clock products prior to May 2011, the IGS used IGS05 as reference frame, which is closely related to the ITRF 2005. Thus, for this time frame the IGS05 antex file must be used to be consistent. For the later years CODE products are related to the IGS08 reference frame and thus are consistent with the new antenna definition IGS08.

### 6.1.2 Resulting orbit products

Based on the input data described in the previous sections, kinematic orbits were computed for all satellites covering the available time frame. The time span of available data varies from mission to mission, due to different launch dates and mission lifetime. Table 3.1 provides an overview. Investigations contained in this thesis cover the time frame 2002-2015. The only mission covering almost the whole time span is GRACE. All other missions are either launched later or already reached their end of lifetime before 2015. In total, kinematic orbits were produced for 21 individual satellites.

## 6 Kinematic POD for different missions

Satellite	x [m]	y [m]	z [m]	source
CHAMP	-1.4880	0.0000	-0.3928	(Lühr et al., 2002)
GRACE A	-0.0004	-0.0004	-0.4514	VGN1B product (Case et al., 2010)
GRACE B	-0.0006	-0.0008	-0.4517	VGN1B product (Case et al., 2010)
GOCE	0.6940 - 0.6570	-0.0040	-1.0932	(Bigazzi and Frommknecht, 2010)
Swarm A	0.2970 - 0.3060	0.0000	-0.4720	(Faust, 2013)
Swarm B	0.2950 - 0.3050	0.0010	-0.4720	(Faust, 2013)
Swarm C	0.2940 - 0.3040	0.0000	-0.4720	(Faust, 2013)
TanDEM-X	1.2000	-0.0177	-1.0690	(Jäggi et al., 2012)
TerraSAR-X	1.5885	-0.0167	-1.0654	(Jäggi et al., 2012)
SAC-C	-0.3450	-0.0294	-0.8108	ftp://cdaac-ftp.cosmic.ucar.edu/sacc
MetOp A	-0.0980	-1.1410	0.9160	RINEX header
MetOp B	-0.0988	-1.1383	0.9000	RINEX header
Jason 1/2	1.4325	-0.2164	-0.4721	CDDIS <sup>1</sup>
C/NOFS	-0.5111	0.2482	0.0532	RINEX header
FORMOSAT-3/COSMIC +X	-0.4680	0.0050	-0.2570	(Tseng et al., 2012)
FORMOSAT-3/COSMIC -X	-0.4740	0.0050	-0.2600	(Tseng et al., 2012)

<sup>1</sup> [ftp://cddis.gsfc.nasa.gov/doris/cb\\_mirror/satellites/macromodels/ja2mod.pdf](ftp://cddis.gsfc.nasa.gov/doris/cb_mirror/satellites/macromodels/ja2mod.pdf)

Table 6.1: Center of mass offsets for all used satellites.

All used satellite missions do provide dual frequency data. Some of them feature two different phase observations on L1 (L1C and L1P) and all of them deliver two code observations for L1 (C1C and C1P). Jäggi et al. (2009a) already observed a lower noise level for L1C than for L1P phase observations. Thus, for orbit computations in the frame of this thesis L1P has been omitted. In case of the code observations C1C observation features the higher noise level due to the larger chip length of the C/A-Code. The used observation types have been L1C, L2P, C1P, and C2P for all missions. Using both code and phase measurements on L1 frequency is not feasible due to the high correlation of these two observations (Tiberius and Kenselaar, 2000).

The orbits were processed on a daily basis without any overlapping data involved. GPS observation files were converted to the internal GROOPS format and strictly cut to the period 00:00:00-23:59:59. Other institutions often use more than 24 h and then cut off preceding and subsequent epochs. The major reason for this procedure is the fact that edge effects at day boundaries shall be reduced. Furthermore, the overlapping periods of consecutive days may be used to analyze the stability of the orbit estimation. However,

Satellite	x [mm]	y [mm]	z [mm]	source
CHAMP, GRACE A/B, TerraSAR-X, TanDEM-X, Jason 1/2: L1	1.49	0.60	-7.01	(Montenbruck et al., 2009)
CHAMP, GRACE A/B, TerraSAR-X, TanDEM-X, Jason 1/2: L2	0.96	0.86	22.29	(Montenbruck et al., 2009)
GOCE: L1	-2.35	2.61	81.11	(Bigazzi and Frommknecht, 2010)
GOCE: L2	1.57	0.16	84.18	(Bigazzi and Frommknecht, 2010)
MetOp A/B: L1	47.00	47.00	0.00	(Montenbruck et al., 2008)
MetOp A/B: L2	-47.00	-47.00	0.00	(Montenbruck et al., 2008)

Table 6.2: Used PCO for different missions given in the antenna reference frame.

investigations revealed that the used precise orbit and clock products are not continuous at the day boundaries, already mentioned by Bock et al. (2007). These steps, especially in the high-rate clock product, have a negative influence on the estimation of phase ambiguities crossing the day boundaries. This influence is bigger than the instabilities caused by short phase tracks, after cutting at the day boundaries.

In addition to the epoch-wise position estimate, the corresponding covariance information for each epoch was computed and saved for later use. Although it would be possible to access the complete and fully populated covariance matrix for one day, only the 3x3 epoch matrices were saved. First of all, this is a matter of disk space, but also a matter of computational effort, as this would require to compute the inverse of the full normal equation matrix. Although, the estimated position parameters are correlated in time, due to the estimation of the epoch independent parameters, like the phase ambiguities, it is not important for most of the applications using orbit positions to know the correlations between consecutive epochs. For dynamic or reduced-dynamic orbit reconstruction from kinematic positions, it has been shown that it is important to take inter-epoch correlations into account (Jäggi et al., 2011b). For gravity field estimation Jäggi et al. (2011b) concluded, that time correlations are of minor importance. Within this work empirical covariance functions are later used to approximate inter-epoch correlations.

## 6.2 Specific aspects of real data processing

### 6.2.1 Estimation of receiver antenna center variations

**Temporal stability of receiver ACVs** In general, ACVs are assumed to be constant in time. This assumption is made for ground based applications and is now transferred to space borne antennas. In case of terrestrial GPS processing, ACVs are taken from calibration campaigns and are thus only type specific. Individual calibrations for a specific combination of antenna and receiver are rarely done. For space borne applications it was already noticed by Montenbruck and Kroes (2003) that changes of the satellite status might cause some changes in the ACVs. They showed that the antenna pattern for code observations on CHAMP depends on whether the occultation antenna is switched on or off. This already indicates that there might occur some changes in the ACV pattern.

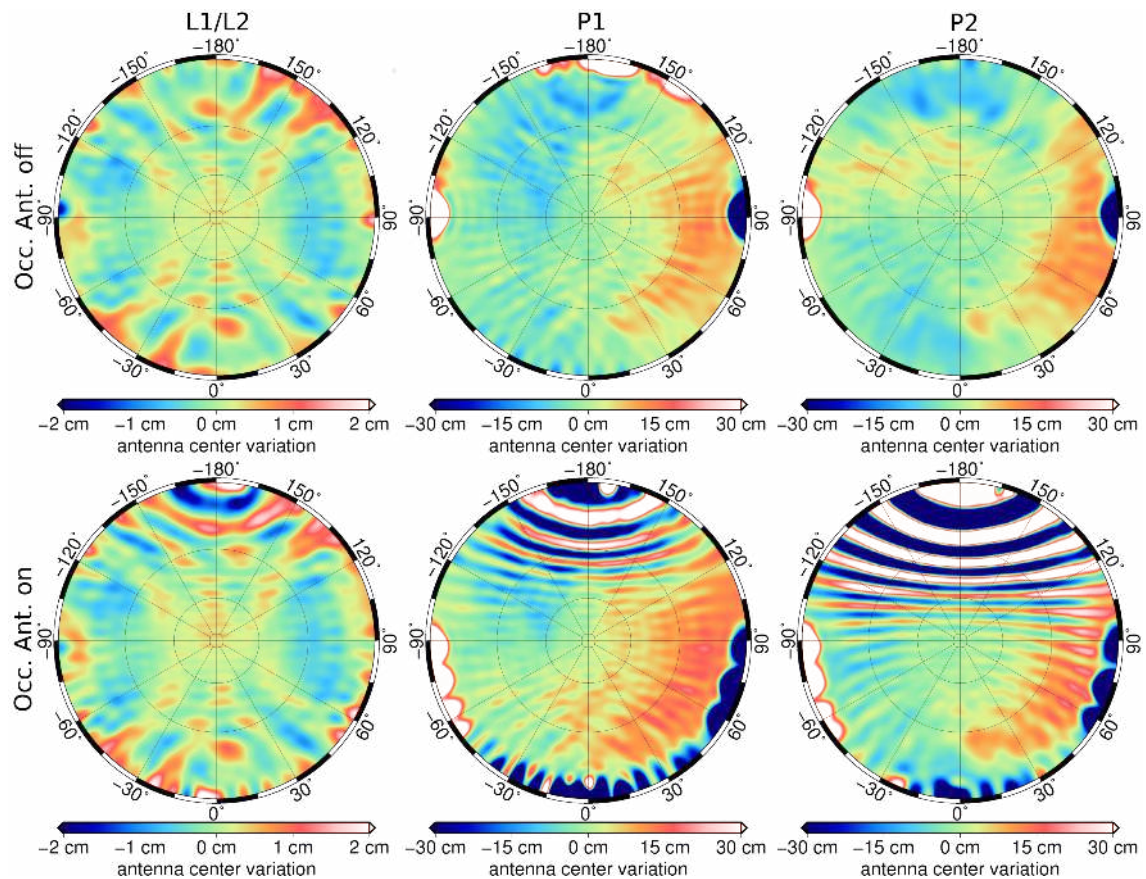


Figure 6.1: ACVs for GRACE A when occultation antenna is switched off (top) or on (bottom), for phase L1/L2 (left) and code P1 and P2 (middle, and right) observations.

Analysis of satellite data from all missions mentioned in chapter 3 revealed similar effects for a few of them. The same relation to the occultation antenna, as seen for CHAMP (Montenbruck and Kroes, 2003), was found for the two GRACE satellites. This has been already encountered by Jäggi et al. (2009b). Figure 6.1 shows estimated ACVs for GRACE A. The top row contains the results obtained for times when the occultation antenna is switched off and the bottom row are the ACVs when the occultation antenna is operating.

This example nicely demonstrates the effect of the occultation antenna on the different ACV patterns.

The biggest influence is on the code observations, but also for phase observation the effect is clearly visible around an azimuth of  $180^\circ$ . In case of code observations an influence can be seen up to the zenith direction. The variation for the P2 observable reaches up to  $\pm 2$  m, but if the occultation antenna is switched off the remaining variation hardly exceeds  $\pm 20$  cm. Dark blue and white areas at low elevations and  $\pm 90^\circ$  azimuth are those regions where no observations are available. For those areas the estimated values are arbitrary. In general, it can be said that the information on operational status of the occultation antenna is of crucial importance for processing GRACE orbits. The information on the status of the occultation antenna can be found in the sequence of events file, provided by JPL <sup>1</sup>.

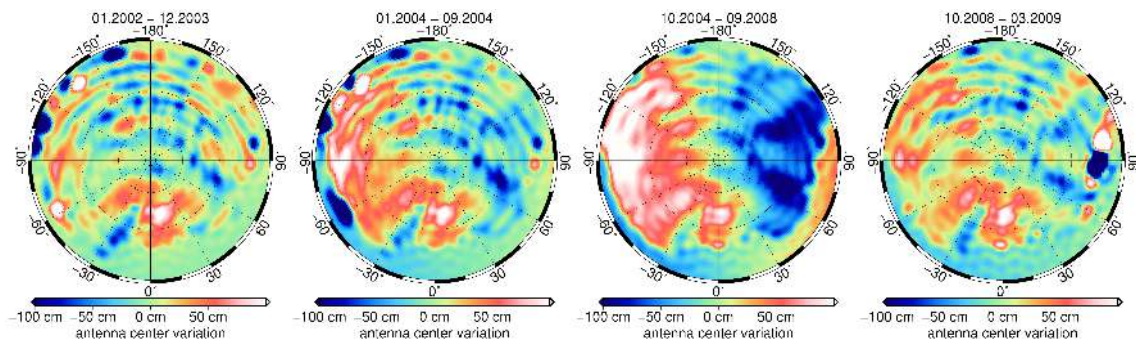


Figure 6.2: Estimated P2 code correction for SAC-C for different periods.

The analysis of SAC-C data revealed some variations in the ACV corrections for different periods. Due to lack of information on possible changes to the receiver settings or the satellites operation mode, the definition of the time periods was found empirically by analyzing observation residuals. In total the available data period was split into 9 different time slots for which individual ACVs were estimated. Figure 6.2 shows the P2 corrections obtained for the first four periods. From period 1 to 3 the overall amplitude of the variation seems to increase, while the principle structure of the pattern remains the same, especially for small scale features. In period 4 the correction returns to almost the same form as it was for period 1. The changes from period to period are of the same size as the corrections themselves. Thus, using only one common set of ACV corrections for the whole lifetime of the satellite would introduce large errors. In order to understand the reason for these changes detailed information about the satellite status and its payload would be necessary, which is not available for SAC-C. Nevertheless, this example demonstrates that for space borne applications ACVs are not necessarily constant over the whole lifetime of a satellite. Similar to the finding that in-orbit calibrations must be conducted to fully cover the specific variations, it is also important to analyze the temporal stability of these variations.

<sup>1</sup>[ftp://podaac.jpl.nasa.gov/allData/grace/docs/TN-01\\_SOE.txt](ftp://podaac.jpl.nasa.gov/allData/grace/docs/TN-01_SOE.txt)

**Impact of ACV resolution on gravity field results** The parametrization of ACVs as spherical harmonics raises one question: what is the appropriate maximum degree and order that should be used? If ACVs are estimated by analyzing observation residuals, the chosen grid spacing determines the resolution. For spherical harmonics the resolution in degrees can be approximated by the rule  $180^\circ/N$ , where  $N$  is the maximum degree and order. Choosing a higher degree significantly increases the computational effort needed for setting up the normal equations. As it is important to process a long time span of data to get a reasonable stable estimation for the ACVs, some kind of trade off must be found between a high resolution and an acceptable computation time.

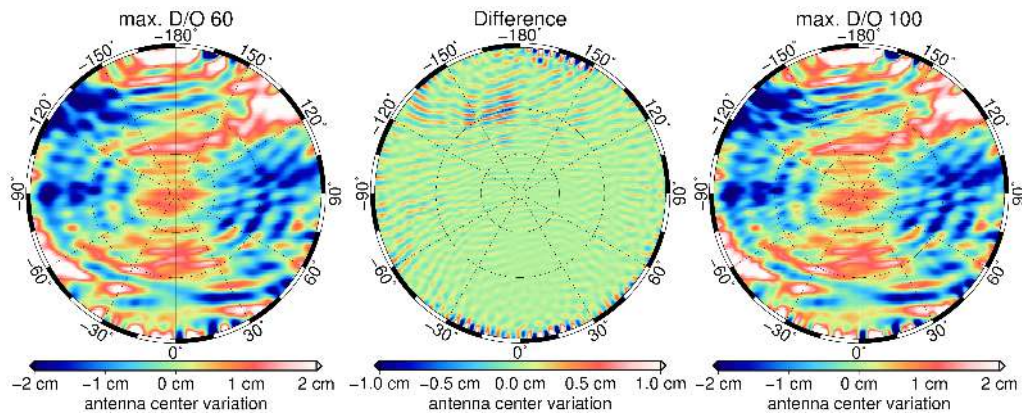


Figure 6.3: GOCE ACVs estimates with different maximum degree and order of the spherical harmonics expansion and the difference between those two.

However, the specific characteristics of each antenna must be taken into account. Investigations have shown that for the GRACE antennas a maximum degree of 50 is sufficient to fully cover all systematic errors. On the other hand, for the GOCE antenna this resolution is too coarse. Figure 6.3 shows two examples of ACVs for GOCE with different resolutions and the deviations between them. On the left hand side a maximum degree and order of 60 is used, whereas for the right solution the chosen maximum degree is 100. Visibly the two correction patterns do not differ much, but the difference between them (shown in the middle) is in the range of  $\pm 1$  cm for some areas. Nevertheless, the majority of the values is below 1 mm.

To assess the importance of this small change in the ACVs for the resulting orbit estimates two different gravity field solutions have been computed, based on kinematic orbits applying the two different ACVs. The first one using the low resolution ACVs and the second one applying the higher resolution corrections. Figure 6.4 shows degree amplitudes of the gravity field solutions computed with two months of data (11.-12. 2009). It can be seen that remaining small systematic errors in the ACV correction are mapped into the high degrees of the gravity field. The degradation of the red solution in figure 6.4 starts shortly below degree 60. This means, if the maximum degree for the ACVs is not sufficiently high enough, the remaining small scale errors are mapped directly into the higher degree gravity field coefficients. The definition of an appropriate maximum degree is subject to trial and error.

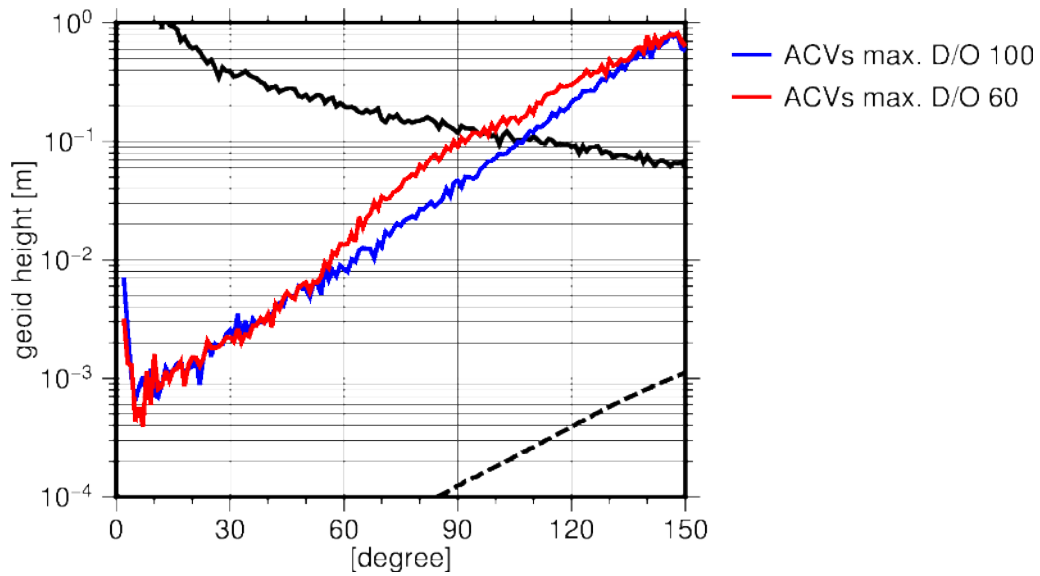


Figure 6.4: Degree amplitudes of two different GOCE gravity fields based on orbits applying ACVs with different resolutions.

### 6.2.2 Estimation of transmitter antenna center variations

In case of GPS, a total number of 73 satellites have been launched so far. Although not all of them are operational anymore it is necessary to include approximately 50 individual satellites, which were in operation between 2002 and 2015. The parametrization of ACVs by means of radial basis functions is described in section 4.3.1.1 and the general processing scheme is explained in section 5.2. In the course of this work two sets of transmitter ACVs were estimated. As already mentioned in section 6.1, the considered time frame was split into several parts, due to differing input data, namely the precise GPS orbits and clocks. For the ACV estimation the sampling of the clock corrections is not important, but the antenna definitions used for the generation of the precise orbits matters. The used CODE products are referred to the reference frame IGS05 until April 17, 2011, and to IGS08 thereafter. The important difference between those two reference frames is a new definition of the GPS antenna offsets and variations (Schmid et al., 2007), adopted by the different IGS ACs. To be consistent with the used orbit products the corresponding antenna offsets were used and the ACVs were estimated for these two time frames, IGS05 and IGS08.

The used LEO satellite data was processed on a daily basis. All other parameters (kinematic positions, receiver clock error, STEC, ambiguities), except for the ACVs, were eliminated from the daily normal equations by means of parameter elimination. All daily normal equations of one month were stacked and saved. On the basis of these monthly normal equations different combinations were made, incorporating variance component estimation to guarantee proper weighting of individual months. Solutions have been generated for single satellite missions or for different time frames, e.g. years. Finally, a combined solution was derived including almost all available LEO satellites and the whole time span. Not all satellites have been included due to cost-benefit considerations.

Costs means in this case computational burden and the benefit would be the contribution to the combined solution. FORMOSAT-3/COSMIC, SAC-C, and C/NOFS have been excluded due to the worse observation quality, their contribution would be marginal. Swarm observations have also been omitted, due to varying receiver characteristics, related to several changes in the tracking properties. All other missions have been combined to generate a stable and complete set of transmitter ACVs. Highest contributions are coming from GRACE (largest data set) and Jason 1 and 2 (highest altitude). Especially the inclusion of the Jason satellites is of great importance, because they reach the highest nadir angles of up to  $17^\circ$ .

Finally ACVs were estimated with the following properties:

- Two different sets for IGS05 (2002-2011) and IGS08 (2011-2015)
- Radial basis functions
  - min. degree: 2
  - max. degree: 66 (in accordance with the chosen base function distribution)
- Distribution: triangle vertex
  - level of densification: 20
  - max. nadir angle:  $17^\circ$
- Total number of basis functions per pattern: 101
- Observation types:
  - Combined L1 and L2 phase pattern
  - Individual patterns for P1 and P2 code observations

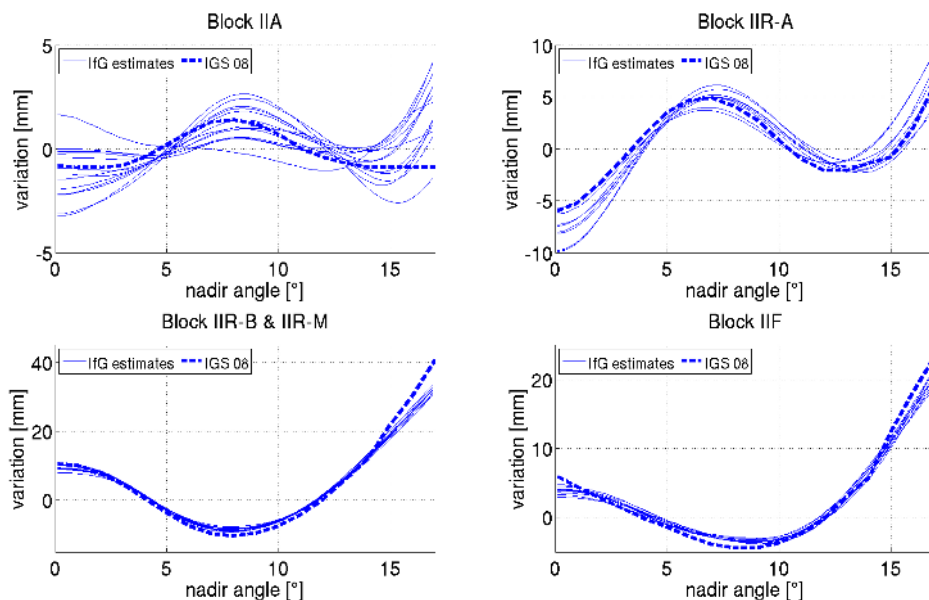


Figure 6.5: Rotational mean of estimated transmitter ACVs (thin blue lines) compared to IGS values (dashed blue line) for L1 and L2 phase observations. IGS values taken from igs08.atx. Note the different scales.

For L1 and L2 phase observations a combined set of ACV parameters had to be used, because due to the estimation of the STEC parameter a separation of L1 and L2 variations

is not possible. The estimated combined correction is compatible to commonly used IGS patterns which are derived for the ionosphere-free combination. The estimated azimuth and nadir dependent ACVs were evaluated on a regular grid (spacing  $0.25^\circ$ ). To facilitate a comparison with the nadir dependent phase corrections, provided by the IGS, a rotational average was formed. Figure 6.5 shows the results obtained for L1 and L2 phase observations in the IGS08 time frame. Thin blue lines show the individual results for all satellites of a specific block and the dashed blue line represents the IGS values. Results obtained for the IGS05 time frame are basically the same and thus not shown in this comparison.

In general, the results agree well with the block averages provided by the IGS. Largest differences, with respect to the IGS values as well as between individual satellites, occur for block IIA and IIR-A. For block IIR-B, IIR-M, and IIF the agreement between different spacecraft is good, whereas some larger deviations to the IGS values are present for specific nadir angles, mainly towards the maximum of  $17^\circ$ . Overall, the differences are in the range of some millimeters. In order to assess the benefit of the additional azimuth dependency, a comparison of the gridded pattern is useful. Figure 6.6 shows the deviations of the estimated phase ACVs with respect to the rotational symmetric IGS patterns for the time frame of IGS08.

From figure 6.6 it can be seen that for all five blocks a clear azimuth dependency is present, already shown by Schmid et al. (2005). The deviations to the rotational symmetric IGS values range up to  $\pm 1$  cm. This shows that the azimuth dependent component has almost the same size as the total amplitude of the correction.

In conclusion, it can be said that there is a clear azimuth dependency in addition to the nadir angle dependent component. This is shown for all types of satellites, from block IIA up to the newest generation block IIF. To fully describe the antenna characteristics of GPS satellites an azimuth and nadir angle dependent representation of ACVs should be considered for future releases by the IGS. The use of averaged patterns for each block is supported by the results shown in figure 6.5 and 6.6. This is at least valid for the newest satellite generations, block IIR-B, IIR-M, and IIF. In case of block IIA and IIR-A, satellites individual calibrations might be favorable, as they show larger inconsistencies, as it can be seen in figure 6.5 and 6.6.

## 6 Kinematic POD for different missions

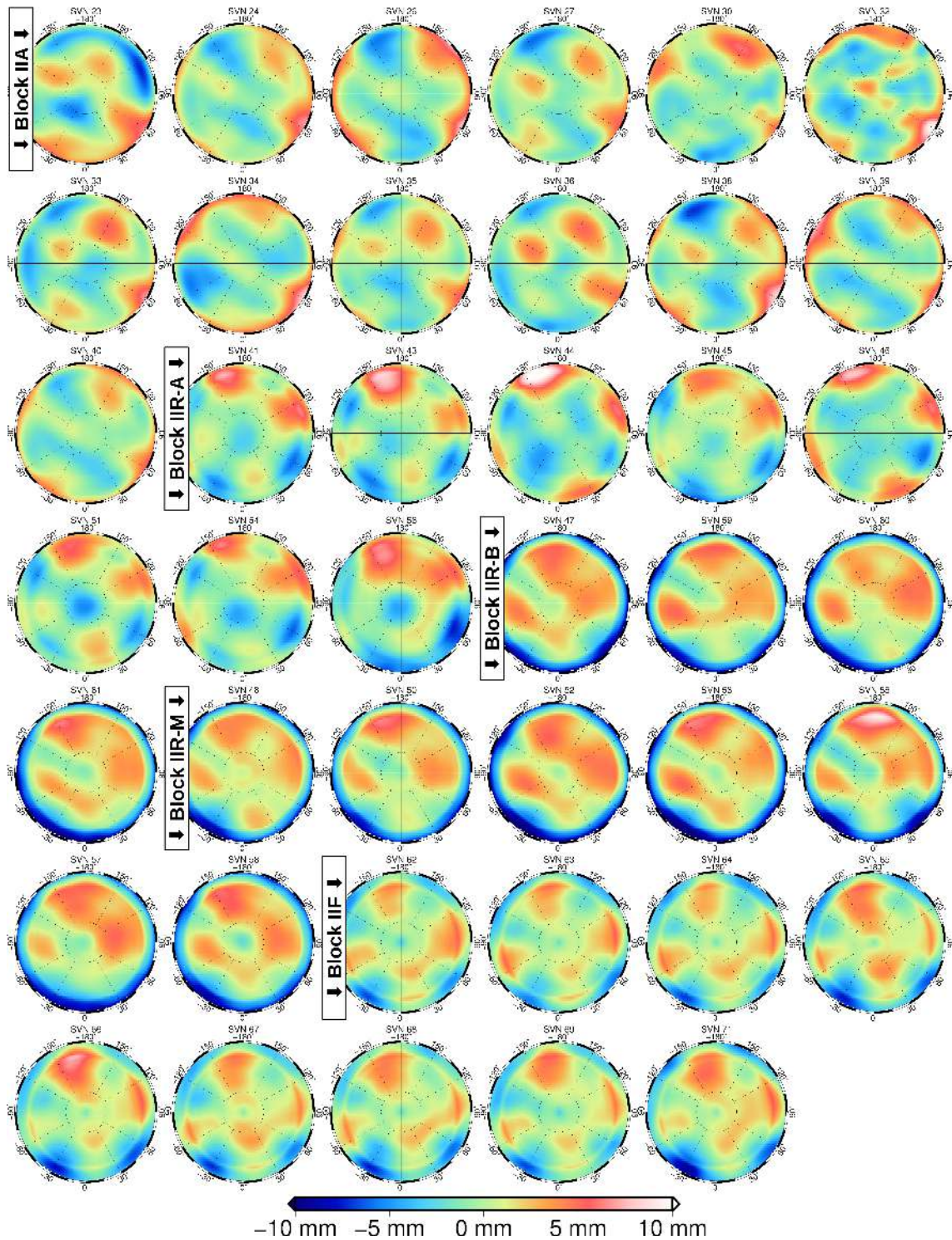


Figure 6.6: Difference of estimated transmitter ACVs (phase L1 and L2) to IGS corrections for all satellites used since the transition to IGS08.

As already mentioned and discussed in sections 4.3.1.1 and 6.2.1 ACVs have been estimated not only for phase observations, but also for code observations. The parametrization was the same as for phase observations, with the only exception that the correction was estimated for each observation type separately. In case of the used satellites three types of code observations are available: P1, P2, and C/A. The correction patterns were estimated for P1 and P2 observations, as the C/A-Code observable was not used. The

C/A-Code observation was omitted due to its higher noise level compared to the P1 code observations. In addition the correlation between P1 and C/A-Code measurements, as for example shown by Tiberius and Kenselaar (2000), would require a weighting scheme, that takes cross correlations into account. As these correlations are not known and might be different depending on the receiver type, they are not considered in this thesis. Only observations which can be considered as uncorrelated are included.

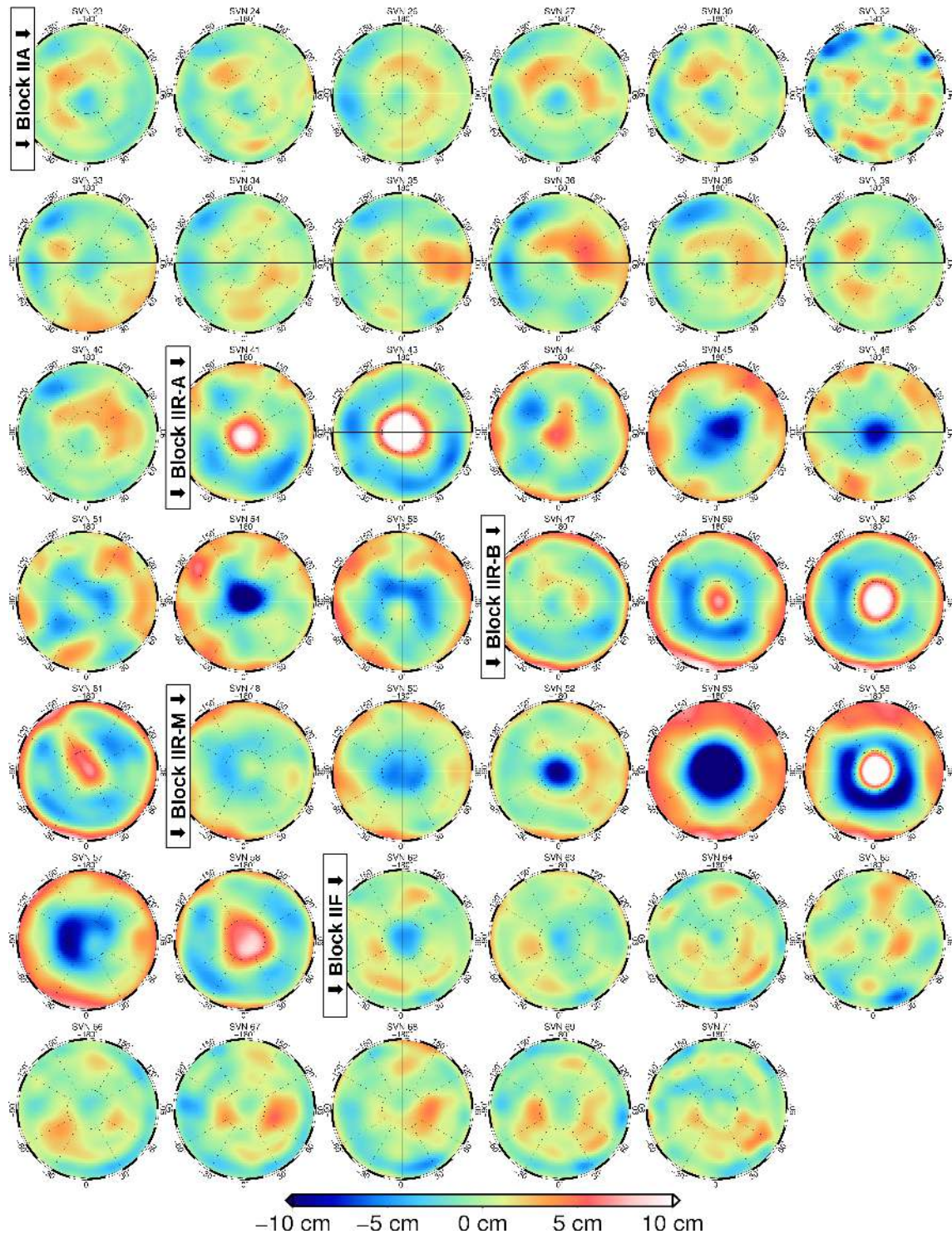


Figure 6.7: Estimated transmitter ACVs for P1 code observations for all satellites used since the transition to IGS08.

The code patterns were estimated along with the phase correction in a combined analysis. The approach includes, similar as for the phase observations, the assumption that a specific spacecraft, identified by its SVN, features a constant antenna pattern throughout its lifetime. Some satellites have been used to broadcast various Pseudo Random Number (PRN) codes, for example SVN 35.

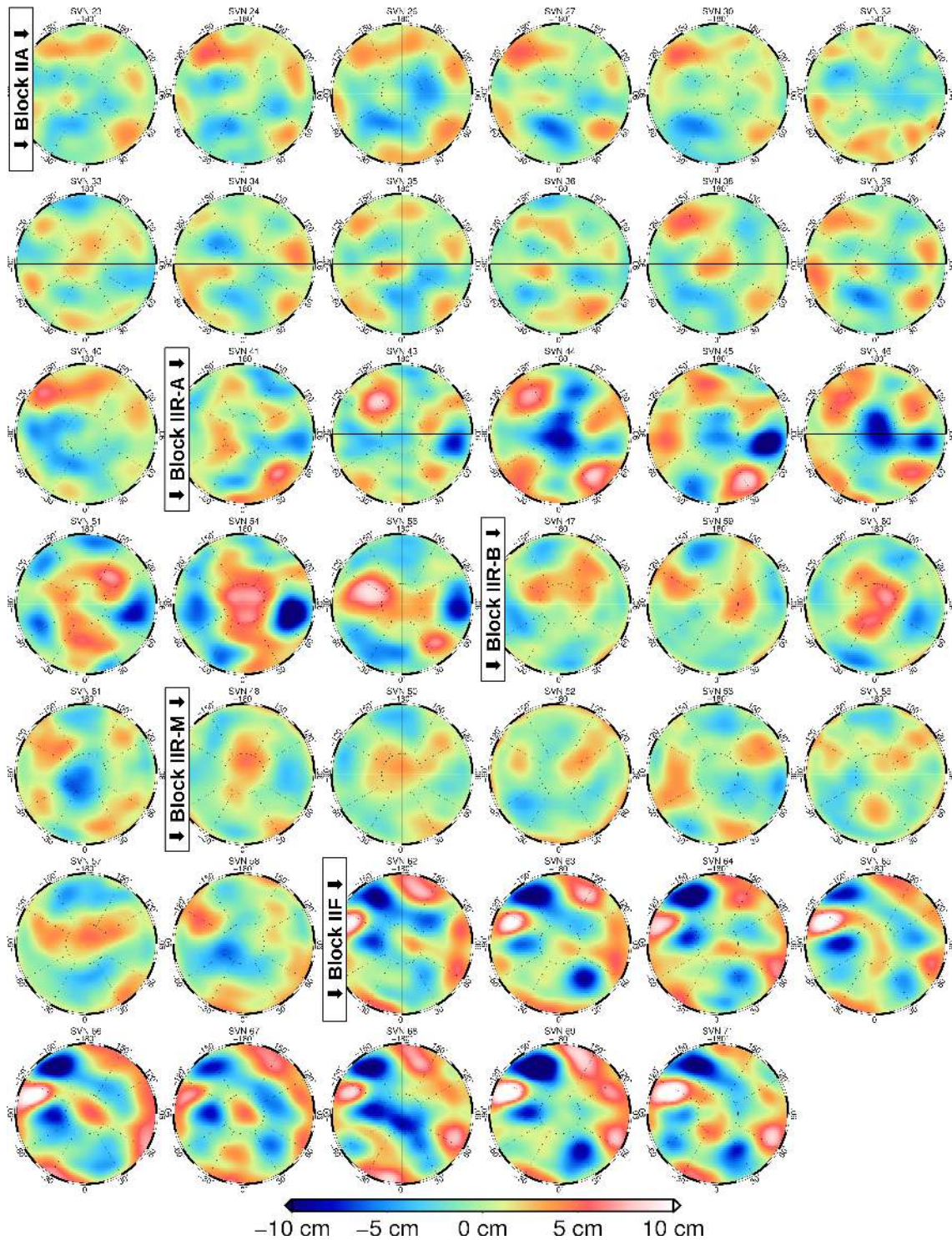


Figure 6.8: Estimated transmitter ACVs for P2 code observations for all satellites used since the transition to IGS08.

These time frames are rather short, only a few weeks, and not all receivers have tracked these satellites. Hence, the available data to estimate individual corrections for those time slots is not sufficient and the above made assumption could not be verified. Due to the fact that these periods are short and the problem only affects a few satellites, the influence on the overall performance can be considered as negligible. Nevertheless, a detailed verification of this assumption should be made in the future with additional observational data, e.g. ground based station observations.

Figure 6.7 and 6.8 show the P1 and P2 corrections for all satellites. The estimated variations are in the range of  $\pm 10$  cm for both observation types and all blocks. Similar to the phase ACVs, code ACVs also show a clear dependency on azimuth and nadir angle. The comparison of all individual patterns reveals that there is no common variation for satellites of the same block, except for IIF satellites. They show similar behavior, especially for P2 code observations. This further supports the theory that individual parameters should be used for each transmitter. For most high precision applications code observations are not important. Nevertheless, including code corrections might be beneficial for purely code based applications or in the context of PPP applications, for example to improve initial ambiguity estimates derived from code observations.

### 6.2.3 Receiver bias estimation

The estimation of the receiver code bias was done by applying the methodology introduced in section 4.3.1.6. This step is only necessary if absolute STEC values are needed, which is the case if the bending correction, as described in section 4.3.1.2, is applied. As it can be seen from equations 4.35 and 4.36 the absolute STEC is needed to derive the correction. The estimation of the receiver code bias may be done at any stage of the processing chain.

Figure 6.9 shows examples of estimated daily DCBs for the receivers on board of GRACE A, GRACE B, TerraSAR-X, Jason 2, and GOCE.

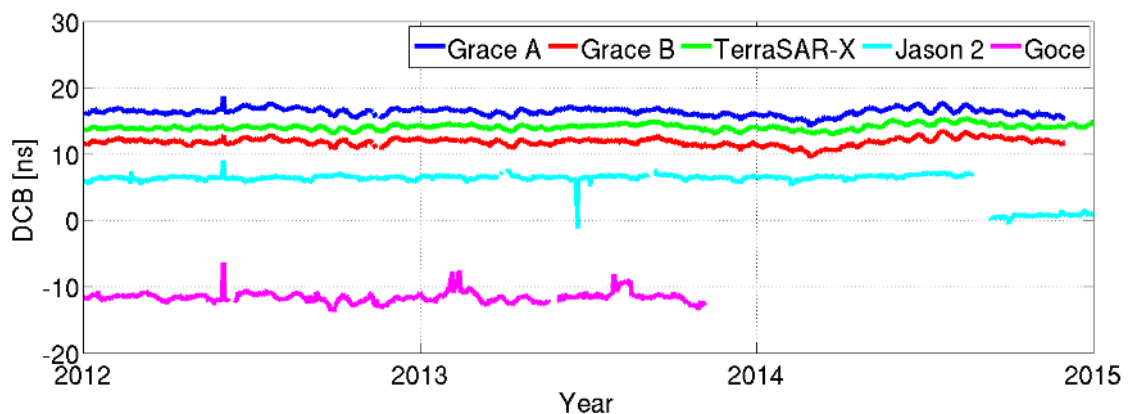


Figure 6.9: Estimated daily receiver DCBs for GRACE A (blue), GRACE B (red), TerraSAR-X (green), Jason 2 (cyan), and GOCE (magenta) from 2012 until 2014.

As it can be seen from figure 6.9, the receiver DCB is rather constant over time, except for some outliers and day to day variations of 1–2 ns. This comparison shows that in principle it is sufficient to use a constant value for the whole lifetime of a satellite. The only exception in this case must be made for Jason 2. In late 2014, a sudden jump occurred in the estimated DCB values. This change in the DCB is related to the failure of the main receiver unit and the following switch to the redundant board in September 2014 (G. Shirtliffe and Guinle, 2014). Although the redundant receiver is of the same type, it exhibits a totally different bias.

#### 6.2.4 Generation of observation weight mask

As outlined in section 4.3.1.3 an azimuth and elevation dependent weighting scheme for GPS observations is introduced. Observation residuals are used to generate accuracy maps for each type and receiver individually. Figure 6.10 shows five examples of accuracy patterns derived for the L1 phase observations for different satellites.

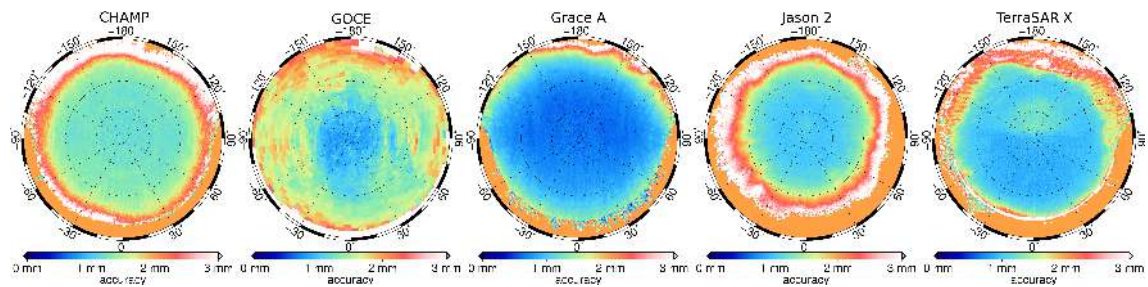


Figure 6.10: L1 phase observation accuracy maps for CHAMP, GOCE, GRACE A, Jason 2, and TerraSAR-X.

First of all, from this comparison it gets obvious that not all receivers perform the same way. Besides the clear elevation dependency, which is dominant for all five examples, the structures are different. GRACE A features a homogenous quality of the phase observation almost for the entire hemisphere. For other receivers, like on Jason 2, a clear degradation of the measurements can be seen for elevations below 30°. The same holds for CHAMP, where a significant increase in the standard deviation is visible below 15° elevation. In case of GOCE the situation is even more complex. The elevation dependent degradation already starts at high elevation angles of 50–60° and continues down to the lowest elevations. In addition, GOCE shows strong non-elevation dependent irregularities in the accuracy map.

Figure 6.11 shows P2 code observation accuracy maps for the same five satellites as in figure 6.10. Again a clear elevation dependency is visible for all five examples. GOCE shows in general the worst performance and strongest degradation towards 0° elevation. Opposed to that, Jason 2 shows only a moderate reduction of the accuracy below 30°. This is possibly related to the high altitude of the Jason 2 satellite. Due to the orbital height of 1300 km, even signals at low elevations are largely unaffected by ionospheric influences. Some interesting features can be seen in the accuracy maps of CHAMP and GRACE

A. These small scale variations towards the aft direction are related to the cross-talk coming from the active occultation antenna. This visible increase in the residual Root Mean Square (RMS) is an indication that the resolution of the used ACV pattern is not sufficient to fully remove these errors. However, due to the small size of the variation and the in general small contribution of code observables to the final result, it is not necessary to use a higher resolution for the ACVs estimation.

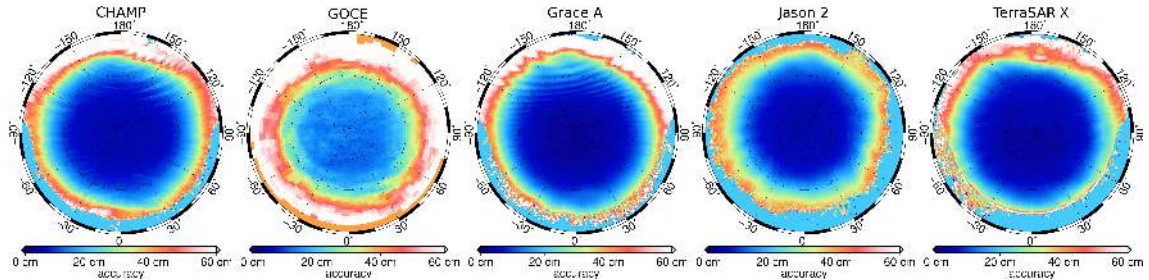


Figure 6.11: P2 code observation accuracy maps for CHAMP, GOCE, GRACE A, Jason 2, and TerraSAR-X.

For most of the satellites it is sufficient to generate and use one accuracy pattern for the whole lifetime. Nevertheless, investigations have shown that, similar to observed changes in the ACVs, there are some satellites that require a re-estimation of the pattern after some major changes occurred. For example, a switch from the main to the redundant receiver or antenna requires a new estimation of ACVs as well as the corresponding accuracy map. In case of GRACE and CHAMP it has to be distinguished between times when the occultation antenna is active or not. But the biggest changes have been observed in the measurement accuracy of SAC-C. Corresponding to the changes found in the ACVs, described in section 6.2.1, the measurements show different behavior for each of these periods. Figure 6.12 shows P2 code observation accuracy maps for four different time periods. The same periods as in figure 6.2 for the ACVs are shown. First of all, it

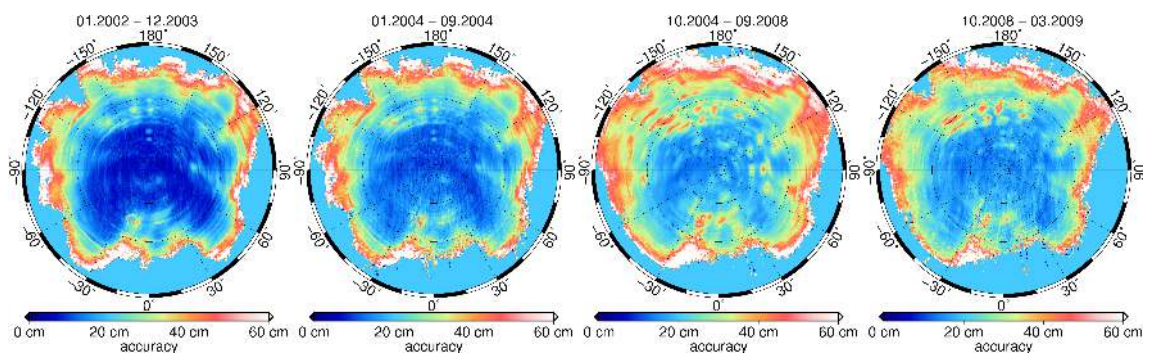


Figure 6.12: P2 code accuracy maps for SAC-C for four different periods.

gets obvious that the structure of these patterns is way more inhomogeneous than for the previous examples. There are small and irregularly distributed areas with significantly reduced observation quality. The general structure is the same for all four periods, but an overall increase in the standard deviation can be observed. Comparing period 1 and 3 shows that the observation accuracy in period 3 is roughly worse by a factor of 2. Due to a lack of additional information, the reason for this degradation and the changes in the

receiver behavior could not be found. However, this example nicely demonstrates the possibility that there might be some changes in the observational quality of a receiver.

In order to assess and demonstrate the influence of various weighting schemes and the usage of receiver and transmitter ACVs, different orbit versions have been computed for one month of data. Data from GRACE A for January 2012 was chosen as an example month. Five different versions of kinematic orbits were computed. The first one uses IGS transmitter ACVs, no receiver ACVs, and a uniform weighting for all observations. The second version adds estimated receiver ACVs, and for the third version the IGS ACVs are exchanged by estimated azimuth and nadir angle dependent corrections. The fourth and fifth version use the same configuration in terms of ACVs as the third, but the uniform weighting is replaced by an elevation dependent weighting and by estimated accuracy maps, respectively. Settings for the different versions are summarized in table 6.3.

Version	Transmitter ACVs	Receiver ACVs	Obs. $\sigma$ (phase;code)
version 1	IGS	no	2 mm; 20 cm
version 2	IGS	yes	2 mm; 20 cm
version 3	IfG	yes	2 mm; 20 cm
version 4	IfG	yes	2 mm/ $\sin(E)$ ; 20 cm/ $\sin(E)$
version 5	IfG	yes	accuracy maps

Table 6.3: Settings for different orbit computations. (E = elevation)

Using above described settings, kinematic orbits were generated for January 2012 and then validated by an orbit comparison and SLR observations. Table 6.4 shows the RMS of orbit differences for the whole month, for each component separately. It also lists the RMS of SLR residuals.

From version 1 to 3 the RMS decreases for all three components significantly. This is also confirmed by the results obtained with the SLR observations, which decrease by 7 mm. The differences between version 3, 4, and 5 are less significant. A slight decrease can be seen in the RMS of the orbit comparison. However, SLR shows the lowest RMS for the solution with uniform observation weighting. This means that due to the more sophisticated observation modeling in version 4 and 5, the high frequency noise can be slightly reduced. In terms of absolute accuracy, the SLR validation tells us that a uniform observation weighting might be preferable. Anyway, the SLR validation is

orbit version	along [mm]	cross [mm]	radial [mm]	SLR RMS [mm]
version 1	3.6	2.3	7.4	25.8
version 2	2.1	1.6	4.7	21.5
version 3	1.8	1.4	4.1	18.6
version 4	1.6	1.3	3.7	19.7
version 5	1.6	1.3	3.6	19.2

Table 6.4: RMS of orbit differences with respect to official JPL reduced-dynamic orbit for different versions of kinematic GRACE A orbits and RMS of SLR residuals.

mainly influenced by the positioning accuracy of the radial component. This component is anyway the least accurate of all three components and a weight reduction for observations at lower elevations might have a negative influence on the radial accuracy of the orbit solution.

The final test to assess the quality of the different orbit versions is to compute monthly gravity field solutions. Figure 6.13 shows degree amplitudes for all five versions compared to the static gravity field GOCO05S. The largest improvement is achieved by including ACVs for the receiver. The gravity field estimate improves over the whole spectrum from version 1 to 2. Compared to this, further refinements are rather small. Nevertheless, it can be seen that from one version to the next a slight improvement can be achieved. The best results are obtained with orbit version 5. Small differences with respect to version 4 can be seen around degree 10 and for higher degrees above 45. In contrast to the results of the SLR validation, orbit version 3, shows slightly worse results compared to version 4 and 5.

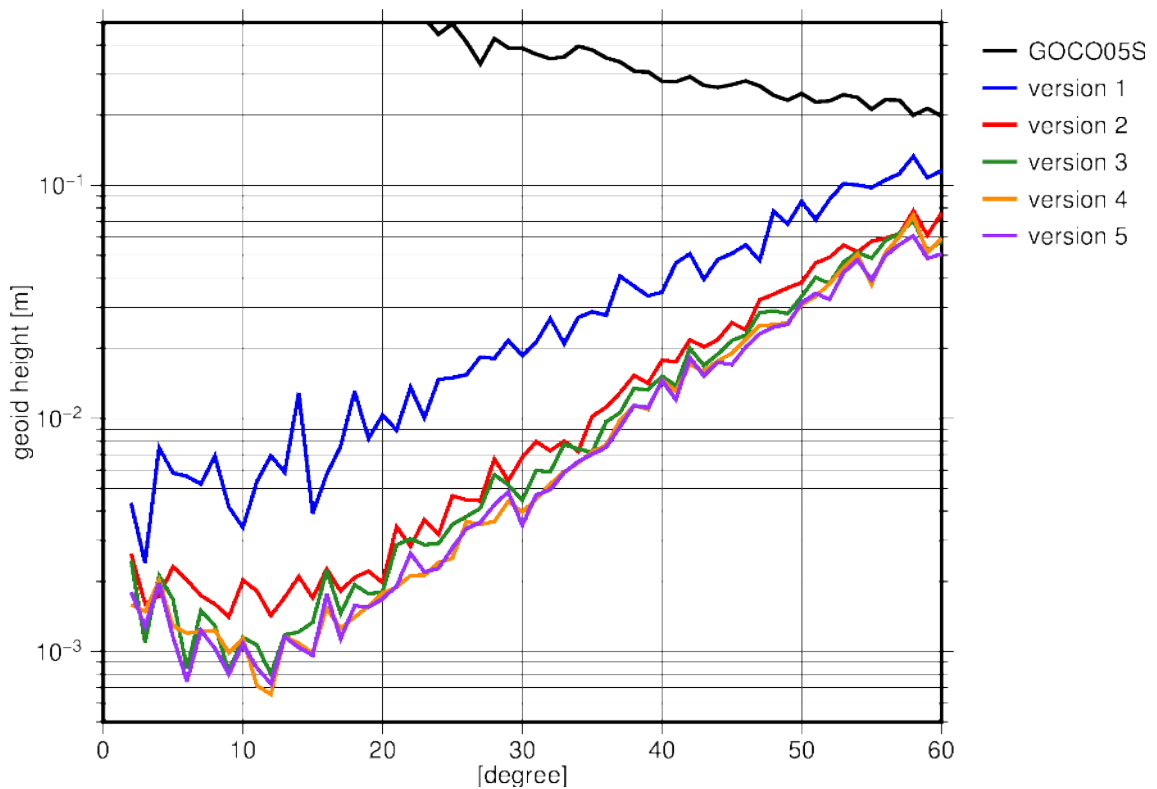


Figure 6.13: Degree amplitudes of gravity field solutions based on GRACE A orbits for January 2012. Kinematic orbits computed with different settings described in table 6.3.

It can be concluded from the orbit comparison and the gravity field results that version 5 generally performs best. The SLR validation gives the lowest RMS for version 3. Including ACVs for receiver and transmitters significantly improves the orbit and gravity field. Using a more realistic weighting scheme further improves the estimated gravity field and also partially the orbit solution.

### 6.2.5 Observation weight scaling

**Signal to noise ratio** Apart from a realistic assumption about the observation accuracy depending on azimuth and elevation of the signal, it would be beneficial to have actual information about the quality of each single measurement. One option in this context is the SNR provided by the receiver. It is a measure for the goodness of signal reception and reflects the conditions at the measurement epoch. Thus, it can provide valuable information on which observation can be trusted. The use of SNR has been investigated to scale the a priori weight of each observation according to the measured SNR value with data from the mission GOCE.

SST-h1 gravity field solutions based on kinematic GOCE orbits show a characteristic error along the geomagnetic equator. This effect is related to small scale and short term variations in the ionosphere at the day to night transition. The tracking of signals that are disturbed and attenuated by any turbulence in the ionosphere is more difficult and thus should have a lower SNR. A very simple scale function to convert the SNR value into a factor that is applied to the a priori weight of each observation, determined from the accuracy pattern, has been tested. The factor was computed by

$$f_{snr} = SNR_0 / SNR_i \quad (6.1)$$

where  $SNR_0$  is a global mean for a certain data set, and  $SNR_i$  is the actual observed SNR value for the specific observation and frequency. In case of GOCE two SNR values are provided, one for each carrier frequency. The values range from 30-50 and 15-42, for L1 and L2 respectively. 45 and 33 have been used as global mean values for the scale factor computation. Consequently the factor is located somewhere between 0.8 and 2.2.

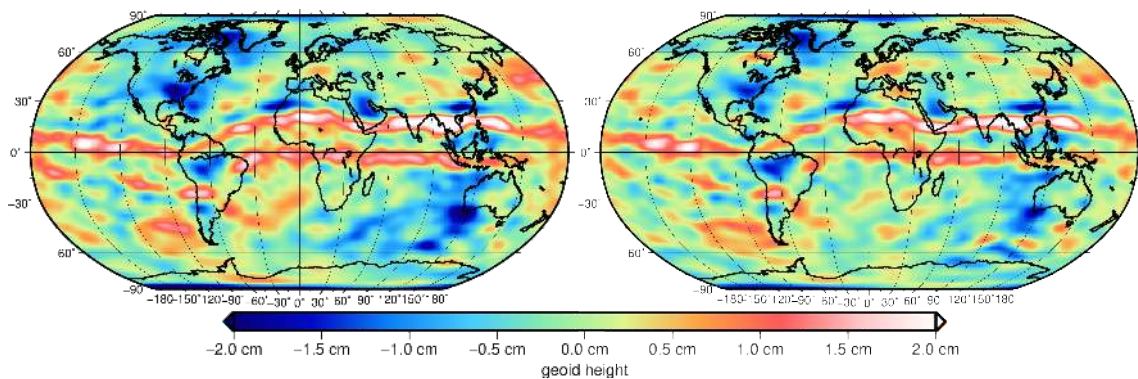


Figure 6.14: Difference in geoid height between monthly GOCE solutions for October 2010 and GOCO05S. Left: no observation SNR information was used, right: SNR values were used to scale the observation weight. 500 km Gaussian filter applied.

Figure 6.14 shows two gravity field solutions for October 2010 based on kinematic GOCE orbits. The left result was obtained without applying the SNR scale factor to the observations, whereas for the right solution it was used. In both plots the prominent feature along the geomagnetic equator is visible. However, the application of the SNR scale factor results in a clear reduction of the phenomenon in the right plot. In terms

of geoid height RMS this manifests in a reduction from 6.6 mm to 5.6 mm. However, this RMS values also contain signal, because only a static reference field is subtracted. Although it is not fully removed, this example shows that knowledge about the individual observation quality can provide some additional information and hence improve the position estimates.

**Rate of TEC index** The aforementioned scaling of observation weights takes into account every influence that results in a reduction of the SNR. However, the comparison in figure 6.14 shows that the effect along the magnetic equator was not fully removed. Thus, a more specific scale factor directly related to the ionospheric conditions is needed. Jäggi et al. (2014) achieved improved results by analyzing the rate of TEC. They removed observations for which the TEC change exceeded a certain threshold. As a consequence, the total amount of observations was reduced and thus also the number of estimable epochs. In accordance to the basic principle of the raw observation approach - 'use all available observation' - a scale function was used to scale the a priori weights and thus reduce the influence of 'bad' observations. The advantage of this approach is that epochs in which several observations would be removed are still solvable. This not only affects the specific epoch, but also stabilizes the estimation of phase ambiguities, because they are not interrupted at these epochs.

Besides the rate of TEC, a possible approach to quantify ionospheric changes or irregularities is the Rate of TEC Index (ROTI), introduced by Pi et al. (1997). It is defined as the variance of the rate of TEC within a specified time window and has been used in several studies to investigate ionospheric irregularities and their effect on ground based GPS observations (Pi et al., 1997; Bhattacharyya et al., 2000; Carrano and Groves, 2007).

$$ROTI^2 = \frac{\langle \Delta TEC^2 \rangle - \langle \Delta TEC \rangle^2}{\delta t^2} \quad (6.2)$$

$\langle \Delta TEC^2 \rangle - \langle \Delta TEC \rangle^2$  is the variance of  $\Delta TEC$  in a predefined time window and  $\delta t$  is the sampling rate of the observations. Most of the studies concerning ROTI computed the index in a five-minute interval. This might be sufficient for terrestrial applications for which the change in the transmitter-receiver geometry is rather slow. For LEO positioning a higher sampling rate is favorable. Due to the high speed of a satellite, the signal constellation is rapidly changing. Hence, a shorter time window was used for the computation of the ROTI in a moving window manner. This way a ROTI can be computed for each single epoch. As a consequence small scale irregularities, which only affect a few measurement epochs, show up in the computed ROTI time series. The above described definition of the ROTI was used to define a scale function for the a priori weights of the observations. This method was mainly applied to data from GOCE and Swarm, as these two missions both suffer from high influences of ionospheric disturbances on the observation quality.

The following example is based on the same GOCE data (October 2010) as used in the previous section. For each satellite mission it is necessary to find an individual relation

between ROTI and an appropriate scale factor, as the characteristics of the ROTI depend on observation sampling and quality. Based on the ROTI a simple scale function was defined:  $f_{ROTI} = 10 \cdot ROTI$ , but in principle any function could be used. The chosen window length for the computation of the ROTI was 30 s. The aim is to reduce the weight of influenced observations but not to change the complete weighting scheme of all observations. Thus, the scale factor was only applied if the factor was higher than 1. On average this resulted in a change of the a priori weight for  $\approx 3\%$  of the total observations available.

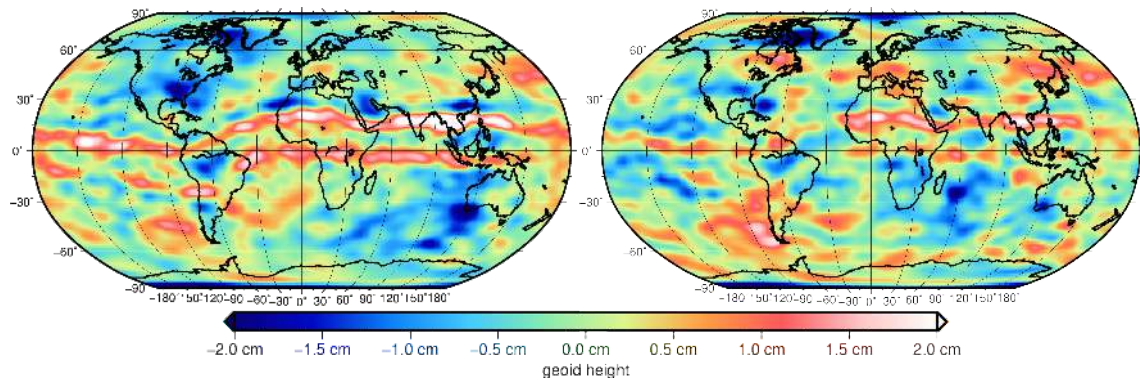


Figure 6.15: Difference in geoid height between GOCO05S and monthly GOCE solutions for October 2010. Left: no ROTI scale function applied, right: ROTI scale function used to scale the observation weight. 500 km Gaussian filter applied.

Figure 6.15 shows geoid height differences of two monthly solutions derived from kinematic GOCE orbits without (left) and with (right) applying the ROTI scale function. The example is for October 2010. The comparison shows a pretty similar result as for the SNR based observation scaling. By applying the scale function to reduce the weight of influenced observations, the effect has been greatly reduced, while maintaining the overall noise level. Although it is not fully removed, the signal amplitude is reduced and now at the same level as the overall noise of the solution. The RMS of the geoid height differences reduces from 6.6 mm (left plot) to 5.6 mm (right plot). In comparison to figure 6.14, it can be seen that the ROTI weighting scheme is slightly more successful in removing the error structure than the SNR based approach. However, the reduction in terms of geoid height RMS is the same.

**Discussion** Both discussed approaches succeed in greatly reducing the influence of ionospheric scintillations on the final gravity field solutions, derived from GOCE data. The application of ROTI based scale functions performs slightly better in removing the error bands. Nevertheless, this type of method is only applicable if high rate GPS observations are available, e.g. 1 Hz like for GOCE and Swarm. If the original observation rate is less than 1 Hz, the ROTI is not able to reliably detect small scale and short term ionospheric irregularities. Thus, for missions like GRACE or TerraSAR-X the only option is to use the SNR observations provided by the receiver. A combination of both methods is also not beneficial because both scale functions affect more or less the same observations.

All in all, the appropriate weight function depends on the satellite characteristics and thus must be found empirically.

### 6.2.6 2-antenna issue with FORMOSAT-3/COSMIC data

As already described in section 3.4.8 the FORMOSAT-3/COSMIC satellites are equipped with two POD antennas, one fore and one aft looking. The specific receiver design allows to operate both antennas simultaneously. Depending on the attitude of the satellite either one or both antennas are receiving GPS signals. As a result two separate observation files are provided during times when both antennas are used. If both antennas are operating, data from only one of them won't be sufficient to estimate a reliable kinematic orbit. That is why an approach to use the observations of both antennas must be found. In this work a method to combine the observation files in advance has been developed.

The method uses the attitude information and an a priori orbit for the LEO satellite along with GPS orbits to relate the observations of both antennas directly to the satellite CoM. Therefore, the antenna offset to the CoM is projected onto the Line-of-Sight (LoS) between LEO and GPS satellite and added to the original observation. This modifies the original observations, related to the electronic center of the receiving antenna, in a way that they are afterwards related to a virtual antenna located at the satellite CoM.

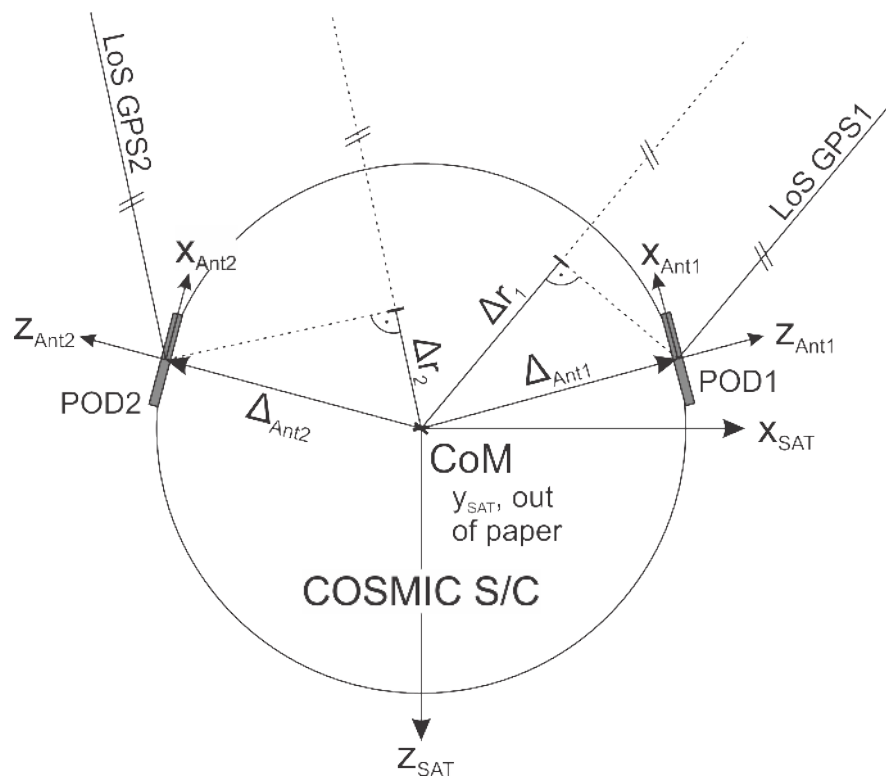


Figure 6.16: Illustration of the FORMOSAT-3/COSMIC satellite geometry and the projection used to combine the data sets of two POD antennas.

Figure 6.16 illustrates the projection used for the FORMOSAT-3/COSMIC observation data. The antenna offsets ( $\Delta_{Ant1}$  and  $\Delta_{Ant2}$ ) are projected onto the signal LoS. Due to

the huge distance between transmitter and receiver, the original LoS and the LoS for the corrected observation are considered to be parallel. The resulting range corrections  $\Delta r_1$  or  $\Delta r_2$  are then added to the respective observations. The modified phase and code observations are now related to a common virtual antenna located in the spacecraft CoM. B.-H. Wu et al. (2005b) noticed that there is a length difference between the cables of the two antennas, which causes a signal delay of a few nanoseconds. The delay has been taken into account by correcting the observations of antenna 1 using the value provided by B.-H. Wu et al. (2005b). After the measurements are transformed to the CoM they can be used jointly in the kinematic orbit estimation. The main advantage of this approach is that no distinction must be made between different antennas throughout the whole process, including the estimation of ACVs and the generation of accuracy maps. Kinematic orbit positions are now estimable even for epochs in which none of the two antennas provides a sufficient number of observations. For example, if each antenna receives the signal of three GPS satellites. Data from only one antenna would not be sufficient to estimate a kinematic position. However, if both data sets are combined, a total number of six satellites are available and kinematic positioning is possible. The disadvantage of this approach is that it is based on the assumption that the cable bias is the same for all six satellites and that it is stable in time. If the data would be introduced separately for each antenna in a joint orbit estimation it would be possible to estimate this bias, for example on a daily basis or two individual clock errors for each of the antennas. Due to the generally worse positioning performance of FORMOSAT-3/COSMIC and the additional efforts needed for implementing an approach to directly use data from two different antennas, the above described simple method has been used in the frame of this thesis.

## 7 Orbit and gravity field validation

This chapter presents different validations carried out for the orbits introduced in the previous chapter. The aim is to show the quality of the produced kinematic orbits and thus prove the applicability of the raw observation approach for kinematic orbit determination of LEO spacecraft. The validation of kinematic orbits is based on three pillars: 1) orbit comparisons, 2) SLR measurements, and 3) gravity field estimates. Each of these approaches provides information about the orbit accuracy. The combination of all three validation results serves as a good indicator for the achieved accuracy of the kinematic orbit.

The first part of the chapter shows some orbit comparisons with independent reduced-dynamic and kinematic orbit solutions provided by different external institutions. The second part uses independent SLR measurements for validation purposes. Finally, the third part introduces the gravity field solutions derived from kinematic orbits and compares them to highly accurate static and time variable gravity field information derived from superior observation methods. All in all, the chapter gives a complete and detailed analysis of the orbit results and thus provides a good evaluation of the approaches introduced in this work.

### 7.1 Orbit comparisons

The most convenient way of validating a satellite orbit would be to compare the estimated positions to an orbit solution or observation with superior accuracy. Unfortunately, no observation method is available which could provide this type of reference solution, except GRACE highly accurate K-Band observations can be used to perform a relative validation. In general the only possible way is to compare solutions based on different estimation procedures, either in terms of orbit modeling (kinematic, reduced-dynamic, or dynamic), in terms of estimation method (differenced, undifferenced, or raw observation approach), or in terms of observation technique (GNSS, DORIS, SLR, or a combination). Every method and approach has its advantages and disadvantages concerning accuracy and precision of the resulting orbit products. GNSS based orbit determination, either kinematic or reduced-dynamic, is among the most precise methods to determine the satellite position. Thus, any validation is always subject to doubts about the origin of observed differences between these two methods. The following validations are all based on a comparison between a kinematic and a reduced-dynamic orbit solution.

For all used satellite missions highly accurate orbit products are available from the satellite operators or from international research institutes. The aim of a comparison between a kinematic and a reduced-dynamic orbit is not to get an absolute measure of the orbit accuracy. This validation shall give an indication of the level of high-frequency noise contained in the kinematic orbit. Concerning the high-frequency content a reduced-dynamic orbit can be considered as much more accurate than a kinematic orbit. In case of the reduced-dynamic orbit the high-frequencies are fully determined by the used force models. This means a reduced-dynamic orbit is much smoother than a kinematic orbit. It can still suffer from low frequency errors and is thus no reference in an absolute sense but well suited to assess short term errors in the kinematic solution.

RMS values of differences between a kinematic orbit and a reduced-dynamic orbit are often used as a validation tool. However, the problem is that the agreement between a kinematic and a reduced-dynamic orbit computed at the same institution with the same software package will most likely be better than between two independent orbits. Figure 7.1 shows the differences between kinematic and reduced-dynamic orbits, both from Astronomical Institute at the University of Bern (AIUB) and IfG.

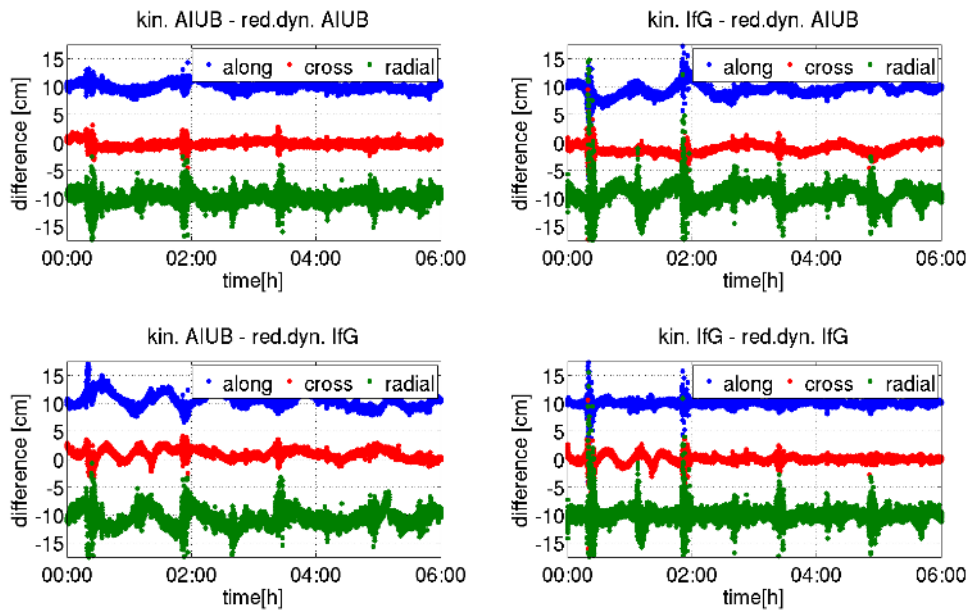


Figure 7.1: Orbit differences between kinematic and reduced-dynamic GOCE orbits. AIUB vs. AIUB (top left), IfG vs. AIUB (top right), AIUB vs. IfG (bottom left), and IfG vs. IfG (bottom right). Along track and radial component shifted by +10 and -10 centimeter.

The top left and the bottom right panel show the differences between orbits computed at the same institutions, whereas top right and bottom left panel show the difference between orbits of different origin. For both kinematic orbit solutions it can be seen that the comparison to a reduced-dynamic orbit from a different institution features larger deviations than the comparison to an orbit computed at the same Institute. Resulting RMS values for the shown time frames are listed in table 7.1. The RMS values confirm the visual impression of figure 7.1. Thus the validation shown in the subsequent paragraphs

concentrates on the high-frequency noise by applying a high-pass filter to the orbit differences.

difference	along [mm]	cross [mm]	radial [mm]
kin. AIUB - red.dyn. AIUB	6.6	5.4	9.7
kin. IfG - red.dyn. AIUB	11.5	13.6	16.0
kin. AIUB - red.dyn. IfG	13.1	12.2	15.5
kin. IfG - red.dyn. IfG	3.8	5.9	10.6

Table 7.1: RMS values for along, cross, and radial component of differences between kinematic and reduced-dynamic orbits.

The validation starts by interpolating the reference orbit to the observation times of the kinematic orbit. For interpolation of the reduced-dynamic orbit a polynomial of degree eight is fitted to the orbit and then evaluated at the observation time. The algorithm takes the nine orbit positions closest to the observation time and computes an interpolating polynomial. The observation epoch is at the center of the chosen interval, which guarantees a stable and accurate interpolation of the position. To facilitate an easier interpretation of the comparison, both orbits are then transformed from the inertial frame into the LORF (along, cross, radial). After forming the difference between the two data sets a high-pass filter is applied to remove low frequencies. This is done in order to guarantee a fair comparison, regardless of the source of the reference orbit. For those missions with a kinematic orbit available from an external institution the different orbits are synchronized in advance. This is done to guarantee that only epochs are considered for which both orbit solutions provide an estimate.

In addition to removing long wavelength deviations from the time series, it is also important to remove large outliers from the data. Kinematic orbit solutions may contain large outliers, with sizes of a few meters up to several 10 000 km. To make the outlier removal process fair and comparable, regardless of the noise level of the considered orbit, the threshold is dynamically adjusted to the RMS of the differences.

The first step is to filter the time series of orbit differences by applying a moving average filter. The chosen filter length of 5 min corresponds to a cut-off frequency of 0.0033 Hz. The five minutes filter length has been chosen in order to guarantee that the high-frequency noise is removed, whereas differences with a period of once or twice per revolution are still contained in the filtered data set. The smoothed time series is now subtracted from the original differences to remove the long wavelength deviations. This process is carried out for each arc and each coordinate component separately.

The second step is now to compute a robust estimate of the RMS. The RMS is computed for daily batches for each position component individually. After this first estimation of the RMS the differences are checked for outliers. Every epoch with differences bigger than 5-times the estimated RMS is removed from the time series. Then, the RMS is recomputed

with the screened data set. This process is iteratively repeated until the change in the estimated RMS is below 1 % between two consecutive iterations.

The whole process is done for daily orbit batches, resulting in a time series of daily RMS values for the kinematic orbit in along-track, cross-track, and radial direction. This representation is a good indicator for the high frequency noise of the kinematic orbit positions. Over long time periods of some years, the time series of daily RMS values can provide valuable information about the tracking performance of the receiver or the level of ionospheric activity within the 11-year solar cycle, possibly affecting the positioning performance. Yearly or total RMS values are then computed as the RMS of the daily values.

**CHAMP** As a reference for the kinematic CHAMP orbit a reduced-dynamic orbit, available from the AIUB, was used. This orbit was computed in the frame of a doctoral thesis (Prange, 2010). Along with the reduced-dynamic orbit AIUB also provides a kinematic orbit for CHAMP also generated by Prange (2010). This enables a cross comparison between two different orbit products, generated with individual software packages and based on different concepts for kinematic orbit estimation.

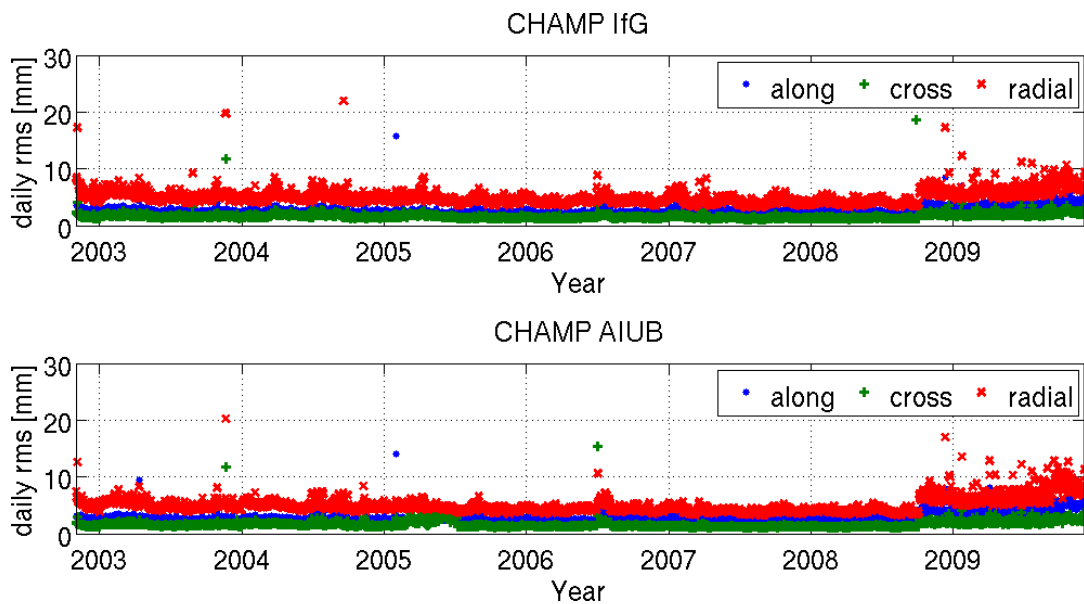


Figure 7.2: Daily RMS of the kinematic CHAMP orbit, computed at IfG (top), and AIUB (bottom), for along-track (blue), cross-track (green), and radial (red) component.

Fig. 7.2 shows daily orbit RMS values for the years 2002 until 2009 for the kinematic IfG orbit and the kinematic orbit from AIUB. Both solutions are compared against the reduced-dynamic orbit computed at AIUB. In general, it can be seen that both solutions feature values in the range of a few millimeters for all three components. The radial component has the highest values and is slightly noisier than the along and cross components. This is an inherent property of GPS derived position estimates. It is already known from ground based positioning, that the vertical component of a position is worse

by a factor of 1.5 to 2.0 (Hofmann-Wellenhof et al., 2008), compared to the horizontal components.

In both orbit solutions a jump in the noise level can be seen in late 2008. This jump can be attributed to a malfunction in the main receiver board, which triggered a switch to the redundant board and lead to a reduction of the maximum number of tracked satellites. After this incident the receiver was only capable of tracking up to 7 satellites simultaneously, opposed to a maximum number of 10 during the previous years (Prange, 2010). In addition to this jump it can be seen that starting from 2002 until 2008 the RMS values slightly decrease for all three components. There are two possible reasons for this decrease in positioning RMS: 1) the 11-year solar cycle had its maximum in 2000/2001 and its minimum in 2008/2009; 2) the quality of precise high-rate GPS clocks increased over time with more and more stations delivering high-rate data. No definite decision can be made what is the root cause for the reduced RMS. However, it is likely to be a combination of both effects. A lower solar activity leads to less ionospheric disturbances and thus to a better observation quality. Whereas better clock corrections allow for a better correction of a system inherent error.

Comparing top and bottom panels, figure 7.2 does not show a significant difference between the two different kinematic orbit solutions. Also the yearly values listed in table 7.2 confirm that both orbit products feature the same quality in terms of high-frequency noise.

year	along [mm]		cross [mm]		radial [mm]	
	IfG	AIUB	IfG	AIUB	IfG	AIUB
2002	3.1	3.4	1.7	1.6	5.8	5.5
2003	2.7	2.7	1.7	1.6	5.3	5.1
2004	2.7	2.7	1.8	1.7	5.2	5.1
2005	2.4	2.6	1.6	2.1	4.7	4.5
2006	2.4	2.7	1.5	1.4	4.5	4.4
2007	2.5	2.7	1.4	1.3	4.4	4.1
2008	2.7	3.1	1.5	1.5	4.7	4.8
2009	3.9	4.5	2.1	2.2	6.5	7.3
<b>Total</b>	<b>2.8</b>	<b>3.1</b>	<b>1.7</b>	<b>1.7</b>	<b>5.2</b>	<b>5.2</b>

Table 7.2: Yearly and total RMS values for the kinematic CHAMP orbit computed at the IfG and AIUB.

**GOCE** For validating the kinematic orbit of GOCE, official orbit products provided by ESA are at hand. ESA provides several different orbit products for the GOCE mission, among them are precise post-processed kinematic and reduced-dynamic orbit solutions computed at AIUB (Bock et al., 2011b) in the frame of the GOCE High-Level Processing Facility (HPF) (Koop et al., 2006). This enables, similar as for CHAMP, a comparison

with an independently determined kinematic orbit. Both kinematic orbits are validated against the reduced-dynamic orbit provided by ESA.

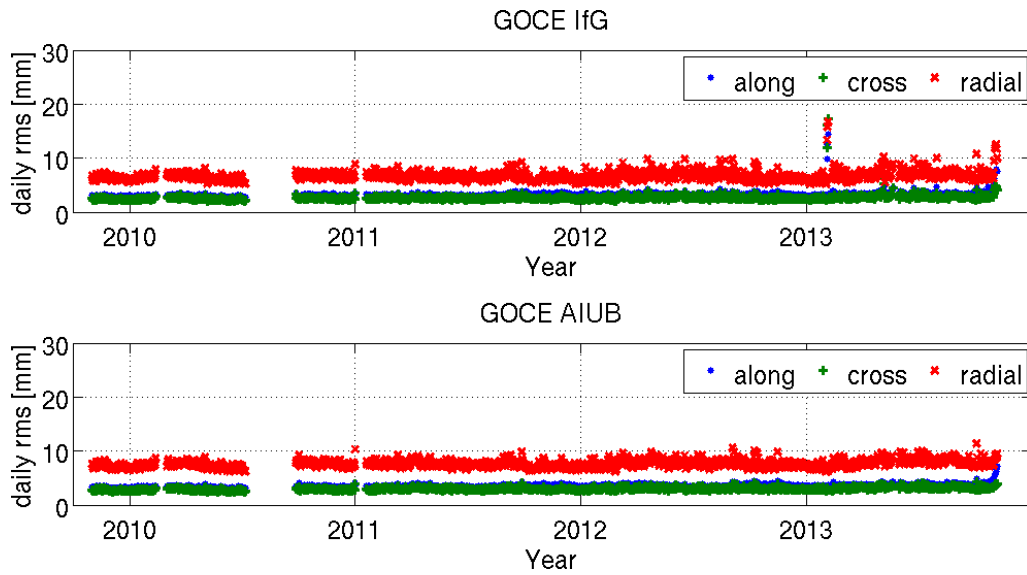


Figure 7.3: Daily RMS of the kinematic GOCE orbit, computed at IfG (top) and AIUB (bottom), for along-track (blue), cross-track (green), and radial (red) component.

Figure 7.3 shows daily RMS values for along-track, cross-track, and radial components, for kinematic orbits computed at IfG and AIUB. Both validations cover the whole operational lifetime of the GOCE satellite, until November 5, 2013, just six days before its reentry into the Earth's atmosphere. Comparable to the results obtained for CHAMP, also GOCE features RMS values in the range of some millimeters for all three components. The radial component is again worse by a factor of 2 compared to along- and cross-track. Visually there is not much difference between the top and bottom panel in figure 7.3. Nevertheless, from table 7.3 it may be seen that the IfG orbit slightly outperforms the AIUB orbit in all three components and for the whole considered time frame.

year	along [mm]		cross [mm]		radial [mm]	
	IfG	AIUB	IfG	AIUB	IfG	AIUB
2009	3.0	3.3	2.4	2.8	6.3	7.2
2010	3.1	3.4	2.5	2.8	6.5	7.4
2011	3.2	3.6	2.6	3.0	6.6	7.5
2012	3.3	3.6	2.7	3.1	6.7	7.7
2013	3.6	3.9	2.9	3.2	7.1	8.0
<b>Total</b>	<b>3.3</b>	<b>3.6</b>	<b>2.7</b>	<b>3.0</b>	<b>6.7</b>	<b>7.6</b>

Table 7.3: Yearly and total RMS values for the kinematic GOCE orbit computed at IfG and AIUB.

From table 7.3 it can be seen that from 2009 until 2013 the positioning RMS slightly increases. This is true for all three components and can be observed with IfG as well as AIUB orbits. This can be attributed to the increasing solar activity in this particular time frame and the high sensitivity of the GOCE receiver for ionospheric disturbances.

Starting at a very low level in 2009 the solar activity gradually increased until it reached its maximum in 2013/2014, exactly when GOCE reached its end of lifetime.

**GRACE** A reduced-dynamic orbit for both GRACE satellites is provided by JPL as part of the GRACE level 1B data (Case et al., 2010). This orbit is used as reference in the following orbit comparisons for GRACE A and B. A kinematic orbit is not part of the official level 1B data set. However, AIUB provides kinematic orbits for GRACE until the end of 2014 (Meyer et al., 2016). This combination of different orbits enables a completely independent comparison, as both kinematic orbits and the reduced-dynamic orbit are computed by different institutions, using different software packages. The only drawback of the comparison is the fact that the AIUB orbit is only given with a sampling of 30 s. In case of the IfG orbit in general a 10 s sampled orbit is used, except for the year 2002 and for January 2007 until April 2008.

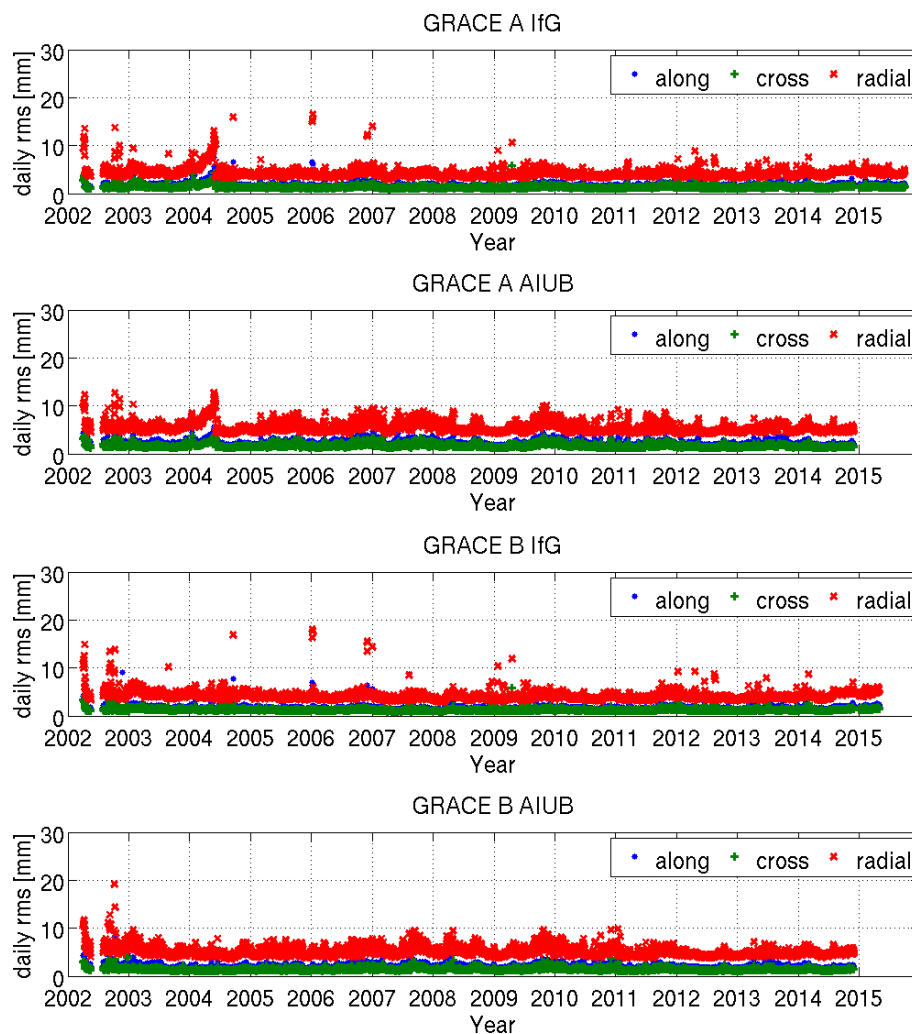


Figure 7.4: Daily RMS of the kinematic GRACE A and B orbits, computed at IfG (first and third panel) and AIUB (second and fourth panel), for along-track (blue), cross-track (green), and radial (red) component.

Figure 7.4 shows daily RMS values of the kinematic orbits computed in the frame of this thesis and at AIUB for GRACE A and B. In general, all four comparisons draw the same

picture. The daily RMS values are in general stable in time, except for some outliers and some small variations from month to month. They do not show a strong dependency on the solar cycle. This is true for GRACE A and B, and both orbit solutions, from IfG as well as AIUB. Jäggi et al. (2016) have shown that observations affected by ionospheric disturbances are simply missing in GRACE observation data. An interesting feature can be seen at the beginning of 2004 in the GRACE A orbit RMS. Within the first five months of 2004 the RMS values increase significantly from day to day. Investigations revealed that during these months, the receiver of GRACE A shows varying behavior in terms of ACVs. The reason for these anomalous changes in the ACVs is not known. However, the changes affect the positioning accuracy as the estimated and used receiver ACVs are considered to be stable in time. A separate estimation of ACVs for this particular time frame would possibly remove parts of this error. But an analysis of observation residuals, for this time span, revealed that the characteristics of the ACVs change over time during this five month period. Thus, an estimation of receiver ACVs for this period would only reduce and not fully remove the error, because the changes are not stable within this time frame.

year	along [mm] A/B		cross [mm] A/B		radial [mm] A/B	
	IfG	AIUB	IfG	AIUB	IfG	AIUB
2002	1.9/2.1	2.4/2.6	1.5/1.6	1.8/1.9	5.0/5.5	6.1/6.6
2003	1.9/1.9	2.2/2.1	1.5/1.4	1.6/1.4	4.6/4.7	5.5/5.4
2004	2.4/1.8	2.6/1.8	1.8/1.3	1.8/1.3	5.6/4.4	6.3/4.7
2005	1.7/1.6	2.3/2.0	1.3/1.2	1.8/1.4	4.1/4.0	5.7/5.0
2006	2.0/1.8	2.6/2.1	1.5/1.3	1.8/1.5	4.5/4.3	5.7/5.1
2007	1.7/1.6	2.6/2.3	1.3/1.1	1.9/1.6	4.1/3.8	6.3/5.6
2008	1.6/1.6	2.3/2.3	1.2/1.2	1.7/1.5	3.8/3.9	5.4/5.4
2009	1.8/1.7	2.4/2.2	1.4/1.2	1.9/1.6	4.1/4.0	5.8/5.5
2010	1.7/1.7	2.3/2.2	1.3/1.2	1.7/1.5	3.9/3.9	5.4/5.3
2011	1.8/1.7	2.3/2.0	1.4/1.2	1.7/1.4	4.2/4.0	5.4/4.9
2012	1.7/1.7	2.0/1.8	1.3/1.2	1.5/1.3	3.9/4.0	4.8/4.4
2013	1.9/1.7	2.4/2.1	1.3/1.2	1.6/1.4	4.1/3.9	5.2/4.7
2014	1.9/1.8	2.0/1.9	1.3/1.3	1.5/1.4	4.4/4.4	5.1/4.9
2015	1.9/2.0	-/-	1.4/1.5	-/-	4.4/4.9	-/-
<b>Total</b>	<b>1.9/1.7</b>	<b>2.3/2.1</b>	<b>1.4/1.3</b>	<b>1.7/1.5</b>	<b>4.3/4.2</b>	<b>5.6/5.2</b>

Table 7.4: Yearly and total RMS values for the kinematic orbits of GRACE A and B, computed at IfG and AIUB.

The comparison between GRACE A and B reveals almost no difference between the two spacecraft. The only small difference that can be observed gets obvious when looking at the yearly RMS values listed in table 7.4. RMS values obtained for GRACE B are marginally smaller than those of GRACE A, especially for along- and cross-track component. This is a rather small difference and manifests itself as a reduction of only

0.1 mm in the total RMS. Taking both orbit solutions into consideration, it can be said that both spacecraft perform in a similar manner with comparable noise level.

When it comes to the difference between the two kinematic orbit solutions, deviations are a little bit more obvious and clear. Throughout the whole time span of more than 13 years, the IfG kinematic orbit outperforms the AIUB solution, as it can be seen from table 7.4. This is true for both, GRACE A and B, as well as for all three different position components. Taking into account the different sampling of the orbit for most of the analyzed years, the results clearly demonstrate the low noise level of the IfG orbit.

**Swarm** The reduced-dynamic orbit used in the orbit comparison of Swarm is provided by ESA as part of the official level 1B products (Tøffner-Clausen, 2013). The orbit is generated at European Space Operations Centre (ESOC) and thus independent from all three orbit products used in the subsequent analysis. Besides the IfG kinematic orbit, two additional solutions are available. The first one is provided by ESA as part of the official Swarm level 2 products (Stolle, 2013). This kinematic orbit is produced at the Delft University of Technology (van den IJssel et al., 2015) using the software package GPS High-precision Orbit Determination Software Tools (GHOST) (Van Helleputte, 2004). The second kinematic orbit is provided by AIUB (Jäggi et al., 2015). AIUB uses the GNSS software Bernese (Dach et al., 2015) for LEO orbit processing. All orbit products are available with the highest possible sampling rate, which is 10 s for the first 9 months and 1 s thereafter.

	along [mm]	cross [mm]	radial [mm]
Swarm A IfG	4.5	3.5	10.1
Swarm A AIUB	4.7	3.7	10.9
Swarm A ESA	4.9	3.8	11.0
Swarm B IfG	4.3	3.3	9.9
Swarm B AIUB	4.4	3.5	10.5
Swarm B ESA	4.6	3.6	10.6
Swarm C IfG	4.3	3.4	9.8
Swarm C AIUB	4.4	3.5	10.2
Swarm C ESA	4.6	3.6	10.4

Table 7.5: Total RMS values for the kinematic orbits of Swarm A, B, and C, computed at IfG, AIUB, and ESA.

Figure 7.5 shows daily RMS values for all three satellites and all three kinematic orbits. Generally, all 9 plots show the same behavior. This means all three satellites perform similar and also the different orbit solutions feature almost the same high-frequency noise. Only a look at the overall RMS values for each satellite and component, listed in table 7.5, reveals some small differences between the three solutions. The IfG solution features the smallest RMS for almost every satellite and component, whereas the largest

## 7 Orbit and gravity field validation

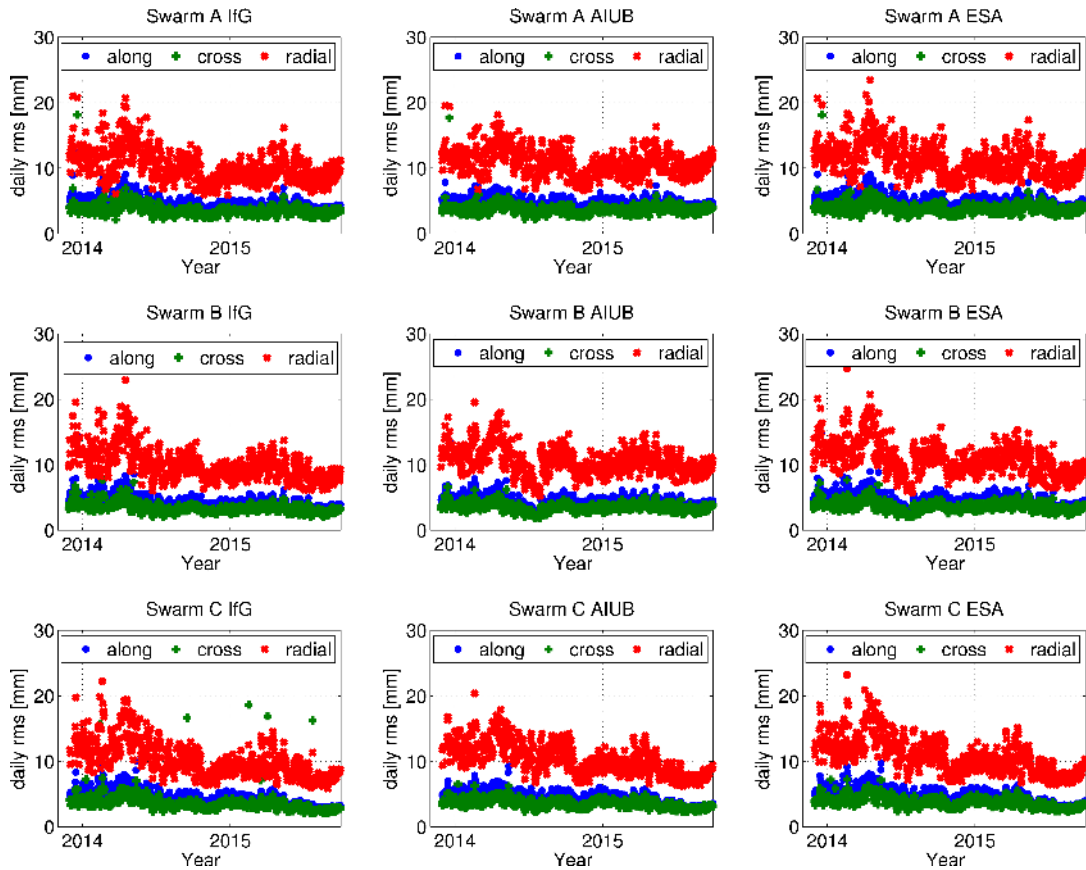


Figure 7.5: Daily RMS of the kinematic Swarm orbits, computed at IfG (left), AIUB (middle), and TU Delft (right), for along-track (blue), cross-track (green), and radial (red) component.

values are seen for the ESA orbit. Although the differences are smaller than 1 mm for all components and satellites, it indicates a tendency towards the IfG solution being less affected by high-frequency noise. Compared to other satellite missions it can be said that the noise level in Swarm kinematic orbits is not as stable as, for example, seen for GRACE or GOCE.

**TerraSAR-X and TanDEM-X** For TerraSAR-X and TanDEM-X orbit analysis a dynamic orbit computed at the GFZ is used (König et al., 2006). This orbit is provided via ISDC as so called rapid science orbit product.

Figure 7.6 shows the results obtained for TerraSAR-X and TanDEM-X. In general, it can be said that the level of high frequency noise is rather low for both kinematic orbits. However, both plots indicate a slight degradation of the RMS over time. For TerraSAR-X it might be related to increased ionospheric activity. The time series starts in 2008, during very low solar activity, reaching highest RMS values in 2013, during high solar activity. For TanDEM-X the situation looks a little bit different. The bottom panel in figure 7.6 shows increased noise starting from mid-2013 until the end of 2014. Within this time frame the solar activity was already decreasing, thus the reason for the increased noise is not clear.

Analyzing the yearly RMS values shows the same behavior as already visible in the

## 7 Orbit and gravity field validation

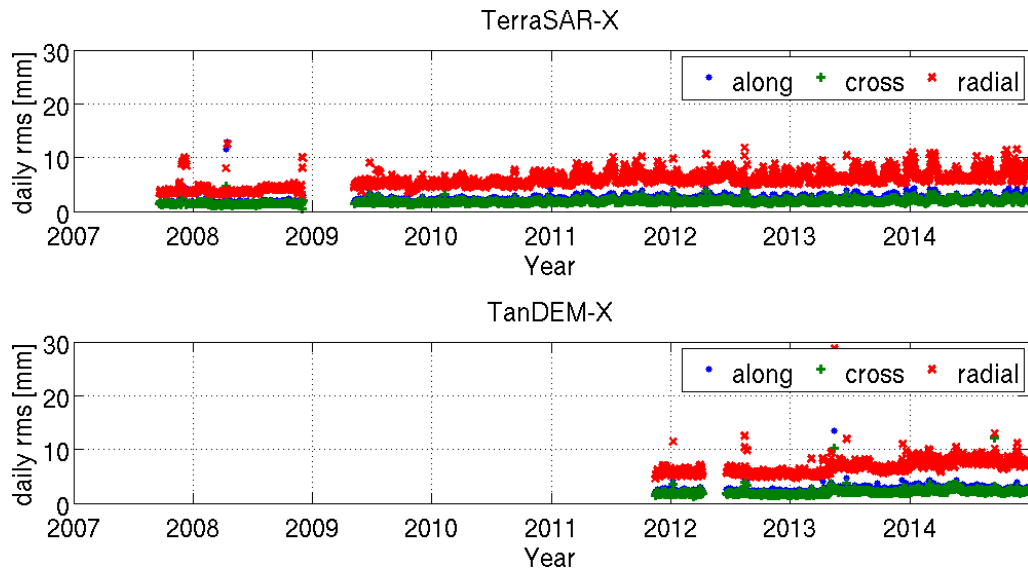


Figure 7.6: Daily RMS of the kinematic TerraSAR-X (top) and TanDEM-X (bottom) orbit, for along-track (blue), cross-track (green), and radial (red) component.

daily time series. Comparing TerraSAR-X to TanDEM-X indicates that both satellites perform similar in terms of high frequency noise. Anyway, this can be expected, due to the fact that both spacecraft are almost identical, including the GPS equipment. In addition, they operate in a close formation, separated only by a few hundred meters, hence they experience the same environmental conditions along the orbit.

year	along [mm]		cross [mm]		radial [mm]	
	TerraSAR	TanDEM	TerraSAR	TanDEM	TerraSAR	TanDEM
2007	2.2	-	1.8	-	4.8	-
2008	1.9	-	1.4	-	3.9	-
2009	2.1	-	1.7	-	5.1	-
2010	2.2	-	1.7	-	5.4	-
2011	2.6	2.4	1.9	1.8	6.4	5.9
2012	2.5	2.3	1.9	1.8	6.4	5.8
2013	2.6	2.6	1.9	2.0	6.5	6.4
2014	2.8	2.9	2.1	2.3	7.1	7.9
<b>Total</b>	<b>2.4</b>	<b>2.6</b>	<b>1.8</b>	<b>2.1</b>	<b>5.9</b>	<b>6.8</b>

Table 7.6: Yearly and total RMS values for the kinematic orbits of TerraSAR-X and TanDEM-X.

**MetOp A and B** The reference orbit chosen for the orbit comparisons of MetOp A and B is provided by UCAR. It is a reduced-dynamic orbit mainly used for the purpose of radio occultation. For the generation of these orbits the Bernese GNSS software was used (UCAR, 2016).

Figure 7.7 shows the time series of daily RMS values for both satellites. In case of MetOp A (top panel fig. 7.7) the values are rather constant throughout the whole time frame.

Only a slight degradation can be seen for the time period mid-2011 until beginning of 2013. This corresponds very well with the period of highest solar activity within the last 11-year solar cycle. The increased RMS is also reflected in the yearly RMS values, listed in table 7.7. For example, the highest value for the radial component is achieved in 2012 and for the along track component in 2013.

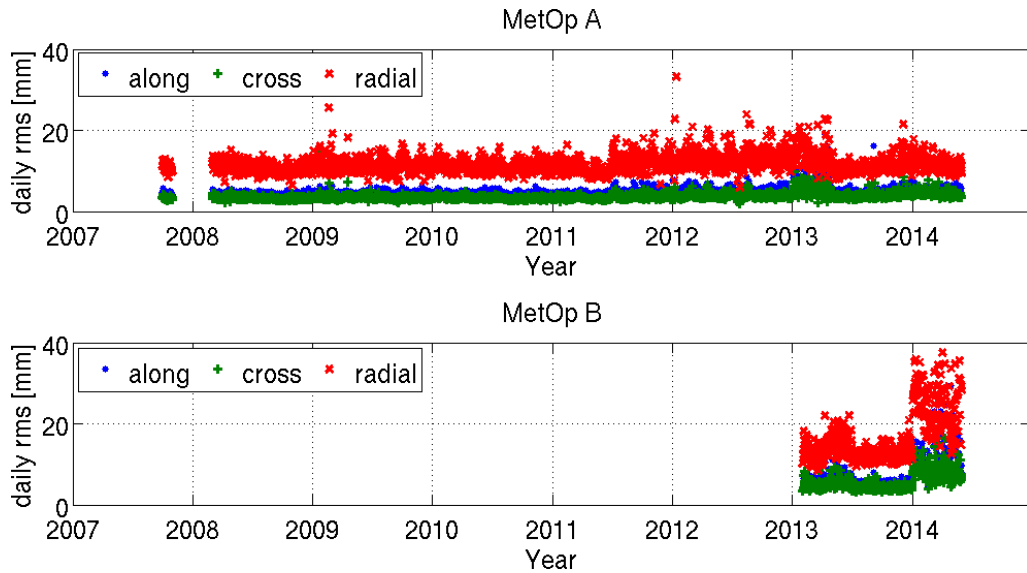


Figure 7.7: Daily RMS of the kinematic MetOp A (top) and B (bottom) orbit, for along-track (blue), cross-track (green), and radial (red) component.

A slightly different picture is obtained for MetOp B (bottom panel fig. 7.7). In 2013 the performance is comparable to the one of MetOp A, whereas in 2014 a significant degradation is visible. The values are twice as high as for 2013. The reason for this sudden increase in high frequency noise is not known. A lack of additional information about the satellite and receiver status makes a detailed analysis of the effect difficult.

year	along [mm]		cross [mm]		radial [mm]	
	MetOp A	MetOp B	MetOp A	MetOp B	MetOp A	MetOp B
2007	4.4	-	3.3	-	10.8	-
2008	4.4	-	3.3	-	10.7	-
2009	4.6	-	3.5	-	11.4	-
2010	4.5	-	3.4	-	11.0	-
2011	4.7	-	3.5	-	11.4	-
2012	5.0	-	3.8	-	12.5	-
2013	5.2	6.1	4.2	4.9	11.4	13.4
2014	5.4	12.1	4.5	8.8	11.6	25.7
<b>Total</b>	<b>4.8</b>	<b>8.4</b>	<b>3.7</b>	<b>6.3</b>	<b>11.4</b>	<b>18.1</b>

Table 7.7: Yearly and total RMS values for the kinematic orbits of MetOp A and B.

In general, it can be said that the positioning performance of the MetOp satellites is in line with results obtained for other missions, featuring RMS values in the range of

some millimeters or a few centimeters. However, the analysis shows that the performance of the GRAS receiver is slightly worse, in terms of high frequency noise, compared to the best results achieved for missions like CHAMP or GRACE. This confirms results published by Montenbruck et al. (2008).

**SAC-C** SAC-C orbits are available from several institutions. In this comparison the reduced-dynamic orbit provided by JPL is used. It was computed using the GNSS processing software GNSS-Inferred Positioning System and Orbit Analysis Simulation Software (GIPSY-OASIS) (Zumberge et al., 1997) developed at JPL.

From figure 7.8 it can be seen that the RMS values are significantly higher than for other missions and the noise level varies over time. For the first two and a half years the RMS is comparable to other satellites in the range of some millimeters. However, in 2004 there is a significant increase in the RMS lasting until mid-2008. In later years the RMS is again slightly lower, except for the last available months in 2012 and 2013 for which the results are again worse. In general, there are a lot of days throughout the whole time span with high RMS values. An additional effect can be seen in 2005 for the cross track component. The daily RMS strongly increases during this year, reaching values of almost 10 cm. Some of these variations in the behavior might be related to the same effects already seen in the estimated ACVs and accuracy maps (see section 6.2.1 and 6.2.4). Table 7.8 lists RMS values for all 12 years, until the end of the mission in 2013. They also reflect the changing performance of the CORISS receiver installed on SAC-C.

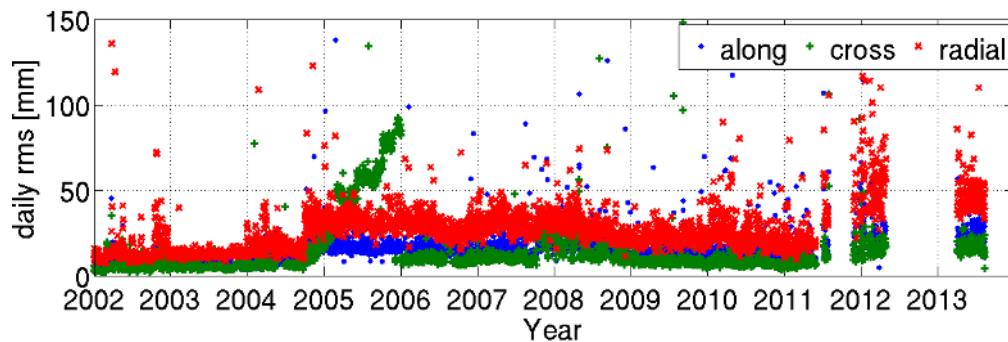


Figure 7.8: Daily RMS of the kinematic SAC-C orbit, for along-track (blue), cross-track (green), and radial (red) component.

In general, it can be said that the results for SAC-C are similar to other missions within the first years of the mission. Different influences led to a strong degradation of the positioning accuracy during later years. The worse positioning performance can be partially attributed to the lack of attitude information. For the orbit computations nominal orientation of the satellite was assumed, which cannot reflect the true attitude of the satellite during all times. However, a detailed analysis of the varying behavior would require additional information about the satellite status and operational settings which is not publicly available for SAC-C.

## 7 Orbit and gravity field validation

year	along [mm]	cross [mm]	radial [mm]
2002	7.8	6.9	17.2
2003	6.6	5.7	12.9
2004	13.5	12.1	23.5
2005	18.7	55.2	33.0
2006	17.6	12.6	29.2
2007	20.1	16.7	32.5
2008	19.7	19.5	29.1
2009	14.8	11.9	22.9
2010	17.7	8.0	27.2
2011	16.1	7.9	24.4
2012	25.3	17.2	57.6
2013	25.4	17.5	47.7
<b>Total</b>	<b>16.4</b>	<b>21.2</b>	<b>27.5</b>

Table 7.8: Yearly and total RMS values for the kinematic orbit of SAC-C.

**Jason 1 and 2** For the two altimeter missions Jason 1 and 2 several institutions provide orbit solutions based on either DORIS, SLR, or GPS data. The CDDIS <sup>1</sup> distributes some of these products as part of the International DORIS Service (IDS) (Willis et al., 2010). In this comparison the orbit products provided by Segment sol Multi-Missions d’Altimetrie, d’Orbitographie et de Localisation Précise (SSALTO)<sup>2</sup>, a dedicated system for processing of altimeter mission data operated by CNES were used. SSALTO utilizes all three positioning technologies installed on the satellites, DORIS, SLR, and GPS <sup>3</sup>.

The results for Jason 1 show a considerable stable noise level from 2002 until the end of 2006, below 1 cm for all three components. In late 2006 a failure occurred on the main receiver board. A switch to the redundant board was not possible due to loss of the instrument in mid-2006. After the failure, the main receiver suffered from repeated tracking losses and a low number of tracked satellites (G. M. Shirliffe, 2007). From 2007 until April 2009 the number of available kinematic orbit positions is limited. GPS tracking on board of Jason 1 came to an end in April 2009, when the main receiver completely failed (G. M. Shirliffe, 2009). In figure 7.9 the effect of the receiver failure is clearly visible. After 2006, the daily RMS values are significantly higher. This also gets obvious when looking at the yearly RMS values, listed in table 7.9. RMS values are almost twice as high for the years 2007-2009 as they are for previous years.

<sup>1</sup><http://cddis.nasa.gov/>

<sup>2</sup>The altimeter products were produced and distributed by Aviso (<http://www.aviso.altimetry.fr/>), as part of the SSALTO ground processing segment.

<sup>3</sup>[ftp://ftp.ids-doris.org/pub/ids/data/POD\\_configuration\\_GDRE.pdf](ftp://ftp.ids-doris.org/pub/ids/data/POD_configuration_GDRE.pdf)

## 7 Orbit and gravity field validation

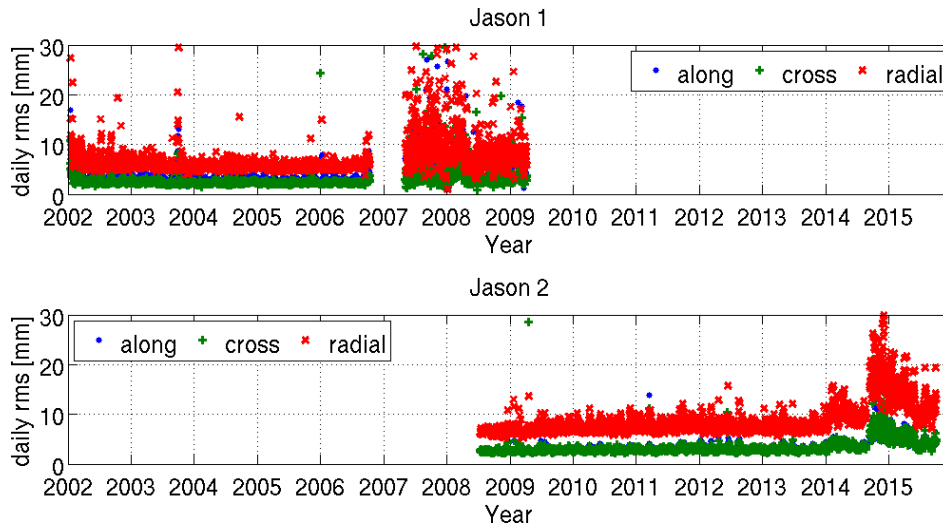


Figure 7.9: Daily RMS of the kinematic Jason 1 (top) and 2 (bottom) orbit, for along-track (blue), cross-track (green), and radial (red) component.

The picture is slightly different for Jason 2. At the beginning of the mission, RMS values are comparable to those obtained for Jason 1. Nevertheless, from 2009 until 2012, daily RMS values gradually increase, especially for the radial component. This increased variability might be related to the ionospheric activity, which reached its maximum in 2012/2013, due to the solar activity. In addition to this increase in RMS, a periodic effect is visible. Investigations revealed that the effect occurs with a period of approximately 58 days. The same periodic signal is also present in the Jason 1 time series, however not as

year	along [mm]		cross [mm]		radial [mm]	
	Jason 1	Jason 2	Jason 1	Jason 2	Jason 1	Jason 2
2002	3.8	-	2.8	-	7.3	-
2003	3.3	-	2.5	-	6.6	-
2004	3.0	-	2.3	-	5.7	-
2005	4.2	-	2.6	-	5.5	-
2006	4.7	-	3.3	-	5.9	-
2007	7.2	-	5.6	-	13.8	-
2008	6.0	2.7	4.7	2.6	10.3	6.5
2009	5.4	3.4	3.8	3.1	10.5	7.1
2010	-	3.0	-	2.9	-	7.5
2011	-	3.2	-	3.0	-	8.0
2012	-	3.1	-	5.5	-	7.7
2013	-	3.0	-	2.9	-	7.7
2014	-	6.2	-	5.5	-	14.8
2015	-	5.1	-	5.0	-	13.6
<b>Total</b>	<b>4.6</b>	<b>3.9</b>	<b>3.4</b>	<b>4.0</b>	<b>8.0</b>	<b>9.6</b>

Table 7.9: Yearly and total RMS values for the kinematic orbits of Jason 1 and 2.

prominent as in the Jason 2 results. This variation is related to the variation of the  $\beta$ -angle. The  $\beta$ -angle is defined as the angle between the orbital plane and the direction to the sun. For both satellites, due to the same orbit, the  $\beta$ -angle is close to zero approximately every 58 days. During times when the absolute value of the  $\beta$ -angle is below  $15^\circ$ , the Jason satellites change the attitude control mode from yaw steering to fixed yaw mode. The analysis of the daily orbit RMS time series revealed that especially for those periods the orbit accuracy is degraded. In 2014 a further degradation of the orbit quality can be seen until September 2014, when the main receiver board failed. After this event the redundant board was switched on. However, the orbit quality is considerably worse than before the switch. The redundant receiver suffered from an increased number of tracking losses and a lower number of tracked satellites in total (G. Shirtliffe and Guinle, 2014). In combination this leads to a reduced orbit quality.

**C/NOFS** The orbit comparison for C/NOFS is based on a reduced-dynamic orbit provided by UCAR. UCAR utilizes the Bernese software in the frame of a standardized processing scheme for all satellite missions (UCAR, 2016).

Figure 7.10 shows daily RMS values for the years 2010 and 2011. The publicly available data for C/NOFS is restricted to this short time period. Compared to previously shown results for other missions, the level of high frequency noise in the C/NOFS positioning time series is rather high. This is also clearly reflected in the RMS values for both years shown in table 7.10. The values are in the range of 1 to 2 centimeters. An interesting effect is that the along track component is worse than the radial component. The reason for the overall worse performance and the degradation for the along track component might be the fact that neither observed attitude information is available for this mission nor a nominal attitude law is published. The orientation of the satellite, used in the orbit computation, was derived from the reduced-dynamic orbit assuming a constant orientation of the satellite body with respect to the local orbital frame.

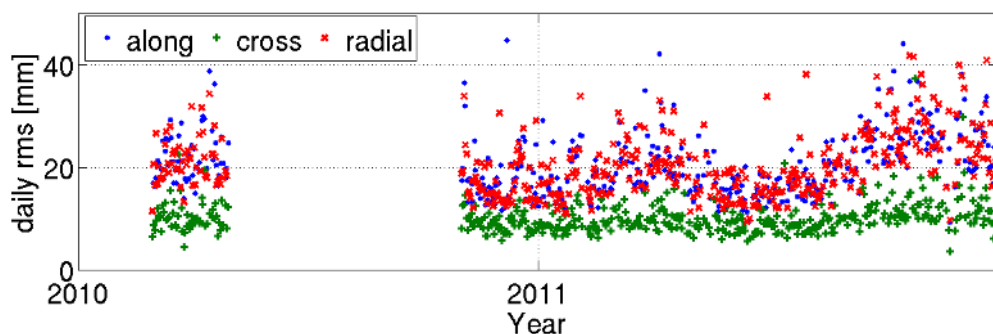


Figure 7.10: Daily RMS of the kinematic C/NOFS orbit, for along-track (blue), cross-track (green), and radial (red) component.

## 7 Orbit and gravity field validation

year	along [mm]	cross [mm]	radial [mm]
2010	20.7	10.1	20.6
2011	22.3	10.7	22.5
<b>Total</b>	<b>21.8</b>	<b>10.6</b>	<b>22.0</b>

Table 7.10: Yearly and total RMS values for the kinematic orbit of C/NOFS.

**FORMOSAT-3/COSMIC** The comparison for all six FORMOSAT-3/COSMIC satellites is based on a reduced-dynamic orbit provided by UCAR (UCAR, 2016). The used orbit product was computed with the Bernese GNSS processing software. It is part of the official radio occultation processing for the FORMOSAT-3/COSMIC mission carried out at UCAR.

Figure 7.11 shows daily RMS values for all six satellites from 2006 until the end of 2013. The time series show a lot of days with increased RMS and only a few periods for which the results are stable. For example in 2008 and 2009 the daily RMS for FM 4 show only a few outliers, whereas for earlier and later years the number is significantly higher. In general, all spacecraft perform quite similar. Only the total RMS values, listed in table 7.11, reveal that FM 1, 5, and 6 are worse compared to the other three satellites. Especially the number of anomalous high daily RMS values is lower for FM 2, 3, and 4.

year	along [mm]	cross [mm]	radial [mm]
FM 1	27.5	27.2	21.2
FM 2	13.2	17.0	14.9
FM 3	16.7	18.9	18.5
FM 4	19.5	18.5	20.0
FM 5	26.5	18.7	20.2
FM 6	23.7	19.8	21.3

Table 7.11: Total RMS for the kinematic orbit of FORMOSAT-3/COSMIC.

Similar to the results of C/NOFS, all three components feature the same level of high frequency noise. This behavior might be related to the bad attitude determination in combination with a generally worse attitude control system of the spacecraft. In addition, the observation constellation is different compared to other satellites. Due to the aft and forward looking orientation of the POD antennas, the FORMOSAT-3/COSMIC receivers are tracking only a few signals in zenith direction and signals are also tracked below the local horizon, even down to elevations of  $-30^\circ$ . This leads to observations with higher noise, due to the signal being distorted by the Earth's upper atmosphere. Although both antennas can be operated simultaneously, for most of the time only one is actually receiving signals. This leads to a situation where only observations located in one half of the hemisphere are available. An additional characteristic that might contribute to

## 7 Orbit and gravity field validation

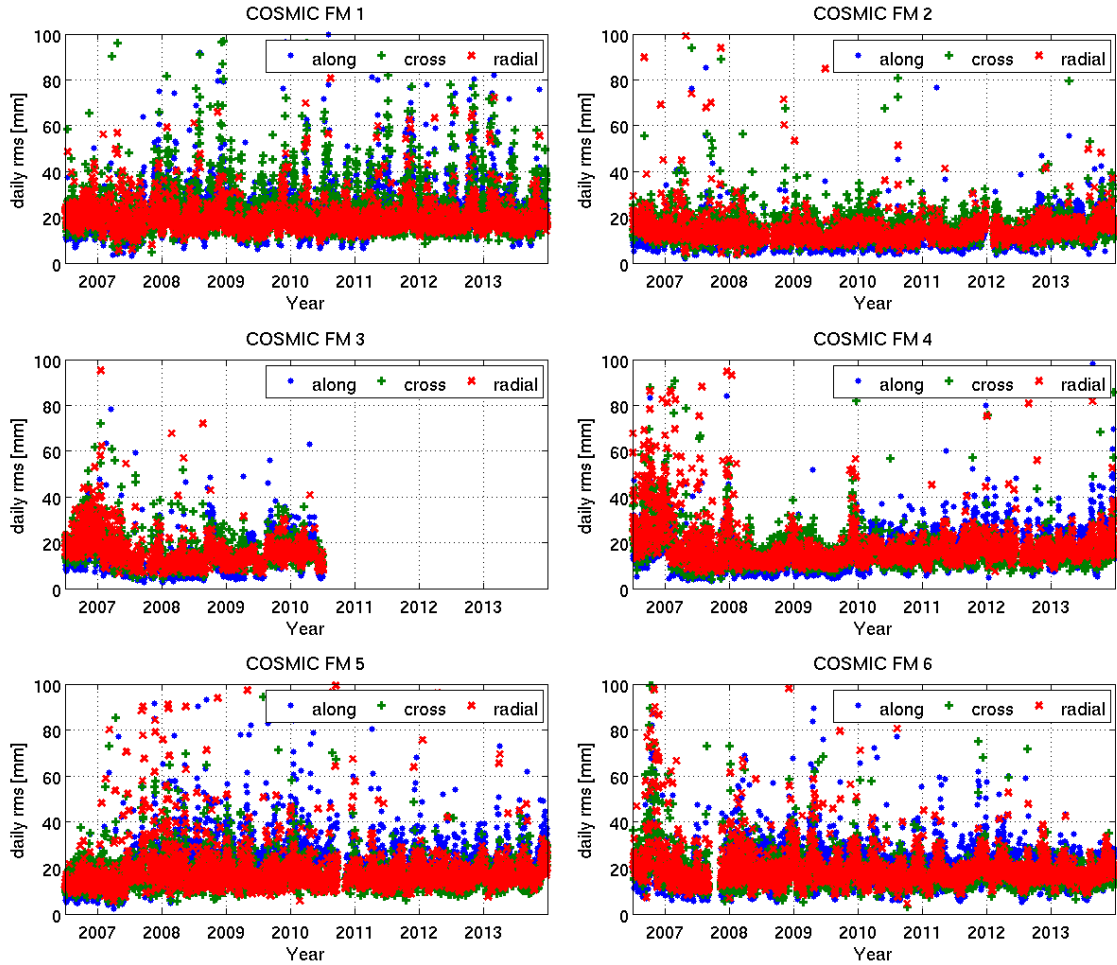


Figure 7.11: Daily RMS of the kinematic FORMOSAT-3/COSMIC orbit (FM 1 - FM 6), for along-track (blue), cross-track (green), and radial (red) component.

the degradation of the positioning performance are the POD antennas. FORMOSAT-3/COSMIC uses small patch antennas without choke rings, or similar measures, to mitigate signal distortions. This leads to an overall worse tracking performance of the GPS receiver (Hwang et al., 2008).

All in all, the performance of the FORMOSAT-3/COSMIC satellites is significantly worse than for any other mission analyzed in the course of this thesis. The cause for this is most likely a combination of the attitude error, the observation constellation, and the tracking performance of the receiver in general.

**Summary of orbit comparisons** Especially the results obtained for GRACE B, with total RMS values of 1.7, 1.3, and 4.2 mm for along, cross, and radial component, demonstrate the low noise level which can be achieved with good GPS observation data. Taking into account the basic noise level of GPS phase measurements, which is in the range of 1–2 mm, this indicates that the high-frequency noise of the estimated positions is mainly limited by the observation noise itself.

The orbit comparison also shows that not all satellites perform as it could be expected from instrument specifications. As an example the FORMOSAT-3/COSMIC mission shall be mentioned. Although the satellites are equipped with a geodetic GPS receiver, similar as those used on GRACE or CHAMP, the positioning accuracy is by far worse than it is for GRACE or CHAMP. There are additional factors which influence the achievable accuracy apart from the receiver quality. In terms of receiving equipment the antenna is as important as the receiver itself. In fact, only the combination of a good receiver and a good antenna is providing high quality observations. In case of FORMOSAT-3/COSMIC, only small patch antennas are used. Highest accuracies are achieved for satellites using circular patch antennas, protected against signal distortions by one or more choke rings. The only mission using a helix antenna, GOCE, achieves comparable results. Other satellites, like MetOp or SAC-C equipped with small patch antennas, perform considerably worse.

Besides the receiver/antenna configuration the accuracy of the available attitude information is important. Not only for shifting the estimated position from the antenna center to the satellite center of mass by correctly adding the antenna offset. Even more important is the attitude to calculate correct values for azimuth and elevation, which are important in the context of ACVs. A correct attitude is important during the process of estimating ACVs and also later when they are applied as corrections. In this context it is not very important to keep the satellite orientation stable, but to observe it with high accuracy. Again the mission FORMOSAT-3/COSMIC can be seen as a non-optimal example. These satellites use a Sun and an Earth sensor in combination with a magnetometer to determine their attitude. The stated accuracy of this data is  $2^\circ$  for roll, pitch, and yaw angles (Tseng et al., 2012). This accuracy level is not sufficient to correctly determine azimuth and elevation. For some satellites no observed attitude data is provided by the operator, hence simulated information was used. Then the results heavily depend on the accuracy of the attitude control of the satellite and how often the nominal attitude law is violated.

In summary, it can be concluded that there is no general rule describing the accuracy of GNSS based LEO POD. The situation is different for each and every satellite and so are the achieved accuracies. More precise, the high-frequency noise behavior of the kinematic orbit solutions based on the raw observation approach is determined by the quality of the receiver, the antenna, the attitude data, and the auxiliary data.

## 7.2 GRACE K-band validation

The twin satellites GRACE offer a unique possibility for orbit validations. The highly accurate microwave ranging system measures the inter-satellite range variation with accuracies below  $10\ \mu\text{m}$ . Although the measured ranges are not absolute, they are biased by a constant value, it is possible to use them as a reference for GPS derived inter-satellite ranges. Due to the constellation of GRACE, one satellite chasing the other on the same orbit, this comparison is a validation for the relative positioning accuracy in along track direction. The first step is to compute the distance between the two satellites from the kinematic orbit positions. Then, the difference between computed and observed inter-satellite ranges is computed. Finally, a constant offset is estimated for each continuous arc of microwave observations, to remove the bias. A new bias is estimated whenever a phase jump or gap occurs in the original microwave range observations.

Based on the K-band residuals, an analysis of the complete GRACE data set was performed. For this purpose daily RMS values of the range residuals were computed. This was done for the IfG as well as the AIUB kinematic orbit (Meyer et al., 2016). Figure 7.12 shows the results obtained for the entire time frame. Obviously there is a periodic signal visible in the daily RMS of K-band range residuals. Investigations showed that this variation is related to a 162 days period in the GRACE orbit. This corresponds to the variation of the angle between orbital plane and the sun, the  $\beta$ -angle, shown in figure 7.12 as green curve. It can be seen that during times when the  $\beta$ -angle is close to zero, the RMS increases, and vice versa. Apart from this periodic effect the RMS is stable throughout the whole time frame.

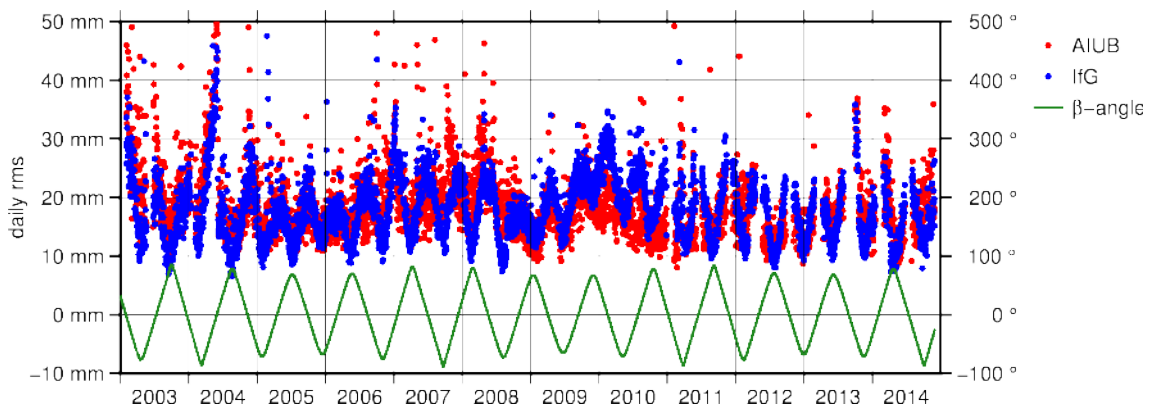


Figure 7.12: Daily RMS of GRACE K-band range residuals for IfG and AIUB kinematic orbits. The green line shows the  $\beta$ -angle.

Figure 7.13 shows the residuals for day June 15, 2008, a day with large daily RMS (24 mm) and a  $\beta$ -angle close to zero, and August 1, 2008, a day with small daily RMS (7 mm) and large  $\beta$ -angle. These two examples of daily K-band residuals show that there is a periodic deviation related to the revolution period of the satellites. The amplitude of this signal is different for these days and explains the observed difference in the daily RMS.

The reason for this behavior is not fully understood, although the sun can be identified

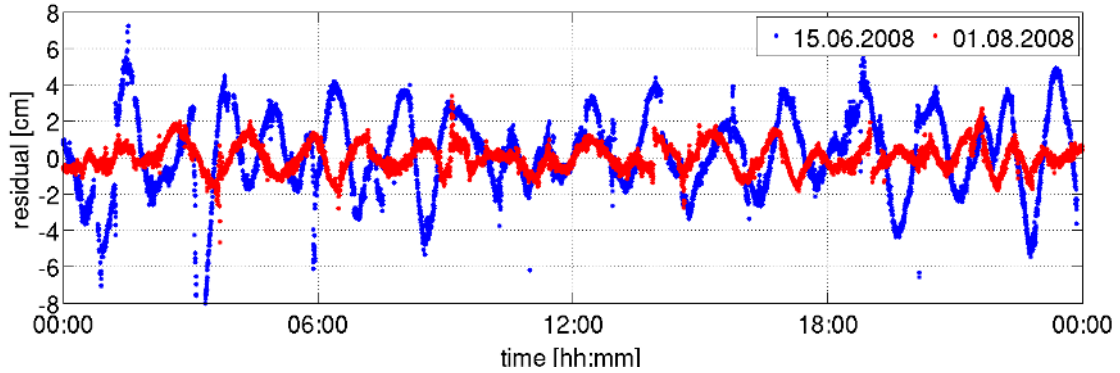


Figure 7.13: GRACE K-band range residuals for 15.06.2008 and 01.08.2008.

as the main driver. If the  $\beta$ -angle is small, the satellite experiences full sunlight and the Earth's shadow on each orbital revolution. Whereas during times of a high  $\beta$ -angle, the illumination of the sun is almost constant for the whole orbit. The sunlight affects different components important for the GPS based positioning. First of all, depending on the  $\beta$ -angle, the satellite crosses different ionospheric regions, either day and night side or sunrise and sunset conditions. This might affect the quality of the GPS observations. A second possibility is higher thermal variations between day and night, which could cause some degradations of the observables. Even a systematic error related to solar radiation in the K-band observations cannot be completely ruled out.

However, the amplitude is in the range of some centimeters, whereas the high frequency noise is far below one centimeter (see section 7.1). The total RMS values for the entire time span are 19.5 mm and 21.8 mm, for IfG and AIUB respectively. However, the daily RMS of the AIUB solution shows less correlation to the  $\beta$ -angle. Hence, the analysis of K-band range residuals proves the high accuracy of both kinematic orbit solutions and further supports the findings of section 7.1.

### 7.3 SLR validation

A widely used method to validate satellite orbits is SLR. The big advantage of using SLR observations is the fact that it represents a completely independent measurement system. This is not only true in terms of the used sensors, on ground as well as on board the satellite, beyond this SLR is based on a different measurement principle, compared to GPS. The basic observable is a two-way run time measurement of a laser pulse, located within the visible band of the electromagnetic spectrum. The ground station emits laser pulses, which are reflected by the retro reflector mounted on the satellite. The pulse is received by a photon detector in the telescope of the ground station. Due to signal attenuation and scattering in the atmosphere only a fraction of the emitted signal is received at the detector, in some cases only a single photon is detected. The station measures the time between emission and reception. Divided by the speed of light this corresponds to the

distance between station position at emission time, the satellite position, and the station position at the time of reception (Hausleitner et al., 2010).

Depending on the station setup, the observation frequency is in the range of a few Hz up to some kHz (Hausleitner et al., 2010). For further computations, as for example orbit validation, it is common practice to use so-called normal points and not the original full rate observation data. Normal points are generated from the full rate data by dividing the satellite pass into bins with a specified size of some seconds (Appleby and Sinclair, 1993). The process includes the computation of range residuals by subtracting a trend function and removal of outliers. Within a bin the observation closest to the mean observation time, corrected for the mean range residual, is then used as the normal point observation. All other measurements within the bin are discarded. The accuracy of normal points is in the range of a few millimeters (Hausleitner et al., 2010).

For validation of kinematic orbits a software package, kindly provided by Harald Wirnsberger, developed at the Institut für Weltraumforschung (IWF) at the Austrian Academy of Sciences (AAS) was used (Wirnsberger et al., 2014). Important to notice is that the software currently does not support direction dependent range corrections. This might lead to slightly different results compared to values published in literature. Normal point data and auxiliary information, such as the reflector offset (summarized in table 7.12) to the center of mass for all satellites, was obtained from the International Laser Ranging Service (ILRS)<sup>1</sup> (Pearlman et al., 2002). The ILRS is a service provided by the International Association of Geodesy (IAG) dedicated to the collection, organization and distribution of SLR observations from SLR stations worldwide, to support geodetic and geophysical research activities. The ILRS also contributes to the observation of Earth rotation parameters or the realization of the ITRF.

satellite	X [m]	Y [m]	Z [m]
CHAMP	0.0000	0.0000	0.2498
GRACE	-0.6000	-0.3275	0.2178
GOCE	2.4076 - 2.3706	-0.0036	0.5580
Swarm	-0.4650	0.5190	0.3030
TerraSAR-X	-1.3077	-0.2121	0.9476
TanDEM-X	-1.3077	-0.2121	0.9476
Jason 1 & 2	0.2170	0.5980	0.6830

Table 7.12: Laser retro reflector offsets for individual missions in the satellite body frame. Taken from ILRS website <sup>1</sup>, except for GOCE (Bigazzi and Frommknecht, 2010).

**CHAMP** Figure 7.14 shows monthly RMS values obtained for the kinematic orbits computed at IfG and AIUB (Prange, 2010). In general, both orbit products perform quite similar with RMS values between 3 and 4 cm. The only exception are some outliers in

<sup>1</sup><http://ilrs.gsfc.nasa.gov/>

2004 and 2007, as well as all months after September 2008, when the main receiver failed and the redundant unit was switched on. This effect was already discussed in section 7.1. In total, the IfG orbit features a RMS of 33.4 mm, which is slightly lower than 36.1 mm obtained for the AIUB orbit. The IfG orbit has a slight offset to the SLR observations of  $-14.8$  mm in contrast to  $-5.5$  mm for the AIUB solution. After the switch to the redundant receiver in 2008, it can be seen that the IfG orbit performs constantly better than the AIUB orbit.

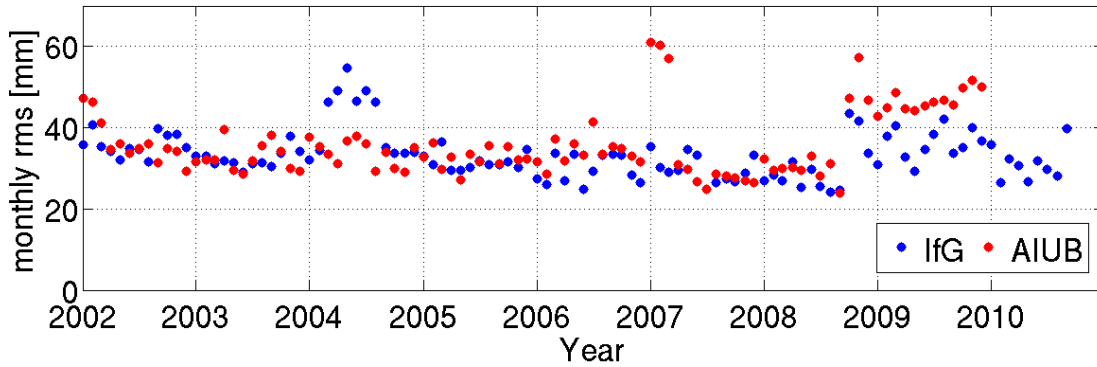


Figure 7.14: Monthly RMS of the SLR residuals for IfG and AIUB kinematic orbits of CHAMP.

**GOCE** SLR validation of the GOCE orbits shows similar results for IfG and AIUB solutions (Bock et al., 2011b). Generally, the monthly RMS is in the range of 2 to 4 cm. From figure 7.15 it can be seen that the RMS increases from 2009 until 2013. This can be attributed to the increase in solar activity during the satellite's lifetime and its high influence on GOCE GPS measurements. In total, the IfG kinematic orbit features a RMS of 24.7 mm, which is lower than 26.8 mm obtained for the AIUB orbit. The value obtained for the AIUB orbit is close to the results published by Bock et al. (2014). Differences in the SLR processing might be the cause for small deviations. However, both solutions show almost no offset with respect to the SLR measurements (IfG: 0.9 mm, AIUB:  $-3.4$  mm). This indicates that center of mass offsets for the GPS antenna as well as the SLR reflector are taken into account consistently.

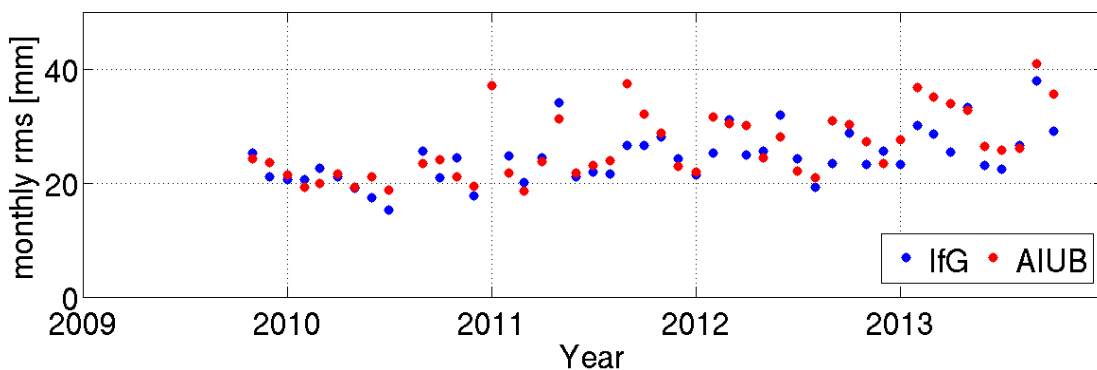


Figure 7.15: Monthly RMS of the SLR residuals for IfG and AIUB kinematic orbits of GOCE.

**GRACE** Figure 7.16 shows the monthly RMS values of SLR residuals for GRACE A and B for IfG and AIUB orbit (Meyer et al., 2016) solutions. It can be seen that the IfG orbit performs better than the AIUB product, throughout the whole time span of more than 13 years. In general, the results obtained for the two GRACE satellites are the best compared to all other validated missions, listed in table 7.13. The total RMS values obtained for the IfG orbit of 24.1 (GRACE A) and 23.2 mm (GRACE B) are smaller than those for the AIUB solution (27.1 and 28.6 mm). Figure 7.16 also shows that the monthly RMS is very stable over the whole time span. No obvious relation to any kind of influence, like the solar activity, can be seen. Only a slight tendency, that earlier years (2002-2005) are marginally worse compared to later years.

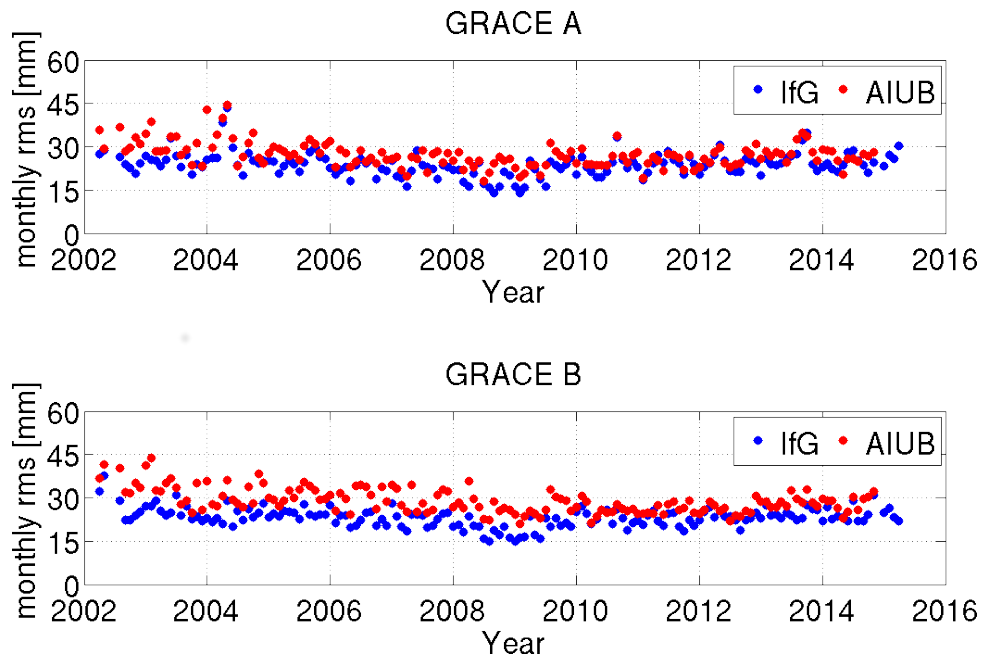


Figure 7.16: Monthly RMS of the SLR residuals for IfG and AIUB kinematic orbits of GRACE A and B.

**Swarm** In case of Swarm, the SLR validation is carried out with three different kinematic orbit products. In addition to the IfG orbits, solutions are available from AIUB (Jäggi et al., 2015) and ESA (van den IJssel et al., 2015). These orbits are the same products already used in section 7.1 for the Swarm orbit comparison.

Figure 7.17 shows monthly RMS values for all three satellites obtained with the three different orbit products. In general, all three satellites perform similar. The same holds for the comparison of the different orbit solutions. Nevertheless, some small differences are present. For all three satellites highest RMS values are obtained for the ESA orbit. This is also evident in the total RMS for each satellite, listed in table 7.13. For Swarm A and B, the IfG orbit performs best. Whereas, for Swarm C the AIUB solution achieves a slightly lower RMS (31.1 mm), than the IfG orbit (31.7 mm). All in all, the SLR validation of Swarm orbits shows that the solutions generated in the frame of this work, applying the raw observation approach feature the same level of accuracy as two independent state-of-the-art solutions.

## 7 Orbit and gravity field validation

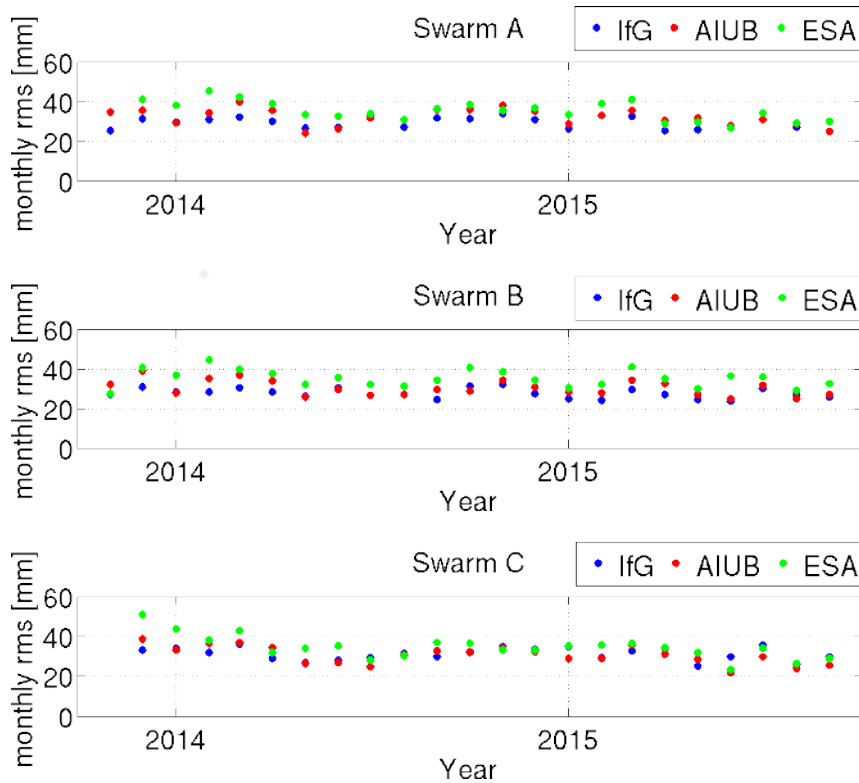


Figure 7.17: Monthly RMS of the SLR residuals for IfG, AIUB and ESA kinematic orbits of all three Swarm satellites.

**TerraSAR-X and TanDEM-X** TerraSAR-X and TanDEM-X are very much the same in terms of design and instrumentation. As a consequence their performance in terms of positioning accuracy is quite similar, as it can be seen from figure 7.18. The SLR validation indicates that TerraSAR-X is slightly superior compared to the results obtained for TanDEM-X. In case of TerraSAR-X a slight degradation of the results from year to year can be seen. Increasing solar activity and thus higher ionospheric activity is a possible explanation for this behavior. This small dependency on the solar cycle is also visible in the results obtained for the GOCE mission. Total RMS values of 25.3 and 31.9 mm, for TerraSAR-X and TanDEM-X respectively, indicate a receiver performance comparable to those of dedicated gravity field missions. The fact that the mean offset to the SLR residuals is small, 3.0 and  $-8.0$  mm, shows that offsets and systematic effects have been modeled accurately.

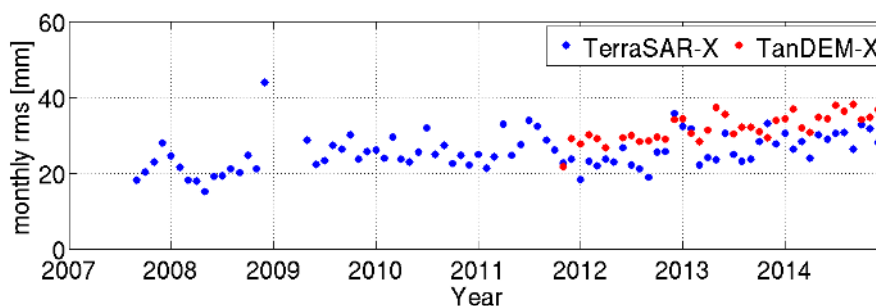


Figure 7.18: Monthly RMS of the SLR residuals for IfG kinematic orbits of TerraSAR-X (blue) and TanDEM-X.

**Jason 1 and 2** The SLR residuals for Jason 1 and 2 result in total RMS values of 36.0 and 49.1 mm, respectively. For Jason 1 this is comparable to results obtained for CHAMP or Swarm, whereas for the higher value for Jason 2 no reasonable explanation could be found. A possible explanation would be errors in the orientation in combination with errors in the used offset values for the GPS antennas and the retro reflector. An indication to justify this hypothesis is the mean offset of SLR residuals. For Jason 1 the mean value is almost zero (3.0 mm), whereas for Jason 2 a mean value of  $-27.3$  mm is obtained. This assumption is also supported by the results obtained with the orbit comparison, shown in section 7.1, where bias and long term periodic effects have been removed. This comparison showed similar results for Jason 1 and 2. Even compared to other missions the performance of Jason 2 was comparable in terms of the RMS. Thus, it seems reasonable that an error in the reflector or antenna offset might be the cause for the higher RMS in the SLR validation.

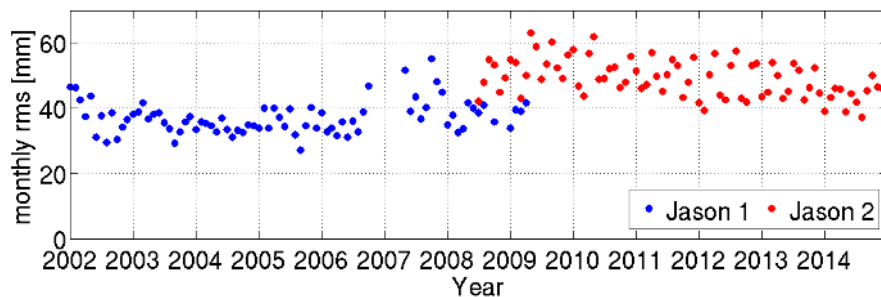


Figure 7.19: Monthly RMS of the SLR residuals for Jason 1 and 2 kinematic orbits.

**Summary SLR validation** SLR is an independent observation method and very well suited for the purpose of orbit validation. The validations described in the previous paragraphs are a good indicator to assess the positioning accuracy obtained with the raw observation approach in an absolute sense. There are only two minor drawbacks. Firstly, SLR observations are a one dimensional observation and thus provide limited information about the orientation of differences. Main contributor to SLR residuals is the radial component. Only for satellites at low altitudes it has been shown that also cross- and along track components can be validated (Bock et al., 2011a). Secondly, the accuracy of SLR observations is in the same regime as it is for GNSS. Thus, SLR residuals do not only represent the error in the GNSS derived orbit position, but also errors introduced by the SLR processing or the SLR observations themselves.

Keeping these two drawbacks in mind leads to the overall conclusion that for all tested missions the achieved 1-D positioning accuracy is in the range of 2 to 4 cm, on average. The RMS for all validated kinematic orbits are listed in table 7.13 along with the mean offsets and the number of used SLR observations. The SLR validation of orbits computed at different institutions shows that the raw observation approach implemented in the frame of this thesis is producing the same or better results. For CHAMP, GRACE, GOCE, and Swarm the IfG solution achieves results comparable to orbits provided by AIUB or ESA.

## 7 Orbit and gravity field validation

orbit	origin	RMS [mm]	mean [mm]	number of observations
CHAMP	IfG	33.4	-14.8	283741
CHAMP	AIUB	36.1	-5.5	266713
GOCE	IfG	24.7	0.9	80666
GOCE	AIUB	26.8	-3.4	81929
GRACE A	IfG	24.1	-1.7	473126
GRACE A	AIUB	27.1	-7.9	464446
GRACE B	IfG	23.2	-0.1	454456
GRACE B	AIUB	28.6	-9.0	451647
Swarm A	IfG	29.8	-4.0	41612
Swarm A	AIUB	32.4	-0.8	41321
Swarm A	ESA	34.7	-5.5	37058
Swarm B	IfG	27.6	-5.4	103126
Swarm B	AIUB	29.7	-2.5	107911
Swarm B	ESA	34.9	-7.9	99995
Swarm C	IfG	31.7	-6.7	42368
Swarm C	AIUB	31.1	-3.3	42934
Swarm C	ESA	34.6	-7.2	39052
TerraSAR-X	IfG	25.3	3.0	400811
TanDEM-X	IfG	31.9	-8.0	122245
Jason 1	IfG	36.0	3.0	452297
Jason 2	IfG	49.1	-27.3	1052439

Table 7.13: Total RMS and mean value of SLR residuals for different orbit solutions.

The mean offset, with respect to the SLR observations, is below 1 cm for almost every tested orbit solution. This is a clear indication that offsets and systematic effects are properly taken into account on both sides, the kinematic orbit estimation as well as the SLR processing. The remaining mean values for some satellites and orbit solutions might also be related to the fact that the software used for SLR validation does not support direction dependent range corrections for the laser retro reflector.

Concerning the different satellite missions, it can be seen from table 7.13 that the GRACE satellites perform best. The worst validation results are obtained for Jason. For Jason, especially Jason 2, the reason for the degraded performance is not clear. It might be related to some errors in the orientation of the satellite in combination with not sufficiently accurate offset parameters for the GPS antenna and the SLR reflector. For Swarm the higher RMS values, in comparison to GRACE and GOCE, are an indication for a slightly worse performance of the used receiver, in combination with the limited number of tracked GPS satellites (max. 8).

## 7.4 Gravity field

Based on the kinematic orbits and the corresponding covariance information, described in section 6.1, gravity field computations have been carried out on a monthly basis. To infer the sought for coefficients of the spherical harmonics expansion, the short arc integral method, described in section 2.4, was used. Due to the large number of available satellites and for sake of computational efficiency, monthly solutions were computed individually for each satellite. To facilitate a combination of different missions, not only the resulting coefficients were stored, but more importantly the resulting normal equations of each month have been archived. This enables the combination of arbitrary months on the basis of normal equations. To guarantee a realistic weighting of different missions or months in a combined solution, the method of variance component estimation has been used to determine proper weights for each individual contributing normal equation.

In order to make all solutions of different satellites comparable and combinable, it is of high importance to make the gravity field processing as consistent as possible. Therefore, the same background models and parameter settings have been used for all missions, as far as possible. Some minor settings had to be changed due to differing observation samplings. Table 7.14 lists the most important background models and parameter settings used for the gravity field estimation.

Model/parameter	Name/value
A priori gravity field model	GOCO03S (D/O 120) (Mayer-Gürr et al., 2012)
Third body forces	JPL DE421 (Folkner et al., 2009)
Solid Earth tides	IERS 2010 (Petit and Luzum, 2010)
Ocean tides	EOT11a (Savcenko and Bosch, 2008)
Pole tides	IERS 2010 (Petit and Luzum, 2010)
Atm. and ocean dealiasing	AOD1B RL05 (Flechtner et al., 2015)
Earth rotation	IERS 2010 (Petit and Luzum, 2010)
max. degree of estimation	60
min. arc length	15 min
max. arc length	45 min
non-conservative forces	accelerometer observations or not considered
empirical parameters	accelerometer bias as polynomial (degree 1) per arc and coordinate axis
covariance information	3x3 epoch covariance matrix in combination with empirical covariance function
Sampling	1, 10, or 30 s

Table 7.14: Settings for the gravity field estimation.

Before the actual gravity field estimation was carried out, several pre-processing steps were done. Such as resampling of auxiliary information like the attitude information to fit the time stamps of the kinematic orbits. All necessary data sets have been synchronized and split into arcs according to the definitions of minimum and maximum arc length. As part of this pre-processing, also an outlier detection was done to remove large outliers from the kinematic orbits, which would possibly disturb the parameter estimation. For outlier removal a reference orbit, mostly a reduced-dynamic orbit, was used and epochs with differences larger than a threshold, e.g. 100 m, have been removed. The outlier detection was only done to remove large outliers and thus no statistical method was applied.

The total number of individual monthly solutions computed from kinematic orbits of the 21 satellites was approximately 1500. The processed data covers a time span of more than 13 years, starting from January 2002 until mid-2015, which corresponds to more than 160 months. The following small thought experiment shall give an impression of the total computational effort necessary to derive a gravity field solution from kinematic orbits, which in turn were derived from raw GNSS observations.

Think of GOCE GPS observations for one month. The receiver was delivering data with a sampling rate of 1 Hz, this results in 86 400 observation epochs for each of the 30 days in one month. On average GOCE was tracking 10 GPS satellites simultaneously and for each tracked transmitter 4 different observation types are available. Finally, this gives a total amount of  $4 \cdot 10 \cdot 86\,400 \cdot 30 = 103\,680\,000$  observations per month. These observations are used to estimate 2 592 000 positions ( $3 \cdot 2\,592\,000$  parameters), 2 592 000 receiver clock errors,  $10 \cdot 2\,592\,000$  ionospheric parameters, and somewhere between 30 000 and 90 000 ambiguities for the phase observations. After the orbit estimation providing  $86\,400 \cdot 30 = 2\,592\,000$  kinematic positions, each consisting of 3 components ( $x, y, z$ ), these 7 776 000 observations are now used to estimate 3717 gravity field parameters. This rather simple example shows nicely the complexity and computational effort needed to finally arrive at the sought parameters.

### 7.4.1 Monthly gravity field solutions

Due to the large number of monthly solutions, it is not possible to address each and every satellite and month individually at this point. The following comparisons to solutions based on similar data or much more accurate gravity field solutions shall give the reader an impression on what is possible with SST-hl data in terms of gravity field recovery. Furthermore, it shall complement the validation of the kinematic orbit solutions based on the concept of raw GNSS observations. In combination with the previously shown orbit comparisons and SLR validation, it gives a pretty good and profound picture of the performance of the raw observation approach and its implementation done in the frame of this work.

### 7.4.1.1 Single mission solutions

A convenient way of getting a first impression of the accuracy of a gravity field solution is to take a look at degree amplitudes. Figure 7.20 shows difference degree amplitudes for some examples of single mission monthly gravity field solutions with respect to the much more accurate static model GOCO05S (Mayer-Gürr et al., 2012). All solutions are for the month January, but not all are for the same year, because there is no month for which all of the satellites are available.

The first thing that gets obvious from figure 7.20 is the fact that not all satellite missions perform in the same way. For example, the worst results in this case are achieved using MetOp A data, only slightly outperformed by data from the SAC-C satellite. For all other missions the comparison is quite heterogeneous and much more difficult to interpret. To fully understand the relative performance of these example months with respect to each other, a few things must be taken into account.

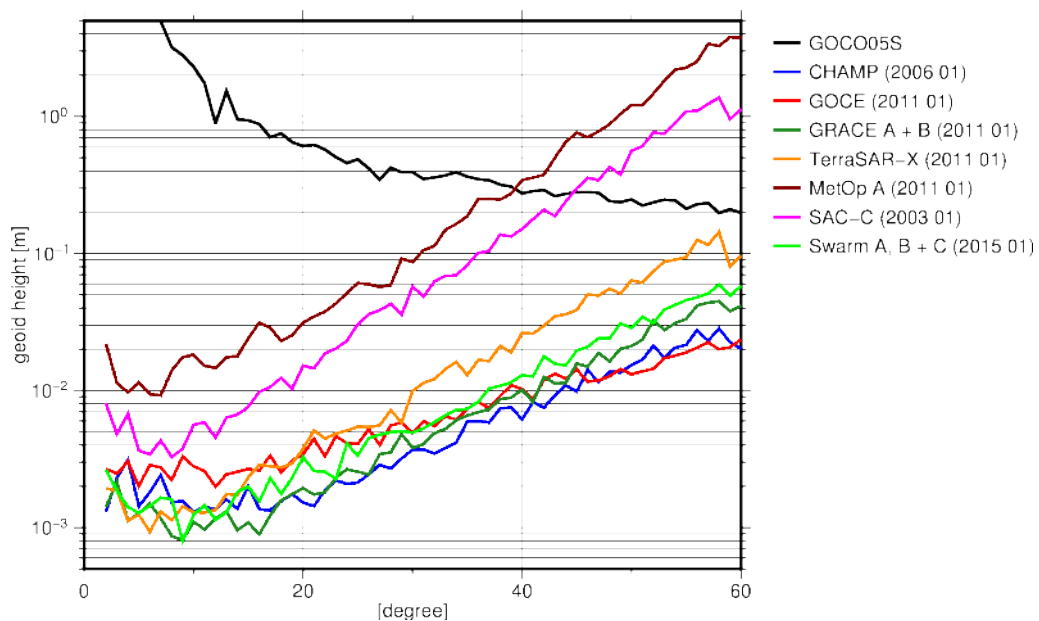


Figure 7.20: Examples of monthly gravity field solutions compared to the static field GOCO05S. Polar gap of  $8^\circ$  taken into account according to the rule described by van Gelderen and Koop (1997).

The basic rule is the lower the curve the better the solution. However, several things are influencing the shape of the curve. The most important factor is the general position accuracy of the kinematic orbit used for the gravity field estimation. For example, if the positioning accuracy of an orbit solution is worse by a factor of two compared to another solution, the difference degree amplitudes will be also shifted by a factor of two upwards, at least in those wavelengths for which the difference is dominated by noise. Almost as important as the positioning accuracy is the altitude of the satellite. Satellite orbits are less affected by gravity with increasing orbital height. This means higher satellites are less sensitive when it comes to measuring the gravity field. This relation determines the steepness of the difference degree amplitude curve. In figure 7.20 it can be seen that the

yellow curve for SAC-C ( $\approx 700$  km orbital height) is much steeper than the red curve, representing the GOCE data ( $\approx 255$  km orbital height).

Some other minor effects contribute to the shape of the curve. A proper weighting scheme for the kinematic orbit positions, depending on the actual quality of each estimated epoch, in combination with a realistic description of the correlations in time can have a positive influence on the resulting gravity field parameters. To minimize the risk of aliasing, the used a priori model should be of good quality. Also the sampling of the observation data has an impact on the quality of the results, even though this is not a strictly linear relation in the sense of the laws of variance propagation - more observations lead to better estimates of the parameters. In this case it is more or less a matter of information content. If the kinematic orbit solution only contains information up to a certain frequency, then the solution will not improve by just increasing the observation sampling (Jäggi et al., 2011a). The last effect that shall be mentioned at this point is the inclination of the orbital plane. An inclination smaller or greater than  $90^\circ$  results in a polar gap, meaning no observations in polar regions. The size of the gap is determined by the deviation of the inclination from  $90^\circ$ . Missing observations in polar regions mainly affect the zonal coefficients of the harmonics expansion. However, it makes the whole estimation of the spherical harmonics coefficients unstable and results in a reduced quality of the gravity field solution in general.

**Ocean variability** To assess the performance of the IfG orbit solutions with respect to other orbit estimation methods a comparison on the level of gravity field results is well suited. For the GOCE mission ESA provided an official kinematic orbit product, which was generated at AIUB. This orbit was already used for the orbit comparison (sec. 7.1) and the SLR validation (sec. 7.3). In this case monthly gravity field solutions based on either the IfG or the AIUB orbit are compared. To see the impact of the orbit product on the gravity field estimates, monthly RMS values over the oceans are used. Geoid heights are computed on a regular grid for each month, reduced by a static gravity field of superior accuracy. Then, land areas are excluded and the RMS of all remaining grid values is computed. Short term ocean and atmosphere variations have been removed within the gravity estimation using the atmosphere and ocean dealiasing product AOD1B-RL05 (Flechtner et al., 2015). Hence, there should be no signal over the oceans, at least no signal with amplitudes large enough to be visible in the SST-hl solutions. Thus, any difference between a monthly solution and a highly accurate static gravity field can be considered as observational noise coming from the orbit estimation.

Figure 7.21 shows monthly geoid height RMS values derived from the two different solutions, based on the IfG or the AIUB orbits. As reference, the static gravity field GOCO05S is subtracted and to suppress high frequency noise a Gaussian filter with 500 km radius is applied. The comparison clearly demonstrates the reduced noise content of the IfG solutions in contrast to those based on AIUB orbits. This further supports the

## 7 Orbit and gravity field validation

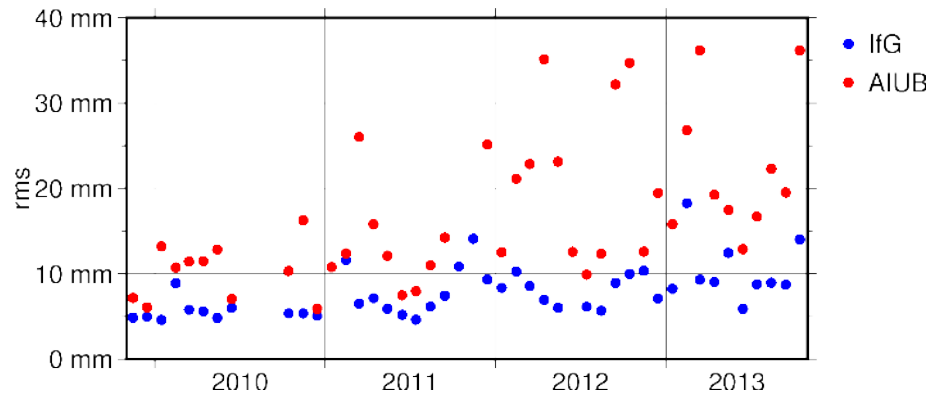


Figure 7.21: Geoid height RMS of GOCE monthly solutions over the oceans, for solutions derived from IfG (blue) and AIUB (red) orbits. 500 km Gaussian smoothing applied.

findings of section 7.1 and 7.3, which already indicated a better performance of the IfG orbit.

The same analysis was carried out using GRACE orbits. The IfG results are again compared to gravity field results achieved using a kinematic orbit computed at AIUB. In principle, the monthly gravity fields were computed using the same settings, except for the orbit product. In this case the AIUB solution was only available with 30 s sampling, opposed to the 10 s interval used for the IfG orbit. This means that the monthly estimates based on the IfG orbit contain three times as much observations as those based on the AIUB orbit. However, an investigation for which the IfG orbit was reduced to the same sampling showed that this produces the same or even better results compared to the 10 s sampled orbit. Some example months are shown in figure 7.22. In general, the quality of the solutions is pretty stable in time, except for some months for which less data is available. A slight degradation of the results is also visible for the year 2002, which may be attributed to the reduced amount of data during the first months of the mission. Another drawback for these months is the fact that for this time frame only 30 s sampled GPS clock corrections are available. All in all, the GRACE comparison also supports the findings of section 7.1 and 7.3, that the IfG orbit outperforms the AIUB orbit.

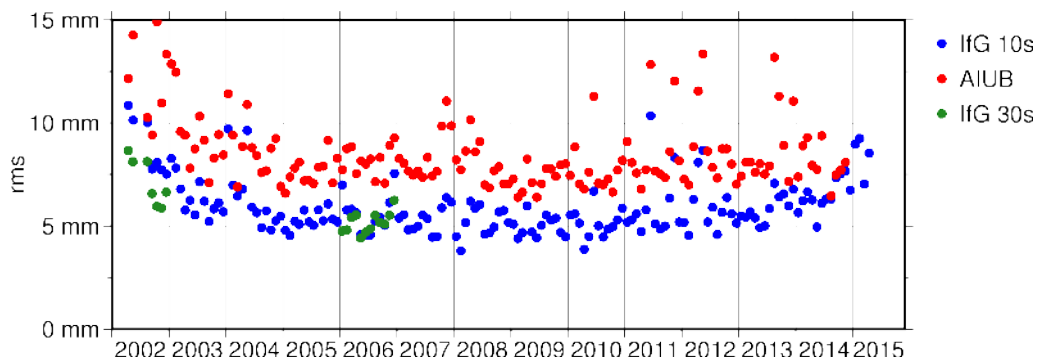


Figure 7.22: Geoid height RMS of GRACE monthly solutions over the oceans, for solutions derived from IfG (blue) and AIUB (red) orbits. Exemplary results based on 30 s sampled IfG orbits are shown in green. 500 km Gaussian smoothing applied.

### 7.4.1.2 Combined solutions

As already mentioned in section 6.1.2, kinematic orbits were produced for 21 satellites in total. All these orbits, except for FORMOSAT-3/COSMIC, were used to generate combined monthly gravity field solutions. On the basis of normal equations, applying variance component estimation, they were combined to get the best possible time series of monthly gravity field estimates, subsequently denoted as *IfG-all*. FORMOSAT-3/COSMIC orbits were not included in the combined gravity field analysis, due to their low accuracy, the huge number of outliers and gaps, and the low inclination of the satellite orbit. Investigations also revealed that their contribution to a combined solution is generally below the perception threshold. The number of used satellites varies from month to month and is at the minimum two and at the maximum ten. In order to assess the possible performance of a SST-hl solution if no dedicated gravity field mission is available, a separate time series was generated by only combining data from non-dedicated missions. This means no data from CHAMP, GRACE, or GOCE was used. This solution will be subsequently denoted as *IfG-nonD*.

**Ocean variability** Figure 7.23 shows the monthly geoid height RMS over the oceans for the two solutions *IfG-all* and *IfG-nonD*. As it can be expected, the time series based on all available data performs considerably better than the one without data from dedicated satellite missions. Furthermore, the *IfG-all* time series provides almost the same accuracy throughout the whole time span. Whereas the *IfG-nonD* solution is significantly worse for the years 2002 until mid-2007. This corresponds to the time frame for which only data from Jason 1 and SAC-C is available. A similar situation occurs for December 2008 until April 2009. For these five months only data from Jason 1 and 2, MetOp A, and SAC-C is available. The critical mission which causes the drop in the RMS, is TerraSAR-X. Additionally, an increase in the RMS can be seen after the year 2003. This is related to a degradation of the positioning performance of SAC-C. All in all, it can be said that as long as a mission with sufficiently good positioning performance is available, it is possible to achieve accuracies below 1 cm geoid height with data from non-dedicated satellites and applying a Gaussian filter with a radius of 500 km.

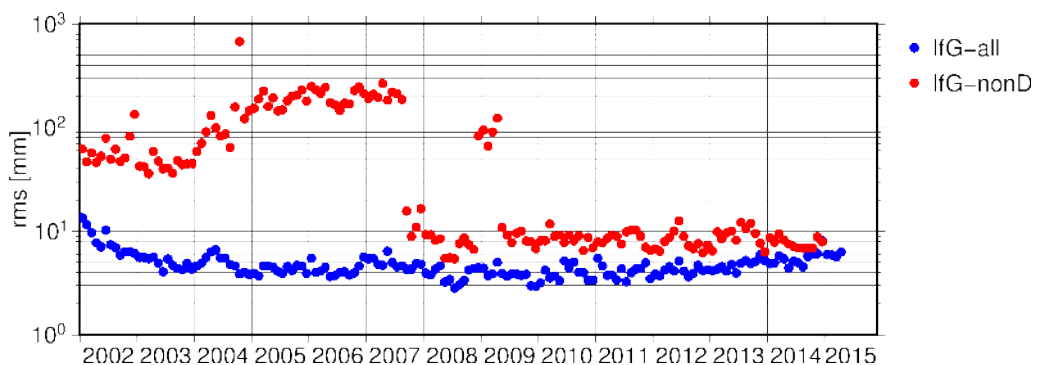


Figure 7.23: Geoid height RMS of *IfG-all* (blue) and *IfG-nonD* (red) over the oceans. 500 km Gaussian smoothing applied.

**Gridded RMS** In order to assess the spatial distribution of errors in the time series it is beneficial to compute RMS values on a geographic grid. Therefore, each monthly solution is evaluated on a regular grid relative to a static reference gravity field. This gives a time series of differences between the monthly solution and the reference field for each grid point. Now the RMS can be computed for each grid point. Figure 7.24 shows the temporal RMS on a  $1^\circ \times 1^\circ$  grid for the time frame February 2003 until December 2014. On the left-hand side it shows the RMS derived for the *ITSG-Grace2014* solution and on the right-hand side the results obtained for the SST-hl only solution *IfG-all*. Both gravity field time series have been filtered with a Gaussian filter (radius 500 km) to suppress short wavelength noise. The RMS in *ITSG-Grace2014* is much lower and smoother as for *IfG-all*. This can be expected, due to the superior measurement accuracy of the GRACE K-band instrument. Nevertheless, it shows that in general the error of the SST-hl only solutions is somewhere around 5 mm, at spatial scales above 500 km. Areas with higher variability are also reflected in the SST-hl solutions, e.g. Greenland, the Amazon River, or western Antarctica. Size, shape and amplitude of these visible variations correspond very well with those seen in the *ITSG-Grace2014* result. As the monthly solutions were only reduced by a static reference field (GOCO05S), this is already a first indication that at least large geophysical signals are contained in the SST-hl solution.

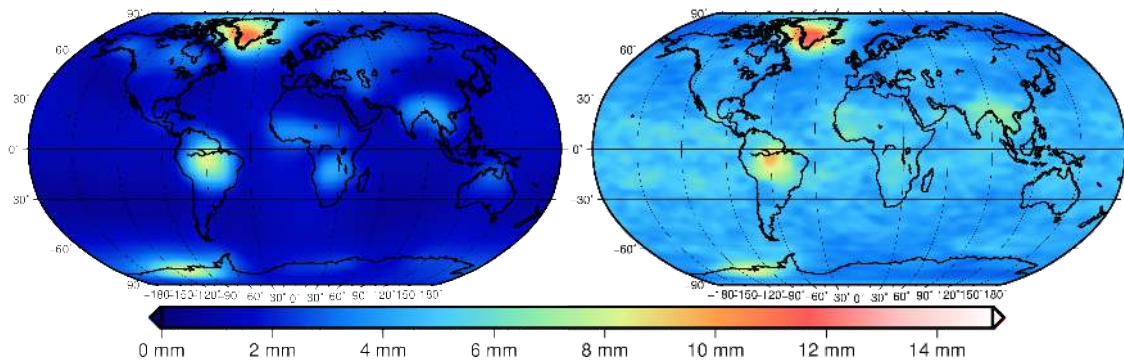


Figure 7.24: Temporal RMS of geoid heights from *ITSG-Grace2014* (left) and *IfG-all* (right). 500 km Gaussian smoothing applied. Time span: 02.2003 - 12.2014.

**Degree amplitudes** As already done in figure 7.20, degree amplitudes are an informative way to look at different gravity field solutions. In order to compare the two SST-hl solutions *IfG-all* and *IfG-nonD* to the reference *ITSG-Grace2014*, difference degree amplitudes for all available months are plotted as color coded values in a matrix. Figure 7.25 shows the difference degree amplitudes for all three solutions with respect to the static gravity field GOCO05S. Columns represent the spherical harmonic degree and rows are the months, starting from January 2002.

Figure 7.25 nicely demonstrates the different accuracy levels of these three solutions. On the one hand, *ITSG-Grace2014* is obviously much more accurate than the solutions based on SST-hl data. On the other hand, there are several missing months (white lines), which is not the case for *IfG-all* and *IfG-nonD*. Comparing the two SST-hl time series reveals the same fact as already noticed in the ocean variability (figure 7.23): The results based

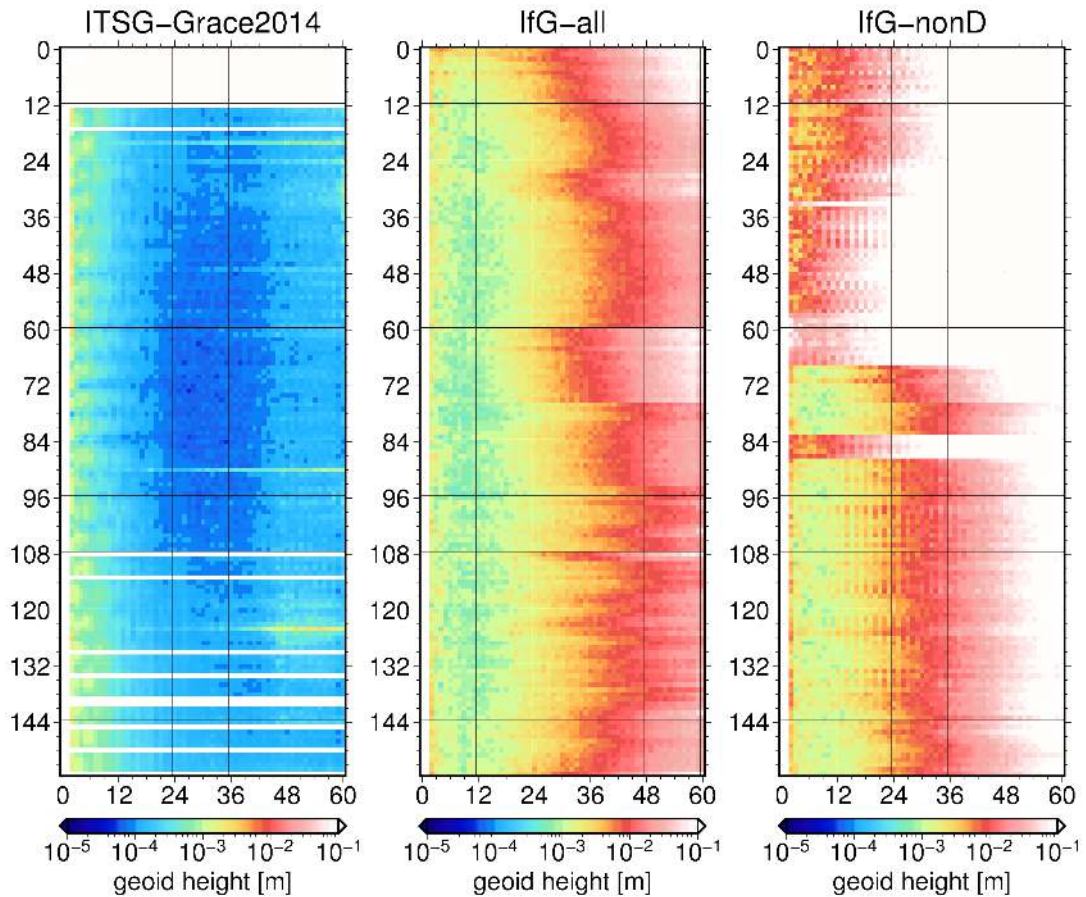


Figure 7.25: Monthly difference degree amplitudes for *ITSG-Grace2014* (left), *IfG-all* (middle), and *IfG-nonD* (right) with respect to *GOCO05S*. Columns are the spherical harmonic degree, rows are the months since January 2002.

on non-dedicated satellites are significantly worse for the first six years up to the point when TerraSAR-X became operational. Another interesting feature is visible in the time series *IfG-all*. For months 60 to 75, this corresponds to January 2007 until April 2008, a clear degradation is visible. Especially higher degrees, above 20, are consistently worse compared to months before or after this time frame. The reason for this degradation can be found in the missing high-rate GPS clock products. For this time frame only 30 s sampled clock information was used in the kinematic orbit processing, opposed to the 5 s corrections used by default. This effect nicely demonstrates the relation between the kinematic orbit quality and the estimated gravity field. Although 10 s sampled GPS observations have been used, like for all other months, and the general observation quality is assumed to be unchanged, the information content of the orbit solution is reduced. The lower rate of the GPS clock correction, which is interpolated to the observation sampling, introduces an additional error for epochs in between the 30 s interval. This error exceeds the original measurement noise and diminishes the orbit quality and thereby also the gravity field results, already shown by (Bock et al., 2009a).

### 7.4.2 Mass variations

**Global trend and annual signal estimation** One of the major goals of this thesis is to assess the possibility of measuring mass variations by using SST-hl observations. The previous section introduced the final gravity field results based on kinematic orbits of dedicated and non-dedicated satellites. The next step is now to analyze to which extent it is possible to infer mass variations from these time series of monthly gravity field solutions.

First of all, the whole Earth shall be considered. Therefore, the time series is used to estimate trend and annual signals on a regular grid. This is done by computing the geoid height from each monthly solution for each grid point. Subsequently, a linear trend and an annual sine and cosine function is fitted to the time series by means of least squares adjustment. Again it is important to have some sort of reference to validate findings based on the SST-hl solutions. The chosen reference is once more the *ITSG-Grace2014* time series. Figure 7.26 shows the results obtained for the reference (left column) and the SST-hl solution (right column). From top to bottom trend, total amplitude, sine, and cosine amplitude are plotted.

It is again obvious that the SST-hl solution is noisier than the reference. This can be seen very nicely for example over the Pacific Ocean. However, the general agreement is pretty good. In the trend estimate (top row) prominent areas where a trend signal can be expected are visible. Regions like Greenland and western Antarctica, where mass loss occurs due to melting of ice sheets, are clearly visible in the *IfG-all* results. These patterns are confirmed in size, shape and magnitude by the estimates derived from *ITSG-Grace2014*. The same holds in principle for the total amplitude of the annual signal or the sine and cosine contribution. These plots show areas where seasonal variations affect the Earth's gravity field. For example, the region with highest amplitudes is South America, where the changes in the hydrological cycle due to summer and winter season are large. In Africa the time shift between regions north and south of the equator can be seen especially in the amplitude of the sine component. Another well resolved process is the monsoon, present in India and south-east Asia, creating a pronounced seasonal signal. In general, it can be said that the SST-hl solution corresponds reasonably well with the results obtained from the reference solution *ITSG-Grace2014*. The RMS of differences between reference and SST-hl solution can be used as an indicator for the agreement between the two results. For the trend an RMS of 0.2 mm is achieved. The RMS values for sine and cosine estimates are 0.6 and 0.9 mm. These values demonstrate the good agreement between the solution purely based on SST-hl and the reference.

## 7 Orbit and gravity field validation

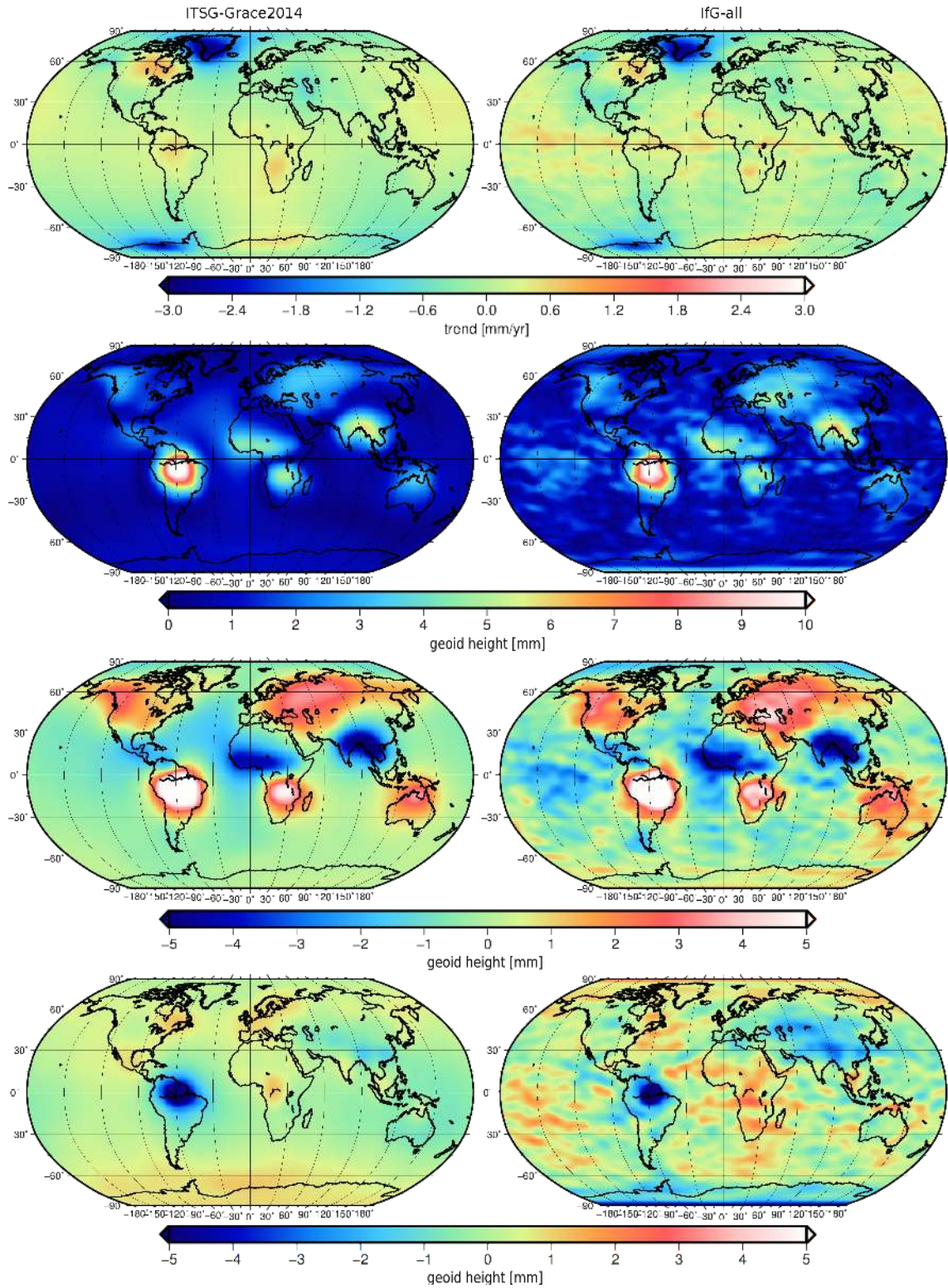


Figure 7.26: Trend (top), annual amplitude (second row), annual sine (third row), and annual cosine (bottom) estimated from ITSG-Grace2014 (left) and *IfG-all* (right), in geoid heights. 500 km Gaussian smoothing applied.

**Selected regions** To see the agreement between *IfG-all* and a reference solution, a closer look at some selected regions is helpful. Up to now, *ITSG-Grace2014* was used as the only reference solution. To demonstrate the feasibility of this solution, the *CSR-RL05* (Bettadpur, 2012) time series is added as a second reference. These monthly gravity fields are computed at CSR using the same GRACE K-band observations as used for *ITSG-Grace2014*.

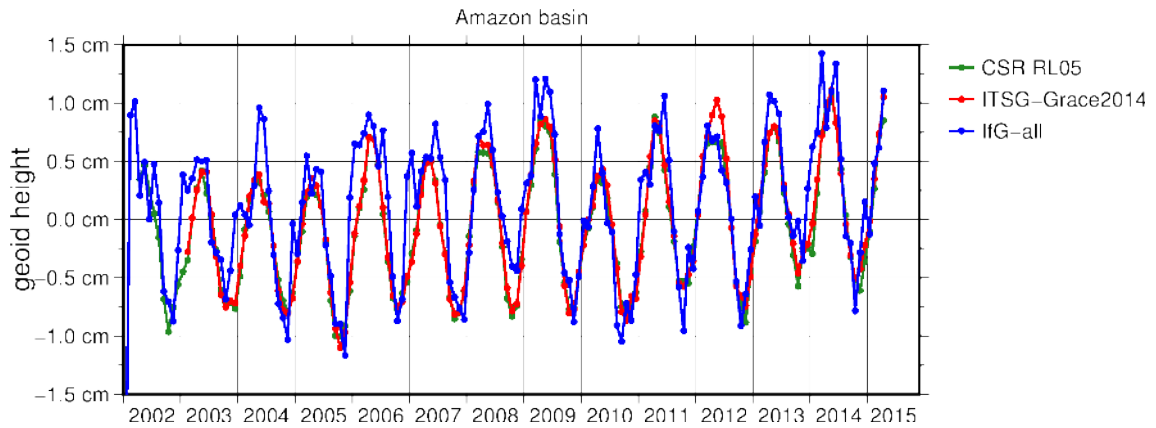


Figure 7.27: Monthly area mean values for the Amazon River basin from the time series *IfG-all* (blue), *ITSG-Grace2014* (red), and *CSR-RL05* (green).

To analyze the variations in a certain region, the geoid height is computed on a regular grid within the area of interest. The static part of the gravity field is removed by subtracting the model GOCO05S and to suppress small scale noise, a Gaussian filter with a radius of 500 km is applied. The grid values are then averaged for the whole region taking into account the size of each grid cell. This finally results in a time series of area mean values given in a monthly interval. Figure 7.27 displays the results obtained from *IfG-all* and the two reference models for the Amazon River basin. First of all, the figure shows that *ITSG-Grace2014* and *CSR-RL05* agree very well. In fact, the two curves (red and green) are almost identical. More important is the fact that the blue curve also matches with these two lines. The *SST-hl* solution not only recovers the annual gravity variation in the Amazon basin. It also shows the inter-annual differences. For example, the difference between the maxima in 2009 and 2010 is clearly resolved by the *SST-hl* time series. It must be admitted that the noise in the blue curve is definitely higher and it contains some outliers or ‘bad’ months, but in general the agreement is good.

The Amazon River basin features the highest annual variation worldwide. The region with the biggest trend is definitely Greenland. Figure 7.28 shows the same area mean time series for the whole area of Greenland. The negative trend in geoid height, caused by ice melt, is clearly visible. Also for this region a good agreement between *IfG-all* and the reference time series is obtained. Except for early years, 2002 and 2003, in which a small offset seems to be present in the *SST-hl* solution. The reason for this systematic offset is not known. Nevertheless, after the year 2004 a long term trend estimation for whole Greenland would produce the same results as it would be the case with any of the two reference solutions.

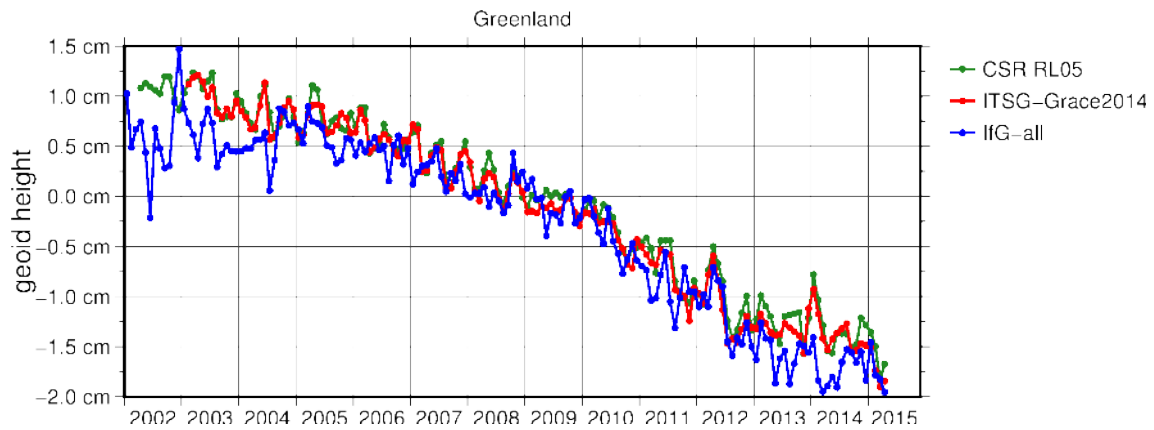


Figure 7.28: Monthly area mean values for Greenland derived from the time series IfG-all (blue), ITSG-Grace2014 (red), and CSR-RL05 (green).

Figure 7.29 shows some other regions or river basins for which the analysis of the *IfG-all* time series reveals a good agreement to the reference solutions. The first two rows in figure 7.29 depict some areas with positive or negative trends. The negative trend in west Antarctica, already visible in figure 7.26, is caused by deglaciation due to the global climate change (Cazenave and J. Chen, 2010). In contrast to this, the small positive trends for Scandinavia and northern Canada can be attributed to land uplift after end of the last ice age, denoted as Glacial Isostatic Adjustment (GIA) or post-glacial rebound (Cazenave and J. Chen, 2010). During the last ice age large ice caps in the northern hemisphere have pressed the underlying crust deep into the Earth's mantle. After the ice age the glaciers melted and the mass load on the crust disappeared. Now the crust performs an upward motion until it reaches its original position. This process is still ongoing and reaches uplift rates of some millimeters per year. For Canada the effect of GIA is stronger than for Scandinavia. Nevertheless, the *IfG-all* time series does not reproduce the results of the reference solution satisfactory in both cases. The reason for the different slope of the curve for Canada is not understood yet. In case of Scandinavia the ratio between the size of the region and the signal amplitude might be insufficient to reliably observe the ongoing GIA process.

The top right plot shows the time series for the Caspian Sea. This time series is rather special. It shows a positive trend until 2005 and a negative trend thereafter. In addition, the Caspian Sea features a small but clearly visible annual signal. Both, trend and annual signal, are recovered by the SST-hl solution. The annual signal is related to the change of the seasons between winter and summer and the negative trend after 2005 reflects a drop of the water level (Arpe et al., 2012). In addition to the diverse behavior over time, the Caspian Sea is the smallest of all regions shown, with an extent of  $\approx 400\,000\text{ km}^2$ . Thus, it is even more impressive that the geophysical signal can be seen in the SST-hl solution.

The plots in row three and four show the time series of area mean values for the Danube river, the river basins of Brahmaputra, Ganges and Irrawaddy, the combined drainage areas of Okavango and Zambezi, and the catchments of Lake Chad, Niger and Volta. In all four examples the annual variation related to the seasons is recovered by the SST-hl

solution. Even for a basin as small as the Danube River ( $\approx 800\,000\text{ km}^2$ ) the results fit to the reference curves.

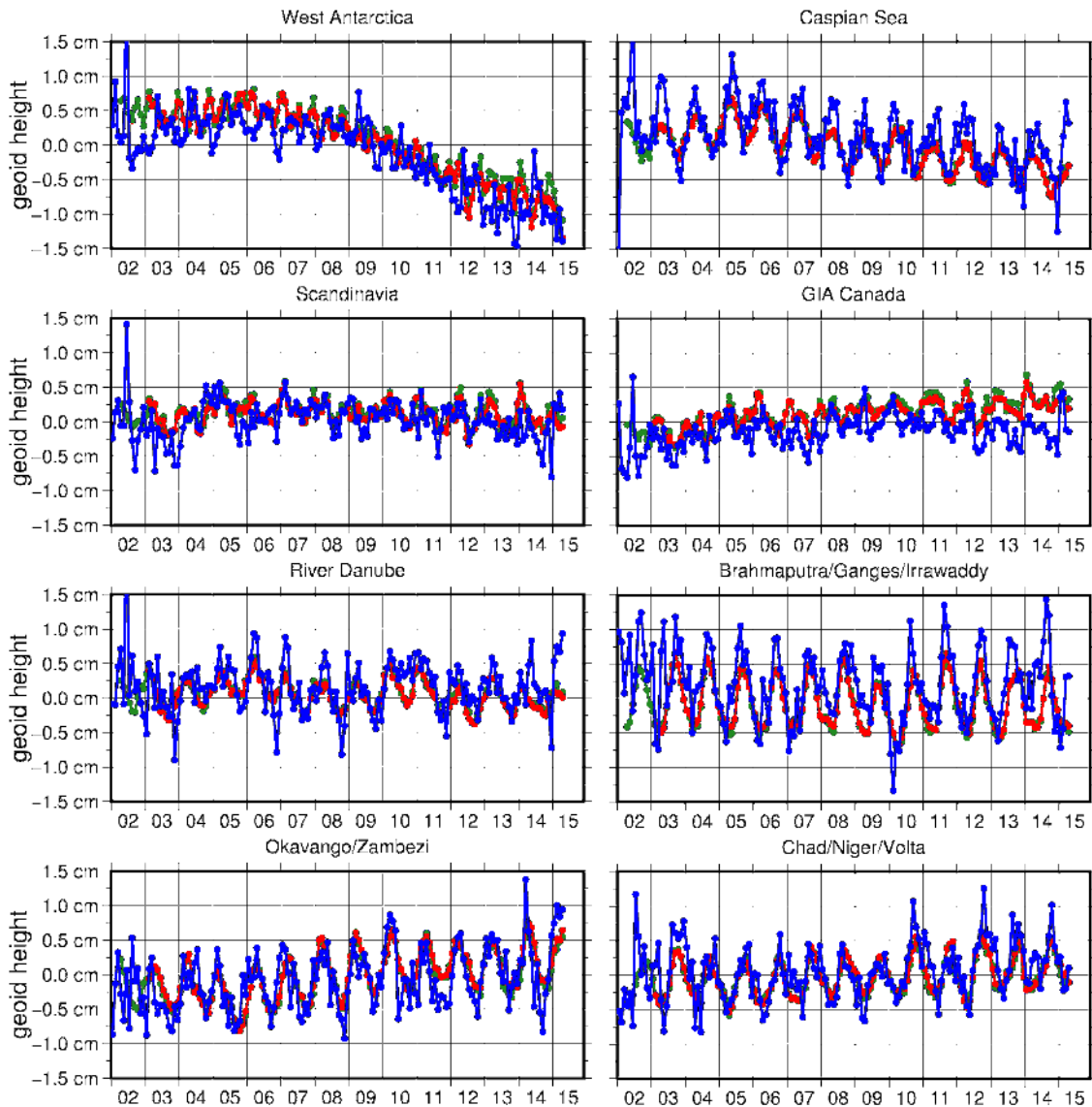


Figure 7.29: Monthly area mean values for some example regions derived from the time series *IfG-all* (blue), *ITSG-Grace2014* (red), and *CSR-RL05* (green).

To get an overall picture for which regions the signal is recovered or not, the correlation between time series derived from *IfG-all* and *ITSG-Grace2014* was computed for the 56 largest river basins worldwide. The definition of the river basins was taken from the Global Runoff Data Center (GRDC)<sup>1</sup>. These 56 basins are all larger than  $300\,000\text{ km}^2$ . Figure 7.30 shows the resulting correlation coefficient color coded for each basin. For a large number of rivers a correlation above 0.5 is achieved. However, there are also some large basins for which the correlation is small or even zero. In general, basins with a good correlation are situated in those areas with a sufficiently large annual signal. These regions correspond to those areas which are visible in the global amplitude plot in figure 7.26. Five major regions can be identified: South America, North America, Africa

<sup>1</sup>Global Runoff Data Centre (2007): Major River Basins of the World / Global Runoff Data Centre. Koblenz, Germany: Federal Institute of Hydrology (BfG).

(north and south of the equator), the monsoon region in Asia, and northern Eurasia. In other regions the annual signal or the area of the river basin is too small, as for example Australia, Eastern Asia, South Africa, and Europe (except for the Danube).

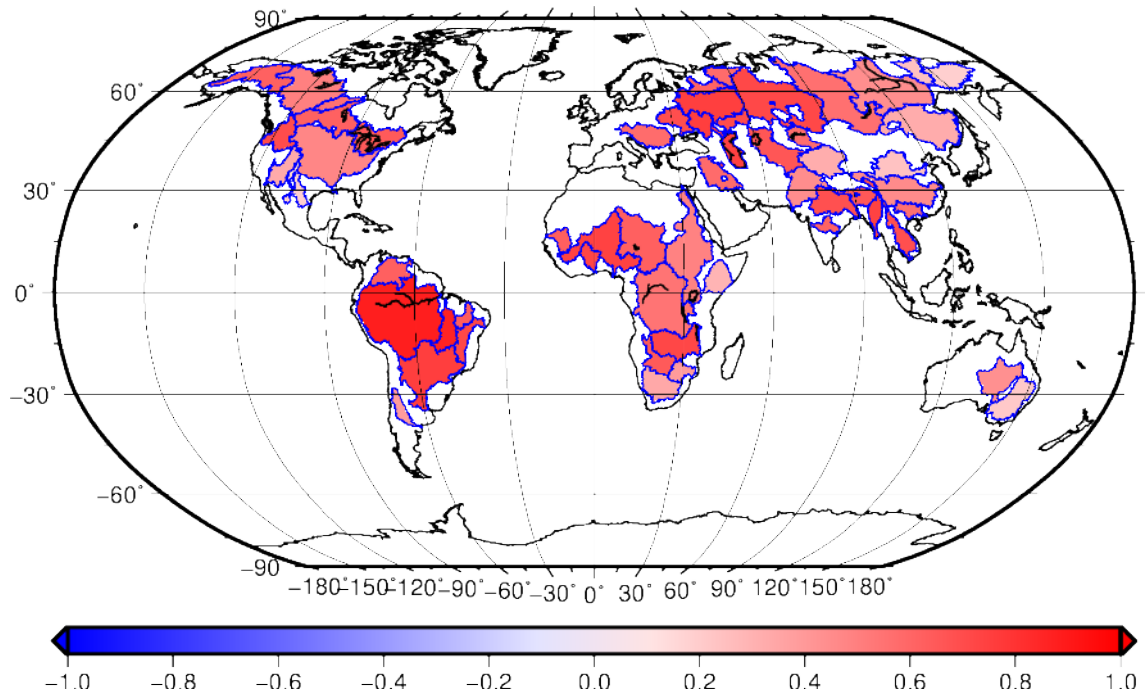


Figure 7.30: Correlation between IfG-all and ITSG-Grace2014 monthly gravity field models for the 56 largest river basins worldwide.

The mentioned examples of different river basins and other regions clearly demonstrate the ability to recover time variable gravity signals from the SST-h1 solution. In fact, the generated time series are noisier than those derived from GRACE K-band observations and have a lower spatial resolution. However, the presented results for the Danube River and the Caspian Sea suggest that the lower limit for areas to be recovered is in the range of 500 000 km<sup>2</sup>. Besides the restriction to large areas, the size of the trend or annual signal is equally important. In general, the key factor is the signal to noise ratio. This means, a large signal is observable even for smaller regions, whereas small signals are only detectable for large areas.

## 8 Conclusions

Highly accurate knowledge of the satellite position is important for almost every scientific application dealing with space borne observations. In this context GNSS is playing an increasingly important role. The key features which makes the technology superior compared to other existing methods are its high availability, reliability, accuracy, and the global coverage. Furthermore, the needed equipment is lightweight, small, and has a low power consumption. On top of this technical and operational advantages, space qualified GNSS receivers may be considered as cheap in contrast to the overall costs of a satellite mission. All together, this led to the fact that within the last two decades GNSS became the most popular technology for precise satellite positioning. In addition, GNSS not only provides position information but also highly accurate timing information, which might be equally important for some applications.

Besides scientific satellite missions, an increasing number of commercial satellites are equipped with GNSS receivers. This trend will certainly continue as more and more commercial operators are planning to launch a large number of satellites for different purposes. Especially the trend towards small and cheap micro satellite constellations will further increase the number of space borne GNSS equipment.

This work presents a new and straightforward approach for precise kinematic orbit determination based on raw GNSS measurements. Unlike existing methods, observations are used as they are observed by the receiver. No a priori combination or modification of the measurements is performed to reduce errors or influences. Instead, all present effects are modeled in a least-squares adjustment by either estimating it as parameter or subtracting known corrections. The process is complemented by a sophisticated weighting scheme to fully exploit the accuracy of the observations. Measurement weights are not only determined by sophisticated azimuth and elevation dependent accuracy maps but also reassessed within the iterative least-squares adjustment by means of variance component estimation. This approach provides the advantage that outlier detection is an embedded part of the parameter estimation. Hence, there is no need for screening the observations in advance.

Two major systematic effects have been investigated in detail within this work. Firstly, ACVs for receivers and transmitters have been estimated and analyzed. For both cases ACVs are set up as additional parameters in the least-squares adjustment, either as spherical harmonics or radial basis functions. This enables an azimuth and elevation dependent representation on the receiver as well as on the transmitter side. For receivers,

## 8 Conclusions

azimuth and elevation dependent variations are rather common, whereas for transmitters this is not the case. Validation results proofed that a detailed modeling of transmitter characteristics improves the final positioning results. In addition, not only variations for precise phase observations were estimated. Separate corrections for code observables have been included into the whole process in order to fully exploit the information contained in code measurements. Despite their reduced accuracy, code observations do contribute to the overall solution. Especially systematic errors contained in code measurements may distort the quality of the solution. In fact, without code measurements the system could not be solved.

Secondly, the ionospheric influence on GNSS signals plays an important role if highest accuracies are envisaged. The presented approach includes 1<sup>st</sup>, 2<sup>nd</sup>, and 3<sup>rd</sup> order terms in the STEC parametrization. Additionally, the effect of bending is considered by applying a correction to the observations. Apart from the parametrization and correction of ionospheric influences, a weighting scheme has been developed in the frame of this work to take strong disturbances into account. Especially for the satellite mission GOCE, observation weighting based on ionospheric indices significantly improved the quality of the orbits. Systematic effects, which showed up in derived gravity field solutions, have been removed to a large extent.

The presented approach has been used to produce kinematic orbits for 21 different satellites. Intensive quality checks by comparing to third party orbit solutions, SLR validation, and the computation of gravity field solutions, clearly shows that the method is competitive. The comparison to products generated with state-of-the-art processing software revealed a similar or slightly better performance of the presented raw observation approach. For example, SLR validation of GRACE B orbits gives a 19% lower RMS value for the IfG solution compared to an orbit from AIUB. All validations shown within this work, convincingly demonstrate the ability of the raw observation approach to produce kinematic orbits of highest accuracies. Results from GRACE showed that the high-frequency noise in orbit positions is approaching the basic measurement accuracy of millimeters for GNSS phase observations.

Concerning the different satellite missions that have been used, the analysis revealed some key aspects to achieve highest accuracies. In addition to the receiver quality, the characteristics of the antenna and the satellite itself contribute greatly to a good or bad positioning performance. Precise knowledge of the satellite attitude is necessary to correctly estimate and apply ACVs and a high quality antenna reduces signal distortions produced by the satellite structure.

All satellites have been used to produce gravity field solutions. The data was combined to get the best possible monthly estimates for a time period covering more than 13 years without interruptions. The validation of this time series against much more accurate monthly solutions, based on GRACE K-band measurements, showed that it is possible to observe gravity variations in time. Trend and annual signals are seen in the time

series for areas as small as the Danube river basin or the Caspian Sea. Although signals are recovered for these regions, it is not possible for others, even larger areas, due to a small signal amplitude. In general, it can be said that it is possible to observe time variable components of the gravity field solely by using SST-hl data. In view of the trend towards more and more LEO satellites being equipped with geodetic GNSS receivers the technology might be considered as alternative or at least as supplement and backup to other methods to observe variations of the Earth's gravity field.

Apart from ever more satellites being equipped with geodetic GNSS receivers, the method of SST-hl will certainly benefit from the general evolution of GNSS. Future space borne receivers will not only track GPS signals, but also those of GLONASS, Galileo, and Beidou. This will dramatically increase the number of tracked satellites per epoch and thus also the achievable positioning accuracy. In addition to tracking more than one GNSS, the ongoing modernization brings new frequencies to be used. On the one hand, this will further increase the amount of observations. On the other hand, it will enable a better estimation of the ionospheric influence. Both aspects will contribute significantly to an improved accuracy. However, inclusion of new GNSS also brings some disadvantages. Due to inconsistencies between different systems new parameters will be introduced. As for example, each system realizes its own time frame. Although they are closely related, it will be necessary for high accuracy applications to estimate the offset between different time frames properly. Apart from timing, observation biases will become important to facilitate the usage of different observations within a common least-squares adjustment. The presented approach based on raw GNSS observations is well suited to directly combine different systems. Observation equations are simply extended for system specific or offset parameters and then used together in the least-squares adjustment. Due to the individual treatment of each observation this will open up new opportunities for investigating specific aspects of a particular observation type or a specific GNSS. A lot of research will be necessary to achieve an optimal combination of modernized systems. Nevertheless, LEO orbit determination, in particular kinematic orbit estimation, will certainly benefit and thus play an increasingly important role for future satellite missions.

## Bibliography

- Alonso, C. and Hofmann, C. (Aug. 2002). *SAC-C Mission*. Comisión Nacional de Actividades Espaciales. Buenos Aires. URL: <https://www.conae.gov.ar/satelites/sac-c/SAC-CPUBLI200208.pdf>.
- Altamimi, Z., Collilieux, X., and Métivier, L. (Aug. 2011). "ITRF2008: an improved solution of the international terrestrial reference frame." In: *Journal of Geodesy* 85.8, pp. 457–473. DOI: [10.1007/s00190-011-0444-4](https://doi.org/10.1007/s00190-011-0444-4).
- Anderson, D. (Mar. 1973). "A theoretical study of the ionospheric F region equatorial anomaly." I. Theory." In: *Planetary and Space Science* 21.3, pp. 409–419. ISSN: 00320633. DOI: [10.1016/0032-0633\(73\)90040-8](https://doi.org/10.1016/0032-0633(73)90040-8). URL: <http://linkinghub.elsevier.com/retrieve/pii/0032063373900408>.
- Appleby, G. M. and Sinclair, A. T. (1993). "Formation of on-site normal points." In: *Eighth International Workshop on Laser Ranging Instrumentation*. Cambridge: Goddard Space Flight Center, pp. 19–25. URL: <http://ntrs.nasa.gov/search.jsp?R=19940011119>.
- Arpe, K., Leroy, S. A. G., Lahijani, H., and Khan, V. (Jan. 2012). "Impact of the European Russia drought in 2010 on the Caspian Sea level." In: *Hydrology and Earth System Sciences* 16.1, pp. 19–27. ISSN: 1607-7938. DOI: [10.5194/hess-16-19-2012](https://doi.org/10.5194/hess-16-19-2012).
- Ashby, N. (2003). "Relativity in the Global Positioning System." In: *Living Reviews in Relativity* 6. ISSN: 1433-8351. DOI: [10.12942/lrr-2003-1](https://doi.org/10.12942/lrr-2003-1).
- Banville, S., Santerre, R., Cocard, M., and Langley, R. B. (2008). "Satellite and Receiver Phase Bias Calibration for Undifferenced Ambiguity Resolution." In: *Proceedings of the 2008 National Technical Meeting of The Institute of Navigation*. San Diego, CA, pp. 711–719. URL: <http://citeseerx.ist.psu.edu/viewdoc/download?doi=10.1.1.567.95&rep=rep1&type=pdf>.
- Bartusch, M., Hajnsek, I., Janoth, J., Marschner, C., Miller, D., Moreira, A., Sparwasser, N., and Zink, M. (Nov. 2009). "TanDEM-X Die Erde in drei Dimensionen." In: pp. 1–24. URL: [http://www.dlr.de/dlr/Portaldata/1/Resources/documents/TanDEM-X\\_web.pdf](http://www.dlr.de/dlr/Portaldata/1/Resources/documents/TanDEM-X_web.pdf).
- Bassiri, S. and Hajj, G. A. (1993). "Higher order ionospheric effects on the GPS observables and means of modeling them." In: *Advances in the Astronautical Sciences*. Vol. 82. pt 2. Pasadena, California: American Astronautical Society, pp. 1071–1086. ISBN: 0877033684. URL: [https://www.researchgate.net/publication/23819508\\_Higher-order\\_ionospheric\\_effects\\_on\\_the\\_GPS\\_observabl%20es\\_and\\_means\\_of\\_modeling\\_them](https://www.researchgate.net/publication/23819508_Higher-order_ionospheric_effects_on_the_GPS_observabl%20es_and_means_of_modeling_them).

## Bibliography

- Baur, O., Bock, H., Höck, E., Jäggi, A., Krauss, S., Mayer-Gürr, T., Reubelt, T., Siemes, C., and Zehentner, N. (June 2014). "Comparison of GOCE-GPS gravity fields derived by different approaches." In: *Journal of Geodesy*. ISSN: 0949-7714. DOI: [10.1007/s00190-014-0736-6](https://doi.org/10.1007/s00190-014-0736-6).
- Bertiger, W. I., Bar-Sever, Y. E., Christensen, E. J., Davis, E. S., Guinn, J. R., Haines, B. J., Ibanez-Meier, R. W., Jee, J. R., Lichten, S. M., Melbourne, W. G., Muellerschoen, R. J., Munson, T. N., Vigue, Y., Wu, S. C., Yunck, T. P., Schutz, B. E., Abusali, P. A. M., Rim, H. J., Watkins, M. M., and Willis, P. (Dec. 1994). "GPS precise tracking of TOPEX/POSEIDON: Results and implications." en. In: *Journal of Geophysical Research* 99.C12, p. 24449. ISSN: 0148-0227. DOI: [10.1029/94JC01171](https://doi.org/10.1029/94JC01171). URL: <http://onlinelibrary.wiley.com/doi/10.1029/94JC01171/abstract>.
- Bertiger, W., Desai, S. D., Haines, B., Harvey, N., Moore, A. W., Owen, S., and Weiss, J. P. (2010). "Single receiver phase ambiguity resolution with GPS data." In: *Journal of Geodesy* 84.5, pp. 327–337. ISSN: 09497714. DOI: [10.1007/s00190-010-0371-9](https://doi.org/10.1007/s00190-010-0371-9).
- Bettadpur, S. (2012). *UTCSR Level-2 Processing Standards Document*. Tech. rep. Austin, Texas: Center for Space Research. URL: [ftp://podaac.jpl.nasa.gov/allData/grace/docs/L2-CSR0005\\_ProcStd\\_v4.0.pdf](ftp://podaac.jpl.nasa.gov/allData/grace/docs/L2-CSR0005_ProcStd_v4.0.pdf).
- Beutler, G., Jäggi, A., Mervart, L., and Meyer, U. (2010). "The celestial mechanics approach: theoretical foundations." In: *Journal of Geodesy* 84.10, pp. 605–624. ISSN: 0949-7714. DOI: [10.1007/s00190-010-0401-7](https://doi.org/10.1007/s00190-010-0401-7).
- Beutler, G. (2005). *Methods of Celestial Mechanics*. Astronomy and Astrophysics Library. Berlin, Heidelberg: Springer Berlin Heidelberg. ISBN: 978-3-540-40750-8. DOI: [10.1007/b137725](https://doi.org/10.1007/b137725). URL: <http://link.springer.com/10.1007/b137725>.
- Bhattacharyya, A., Beach, T. L., Basu, S., and Kintner, P. M. (2000). "Nighttime equatorial ionosphere: GPS scintillations and differential carrier phase fluctuations." In: *Radio Science* 35.1, pp. 209–224. ISSN: 00486604. DOI: [10.1029/1999RS002213](https://doi.org/10.1029/1999RS002213).
- Bigazzi, A. and Frommknecht, B. (2010). *Note on GOCE instruments Positioning*.
- Bilitza, D., McKinnell, L.-A., Reinisch, B., and Fuller-Rowell, T. (Nov. 2011). "The international reference ionosphere today and in the future." In: *Journal of Geodesy* 85.12, pp. 909–920. ISSN: 0949-7714. DOI: [10.1007/s00190-010-0427-x](https://doi.org/10.1007/s00190-010-0427-x).
- Bock, H. (2003). *Efficient Methods for Determining Precise Orbits of Low Earth Orbiters Using the Global Positioning System*. Vol. 65. Schweizerischen Geodätischen Kommission, p. 239. ISBN: 3-908440-08-4. URL: <http://www.sgc.ethz.ch/sgc-volumes/sgk-65.pdf>.
- Bock, H., Dach, R., Jäggi, A., and Beutler, G. (June 2009a). "High-rate GPS clock corrections from CODE: support of 1 Hz applications." In: *Journal of Geodesy* 83.11, pp. 1083–1094. ISSN: 0949-7714. DOI: [10.1007/s00190-009-0326-1](https://doi.org/10.1007/s00190-009-0326-1).
- Bock, H., Jäggi, a., Dach, R., Schaer, S., and Beutler, G. (Mar. 2009b). "GPS single-frequency orbit determination for low Earth orbiting satellites." In: *Advances in Space Research* 43.5, pp. 783–791. ISSN: 02731177. DOI: [10.1016/j.asr.2008.12.003](https://doi.org/10.1016/j.asr.2008.12.003). URL: <http://linkinghub.elsevier.com/retrieve/pii/S0273117708006340>.

## Bibliography

- Bock, H., Jäggi, A., Meyer, U., Dach, R., and Beutler, G. (2011a). "Impact of GPS antenna phase center variations on precise orbits of the GOCE satellite." In: *Advances in Space Research* 47.11, pp. 1885–1893. ISSN: 02731177. DOI: [10.1016/j.asr.2011.01.017](https://doi.org/10.1016/j.asr.2011.01.017).
- Bock, H., Jäggi, A., Meyer, U., Visser, P., IJssel, J. van den, Helleputte, T. van, Heinze, M., and Hugentobler, U. (Nov. 2011b). "GPS-derived orbits for the GOCE satellite." In: *Journal of Geodesy* 85.11, pp. 807–818. ISSN: 0949-7714. DOI: [10.1007/s00190-011-0484-9](https://doi.org/10.1007/s00190-011-0484-9).
- Bock, H., Jäggi, A., Švehla, D., Beutler, G., Hugentobler, U., and Visser, P. (Jan. 2007). "Precise orbit determination for the GOCE satellite using GPS." In: *Advances in Space Research* 39.10, pp. 1638–1647. ISSN: 02731177. DOI: [10.1016/j.asr.2007.02.053](https://doi.org/10.1016/j.asr.2007.02.053). URL: <http://linkinghub.elsevier.com/retrieve/pii/S0273117707001718>.
- Bock, H., Jäggi, A., Beutler, G., and Meyer, U. (Nov. 2014). "GOCE: precise orbit determination for the entire mission." In: *Journal of Geodesy* 88.11, pp. 1047–1060. ISSN: 0949-7714. DOI: [10.1007/s00190-014-0742-8](https://doi.org/10.1007/s00190-014-0742-8). URL: <http://link.springer.com/10.1007/s00190-014-0742-8>.
- Brunner, F. K. and Gu, M. (1991). "An improved model for the dual frequency ionospheric correction of GPS observations." In: *manuscripta geodeatica* 16, pp. 205–214.
- Buckreuss, S., Balzer, W., Muhlbauer, P., Werninghaus, R., and Pitz, W. (2003). "The terraSAR-X satellite project." In: *IGARSS 2003. 2003 IEEE International Geoscience and Remote Sensing Symposium. Proceedings (IEEE Cat. No.03CH37477)* 5.C, pp. 3096–3098. DOI: [10.1109/IGARSS.2003.1294694](https://doi.org/10.1109/IGARSS.2003.1294694).
- Budden, K. G. (1985). *The Propagation of Radio Waves*. Cambridge Books Online. Cambridge University Press. ISBN: 9780511564321. DOI: [10.1017/CB09780511564321](https://doi.org/10.1017/CB09780511564321).
- Caissy, M., Agrotis, L., Weber, G., Hernandez-Pajares, M., and Hugentobler, U. (2012). "Innovation: Coming Soon - The International GNSS Real-Time Service." In: *GPS World* June. URL: <http://gpsworld.com/gnss-systemaugmentation-assistanceinnovation-coming-soon-13044/>.
- Carrano, C. S. and Groves, K. M. (2007). "TEC Gradients and Fluctuations at Low Latitudes Measured with High Data Rate GPS Receivers." In: *ION 63rd Annual Meeting*, pp. 156–163. URL: <https://www2.bc.edu/~carranoc/carrano-ion-am.pdf>.
- Case, K., Kruizinga, G., and Wu, S. (2010). *GRACE Level 1B Data Product User Handbook*. Jet Propulsion Laboratory, California Institute of Technology. URL: [ftp://podaac.jpl.nasa.gov/allData/grace/docs/Handbook\\_1B\\_v1.3.pdf](ftp://podaac.jpl.nasa.gov/allData/grace/docs/Handbook_1B_v1.3.pdf).
- Cazenave, A. and Chen, J. (Oct. 2010). "Time-variable gravity from space and present-day mass redistribution in the Earth system." In: *Earth and Planetary Science Letters* 298.3-4, pp. 263–274. ISSN: 0012821X. DOI: [10.1016/j.epsl.2010.07.035](https://doi.org/10.1016/j.epsl.2010.07.035).
- Chapman, S. (1931). "The absorption and dissociative or ionizing effect of monochromatic radiation in an atmosphere on a rotating earth." In: *Proceedings of the Physical Society* 43.1, p. 26. ISSN: 0959-5309. DOI: [10.1088/0959-5309/43/5/302](https://doi.org/10.1088/0959-5309/43/5/302).
- Chen, X., Allison, T., Cao, W., Ferguson, K., Grünig, S., Gomez, V., Kipka, A., Köhler, J., Landau, H., Leandro, R., Lu, G., Stolz, R., and Talbot, N. (2011). "Trimble RTX ,

## Bibliography

- an Innovative New Approach for Network RTK." URL: [http://www.trimble.com/positioning-services/pdf/WhitePaper\\_RTX\\_Fast.pdf](http://www.trimble.com/positioning-services/pdf/WhitePaper_RTX_Fast.pdf).
- Collins, P., Lahaye, F., Heroux, P., and Bisnath, S. (2008). "Precise Point Positioning with Ambiguity Resolution using the Decoupled Clock Model." In: *Proceedings of the 21st International Technical Meeting of the Satellite Division of The Institute of Navigation (ION GNSS 2008)*. September. Savannah, GA, pp. 1315–1322. ISBN: 9781605606897. URL: <http://www.ion.org/publications/abstract.cfm?jp=p&articleID=8043>.
- Colomb, F., Alonso, C., Hofmann, C., and Nollmann, I. (2004). "SAC-C mission, an example of international cooperation." In: *Advances in Space Research* 34.10, pp. 2194–2199. ISSN: 02731177. DOI: [10.1016/j.asr.2003.10.039](https://doi.org/10.1016/j.asr.2003.10.039).
- Dach, R., Brockmann, E., Schaer, S., Beutler, G., Meindl, M., Prange, L., Bock, H., Jäggi, A., and Ostini, L. (Feb. 2009). "GNSS processing at CODE: status report." In: *Journal of Geodesy* 83.3-4, pp. 353–365. ISSN: 0949-7714. DOI: [10.1007/s00190-008-0281-2](https://doi.org/10.1007/s00190-008-0281-2).
- Dach, R., Lutz, S., Walser, P., and Fridez, P. (2015). *Bernese GNSS Software, Version 5.2*. November. Astronomical Institute, University of Bern, p. 884. ISBN: 1879621142. DOI: [10.7892/boris.72297](https://doi.org/10.7892/boris.72297). URL: <http://www.bernese.unibe.ch/docs/D0CU52.pdf>.
- de La Beaujardière, O. (Nov. 2004). "C/NOFS: a mission to forecast scintillations." In: *Journal of Atmospheric and Solar-Terrestrial Physics* 66.17, pp. 1573–1591. ISSN: 13646826. DOI: [10.1016/j.jastp.2004.07.030](https://doi.org/10.1016/j.jastp.2004.07.030).
- Dow, J. M., Neilan, R. E., and Rizos, C. (Feb. 2009). "The International GNSS Service in a changing landscape of Global Navigation Satellite Systems." In: *Journal of Geodesy* 83.3-4, pp. 191–198. ISSN: 0949-7714. DOI: [10.1007/s00190-008-0300-3](https://doi.org/10.1007/s00190-008-0300-3). URL: <http://link.springer.com/10.1007/s00190-008-0300-3>.
- Drinkwater, M., Haagmans, R., Muzi, D., Popescu, A., Floberghagen, R., Kern, M., and Fehringer, M. (Nov. 2007). "The GOCE Gravity Mission: ESAs First Core Earth Explorer." In: *Proceedings of the 3rd International GOCE User Workshop*. Frascati, Italy, pp. 1–8. ISBN: 92-9092-938-3.
- Dunn, C., Bertiger, W., Bar-sever, Y., Desai, S., Haines, B., Kuang, D., Franklin, G., Harris, I., Meehan, T., Nandi, S., Nguyen, D., Rogstad, T., Thomas, J. B., Tien, J., Romans, L., Wu, S.-c., Bettadpur, S., and Kim, J. (2003). "Instrument of Grace." In: *GPS World* 14.2, pp. 16–28. URL: [http://www.csr.utexas.edu/grace/publications/press/03-02-01-GRACE\\_gpsworld.pdf](http://www.csr.utexas.edu/grace/publications/press/03-02-01-GRACE_gpsworld.pdf).
- Dunn, M. J., ed. (2013). *Interface Specification, Navstar GPS Space Segment/Navigation User Interface, IS-GPS-200H*. Global Positioning Systems Directorate - Systems Engineering and Integration. URL: <http://www.gps.gov/technical/icwg/IS-GPS-200H.pdf>.
- Edwards, P. G., Berruti, B., Blythe, P., Callies, J., Carlier, S., Fransen, C., Krutsch, R., Lefebvre, A.-R., Loiselet, M., and Stricker, N. (2006). "The MetOp Satellite - Weather Information from Polar Orbit." In: *ESA bulletin* 127.
- Eicker, A. (2008). "Gravity Field Refinements by Radial Basis Functions from In-situ Satellite Data." PhD thesis. Bonn: Rheinischen Friedrich-Wilhelms-Universität. URL: <http://hss.ulb.uni-bonn.de/2008/1375/1375-1.pdf>.
- Faust, M. (2013). *Swarm Instrument Positions in Spacecraft Coordinates*.

## Bibliography

- Flechtner, F., Dobslaw, H., and Fagiolini, E. (Apr. 2015). *AOD1B Product Description Document for Product Release 05*. GFZ German Research Center for Geosciences.
- Flechtner, F., Morton, P., Watkins, M., and Webb, F. (2014). "Status of the GRACE Follow-On Mission." In: *Proceedings of the International Association of Geodesy Symposia Gravity, Geoid and Height System*. IAGS-D-12-00141, pp. 117–121. DOI: [10.1007/978-3-319-10837-7\\_15](https://doi.org/10.1007/978-3-319-10837-7_15).
- Flechtner, F., Dahle, C., Neumayer, K. H., König, R., and Förste, C. (2010). "The Release 04 CHAMP and GRACE EIGEN Gravity Field Models." In: *System Earth via Geodetic-Geophysical Space Techniques*. Ed. by Flechtner, F. M., Gruber, T., Güntner, A., Manda, M., Rothacher, M., Schöne, T., and Wickert, J. Berlin, Heidelberg: Springer Berlin Heidelberg, pp. 41–58. ISBN: 978-3-642-10228-8. DOI: [10.1007/978-3-642-10228-8\\_4](https://doi.org/10.1007/978-3-642-10228-8_4). URL: [http://dx.doi.org/10.1007/978-3-642-10228-8\\_4](http://dx.doi.org/10.1007/978-3-642-10228-8_4).
- Floberghagen, R., Fehringer, M., Lamarre, D., Muzi, D., Frommknecht, B., Steiger, C., Piñeiro, J., and Costa, A. da (Nov. 2011). "Mission design, operation and exploitation of the gravity field and steady-state ocean circulation explorer mission." In: *Journal of Geodesy* 85.11, pp. 749–758. ISSN: 0949-7714. DOI: [10.1007/s00190-011-0498-3](https://doi.org/10.1007/s00190-011-0498-3).
- Folkner, W., Williams, J., and Boggs, D. (2009). "The planetary and lunar ephemeris DE 421." In: *IPN Progress Report 42-178* 005, pp. 1–34. URL: [http://ipnpr.jpl.nasa.gov/progress\\_report/42-178/178C.pdf](http://ipnpr.jpl.nasa.gov/progress_report/42-178/178C.pdf).
- Fritsche, M., Dietrich, R., Knöfel, C., Rülke, A., Vey, S., Rothacher, M., and Steigenberger, P. (2005). "Impact of higher-order ionospheric terms on GPS estimates." In: *Geophysical Research Letters* 32.23, p. L23311. ISSN: 0094-8276. DOI: [10.1029/2005GL024342](https://doi.org/10.1029/2005GL024342).
- Ge, M., Gendt, G., Rothacher, M., Shi, C., and Liu, J. (Oct. 2008). "Resolution of GPS carrier-phase ambiguities in Precise Point Positioning (PPP) with daily observations." In: *Journal of Geodesy* 82.7, pp. 389–399. ISSN: 09497714. DOI: [10.1007/s00190-007-0187-4](https://doi.org/10.1007/s00190-007-0187-4).
- Geng, J., Teferle, F. N., Shi, C., Meng, X., Dodson, A. H., and Liu, J. (2009). "Ambiguity resolution in precise point positioning with hourly data." In: *GPS Solutions* 13.4, pp. 263–270. ISSN: 10805370. DOI: [10.1007/s10291-009-0119-2](https://doi.org/10.1007/s10291-009-0119-2).
- Gerlach, C., Földvary, L., Švehla, D., Gruber, T., Wermuth, M., Sneeuw, N., Frommknecht, B., Oberndorfer, H., Peters, T., Rothacher, M., Rummel, R., and Steigenberger, P. (Oct. 2003). "A CHAMP-only gravity field model from kinematic orbits using the energy integral." In: *Geophysical Research Letters* 30.20, pp. 1–4. ISSN: 0094-8276. DOI: [10.1029/2003GL018025](https://doi.org/10.1029/2003GL018025).
- Görres, B., Campbell, J., Becker, M., and Siemes, M. (May 2006). "Absolute calibration of GPS antennas: laboratory results and comparison with field and robot techniques." In: *GPS Solutions* 10.2, pp. 136–145. ISSN: 1080-5370. DOI: [10.1007/s10291-005-0015-3](https://doi.org/10.1007/s10291-005-0015-3).
- Griffiths, J. (Dec. 2013). "Status of IGS Core Products." In: *AGU Fall Meeting 2013*. URL: [https://www.researchgate.net/publication/264005004\\_Status\\_of\\_IGS\\_core\\_products](https://www.researchgate.net/publication/264005004_Status_of_IGS_core_products).

## Bibliography

- Grunwaldt, L. and Meehan, T. K. (2003). "CHAMP orbit and gravity instrument status." In: *First CHAMP Mission Results for Gravity, Magnetic and Atmospheric Studies*. Springer, pp. 3–10.
- Gurtner, W. (2007). *RINEX: The Receiver Independent Exchange Format Version 2.10*. Astronomical Institute, University of Bern. URL: <ftp://ftp.unibe.ch/aiub/rinex/rinex210.txt>.
- Gurtner, W. and Estey, L. (2002). *RINEX Version 2.20: Modifications to Accomodate Low Earth Orbiter Data*. Astronomical Institute, University of Bern. URL: [ftp://ftp.unibe.ch/aiub/rinex/rnx\\_leo.txt](ftp://ftp.unibe.ch/aiub/rinex/rnx_leo.txt).
- Gurtner, W. and Estey, L. (Nov. 2007). *RINEX The Receiver Independent Exchange Format*. Astronomical Institute, University of Bern. URL: <ftp://ftp.unibe.ch/aiub/rinex/rinex300.pdf>.
- Haagmans, R., Bock, R., and Rider, H. (2013). *Swarm - ESA's magnetic field mission*. European Space Agency. ISBN: 9789292210670. URL: <https://earth.esa.int/documents/700255/1805948/ESA+magnetic+field+mission/36942f02-b2d4-4787-af81-eb19efb74265>.
- Haines, B. J., Armatys, M. J., Bertiger, W. I., Desai, S. D., Dorsey, A. R., Lane, C. M., and Weiss, J. P. (2011). "One-Centimeter Orbits in Near-Real Time : The GPS Experience on OSTM / Jason-2." In: 58.September, pp. 445–459. ISSN: 00219142. DOI: [10.1007/BF03321179](https://doi.org/10.1007/BF03321179).
- Han, S.-C. (2002). "Efficient gravity field recovery using in situ disturbing potential observables from CHAMP." In: *Geophysical Research Letters* 29.16, pp. 1–4. ISSN: 0094-8276. DOI: [10.1029/2002GL015180](https://doi.org/10.1029/2002GL015180).
- Hartmann, G. K. and Leitinger, R. (1984). "Range errors due to ionospheric and tropospheric effects for signal frequencies above 100 MHz." In: *Bulletin Geodesique* 58.2, pp. 109–136. ISSN: 00074632. DOI: [10.1007/BF02520897](https://doi.org/10.1007/BF02520897).
- Hausleitner, W., Kirchner, G., Krauss, S., Weingrill, J., Pail, R., Goiginger, H., and Rieser, D. (Mar. 2010). "Improved kHz-SLR tracking techniques and orbit quality analysis for LEO missions." In: *Advances in Space Research* 45.6, pp. 721–732. ISSN: 02731177. DOI: [10.1016/j.asr.2009.11.016](https://doi.org/10.1016/j.asr.2009.11.016). URL: <http://linkinghub.elsevier.com/retrieve/pii/S0273117709007194>.
- Heiskanen, W. and Moritz, H. (1967). *Physical Geodesy*. San Francisco: W. H. Freeman.
- Hilla, S. (Aug. 2010). *The Extended Standard Product 3 Orbit Format (SP3-c)*. URL: <https://igs.cb.jpl.nasa.gov/igs/data/format/sp3c.txt> (visited on 04/28/2016).
- Hofmann-Wellenhof, B., Lichtenegger, H., and Wasle, E. (2008). *GNSS – Global Navigation Satellite Systems*. Springer Wien New York, p. 546. ISBN: 978-3-211-73012-6. DOI: [10.1007/978-3-211-73017-1](https://doi.org/10.1007/978-3-211-73017-1).
- Hofmann-Wellenhof, B. and Moritz, H. (2006). *Physical Geodesy*. Springer Vienna. ISBN: 978-3-211-33544-4. DOI: [10.1007/978-3-211-33545-1](https://doi.org/10.1007/978-3-211-33545-1).
- Holaschutz, D., Bishop, R. H., Harris, R. B., and Tolman, B. (2008). "Inter-frequency bias estimation for the GPS monitor station network." In: *21st International Technical Meeting of the Satellite Division of the Institute of Navigation, ION GNSS 2008* 3.September,

## Bibliography

- pp. 1723–1733. URL: <http://www.scopus.com/inward/record.url?eid=2-s2.0-70349147455&partnerID=tZ0tx3y1>.
- Hoque, M. M. and Jakowski, N. (2012). “Ionospheric Propagation Effects on GNSS Signals and New Correction Approaches.” In: *Global Navigation Satellite Systems: Signal, Theory and Applications*. Ed. by Shuanggen, J. In Tech. ISBN: 978-953-307-843-4. URL: [http://cdn.intechopen.com/pdfs/27723/InTech-Ionospheric\\_propagation\\_effects\\_on\\_gnss\\_signals\\_and\\_new\\_correction%20approaches.pdf](http://cdn.intechopen.com/pdfs/27723/InTech-Ionospheric_propagation_effects_on_gnss_signals_and_new_correction%20approaches.pdf).
- Hoque, M. and Jakowski, N. (Oct. 2008). “Estimate of higher order ionospheric errors in GNSS positioning.” In: *Radio Science* 43.5. ISSN: 00486604. DOI: [10.1029/2007RS003817](https://doi.org/10.1029/2007RS003817).
- Hwang, C., Tseng, T.-P., Lin, T., Švehla, D., and Schreiner, B. (Aug. 2008). “Precise orbit determination for the FORMOSAT-3/COSMIC satellite mission using GPS.” In: *Journal of Geodesy* 83.5, pp. 477–489. ISSN: 0949-7714. DOI: [10.1007/s00190-008-0256-3](https://doi.org/10.1007/s00190-008-0256-3). URL: <http://link.springer.com/10.1007/s00190-008-0256-3>.
- IAU (2000). “Resolution No. B1.3, Definition of barycentric celestial reference system and geocentric celestial reference system.” In: URL: [http://www.iau.org/administration/resolutions/general\\_assemblies/](http://www.iau.org/administration/resolutions/general_assemblies/).
- IGS Antenna Working Group (2012). *IGS antenna files*. URL: [ftp://igs.cb.jpl.nasa.gov/pub/station/general/antenna\\_README.pdf](ftp://igs.cb.jpl.nasa.gov/pub/station/general/antenna_README.pdf).
- Ilk, K. H., Mayer-Gürr, T., and Feuchtinger, M. (2005). “Gravity Field Recovery by Analysis of Short Arcs of CHAMP.” In: *Earth Observation with CHAMP*. Berlin/Heidelberg: Springer-Verlag, pp. 127–132. ISBN: 9783540228042. DOI: [10.1007/3-540-26800-6\\_20](https://doi.org/10.1007/3-540-26800-6_20). URL: [http://link.springer.com/10.1007/3-540-26800-6%7B%5C\\_%7D20](http://link.springer.com/10.1007/3-540-26800-6%7B%5C_%7D20).
- Ingvarson, P., Bonnedal, M., Wettergren, J., and Wastberg, B. (Nov. 2007). “A gps antenna for precise orbit determination of the swarm satellites.” In: *The Second European Conference on Antennas and Propagation EuCAP*, pp. 1–6. ISBN: 978-0-86341-842-6. URL: [http://ieeexplore.ieee.org/xpls/abs\\_all.jsp?arnumber=4458698&tag=1](http://ieeexplore.ieee.org/xpls/abs_all.jsp?arnumber=4458698&tag=1).
- Intelisano, A., Mazzini, L., Notarantonio, A., Landenna, S., Zin, A., Scaciga, L., and Maraldi, L. (2008). “Recent flight experiences of TAS-I on-board navigation equipments.” In: *Proceedings of the 4th ESA workshop on satellite navigation user equipment technologies, NAVITEC*. Noordwijk.
- IPCC (2014). *Climate Change 2014: Synthesis Report. Contribution of Working Groups I, II and III to the Fifth Assessment Report of the Intergovernmental Panel on Climate Change*. Tech. rep. Geneva, Switzerland, pp. 1–151. URL: <http://www.ipcc.ch>.
- Jäggi, A. (2007). *Pseudo-Stochastic Orbit Modeling of Low Earth Satellites Using the Global Positioning System*. Vol. 85. Schweizerischen Geodätischen Kommission, p. 186. ISBN: 9783908440178. URL: <http://www.sgc.ethz.ch/sgc-volumes/sgk-85.pdf>.
- Jäggi, A., Beutler, G., Prange, L., Dach, R., and Mervart, L. (2009a). “Assessment of GPS-only Observables for Gravity Field Recovery from GRACE.” In: *Observing our Changing Earth*. Vol. 133. Berlin, Heidelberg: Springer Berlin Heidelberg, pp. 113–123. ISBN: 9783540854258. DOI: [10.1007/978-3-540-85426-5\\_14](https://doi.org/10.1007/978-3-540-85426-5_14). URL: [http://link.springer.com/10.1007/978-3-540-85426-5%7B%5C\\_%7D14](http://link.springer.com/10.1007/978-3-540-85426-5%7B%5C_%7D14).

## Bibliography

- Jäggi, A., Bock, H., Meyer, U., Beutler, G., and IJssel, J. van den (2014). "GOCE: assessment of GPS-only gravity field determination." In: *Journal of Geodesy* 89.1, pp. 33–48. ISSN: 0949-7714. DOI: [10.1007/s00190-014-0759-z](https://doi.org/10.1007/s00190-014-0759-z).
- Jäggi, A., Bock, H., Prange, L., Meyer, U., and Beutler, G. (Mar. 2011a). "GPS-only gravity field recovery with GOCE, CHAMP, and GRACE." In: *Advances in Space Research* 47.6, pp. 1020–1028. ISSN: 02731177. DOI: [10.1016/j.asr.2010.11.008](https://doi.org/10.1016/j.asr.2010.11.008).
- Jäggi, A., Dach, R., Montenbruck, O., Hugentobler, U., Bock, H., and Beutler, G. (Dec. 2009b). "Phase center modeling for LEO GPS receiver antennas and its impact on precise orbit determination." In: *Journal of Geodesy* 83.12, pp. 1145–1162. ISSN: 0949-7714. DOI: [10.1007/s00190-009-0333-2](https://doi.org/10.1007/s00190-009-0333-2).
- Jäggi, A., Dahle, C., Arnold, D., Bock, H., Meyer, U., Beutler, G., and IJssel, J. van den (Jan. 2016). "Swarm kinematic orbits and gravity fields from 18 months of GPS data." In: *Advances in Space Research* 57.1, pp. 218–233. ISSN: 02731177. DOI: [10.1016/j.asr.2015.10.035](https://doi.org/10.1016/j.asr.2015.10.035). URL: <http://linkinghub.elsevier.com/retrieve/pii/S0273117715007541>.
- Jäggi, A., Dahle, C., Arnold, D., Bock, H., Meyer, U., Beutler, G., and van den IJssel, J. (2015). "Swarm kinematic orbits and gravity fields from 18 months of GPS data." In: *Advances in Space Research*. ISSN: 02731177. DOI: [10.1016/j.asr.2015.10.035](https://doi.org/10.1016/j.asr.2015.10.035).
- Jäggi, A., Montenbruck, O., Moon, Y., Wermuth, M., König, R., Michalak, G., Bock, H., and Bodenmann, D. (July 2012). "Inter-agency comparison of TanDEM-X baseline solutions." In: *Advances in Space Research* 50.2, pp. 260–271. ISSN: 02731177. DOI: [10.1016/j.asr.2012.03.027](https://doi.org/10.1016/j.asr.2012.03.027).
- Jäggi, A., Prange, L., and Hugentobler, U. (May 2011b). "Impact of covariance information of kinematic positions on orbit reconstruction and gravity field recovery." In: *Advances in Space Research* 47.9, pp. 1472–1479. ISSN: 02731177. DOI: [10.1016/j.asr.2010.12.009](https://doi.org/10.1016/j.asr.2010.12.009).
- Jakowski, N., Porsch, F., and Mayer, G. (1994). "Ionosphere-Induced Ray-Path; Bending Effects in Precision; Satellite Positioning Systems." In: *Zeitschrift f. satellitengestützte Positionierung, Navigation und Kommunikation* 1, pp. 6–13.
- Jean, Y. and Dach, R. (May 2015). *IGS - Technical report 2014*. Tech. rep. International GNSS Service. URL: <http://www.igs.org>.
- Johannessen, J. A., Balmino, G., Le Provost, C., Rummel, R., Sabadini, R., Sünkel, H., Tscherning, C., Visser, P., Woodworth, P., Hughes, C., Legrand, P., Sneeuw, N., Perosanz, F., Aguirre-Martinez, M., Rebhan, H., and Drinkwater, M. (July 2003). "The European Gravity Field and Steady-State Ocean Circulation Explorer Satellite Mission: Its Impact on Geophysics." In: *Surveys in Geophysics* 24.4, pp. 339–386. ISSN: 0169-3298. DOI: [10.1023/B:GEOP.0000004264.04667.5e](https://doi.org/10.1023/B:GEOP.0000004264.04667.5e).
- Jørgensen, J. L. (1999). "In Orbit Performance of a Fully Autonomous Star Tracker." In: *ESA 4th Symposium on Spacecraft Guidance Navigation and Control*. Noordwijk: ESTEC, European Space Agency. URL: <http://adsabs.harvard.edu/abs/2000ESASP.425..103J>.

## Bibliography

- Kenner, H. (1976). *Geodesic Math and How to Use It*. University of California Press Berkeley, p. 183. ISBN: 978-0520239319.
- Koch, K.-R. (2004). *Parameterschätzung und Hypothesentests in linearen Modellen*. 4th ed. Bonn, Germany: Ferd. Dummlers Verlag, Bonn, p. 382.
- Koch, K.-R. and Kusche, J. (May 2002). "Regularization of geopotential determination from satellite data by variance components." In: *Journal of Geodesy* 76.5, pp. 259–268. ISSN: 0949-7714. DOI: [10.1007/s00190-002-0245-x](https://doi.org/10.1007/s00190-002-0245-x).
- Köhler, W. (2001). *RINEX format observable extensions for CHAMP SST Data*. GFZ Potsdam. URL: <http://gfzpublic.gfz-potsdam.de/pubman/faces/viewItemFullPage.jspx?itemId=escidoc:18194>.
- König, R., Michalak, G., Neumayer, K. H., and Zhu, S. (2006). "Remarks on CHAMP Orbit Products." In: *Observation of the Earth System from Space*. Berlin/Heidelberg: Springer-Verlag, pp. 17–26. DOI: [10.1007/3-540-29522-4\\_2](https://doi.org/10.1007/3-540-29522-4_2).
- Koop, R., Gruber, T., and Rummel, R. (Nov. 6–8, 2006). "The status of the GOCE high-level processing facility." In: *3rd GOCE User Workshop*. ESA SP-627. Frascati, Italy, pp. 195–205.
- Kuang, D., Bar-Sever, Y., Bertiger, W., and Desai, S. (2001). "Precise orbit determination for CHAMP using GPS data from BlackJack receiver." In: *ION National Technical Meeting Session E1*. DOI: [10.1.1.457.4042](https://doi.org/10.1.1.457.4042). URL: <http://trs-new.jpl.nasa.gov/dspace/handle/2014/12198>.
- Langley, R. B. (1997). "GPS Receiver System Noise." In: *GPS World* 8.No. 6, pp. 40–45. URL: <http://gauss.gge.unb.ca/papers.pdf/gpsworld.june97.pdf>.
- Lanyi, G. E. and Roth, T. (July 1988). "A comparison of mapped and measured total ionospheric electron content using global positioning system and beacon satellite observations." In: *Radio Science* 23.4, pp. 483–492. ISSN: 00486604. DOI: [10.1029/RS023i004p00483](https://doi.org/10.1029/RS023i004p00483).
- Laurichesse, D., Cerri, L., Berthias, J. P., and Mercier, F. (Sept. 2009). "Real time precise GPS constellation and clocks estimation by means of a Kalman filter." In: *ION GNSS 2013*. Nashville: Centre National d'Etudes Spatiales. URL: [http://www.ppp-wizard.net/Articles/laurichesse\\_ion\\_gnss\\_2013\\_bdp.pdf](http://www.ppp-wizard.net/Articles/laurichesse_ion_gnss_2013_bdp.pdf).
- Laurichesse, D., Mercier, F., and Berthias, J. P. (Sept. 2010). "Real-time PPP with undifferenced integer ambiguity resolution, experimental results." In: *Proceedings of the 23rd International Technical Meeting of The Satellite Division of the Institute of Navigation (ION GNSS 2010)*. Portland, Oregon, pp. 2534–2544. URL: <https://www.ion.org/publications/abstract.cfm?articleID=9361>.
- Loiselet, M., Stricker, N., Menard, Y., and Luntama, J. (2000). "GRAS-MetOp's GPS-based atmospheric sounder." In: *ESA Bulletin* 102.may, pp. 38–44.
- Lühr, H., Grunwaldt, L., Förste, C., Schwintzer, P., and Reigber, C. (Apr. 2002). *CHAMP Reference Systems, Transformations and Standards*. GFZ Potsdam. URL: [http://op.gfz-potsdam.de/champ/docs\\_CHAMP/CH-GFZ-RS-002.PDF](http://op.gfz-potsdam.de/champ/docs_CHAMP/CH-GFZ-RS-002.PDF).
- Mannucci, A. J., Ao, C. O., Meehan, T. K., Iijima, B. a., Komjathy, A., Yunck, T. P., Pestana, M. K., and Wilson, B. D. (2008). "GPS Radio Occultation as Part of the Global Earth

## Bibliography

- Observing System." In: *IGARSS 2008 - 2008 IEEE International Geoscience and Remote Sensing Symposium*. IEEE, pages. ISBN: 978-1-4244-2807-6. DOI: [10.1109/IGARSS.2008.4778855](https://doi.org/10.1109/IGARSS.2008.4778855). URL: <http://ieeexplore.ieee.org/lpdocs/epic03/wrapper.htm?arnumber=4778855>.
- Martin-Neira, M. (1993). *A Passive Reflectometry and Interferometry System(PARIS)- Application to ocean altimetry*.
- Mayer-Gürr, T. (Aug. 2006). "Gravitationsfeldbestimmung aus der Analyse kurzer Bahnbögen am Beispiel der Satellitenmissionen CHAMP und GRACE." PhD thesis. Munich: Rheinischen Friedrich-Wilhelms-Universität. URL: <http://hss.ulb.uni-bonn.de/2006/0904/0904.pdf>.
- Mayer-Gürr, T. (2007). *ITG-Grace03s: The latest GRACE gravity field solution computed in Bonn*. presented at the Joint International GSTM and DFG SPP Symposium. Potsdam, Germany.
- Mayer-Gürr, T., Kurtenbach, E., and Eicker, A. (2010). *ITG-Grace2010: the new GRACE gravity field release computed in Bonn*. presented at the EGU General Assembly 2010. Geophysical Research Abstracts, Vol. 12, EGU2010-2446. Vienna, Austria.
- Mayer-Gürr, T., Rieser, D., Zehentner, N., Pail, R., Gruber, T., Fecher, T., Rexer, M., Schuh, W.-D., Kusche, J., Brockmann, J. M., Krasbutter, I., Becker, S., Eicker, A., Schall, J., Baur, O., Höck, E., Hausleitner, W., Maier, A., Krauss, S., Jäggi, A., Meyer, U., and Prange, L. (2012). "The new combined satellite only model GOCO03s." In: *International Symposium on Gravity, Geoid and Height Systems (GGHS 2012)*. Venice. URL: [www.goco.eu](http://www.goco.eu).
- Mayer-Gürr, T., Zehentner, N., Klinger, B., and Kvas, A. (2014). *ITSG-Grace2014: a new GRACE gravity field release computed in Graz*. presented at the Grace Science Team Meeting 2014. Potsdam, Germany. DOI: [10.13140/RG.2.1.5098.2805](https://doi.org/10.13140/RG.2.1.5098.2805).
- Meissl, P. (1982). *Least Squares Adjustment - A Modern Approach*. Graz: Geodätische Institute der Technischen Universität Graz, p. 488. URL: [ftp://skylab.itg.uni-bonn.de/schuh/Separata\\_Meissl/Meissl\\_1982\\_Least\\_Squares\\_Adjustment\\_A\\_Modern\\_Approach.pdf](ftp://skylab.itg.uni-bonn.de/schuh/Separata_Meissl/Meissl_1982_Least_Squares_Adjustment_A_Modern_Approach.pdf).
- Menge, F. (2003). "Zur Kalibrierung der Phasenzentrumsvariationen von GPS-Antennen für die hochpräzise Positionsbestimmung." PhD thesis. Universität Hannover, p. 215. URL: <https://www.deutsche-digitale-bibliothek.de/binary/04TVNXLG2DA52V42XINY35TIL5TU6R4M/full/1.pdf>.
- Mervart, L., Lukes, Z., Rocken, C., and Iwabuchi, T. (2008). "Precise Point Positioning With Ambiguity Resolution In Real-Time." In: *Proceedings of the 21st International Technical Meeting of the Satellite Division of The Institute of Navigation (ION GNSS 2008)*. September. Savannah, GA, pp. 397–405. URL: <https://www.ion.org/publications/abstract.cfm?articleID=7969>.
- Meyer, U., Jäggi, A., Jean, Y., and Beutler, G. (May 2016). "AIUB-RL02: an improved time-series of monthly gravity fields from GRACE data." In: *Geophysical Journal International* 205.2, pp. 1196–1207. ISSN: 0956-540X. DOI: [10.1093/gji/ggw081](https://doi.org/10.1093/gji/ggw081).

## Bibliography

- Misra, P. and Enge, P. (2006). *Global positioning system: signals, measurements, and performance*. Ganga-Jamuna Press. ISBN: 0-9709544-1-7. URL: <http://www.gpstextbook.com/>.
- Mohr, P. J., Taylor, B. N., and Newell, D. B. (June 2008). "CODATA recommended values of the fundamental physical constants: 2006." In: *Reviews of Modern Physics* 80.2, pp. 633–730. DOI: [10.1103/RevModPhys.80.633](https://doi.org/10.1103/RevModPhys.80.633).
- Montenbruck, O., Andres, Y., Bock, H., Van Helleputte, T., Van Den Ijssel, J., Loiselet, M., Marquardt, C., Silvestrin, P., Visser, P., and Yoon, Y. (Apr. 2008). "Tracking and orbit determination performance of the GRAS instrument on MetOp A." In: *GPS Solutions* 12.4, pp. 289–299. ISSN: 10805370. DOI: [10.1007/s10291-008-0091-2](https://doi.org/10.1007/s10291-008-0091-2).
- Montenbruck, O., Garcia-Fernandez, M., Yoon, Y., Schön, S., and Jäggi, A. (Jan. 2009). "Antenna phase center calibration for precise positioning of LEO satellites." In: *GPS Solutions* 13.1, pp. 23–34. ISSN: 1080-5370. DOI: [10.1007/s10291-008-0094-z](https://doi.org/10.1007/s10291-008-0094-z).
- Montenbruck, O. and Kroes, R. (Aug. 2003). "In-flight performance analysis of the CHAMP BlackJack GPS Receiver." In: *GPS Solutions* 7.2, pp. 74–86. ISSN: 1080-5370. DOI: [10.1007/s10291-003-0055-5](https://doi.org/10.1007/s10291-003-0055-5).
- Montenbruck, O. and Gill, E. (2000). *Satellite Orbits*. Berlin, Heidelberg: Springer Berlin Heidelberg. ISBN: 978-3-540-67280-7. DOI: [10.1007/978-3-642-58351-3](https://doi.org/10.1007/978-3-642-58351-3).
- Montenbruck, O., Hauschild, A., Andres, Y., Engeln, A. von, and Marquardt, C. (Apr. 2013). "(Near-)real-time orbit determination for GNSS radio occultation processing." In: *GPS Solutions* 17.2, pp. 199–209. ISSN: 1080-5370. DOI: [10.1007/s10291-012-0271-y](https://doi.org/10.1007/s10291-012-0271-y). URL: <http://link.springer.com/10.1007/s10291-012-0271-y>.
- NASA (2001). *Black Jack GPS Receiver*. Pasadena. URL: <http://www.techbriefs.com/component/content/article/ntb/tech-briefs/electronics-and-computers/7350>.
- Neeck, S. P. and Vaze, P. V. (2008). "The Ocean Surface Topography Mission (OSTM)." In: vol. 7106. DOI: [10.1117/12.803677](https://doi.org/10.1117/12.803677).
- Pearlman, M. R., Degnan, J. J., and Bosworth, J. M. (2002). "The International Laser Ranging Service." In: *Advances in Space Research* 30.2, pp. 135–143. ISSN: 02731177. DOI: [10.1016/S0273-1177\(02\)00277-6](https://doi.org/10.1016/S0273-1177(02)00277-6).
- Petit, G. and Luzum, B. (2010). "IERS Conventions (2010)." In: ISSN: 1019-4568. URL: <http://www.iers.org/TN36/>.
- Petrie, E. J., Hernández-Pajares, M., Spalla, P., Moore, P., and King, M. A. (Nov. 2010). "A Review of Higher Order Ionospheric Refraction Effects on Dual Frequency GPS." In: *Surveys in Geophysics* 32.3, pp. 197–253. ISSN: 0169-3298. DOI: [10.1007/s10712-010-9105-z](https://doi.org/10.1007/s10712-010-9105-z).
- Pi, X., Mannucci, A. J., Lindqwister, U. J., and Ho, C. M. (1997). "Monitoring of global ionospheric irregularities using the Worldwide GPS Network." In: *Geophysical Research Letters* 24, p. 2283. ISSN: 0094-8276. DOI: [10.1029/97GL02273](https://doi.org/10.1029/97GL02273).
- Prange, L. (2010). "Global Gravity Field Determination Using the GPS Measurements Made Onboard the Low Earth Orbiting Satellite CHAMP." PhD thesis. ISBN: 978-3-908440-25-3. URL: <http://www.sgc.ethz.ch/sgc-volumes/sgk-81.pdf>.

## Bibliography

- Reigber, C., Lühr, H., and Schwintzer, P. (July 2002). "CHAMP mission status." In: *Advances in Space Research* 30.2, pp. 129–134. ISSN: 02731177. DOI: [10.1016/S0273-1177\(02\)00276-4](https://doi.org/10.1016/S0273-1177(02)00276-4).
- Reigber, C., Schwintzer, P., and Lühr, H. (1999). "The CHAMP geopotential mission." In: *Bollettino di Geofisica Teorica ed Applicata* 40.3-4, pp. 285–289. ISSN: 00066729.
- Reigber, C., Schwintzer, P., Neumayer, K. H., Barthelmes, F., König, R., Förste, C., Balmino, G., Biancale, R., Lemoine, J. M., Loyer, S., Bruinsma, S., Perosanz, F., and Fayard, T. (2003). "The CHAMP-only earth gravity field model EIGEN-2." In: *Advances in Space Research* 31.8, pp. 1883–1888. ISSN: 02731177. DOI: [10.1016/S0273-1177\(03\)00162-5](https://doi.org/10.1016/S0273-1177(03)00162-5).
- Reubelt, T., Austen, G., and Grafarend, E. (Aug. 2003). "Harmonic analysis of the Earth's gravitational field by means of semi-continuous ephemerides of a low Earth orbiting GPS-tracked satellite. Case study: CHAMP." In: *Journal of Geodesy* 77.5-6, pp. 257–278. ISSN: 0949-7714. DOI: [10.1007/s00190-003-0322-9](https://doi.org/10.1007/s00190-003-0322-9).
- Rew, R. and Davis, G. (July 1990). "NetCDF: an interface for scientific data access." In: *IEEE Computer Graphics and Applications* 10.4, pp. 76–82. ISSN: 0272-1716. DOI: [10.1109/38.56302](https://doi.org/10.1109/38.56302).
- Rocken, C., Kuo, Y.-H., Schreiner, W. S., Hunt, D., Sokolovskiy, S., and McCormick, C. (Mar. 2000). "COSMIC system description." In: *Terrestrial, Atmospheric and Oceanic Science* 11, pp. 21–52. URL: <http://tao.cgu.org.tw/pdf/v111p021.pdf>.
- Rothacher, M. and Schmid, R. (Sept. 2010). *ANTEX: The Antenna Exchange Format, Version 1.4*. Forschungseinrichtung Satellitengeodäsie, TU München. URL: <ftp://igs.org/pub/station/general/antex14.txt>.
- Rothacher, M., Tapley, B. D., Reigber, C., Koenig, R., Falck, C., Grunwaldt, L., Koehler, W., Massmann, F. H., and Michalak, G. (2007). "The tracking, occultation and ranging (TOR) instrument onboard TerraSAR-X and on TanDEM-X." In: *International Geoscience and Remote Sensing Symposium (IGARSS)*. Ieee, pp. 4983–4986. ISBN: 1424412129. DOI: [10.1109/IGARSS.2007.4423980](https://doi.org/10.1109/IGARSS.2007.4423980).
- Rummel, R., Yi, W., and Stummer, C. (Nov. 2011). "GOCE gravitational gradiometry." In: *Journal of Geodesy* 85.11, pp. 777–790. ISSN: 0949-7714. DOI: [10.1007/s00190-011-0500-0](https://doi.org/10.1007/s00190-011-0500-0). URL: <http://link.springer.com/10.1007/s00190-011-0500-0>.
- Savcenko, R. and Bosch, W. (2008). "EOT08a" Empirical ocean tide model from multi-mission satellite altimetry." In: *Deutsches Geodätisches Forschungsinstitut Report* 81, p. 37. DOI: [10013/epic.43894.d001](https://doi.org/10.1001/epic.43894.d001).
- Schaer, S. (1999). "Mapping and Predicting the Earth's Ionosphere Using the Global Positioning System." PhD thesis, p. 228. ISBN: 9783908440017. URL: <http://www.sgc.ethz.ch/sgc-volumes/sgk-59.pdf>.
- Schmid, R., Dach, R., Collilieux, X., Jäggi, A., Schmitz, M., and Dilssner, F. (Apr. 2016). "Absolute IGS antenna phase center model igs08.atx: status and potential improvements." In: *Journal of Geodesy* 90.4, pp. 343–364. ISSN: 0949-7714. DOI: [10.1007/s00190-015-0876-3](https://doi.org/10.1007/s00190-015-0876-3).
- Schmid, R., Rothacher, M., Thaller, D., and Steigenberger, P. (Apr. 2005). "Absolute phase center corrections of satellite and receiver antennas." In: *GPS Solutions* 9.4,

## Bibliography

- pp. 283–293. ISSN: 1080-5370. DOI: [10.1007/s10291-005-0134-x](https://doi.org/10.1007/s10291-005-0134-x). URL: <http://www.springerlink.com/index/10.1007/s10291-005-0134-x>.
- Schmid, R., Steigenberger, P., Gendt, G., Ge, M., and Rothacher, M. (Apr. 2007). “Generation of a consistent absolute phase-center correction model for GPS receiver and satellite antennas.” In: *Journal of Geodesy* 81.12, pp. 781–798. ISSN: 0949-7714. DOI: [10.1007/s00190-007-0148-y](https://doi.org/10.1007/s00190-007-0148-y). URL: <http://www.springerlink.com/index/10.1007/s00190-007-0148-y>.
- Schneider, M. (1968). *A general method of orbit determination*. Farnborough.
- Schönemann, E. (2014). “Analysis of GNSS raw observations in PPP solutions.” PhD thesis. Technische Universität Darmstadt, p. 133. ISBN: 9783935631310. URL: [http://tuprints.ulb.tu-darmstadt.de/3843/7/Schoenemann\\_Dissertation\\_TUD.pdf](http://tuprints.ulb.tu-darmstadt.de/3843/7/Schoenemann_Dissertation_TUD.pdf).
- Schutz, B. E., Tapley, B. D., Abusali, P. A. M., and Rim, H. J. (Sept. 1994). “Dynamic orbit determination using GPS measurements from TOPEX/POSEIDON.” en. In: *Geophysical Research Letters* 21.19, pp. 2179–2182. ISSN: 00948276. DOI: [10.1029/94GL01040](https://doi.org/10.1029/94GL01040). URL: <http://onlinelibrary.wiley.com/doi/10.1029/94GL01040/abstract>.
- Schwintzer, P., Förste, C., and Reigber, C. (2002). *Format Description: The CHAMP Data Format*. GFZ Potsdam. URL: [http://op.gfz-potsdam.de/champ/docs\\_CHAMP/CH-GFZ-FD-001.pdf](http://op.gfz-potsdam.de/champ/docs_CHAMP/CH-GFZ-FD-001.pdf).
- SERCO/DATAMAT Consortium (2006). *GOCE L1B Products User handbook*. European Space Agency. URL: [https://earth.esa.int/c/document\\_library/get\\_file?folderId=14168&name=DLFE-772.pdf](https://earth.esa.int/c/document_library/get_file?folderId=14168&name=DLFE-772.pdf).
- Shi, J. (2012). “Precise Point Positioning Integer Ambiguity Resolution with Decoupled Clocks.” PhD thesis. University of Calgary, pp. 1–192. URL: [http://www.ucalgary.ca/engo\\_webdocs/YG/12.20367\\_JunboShi.pdf](http://www.ucalgary.ca/engo_webdocs/YG/12.20367_JunboShi.pdf).
- Shi, J. and Gao, Y. (Oct. 2014). “A comparison of three PPP integer ambiguity resolution methods.” In: *GPS Solutions* 18.4, pp. 519–528. ISSN: 1080-5370. DOI: [10.1007/s10291-013-0348-2](https://doi.org/10.1007/s10291-013-0348-2).
- Shirtiliffe, G. M. (2007). “Jason-1 JPL Project Status.” In: *Ocean Surface Topography Science Team Meeting 2007*. Jet Propulsion Laboratory, California Institute of Technology, pp. 1–74. URL: [http://www.marine.csiro.au/conf/ostst/talks/MonPlen/NASA\\_Jason-1\\_Status%20shirtiliffe.ppt](http://www.marine.csiro.au/conf/ostst/talks/MonPlen/NASA_Jason-1_Status%20shirtiliffe.ppt).
- Shirtiliffe, G. M. (2009). “Jason-1 Project Status.” In: *Ocean Surface Topography Science Team Meeting*. June, pp. 1–27. URL: <http://www.avisioceanobs.com/fileadmin/documents/OSTST/2009/oral/Shirtiliffe.pdf>.
- Shirtiliffe, G. and Guinle, T. (2014). *GPSP instrument status and potential impacts for Users*. URL: [http://www.avisio.altimetry.fr/en/news/front-page-news/news-detail.html?tx\\_ttnews\[tt\\_news\]=1681&cHash=2e7512ef2e35475b4cc31cc77b34546d&type=123](http://www.avisio.altimetry.fr/en/news/front-page-news/news-detail.html?tx_ttnews[tt_news]=1681&cHash=2e7512ef2e35475b4cc31cc77b34546d&type=123).
- Siemes, C., Teixeira Encarnação, J. G., Doornbos, E., Peresty, R., Grunwaldt, L., Kraus, J., Olsen, P., IJssel, J. van den, Flury, J., and Apelbaum, G. (2015). *Processing of Swarm Accelerometer Data into Thermospheric Neutral Densities*. presented at AGU Fall Meeting.

## Bibliography

- Abstract SA31D-2371. San Francisco, California. URL: <http://abstractsearch.agu.org/meetings/2015/FM/SA31D-2371.html>.
- Sinander, P. and Silvestrin, P. (2000). "Development of an Advanced GPS GLONASS ASIC." In: URL: [https://amstel.estec.esa.int/tecedm/website/docs\\_generic/AGGA2Intro.pdf](https://amstel.estec.esa.int/tecedm/website/docs_generic/AGGA2Intro.pdf).
- Stolle, C. (2013). *Swarm Level 2 Processing System - Product specification for L2 Products and Auxiliary Products*. National Space Institute " DTU Space. URL: [https://earth.esa.int/documents/10174/1514862/Swarm\\_L2\\_Product\\_Specification](https://earth.esa.int/documents/10174/1514862/Swarm_L2_Product_Specification).
- Švehla, D. and Rothacher, M. (June 2003). "Kinematic and reduced-dynamic precise orbit determination of low earth orbiters." In: *Advances in Geosciences* 1, pp. 47–56. ISSN: 1680-7359. DOI: [10.5194/adgeo-1-47-2003](https://doi.org/10.5194/adgeo-1-47-2003).
- Švehla, D. and Rothacher, M. (2005). "Kinematic Precise Orbit Determination for Gravity Field Determination." In: *A Window on the Future of Geodesy* 128, pp. 181–188. DOI: [10.1007/3-540-27432-4\\_32](https://doi.org/10.1007/3-540-27432-4_32). URL: [http://link.springer.com/10.1007/3-540-27432-4\\_32](http://link.springer.com/10.1007/3-540-27432-4_32).
- Swatschina, P. (2012). "Dynamic and Reduced-Dynamic Precise Orbit Determination of Satellites in Low Earth Orbits." In: *Geowissenschaftliche Mitteilungen* 89.89. ISSN: 1811-8380. URL: [https://geo.tuwien.ac.at/fileadmin/editors/GM/GM89\\_swatschina.pdf](https://geo.tuwien.ac.at/fileadmin/editors/GM/GM89_swatschina.pdf).
- Tapley, B. D., Bettadpur, S., Watkins, M., and Reigber, C. (May 2004). "The gravity recovery and climate experiment: Mission overview and early results." In: *Geophysical Research Letters* 31.9. ISSN: 00948276. DOI: [10.1029/2004GL019920](https://doi.org/10.1029/2004GL019920).
- Thales Alenia Space (2012). *Gps receivers solutions*. Thales Alenia Space. Milano. URL: [https://www.thalesgroup.com/sites/default/files/asset/document/GPS\\_receivers\\_Solutions092012.pdf](https://www.thalesgroup.com/sites/default/files/asset/document/GPS_receivers_Solutions092012.pdf).
- Themens, D. R., Jayachandran, P. T., and Langley, R. B. (Sept. 2015). "The nature of GPS differential receiver bias variability: An examination in the polar cap region." In: *Journal of Geophysical Research: Space Physics* 120.9, pp. 8155–8175. ISSN: 21699380. DOI: [10.1002/2015JA021639](https://doi.org/10.1002/2015JA021639).
- Thomsen, P. L. and Hansen, F. (1999). "Danish Oersted Mission In-Orbit Experiences and Status of The Danish Small Satellite Programme." In: *13th Annual AIAA/USU Conference on Small Satellites*, pp. 1–8. URL: <http://digitalcommons.usu.edu/cgi/viewcontent.cgi?article=2118&context=smallsat>.
- Tiberius, C. and Kenselaar, F. (2000). "Estimation of the stochastic model for GPS code and phase observables." In: *Survey Review* 35.277, pp. 441–454. ISSN: 00396265. DOI: [10.1179/003962600791520686](https://doi.org/10.1179/003962600791520686).
- Tikhonov, A. N. (1963). "Solution of Incorrectly Formulated Problems and the Regularization Method." In: *Sov. Math. Dokl.* 4, pp. 1035–1038.
- Tøffner-Clausen, L. (Oct. 2013). *Swarm Level 1b Product Definition*. National Space Institute, Technical University of Denmark. URL: <https://earth.esa.int/web/guest/document-library/browse-document-library/>.

## Bibliography

- Touboul, P., Willemenot, E., Foulon, B., and Josselin, V. (1999). "Accelerometers for CHAMP, GRACE and GOCE space missions: Synergy and evolution." In: *Bollettino di Geofisica Teorica ed Applicata* 40.3-4, pp. 321–327. ISSN: 00066729. URL: [http://www3.ogs.trieste.it/bgta/pdf/bgta40.3.4\\_TOUBOUL.pdf](http://www3.ogs.trieste.it/bgta/pdf/bgta40.3.4_TOUBOUL.pdf).
- Touboul, P., Foulon, B., and Le Clerc, G. M. (1998). "STAR, the accelerometer of the geodesic mission CHAMP." In: *49th, International astronomical congress*. Melbourne, Australia: International Astronomical Federation. URL: <http://cat.inist.fr/?aModele=afficheN&cpsidt=56987>.
- Tseng, T. P., Hwang, C., and Yang, S. K. (2012). "Assessing attitude error of FORMOSAT-3/COSMIC satellites and its impact on orbit determination." In: *Advances in Space Research* 49.9, pp. 1301–1312. ISSN: 02731177. DOI: [10.1016/j.asr.2012.02.007](https://doi.org/10.1016/j.asr.2012.02.007).
- UCAR (Apr. 12, 2016). *Algorithm Description for LEO Precision Orbit Determination with Bernese v5.0 at CDAAC*. URL: <http://cdaac-www.cosmic.ucar.edu/cdaac/doc/documents/pod.pdf> (visited on 04/12/2016).
- van den IJssel, J., Encarnação, J., Doornbos, E., and Visser, P. (Sept. 2015). "Precise science orbits for the Swarm satellite constellation." In: *Advances in Space Research* 56.6, pp. 1042–1055. ISSN: 02731177. DOI: [10.1016/j.asr.2015.06.002](https://doi.org/10.1016/j.asr.2015.06.002).
- van Gelderen, M. and Koop, R. (May 1997). "The use of degree variances in satellite gradiometry." In: *Journal of Geodesy* 71.6, pp. 337–343. ISSN: 0949-7714. DOI: [10.1007/s001900050101](https://doi.org/10.1007/s001900050101).
- Van Helleputte, T. (2004). *GPS High Precision Orbit Determination Software Tools: User Manual*. Deutsches Zentrum für Luft- und Raumfahrt. Oberpfaffenhofen.
- Viau, P. (2003). *Earth Explorer Ground Segment File Format Standard*. ESTEC Noordwijk The Netherlands. URL: [https://earth.esa.int/documents/10174/1514862/Earth\\_Explorer\\_Ground\\_Segment\\_File\\_Format\\_Standard](https://earth.esa.int/documents/10174/1514862/Earth_Explorer_Ground_Segment_File_Format_Standard).
- Wang, M. and Gao, Y. (Sept. 2006). "GPS Un-Differenced Ambiguity Resolution and Validation." In: *Proceedings of the 19th International Technical Meeting of the Satellite Division of The Institute of Navigation (ION GNSS 2006)*. Fort Worth, Texas, pp. 292–300. URL: <https://www.ion.org/publications/abstract.cfm?articleID=6968>.
- Wermuth, M., Hauschild, A., Montenbruck, O., and Jäggi, A. (2009). "TerraSAR-X rapid and precise orbit determination." In: *21st International Symposium on Space Flight Dynamics*. Vol. 28. 1. Deutsches Zentrum für Luft- und Raumfahrt (DLR).
- Willis, P., Fagard, H., Ferrage, P., Lemoine, F. G., Noll, C. E., Noomen, R., Otten, M., Ries, J. C., Rothacher, M., Soudarin, L., Tavernier, G., and Valette, J.-J. (June 2010). "The International DORIS Service (IDS): Toward maturity." In: *Advances in Space Research* 45.12, pp. 1408–1420. ISSN: 02731177. DOI: [10.1016/j.asr.2009.11.018](https://doi.org/10.1016/j.asr.2009.11.018). URL: <http://linkinghub.elsevier.com/retrieve/pii/S0273117709007212>.
- Wilson, B. D., Yinger, C. H., Feess, W. A., and Shank, C. (Sept. 1999). "New and Improved - The Broadcast Interfrequency Biases." In: *GPS World*, pp. 56–66.
- Wirnsberger, H., Krauss, S., and Baur, O. (Nov. 2014). "Contributions of Satellite Laser Ranging to the Precise Orbit Determination of Low Earth Orbiters." In: *Dragon 3 Mid Term Results*. Vol. 724. ESA Special Publication, p. 120.

## Bibliography

- Witchayangkoon, B. (2000). "Elements of gps precise point positioning." PhD thesis. The University of Maine, p. 286. URL: [http://www.cnavgnss.com/Files/Articles/167\\_0.pdf](http://www.cnavgnss.com/Files/Articles/167_0.pdf).
- Wu, B.-H., Chu, V., Chen, P., and Ting, T. (2005a). "FORMOSAT-3/COSMIC science mission update." In: *GPS Solutions* 9.2, pp. 111–121. ISSN: 1080-5370. DOI: [10.1007/s10291-005-0140-z](https://doi.org/10.1007/s10291-005-0140-z).
- Wu, B.-H., Fu, C.-L., Liou, Y.-A., Chen, W.-J., and Pan, H.-P. (2005b). "Quantitative analysis of the errors associated with orbit uncertainty for FORMOSAT-3." In: *Proceedings of the international symposium on remote sensing (ISRS)*. URL: [https://www.researchgate.net/publication/229045267\\_Quantitative\\_analysis\\_of\\_the\\_errors\\_%20associated\\_with\\_orbit\\_uncertainty\\_for\\_FORMOSAT-3](https://www.researchgate.net/publication/229045267_Quantitative_analysis_of_the_errors_%20associated_with_orbit_uncertainty_for_FORMOSAT-3).
- Wu, J. T., Wu, S. C., Hajj, G. A., Bertiger, W. I., and Lichten, S. M. (Aug. 1992). "Effects of antenna orientation on GPS carrier phase." In: *Astrodynamics 1991*. Ed. by Blumer, P., pp. 1647–1660.
- Wu, S. C., Yunck, T. P., and Thornton, C. L. (Jan. 1991). "Reduced-dynamic technique for precise orbit determination of low earth satellites." In: *Journal of Guidance, Control, and Dynamics* 14.1, pp. 24–30. ISSN: 0731-5090. DOI: [10.2514/3.20600](https://doi.org/10.2514/3.20600). URL: <http://arc.aiaa.org/doi/10.2514/3.20600>.
- Wu, S.-c., Kruizinga, G., and Bertiger, W. (2006). *Algorithm Theoretical Basis Document for GRACE Level-1B Data Processing V1.2*. URL: [ftp://podaac.jpl.nasa.gov/allData/grace/docs/ATBD\\_L1B\\_v1.2.pdf](ftp://podaac.jpl.nasa.gov/allData/grace/docs/ATBD_L1B_v1.2.pdf).
- Wübbena, G., Schmitz, M., and Bagge, A. (2005). "PPP-RTK : Precise Point Positioning Using State-Space Representation in RTK Networks." In: *Proceedings of the 18th International Technical Meeting of the Satellite Division of The Institute of Navigation (ION GNSS 2005)*. Long Beach, California, pp. 2584–2594. URL: <http://www.ion.org/publications/abstract.cfm?articleID=6467>.
- Wübbena, G., Schmitz, M., Menge, F., Böder, V., and Seeber, G. (2000). "Automated Absolute Field Calibration of GPS Antennas in Real-Time." In: *ION GPS 2000*. Salt Lake City, pp. 19–22. URL: [http://www.geopp.com/pdf/Ion2000\\_presented\\_at.pdf](http://www.geopp.com/pdf/Ion2000_presented_at.pdf).
- Wübbena, G., Menge, F., Schmitz, M., Seeber, G., and Völksen, C. (1996). "A New Approach for Field Calibration of Absolute Antenna Phase Center Variations." In: *ION GPS-96*. Kansas City.
- Yoon, Y., Eineder, M., Yague-Martinez, N., and Montenbruck, O. (June 2009). "TerraSAR-X Precise Trajectory Estimation and Quality Assessment." In: *IEEE Transactions on Geoscience and Remote Sensing* 47.6, pp. 1859–1868. ISSN: 0196-2892. DOI: [10.1109/TGRS.2008.2006983](https://doi.org/10.1109/TGRS.2008.2006983). URL: <http://ieeexplore.ieee.org/lpdocs/epic03/wrapper.htm?arnumber=4760272>.
- Young, L. (2001). *The BlackJack GPS Space Receiver - A User Guide for ICESat*. Greenbelt, Maryland. URL: [ftp://sidacs.colorado.edu/pub/DATASETS/nsidc0587\\_ICESAT\\_GLAS\\_LTA/Section1\\_%20Preflight-Pre-Operations%20Calibration/ices-jpl-gpsu-001.pdf](ftp://sidacs.colorado.edu/pub/DATASETS/nsidc0587_ICESAT_GLAS_LTA/Section1_%20Preflight-Pre-Operations%20Calibration/ices-jpl-gpsu-001.pdf).

## Bibliography

- Zehentner, N. and Mayer-Gürr, T. (Oct. 2012). *New approach to estimate time variable gravity fields from high-low satellite tracking data*. presented at the International Symposium on Gravity, Geoid and Height Systems (GGHS 2012). Venice, Italy. URL: <http://www.iag-commission2.ch/GGHS2012/Session%203/GGHSVenice-Zehentner.pdf>.
- Zehentner, N. and Mayer-Gürr, T. (2014). "New approach to estimate time variable gravity fields from high-low satellite tracking data." In: *Gravity, Geoid and Height Systems*. Ed. by Marti, U. Vol. 141. International Association of Geodesy Symposia. Venice: Springer International Publishing, pp. 111–116. ISBN: 978-3-319-10836-0. DOI: [10.1007/978-3-319-10837-7](https://doi.org/10.1007/978-3-319-10837-7).
- Zehentner, N. and Mayer-Gürr, T. (2015). "Precise orbit determination based on raw GPS measurements." In: *Journal of Geodesy*. ISSN: 0949-7714. DOI: [10.1007/s00190-015-0872-7](https://doi.org/10.1007/s00190-015-0872-7).
- Zieger, A. R., Hancock, D., Hayne, G., and Purdy, C. (June 1991). "NASA radar altimeter for the TOPEX/POSEIDON Project." In: *Proceedings of the IEEE* 79.6, pp. 810–826. ISSN: 00189219. DOI: [10.1109/5.90160](https://doi.org/10.1109/5.90160).
- Zin, A., Landenna, S., and Conti, A. (Nov. 2006). *Satellite to Satellite Tracking Instrument*. presented at the 3rd GOCE User Workshop. URL: [http://earth.esa.int/goce06/participants/375/pres\\_zin\\_375.pdf](http://earth.esa.int/goce06/participants/375/pres_zin_375.pdf).
- Zumberge, J. F., Heflin, M. B., Jefferson, D. C., Watkins, M. M., and Webb, F. H. (1997). "Precise point positioning for the efficient and robust analysis of GPS data from large networks." In: *Journal of Geophysical Research* 102.B3, p. 5005. ISSN: 0148-0227. DOI: [10.1029/96JB03860](https://doi.org/10.1029/96JB03860).

## Acronyms

AAS	Austrian Academy of Sciences
AC	Analysis Center
ACV	Antenna Center Variation
AGGA	Advanced GPS/GLONASS ASIC
AIUB	Astronomical Institute at the University of Bern
ARP	Antenna Reference Point
ASCII	American Standard Code for Information Interchange
ASIC	Application Specific Integrated Circuit
BCRS	Barycentric Celestial Reference System
C/A-Code	Coarse Acquisition Code
C/NOFS	Communications/Navigation Outage Forecasting System
CDAAC	FORMOSAT-3/COSMIC Data Analysis and Archive Center
CDDIS	Crustal Dynamics Data Information System
CDMA	Code Division Multiple Access
CHAMP	Challenging Minisatellite Payload
CNES	Centre National d'Etudes Spatiales
CODE	Center for Orbit Determination in Europe
CoM	Center of Mass
CONAE	Comisión Nacional de Actividades Espaciales
CORISS	C/NOFS Occultation Receiver for Ionospheric Sensing and Specification
CSR	Center for Space Research
DCB	Differential Code Bias
DGPS	Differential GPS
DLL	Delay Lock Loop
DLR	German Aerospace Center
DORIS	Doppler Orbitography and Radiopositioning Integrated by Satellite
EADS	European Aeronautic Defence and Space Company
EGG	Electrostatic Gravity Gradiometer

## Acronyms

EGG-C	European GOCE Gravity Consortium
EoL	End of Lifetime
ESA	European Space Agency
ESOC	European Space Operations Centre
EUMETSAT	European Organisation for the Exploitation of Meteorological Satellites
FDMA	Frequency Division Multiple Access
FORMOSAT-3/COSMIC	Constellation Observing System for Meteorology, Ionosphere, and Climate
GCRS	Geocentric Celestial Reference System
GEO	Geostationary Earth Orbit
GFZ	German Research Center for Geosciences
GHOST	GPS High-precision Orbit Determination Software Tools
GIA	Glacial Isostatic Adjustment
GIPSY-OASIS	GNSS-Inferred Positioning System and Orbit Analysis Simulation Software
GLONASS	Globalnaja nawigazionnaja sputnikowaja sistema
GNSS	Global Navigation Satellite System
GOCE	Gravity Field and Steady-State Ocean Circulation Explorer
GOLPE	GPS Occultation and Passive reflection Experiment
GOX	GPS Occultation Experiment
GPS	Global Positioning System
GPSR	GPS/GNSS Receiver
GRACE	Gravity Recovery and Climate Experiment
GRAS	GNSS Receiver for Atmospheric Sounding
GRDC	Global Runoff Data Center
GROOPS	Gravity Recovery Object Oriented Programming System
GSFC	Goddard Space Flight Center
GSO	Geosynchronous Orbit
GUI	Graphical User Interface
HEO	Highly Elliptical Orbit
HPF	High-Level Processing Facility
IAG	International Association of Geodesy
IAU	International Astronomical Union
IDS	International DORIS Service
IERS	International Earth Rotation Service
IfG	Institute of Geodesy
IGOR	Integrated GPS and Occultation Receiver

## Acronyms

IGS	International GNSS Service
ILRS	International Laser Ranging Service
IRI	International Reference Ionosphere
ISDC	Information System and Data Center
ITRF	International Terrestrial Reference Frame
IWF	Institut für Weltraumforschung
JPL	Jet Propulsion Laboratory
LAGRANGE	LABEN GNSS Receiver for Advanced Navigation, Geodesy and Experiments
Laser	Light Amplification by Stimulated Emission of Radiation
LEO	Low Earth Orbit
LORF	Local Orbit Reference Frame
LoS	Line-of-Sight
MEO	Medium Earth Orbit
MetOp	Meteorological Operational Satellite
MSCC	Modified Satellite Clock Correction
NASA	National Aeronautics and Space Administration
NetCDF	Network Common Data Format
NOAA	National Oceanic and Atmospheric Administration
ONERA	Office National d'Études et de Recherches Aérospatiales
OSTM	Ocean Surface Topography Mission
PCO	Phase Center Offset
PCV	Phase Center Variation
PLL	Phase Lock Loop
PO.DAAC	Physical Oceanography Distributed Active Archive Center
POD	Precise Orbit Determination
PPP	Precise Point Positioning
PRN	Pseudo Random Number
radar	Radio Detection and Ranging
RINEX	Receiver Independent Exchange Format
RMS	Root Mean Square
ROTI	Rate of TEC Index
RTK	Real Time Kinematic
SAC-C	Satélite de Aplicaciones Científicas-C

## Acronyms

SAR	Synthetic Aperture radar
SLR	Satellite Laser Ranging
SNR	Signal to Noise Ratio
SPP	Single Point Positioning
SSALTO	Segment sol Multi-Missions d'Altimetrie, d'Orbitographie et de Localisation Précise
SST-hl	Satellite-to-Satellite Tracking in high-low mode
SSTI	Satellite-to-Satellite Tracking Instrument
STEC	Slant TEC
SVN	Satellite Vehicle Number
TanDEM-X	TerraSAR-X-Add-on for Digital Elevation Measurements
TEC	Total Electron Content
TOR	Tracking, Occultation and Ranging
TRF	Terrestrial Reference Frame
TRS	Terrestrial Reference System
TRSR	Turbo Rogue Space Receiver
UCAR	University Corporation for Atmospheric Research
UPD	Uncalibrated Phase Delay
USO	Ultra Stable Oscillator
VLBI	Very Long Baseline Interferometry
VTEC	Vertical TEC
XML	Extensible Markup Language

## List of Figures

2.1	Illustration of Keplerian elements. . . . .	3
2.2	Illustration of the three coordinate systems related to the orbit, the satellite and the antenna. . . . .	6
2.3	Three different variations of degree amplitudes. . . . .	8
3.1	Artist's impression of the CHAMP satellite. . . . .	14
3.2	Rear section of the CHAMP satellite with three different GPS antennas. . . . .	15
3.3	Artist's impression of the GRACE satellites in orbit. . . . .	17
3.4	Artist's impression of the GOCE satellite in orbit around the Earth. . . . .	19
3.5	LAGRANGE receiver (left) and helix antenna (right) used for the GOCE mission. . . . .	20
3.6	Illustration of the three Swarm satellites. . . . .	21
3.7	Patch excited cup antenna used on all Swarm satellites. . . . .	22
3.8	Artist's view of the two satellites TerraSAR-X and TanDEM-X in close formation above the Earth's surface. . . . .	23
3.9	IGOR receiver and antennas used on TerraSAR-X and TanDEM-X. . . . .	24
3.10	The MetOp A satellite in its orbit above the Earth. . . . .	25
3.11	The POD antenna (left) and the GRAS electronics unit (right) used for both MetOp missions. . . . .	25
3.12	Argentinian satellite SAC-C and POD antenna position. . . . .	26
3.13	Illustration of the Jason 2/OSTM satellite in orbit (left) and GPS antennas with choke rings for POD (right). . . . .	27
3.14	Illustration of the C/NOFS satellite in orbit. . . . .	29
3.15	Illustration of the FORMOSAT-3/COSMIC satellite in orbit and stacked for launch. . . . .	30
4.1	Principle of pseudo range positioning in 2D space. . . . .	33
4.2	Example of GPS clock corrections. . . . .	39
4.3	Schematic view of the ionospheric structure. . . . .	42
4.4	Illustration of the ionospheric bending effect on GNSS signals. . . . .	44
4.5	Estimated receiver ACVs for GRACE A. . . . .	56
4.6	Triangle vertex distribution of level 20 and border of 17° spherical cap. . . . .	57
4.7	Estimated transmitter ACVs for SVN 44. . . . .	58
4.8	Estimated observation accuracies for GRACE A, L1 (left), P1 (middle), and P2 (right). . . . .	63

## List of Figures

5.1	Screen shot of the GROOPS GUI showing an example configuration for POD. . . . .	68
5.2	Flow chart of necessary steps for precise kinematic orbit determination. .	72
6.1	ACVs for GRACE A when occultation antenna is switched off or on, for phase and code observations. . . . .	80
6.2	Estimated P2 code correction for SAC-C for different periods. . . . .	81
6.3	GOCE ACVs estimates with different maximum degree and order of the spherical harmonics expansion and the difference between those two. . .	82
6.4	Degree amplitudes of two different GOCE gravity fields based on orbits applying ACV with different resolutions. . . . .	83
6.5	Rotational mean of estimated transmitter ACVs compared to IGS values for L1 and L2 phase observations. . . . .	84
6.6	Difference of estimated transmitter ACVs (phase L1 and L2) to IGS corrections for all satellites used since the transition to IGS08. . . . .	86
6.7	Estimated transmitter ACVs for P1 code observations for all satellites used since the transition to IGS08. . . . .	87
6.8	Estimated transmitter ACVs for P2 code observations for all satellites used since the transition to IGS08. . . . .	88
6.9	Estimated daily receiver DCBs for GRACE A, GRACE B, TerraSAR-X, Jason 2, and GOCE from 2012 until 2014. . . . .	89
6.10	L1 phase observation accuracy maps for CHAMP, GOCE, GRACE A, Jason 2, and TerraSAR-X. . . . .	90
6.11	P2 code observation accuracy maps for CHAMP, GOCE, GRACE A, Jason 2, and TerraSAR-X. . . . .	91
6.12	P2 code accuracy maps for SAC-C for four different periods. . . . .	91
6.13	Degree amplitudes of gravity field solutions based on GRACE A orbits for January 2012. Kinematic orbits computed with different settings described in table 6.13. . . . .	93
6.14	Difference in geoid height between monthly GOCE solutions for October 2010 and GOCO05S. . . . .	94
6.15	Difference in geoid height between GOCO05S and monthly GOCE solutions for October 2010. Left: no ROTI scale function applied, right: ROTI scale function used. . . . .	96
6.16	Illustration of the FORMOSAT-3/COSMIC satellite geometry and the projection used to combine the data sets of two POD antennas. . . . .	97
7.1	Orbit differences between kinematic and reduced-dynamic GOCE orbits.	100
7.2	Daily CHAMP orbit RMS, computed at IfG and AIUB. . . . .	102
7.3	Daily GOCE orbit RMS. . . . .	104
7.4	Daily RMS of the kinematic GRACE A and B orbits. . . . .	105
7.5	Daily RMS of the kinematic Swarm orbits, computed at IfG, AIUB, and TU Delft. . . . .	108

## List of Figures

7.6	Daily RMS of the kinematic TerraSAR-X and TanDEM-X orbit. . . . .	109
7.7	Daily RMS of the kinematic MetOp A and B orbit. . . . .	110
7.8	Daily RMS of the kinematic SAC-C orbit. . . . .	111
7.9	Daily RMS of the kinematic Jason 1 and 2 orbit. . . . .	113
7.10	Daily RMS of the kinematic C/NOFS orbit. . . . .	114
7.11	Daily RMS of the kinematic FORMOSAT-3/COSMIC orbit (FM 1 - FM 6). . . . .	116
7.12	Daily RMS of GRACE K-band range residuals for IfG and AIUB kinematic orbits. . . . .	118
7.13	GRACE K-band range residuals for 01.01.2014 and 01.08.2008. . . . .	119
7.14	Monthly RMS of the SLR residuals for IfG and AIUB kinematic orbits of CHAMP. . . . .	121
7.15	Monthly RMS of the SLR residuals for IfG and AIUB kinematic orbits of GOCE. . . . .	121
7.16	Monthly RMS of the SLR residuals for IfG and AIUB kinematic orbits of GRACE A and B. . . . .	122
7.17	Monthly RMS of the SLR residuals for IfG, AIUB and ESA kinematic orbits of all three Swarm satellites. . . . .	123
7.18	Monthly RMS of the SLR residuals for IfG kinematic orbits of TerraSAR-X (blue) and TanDEM-X. . . . .	123
7.19	Monthly RMS of the SLR residuals for Jason 1 and 2 kinematic orbits. . . . .	124
7.20	Examples of monthly gravity field solutions compared to the static field GOCO05S. . . . .	128
7.21	Geoid height RMS of GOCE monthly solutions over the oceans. . . . .	130
7.22	Geoid height RMS of GRACE monthly solutions over the oceans. . . . .	130
7.23	Geoid height RMS of IfG-all and IfG-nonD over the oceans. . . . .	131
7.24	Temporal RMS of geoid height from ITSG-Grace2014 and <i>IfG-all</i> . . . . .	132
7.25	Monthly degree amplitudes for <i>ITSG-Grace2014</i> , <i>IfG-all</i> , and <i>IfG-nonD</i> . . . . .	133
7.26	Trend, annual amplitude, annual sine, and annual cosine estimated from <i>IfG-all</i> and ITSG-Grace2014. . . . .	135
7.27	Monthly area mean values for the Amazon River basin. . . . .	136
7.28	Monthly area mean values for Greenland. . . . .	137
7.29	Monthly area mean values for some example regions. . . . .	138
7.30	Correlation between IfG-all and ITSG-Grace2014 gravity field models for the 56 largest river basins worldwide. . . . .	139

## List of Tables

2.1	Orbit categories and their characteristics. . . . .	4
3.1	Most important properties of all used satellites. . . . .	31
5.1	Important data handling tools available in GROOPS. . . . .	69
5.2	Basic settings available in the program <i>GnssNetwork</i> . . . . .	70
5.3	Settings for <i>transmitterGPS</i> and <i>lowEarthOrbiter</i> . . . . .	71
6.1	Center of mass offsets for all used satellites. . . . .	78
6.2	Used PCO for different missions given in the antenna reference frame. . . . .	79
6.3	Settings for different kinematic orbit computations. . . . .	92
6.4	RMS of orbit differences with respect to official JPL reduced-dynamic orbit for different versions of kinematic GRACE A orbits and RMS of SLR residuals. . . . .	92
7.1	RMS values for along, cross, and radial component of differences between kinematic and reduced-dynamic orbits. . . . .	101
7.2	Yearly and total RMS values for the kinematic CHAMP orbits. . . . .	103
7.3	Yearly and total RMS values for the kinematic GOCE orbits. . . . .	104
7.4	Yearly and total RMS values for the kinematic GRACE orbits. . . . .	106
7.5	Total RMS values for the kinematic Swarm orbits. . . . .	107
7.6	Yearly and total RMS values for the kinematic orbits of TerraSAR-X and TanDEM-X. . . . .	109
7.7	Yearly and total RMS values for the kinematic orbits of MetOp A and B. . . . .	110
7.8	Yearly and total RMS values for the kinematic orbit of SAC-C. . . . .	112
7.9	Yearly and total RMS values for the kinematic orbits of Jason 1 and 2. . . . .	113
7.10	Yearly and total RMS values for the kinematic orbit of C/NOFS. . . . .	115
7.11	Total RMS for the kinematic orbit of FORMOSAT-3/COSMIC. . . . .	115
7.12	Laser retro reflector offsets for individual missions in the satellite body frame. . . . .	120
7.13	Total RMS and mean value of SLR residuals for different orbit solutions. . . . .	125
7.14	Settings for the gravity field estimation. . . . .	126